THE UNIVERSITY OF SHEFFIELD

Department of Mechanical Engineering

MODELLING THE IMPACT OF TENNIS BALLS ON COURT SURFACES

Richard John Dignall

Submitted for the Degree

of

Doctor of Philosophy

April 2004

THE UNIVERSITY OF SHEFFIELD

Department of Mechanical Engineering

Modelling the impact of tennis balls on court surfaces

Richard John Dignall

A model of tennis balls impacting obliquely on tennis courts was developed in this study. Balls were impacted normally on a force plate to read impact force data, and filmed at high speed during oblique impacts. A normal model was created and then extended to cover oblique impacts. The experimental data was used to verify the model in each case.

A study of surface testing methods found that tennis courts are significantly stiffer than tennis balls; so much so that they can be considered rigid. A coefficient of friction between ball and surface was all that was necessary to define a surface.

Normal impacts were performed on a force plate for four different ball constructions at speeds between 3 and 20 ms^{-1}. Impact speed had a significant effect on coefficient of restitution (ratio of rebound speed to inbound speed) – for example for a pressurised ball, from about 0.8 at an impact speed of 3 ms^{-1} to about 0.6 at 20 ms^{-1}. Pressureless balls bounce at a similar speed to pressurised balls at low impact speeds, but slower at high impact speeds. Punctured balls bounce slower throughout the range of impact speeds. All balls showed a rapid increase in force during the initial part of the impact.

An iterative model was created to simulate normal impact. A numerical method was used to find the effect of deformation shape on the relationship between centre of mass movement and ball deformation. A total force during impact was created by combining structural stiffness, material damping and impulsive reaction forces. This model worked well for all ball types and used quasi-static compression data and a low speed drop test to find the parameters. The impulsive force simulated the initial increase in force well.

A thorough experimental study of oblique impacts was performed by isolating in turn each of the key incoming properties of impact. The incoming speed, spin and angle, together with the ball and surface construction were individually varied in turn and the effect on outgoing characteristics measured using high speed video footage. In most cases there was a distinct change in rebound properties when rolling happened. Footage at up to 7000 frames per second was used to qualitatively explain the effect of deformation shapes on energy losses. It was found that impacts with backspin caused more deformation and an increased energy loss compared to normal impacts with the same vertical velocity. Impacts with topspin had a reduced vertical energy loss.

The normal model was extended to include the horizontal and rotational forces necessary to simulate an oblique impact. A damping compensation factor was included to adjust the vertical energy losses at different spin rates. The oblique test data was used to verify the model, and there was a very good correlation.

Keywords: tennis ball, impacts, tennis court, high-speed cinematography, visco-elastic modelling

Acknowledgements

Contents

This thesis is dedicated to my parents.

1   Introduction

1.1   Background of the study

The following chapters describe a three year study examining the features of tennis ball impacts on court surfaces, and creating a model to predict these impacts which could be verified by experimental data. This experimental data also provided good insights into the behaviour of a ball during impact.

The origins of the game of tennis can be traced back many hundreds of years. There is evidence in Egyptian carvings (dating from as far back as 1500 BC) for a precursor to tennis. Most historians however credit the origins of the modern game to 12th century France, where monks used their hands to hit balls against the monastery walls or over a rope strung across a courtyard, giving the game its name *jeu de paume*, or "game of the palm". Gloves were developed to protect the hand and rackets were gradually introduced from the 16th century. The game developed into what is now known as Real Tennis, and was played indoors. The development of vulcanised rubber in the 19th century led to much softer and more elastic balls, and people began to play the game outside on lawn courts. The rules of the game were developed during the 1870s and the first tournament took place in 1877 at the All England Croquet and Lawn Tennis Club in the London borough of Wimbledon.

The motivation for the research will be investigated more fully in Chapter 2, examining the evidence for recent changes in the way the game is played, and the pressure to control the sport.

This study was part-funded by the ITF (International Tennis Federation), who have also been closely involved in the work. One major reason for the project was to develop a tool which could be used by the ITF in their ongoing attempt to monitor and potentially control the effect of technology within the sport.

1.2   Aims and objectives

The overall aim of the project was to create an analytical model of a tennis ball bouncing on a court surface, and to verify the accuracy of the model.

Specific objectives are as follows,

1. To gain a solid understanding of the basic physics behind ball impacts.

2. To measure the static (or quasi-static) properties of tennis balls under compression, and to measure the dynamic properties of tennis balls impacting normally on a rigid surface by measuring forces and speeds.

3. To develop a model predicting normal impact, and verify with experimental data.

4. To perform a review and study of existing surface test methods, identify those important to an oblique model.

5. To measure the dynamic properties of tennis balls impacting obliquely on a rigid surface by measuring speeds, spins and angles, and improve understanding of the features of oblique impact.

6. To create a model predicting oblique impact on a tennis court surface, and verify against experimental data

7. To link the model to existing models of racket impact and flight. This would facilitate an assessment of the final model. To thus evaluate its effect on the game of tennis, and suggest future research.

Throughout this study, a major secondary aim was to create models which are as easy to understand and use as is practically possible, so that they can have a real usefulness. One implication of this is that model parameters should be simple to measure so that if a new ball or surface was introduced, as few measurements as possible must be taken in order to confidently predict its behaviour.

1.3   The structure of the study

The final model was constructed in a number of steps, broadly following the sequence of the objectives above. This thesis is divided into a series of chapters which follow a logical chronological order of how the work was performed.

2 Literature Review

2.1 Introduction

Over the years there has been a considerable amount of research published in the area of tennis. However, until fairly recently the work has been performed from outside the sport, often by academics with a personal interest in tennis. In 1997 the International Tennis Federation (ITF), who are based in London and are the governing body of the sport, created a Technical Centre whose aim was "*to carry out testing and research into all aspects of the game, and to provide support to the ITF Technical Commission and other ITF Committees on decisions relating to technical issues*" (ITF, 2004).

This chapter will discuss the need and motivation for research into tennis, particularly in the present day. It is divided into sections describing the various areas which must be understood in order to create a model of ball impacts. These range from the properties of the ball (and test methods for finding these properties), the aerodynamics and player data which define the scope and boundary conditions for a model, through the properties of the surface on which the ball bounces, previous work on the dynamics of ball impacts and previous attempts to model a ball (both from tennis and other sports).

2.2 The motivation for tennis research

Recent years have seen significant changes in the sport of tennis. In comparison with some other sports (for example golf) the level of both understanding and control of the physics of the game was relatively low. As the global market for sports has increased dramatically, so has the size of the game of tennis in both amateur and professional terms. The industry worldwide supplies hundreds of millions of balls annually, and many millions of rackets, shoes and other clothing equipment. In today's commercial marketplace, this industry provides a huge potential force for change. The International Tennis Federation as world governing body of the sport recognised their responsibility to understand and control the effects of technology in the game. In the introduction to the first international conference hosted by the ITF on tennis science and technology, Coe (2000) described a strategy for establishing a balance between technology and tradition. He listed a number of quotes from both current (at the time) and past players describing actual and potential problems with the speed of the game. After every Wimbledon tournament there are calls for changes to the game, most commonly in rule changes limiting the specifications of the racket. Coe used the percentage of sets which ended in a tie-break as an index to the changing speed of the game over 31 years. He showed that on all surfaces, the men's game has exhibited a steady increase in tie-breaks. There is also a clear difference between surfaces, so that the faster surfaces produce a significantly higher number of tie-breaks. This is clearly shown

by the Australian Open, where the change from grass to Rebound Ace caused a drop in tie-breaks. The women's game has a somewhat different trend, where three of the four surfaces seem to have a drop in the number of tie-breaks (although this downwards trend is arguable given the scatter).

Fisher (1977) described the introduction of a new style of racket designed by Howard Head of Prince, which was the first racket to have the now-common oversize head (Head, 1976). The increased moment of inertia about the axis of the handle was designed to reduce twisting of the racket when hit by a ball, but also increased the size of the centre of percussion (or "sweet spot") and moved it to an easier part of the racket head to use.
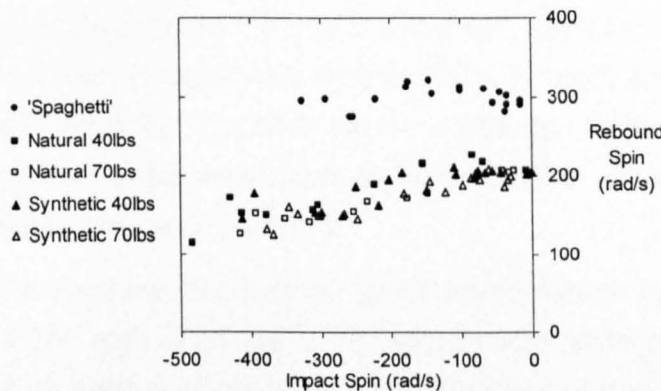
Figure 2.1 Spin generated by the "Spaghetti" strung racket compared to natural and synthetic strings (Goodwill and Haake, 2002).

Another racket innovation which had the potential to significantly change the game was the "spaghetti" stringing system (Fischer, 1977). This allowed a player to apply significantly more spin to the ball than conventional stringing, as shown in data from Goodwill and Haake (2002) in Figure 2.1. Balls were fired at a clamped racket at a speed of 23 ms^{-1} with effective backspin. The "spaghetti" strung rackets had a clear increase in rebound topspin, and this stringing system was banned by the ITF in 1978.
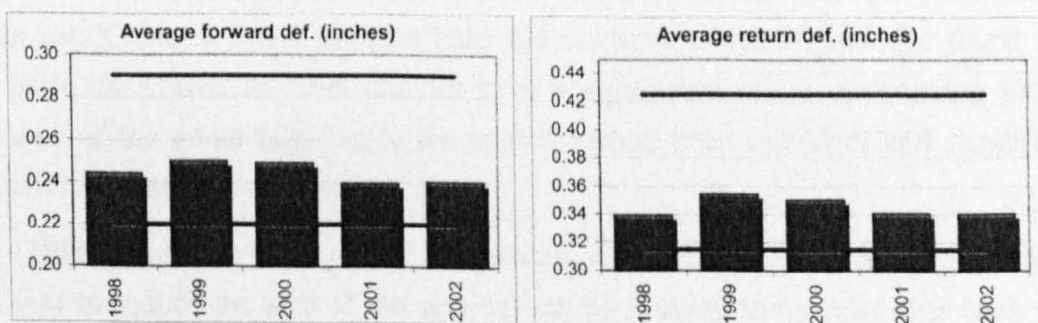
Figure 2.2 The trend in ball deformations from 1998 to 2003 (Miller, 2003).

Miller (2003) looked at the various aspects of the game to see which had the most influence on the game. He found that by splitting the tie-break information presented by

Coe (2000) into two data sets for the times when players predominately used wood and then composite rackets, the change in racket technology does not seem to be the predominant factor. Miller gave hardness information for balls based on the testing performed by the ITF since 1998, where balls were collected from tournaments and the marketplace (shown in Figure 2.2). He noted that in this admittedly small timescale, there seems to have been a trend for the balls to become harder. This means that deformation energy is stored in the strings rather than the ball, and the strings are more efficient - meaning the ball rebounds faster.

Arthur (1992) examined the effect of technology on the game, and concluded that rackets had a huge effect on the speed of the ball. He commented that simply banning certain kinds of rackets was extremely unlikely both practically and legally. Changes in the court size and shape or general rule changes (such as reverting to a single serve) would be extremely unpopular, leaving the ball as a possible source of change. Arthur suggested that making the ball softer, lighter or larger would have the desired effect of slowing it down, although he identified problems with each approach.

Haake et $al.$ (2000) tested the reactions of "good" tennis players by firing simulated serves at speeds of up to 160 mph (71.5 ms^{-1}). The speeds were measured using a radar gun. It was found that the proportion of serves returned into court decreased gradually with speed. There was also a critical speed of around 126 mph (56 ms^{-1}) where the number of aces increased dramatically. Haake et $al.$ also presented data showing that as the serve speed increased for a sample of male players at Grand Slam events, the percentage of sets ending in tie breaks also increased. A break-down of serve speed by player indicated that male players who serve significantly faster than others on a fast surface (grass at Wimbledon) do not necessarily serve faster on slower surfaces (Roland Garros and US Open). This suggests that players modify their game to play on different courts.

Magnus and Klaassen (1999) performed a statistical analysis using Wimbledon data from 1992 to 1995 of the points won on first serve to see if new balls had a benefit to the server. Magnus and Klaassen found the new balls did not have a benefit, and also found that the softer balls introduced in 1995 did not have a significant effect of reducing the serve-dominance of the game (and hence the speed) as had been intended, and suggested that more drastic measures were needed.

Brody (1986) considered one of the suggestions which had been made to slow the game, which was to reduce the size of the service box by moving the service line back towards the net. He found that a reduction of about one foot would have a reasonable effect (for example, a serve hit at 90 mph on a normal court would then have to be hit at 84 mph to have the same "window of opportunity"), but concluded that the idea was unfair as it would penalise shorter players more than taller ones.

Brody and Cross (2000) also addressed the problem of the speed of the game and discussed seven possible solutions aimed at reducing the dominance of the serve:

- Change the surface

- Limit the racket

- Eliminate the second serve

- Change the foot fault rule

- Change the ball

- Shorten the service court

- Raise the net

Although each of these would have the desired effect, Brody and Cross recognised problems with each suggestion and suggested further trials.

In an attempt to control the speed of the game, the ITF introduced the Type 3 ball in 2000, which is typically 6% larger in diameter than a conventional (or Type 2) ball. Its exact properties are described in more detail in Appendix A. Haake *et al.* (2000) provided an analysis of the effect of this ball type on the various mechanisms of a shot. They found that it rebounded off the racket faster, had the same drag coefficient and the same impact characteristics as a conventional ball. The larger diameter will lead to an increased drag force, and it was shown that this would slow the ball down approximately 10 ms on a first serve, and 16 ms on a second serve – which is about half the difference between comparing an acrylic court to a slower clay court.

Summary

There has been an obvious concern on the part of the ITF as to the speed of the game. This has provoked research both within their organisation and elsewhere into the reasons behind this and possible solutions. Evidence for increases in serve speed was demonstrated using tie-break data, and a sharp threshold in speed where players would be unable to return serves faster than a certain level. A common proposal to slow the ball has been to increase its size. This and similar measures clearly illustrate the need for understanding of the behaviour of all forms of equipment in the game.

2.3 Properties of the ball

Manufacturers and ruling bodies have been testing tennis balls for some considerable time. As far back as 1960 (Dunlop Ltd., 1960), balls were tested for compression and bounce height as part of the production process – in this case using an automated machine with photoelectric cells to sort the balls by bounce height. Stevens machines used for

compression testing by the LTA (Lawn Tennis Association, the ruling body before the ITF) date back to at least 1924 – shortly after this, the deformation test was introduced into the rules. The use of the Stevens machine is described in notes of the Wimbledon Lawn Tennis Museum by Robinson (1977).

2.3.a   Specifications of the Rules of Tennis

For a game or tournament to conform to the Rules of Tennis, the ball must be named on the official ITF list of approved balls issued by the ITF. Balls named have been tested to meet a certain set of specified criteria. Extracts from the Rules of Tennis (ITF, 2000a) giving the ball specifications are quoted in Appendix A, including the introduction of two new ball types. These are the harder (and therefore faster) Type 1 ball intended for use on slow courts, and the larger (and therefore aerodynamically slower) Type 3 ball intended for use on fast courts. Also quoted from the Rules is a list of regulations describing how each of the approval tests should be performed.

2.3.b   Experimental testing of balls

Very little work had been performed on the properties of tennis balls before the start of this project, although there has been a large amount of recent research. The fact that the core of the ball is made from a rubber compound suggests the shell is likely to have non linear and viscoelastic properties. The ball undergoes gross deformation and the shell is too thick to be approximated by any thin shell theory.

Quasi-static testing
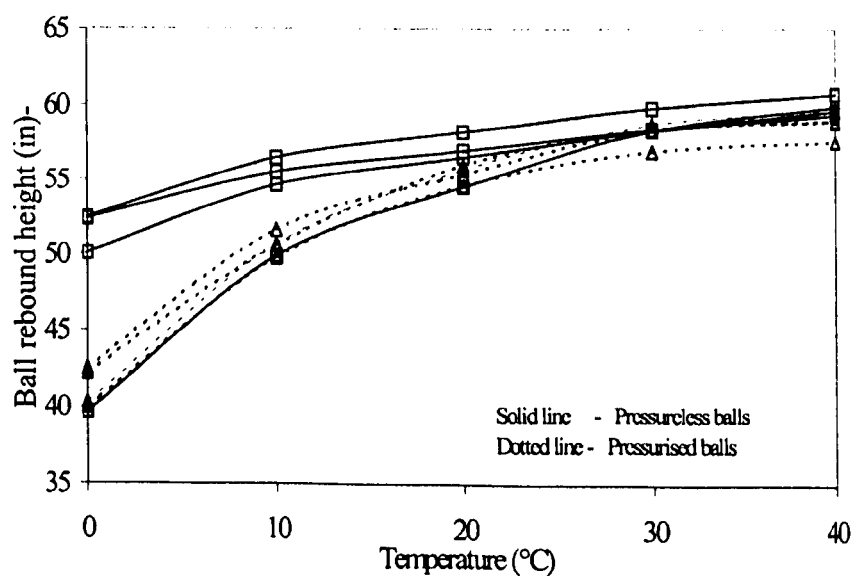
Figure 2.3 The variation of ball rebound height with temperature for a drop test from 100 inches (reproduced from Rose et al., 2000).

Rose et al. (2000) measured the properties of pressurised and pressureless tennis balls between 0 and 40°C. The tests performed were ball rebound height, ball deformation under

quasi-static loading and higher speed coefficient of restitution (up to impact speeds of 45 ms^{-1}). It was found that pressurised balls show a large variation in rebound height over the temperature range as shown in Figure 2.3, much larger than for pressureless balls. The compression test showed little change in forward or return deformation with temperature. In dynamic rebound tests at 25, 35 and 45 ms^{-1}, the COR increased slightly with temperature, in a similar manner for both ball types.

Hendee *et al.* (1998) performed quasi-static compression tests on traditional and modified baseballs (the latter designed to reduce injuries in young players), measuring average stiffness and energy loss. The balls were then fired normally onto a force plate using an air cannon at speeds between 13.4 and 40.2 ms^{-1}. For all balls tested, coefficient of restitution decreased with increasing velocity. They found no way to correlate this with quasi-static test data. Peak force of impact and impulse of impact increased with static ball stiffness and mass respectively.

(a)   (b)
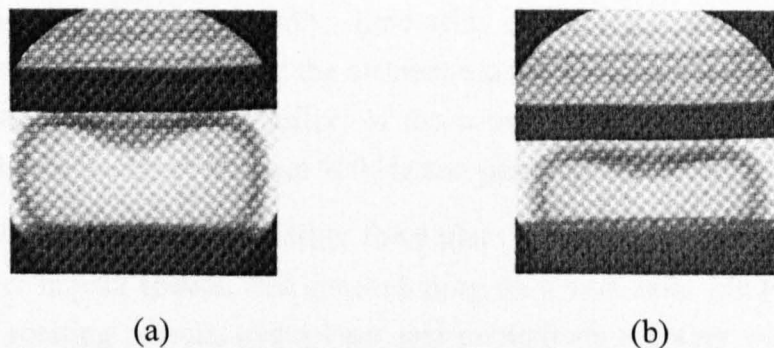
Figure 2.4 X-ray images during compression showing buckling of (a) a pressurised core and (b) a pressurised ball, from Ashcroft and Stronge (2003).

Ashcroft and Stronge (2003) looked at energy losses in tennis balls. They compressed rubber cores of pressurised and pressureless balls which had been punctured to release any pressure. Whole balls (i.e. including cloth) were also tested both with and without the respective internal pressure. For the punctured cores they found that the force-deflection obeyed a linear relationship until a point of critical deflection where the stiffness decreased. This critical deflection was about 26 mm for the core of a pressurised ball. They used X-ray images to show inversions or buckling in the balls (reproduced in Figure 2.4), although the deflection for these images is not stated. When comparing ball types, Ashcroft and Stronge noted that the pressurised ball was stiffer than the pressureless ball at all deflections, but the opposite was true when both balls were punctured. They conclude that the material hysteresis does not account for the significant energy losses during impact.

Dynamic impacts

Bernstein (1977) used a microphone to measure the time of a series of impacts of a bouncing ball and to calculate the coefficient of restitution as a function of impact number. This system was converted to a more sophisticated computer-based device by Smith *et al.*

(1981). In a similar experiment Brody (1990) used a microphone and an oscilloscope triggering a timing system to measure the time in between the first and second bounces of a tennis ball dropped from 100 inches (2.54 m) in order to produce an inexpensive bound height test.

Cross (1999a) bounced a series of balls off a piezo element mounted on a heavy brass rod. Force waveforms were measured and also compared with the results of static force-deflection compression tests. He also found that all the balls remained compressed at the end of the contact period, as the deflection value was finite. This was confirmed by aligning a laser beam to graze the top of an uncompressed ball at rest on the piezo. The beam remained blocked for about 0.5 ms after the impact, approximately 10% of the contact time.

Finally Cross glued a small piezo element to the ball in order to estimate the vibrations. He found that with the element located near the bottom of the ball the force waveform was similar to the large piezo element, with a time delay of about 0.4 ms. The pulse decreased in amplitude and changed in shape as the element moved towards the top of the ball. At the top there was only a small visible effect of the compression and expansion, but a small amplitude oscillation occurred at about 700 Hz and persisted for approximately 2 ms.

Cross (1999b, 2000b) repeated his earlier force plate tests using a ball projection machine to achieve higher impact speeds, and concentrating on tennis balls. He projected the balls using a pair of rotating wheels, and a laser and photodiode together with the force plate data to measure the impact speed. A second force plate positioned so that the ball would impact upon it unless fired in absolutely perfect alignment was used to measure the rebound speed. He found that the force increased rapidly during the first 0.2 ms of the impact, and attributed this to compression of the cloth and rubber around the impact point. An aluminium ball was then covered in cloth, rubber or both in order to investigate the effects of each material. He found that both materials obeyed an exponential force-deflection relationship, and the two stiffnesses could be combined to reproduce the effect of having both on the ball. Evidence was also presented of the ball shell buckling inwards, providing a lower stiffness after the initial peak. By using a small piezoelectric element set into a layer of circuit board, the force was measured centrally and 20 mm away from the initial point of contact. The centre force was found to have two peaks with a time period between them where the force is low. Cross also compared a pressurised and a pressureless ball impacting on the force plate at various speeds up to 15 ms^{-1}. He found the rebound speeds were very similar, but that the pressurised ball was softer, leading to a lower peak force and a longer contact time. He calculated a dynamic stiffness for the pressurised ball of 35 kN/m, which is much higher than the static stiffness of 12.6 kN/m required for the approval tests of the rules of tennis.

Brown and Cooke (2000) divided the subject into four regimes: the impact of ball and racket, the initial unsteady motion, the quasi-steady motion and the impact of ball on court. South (1996) estimated that significant large-scale deformation ends about 5 ms after impact. At a serve speed of 60 ms^{-1} (135 mph), the ball would travel 0.3 m in this time and so this vibration will have little effect.

Capel-Davies and Miller (2003) performed wear tests with three types of balls: pressurised balls with either melton or needle cloth, and pressureless balls using melton cloth. They calculated that on average balls are used in 45 shots during a game, and chose to subject the balls to 50, 100 and 150 impacts to see if the wear had an effect on the approval tests. It was found that bounce height was not affected. Mass was reduced, and this was reflected in the debris of fibres left in the impact rig. Forward and return deformations were initially increased by wear (indicating a reduction in stiffness) after the first 50 tests, but it varied by ball as to whether any further changes (all increasing) were statistically significant. Capel-Davies and Miller commented that the magnitude of any changes is about 10% of the range allowed by the Rules of Tennis.

Summary

Tennis ball testing can be divided into two main categories: static (or quasi-static) and dynamic. Static testing does not provide a huge amount of useful information, as the majority of balls intended for retail are engineered to pass the standard ITF approval tests, and thus tend to have similar properties. The same is true for low speed dynamic tests (in terms of velocities at least), as the approval specifications include a drop test. The use of a force plate has provided some useful information and suggests that there may be a buckling element to the impact, lowering the stiffness after an initial period. There is however an opportunity for much higher speed impacts, which will be considered later in this chapter.

2.4   The aerodynamics of tennis balls

In order to relate any modelling or experimentation of the impact of tennis balls on relevant surfaces to the game, it is important to know how the ball reaches the court. There is a distance of over 18 metres between the baseline and the service line in the opposing half of the court which is a significant distance for aerodynamic effects to alter a ball's behaviour.

Lindemuth (1971) used a series of photocells to capture the position relative to time of a series of different balls falling under gravity, and proved that the effect of air resistance was significant. He verified the accuracy of a force proportional to the square of the velocity.
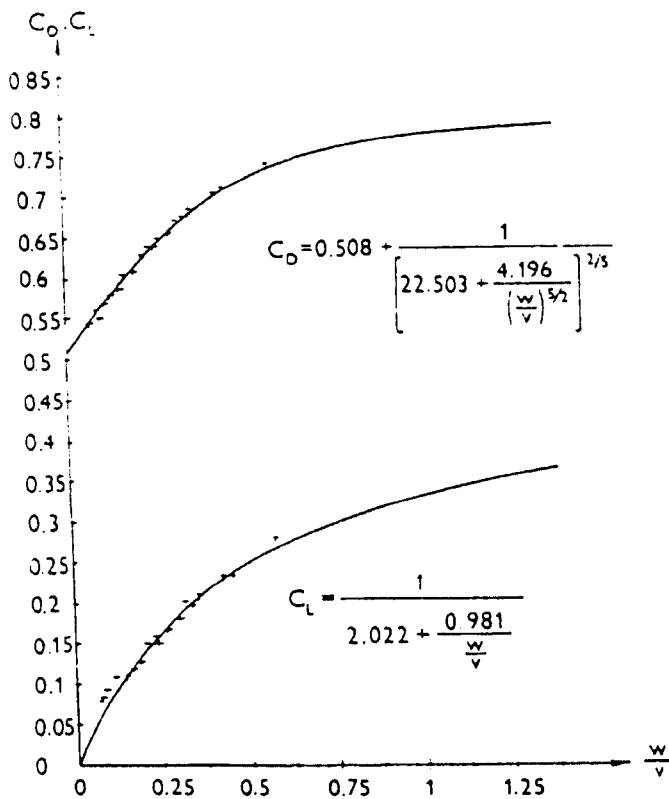
Figure 2.5 Drag and lift coefficients as a function of the w/v ratio, reproduced from Stepanek (1988).

Stepanek (1988) performed the first study of the forces produced by a spinning tennis ball. He constructed a device to drop spinning balls into the air flow of a wind tunnel and measured the variation of drag and lift coefficient with ball spin rate. The experimental data – shown in Figure 2.5 - was fitted by the following regression equations:

$$C_D = 0.508 + \left[22.503 + 4.196 \left(\frac{\omega}{v} \right)^{-\frac{5}{2}} \right]^{-\frac{2}{5}}$$

$$C_L = \left(2.022 + \frac{0.981}{\left(\frac{\omega}{v} \right)} \right)^{-1}$$

A Davis Cup player was asked to hit topspin lobs with as much spin as possible, and the shots filmed using a STALEX high-speed camera. The highest rotation achieved was around 3500 rpm (367 rads^{-1}).

Cooke (2000) gives an overview of the dynamics of a tennis ball flow through air. The physical mechanisms of the fluid flow are not relevant to this project, but Cooke concludes that the initial transient state due to ball deformations can be considered negligible. This

means that for the scope of aerodynamics necessary to predict impact speeds, the only important data are the drag and lift coefficients, as the equations of motion are well understood.
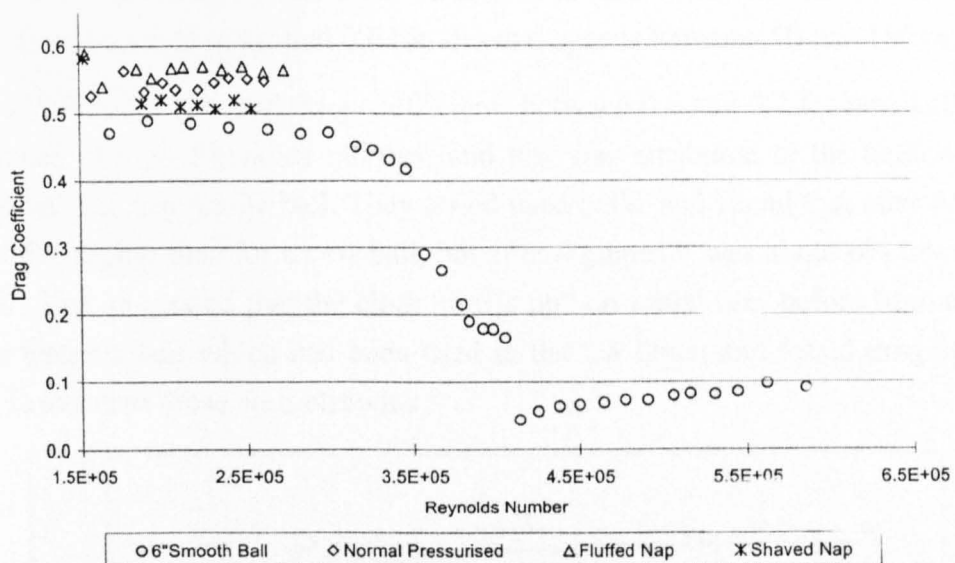
Figure 2.6 Drag coefficients measured by Chadwick and Haake (2000) for normal balls and with shaved and fluffed nap.

Chadwick and Haake (2000) measured the drag coefficient of pressurised balls with a normal napped, a raised "fluffed" nap and a shaved nap. As seen in Figure 2.6, the range of drag coefficient from the shaved to fluffed nap was around 10%. For a normal ball, the value was around 0.55. They also dropped spinning balls through a wind tunnel and filmed the trajectory at 240 frames per second. Manipulating the equations of motion and fitting them to the captured trajectory data enabled lift coefficients to be measured as well as drag coefficients but it was found that care was needed to reduce potential errors. Drag and lift coefficients of about 0.8 and 0.2 respectively were found for a ball dropped with 1600 rpm (168 rads^{-1}) through an air stream moving at 11.6 ms^{-1}.

(a)	(b)
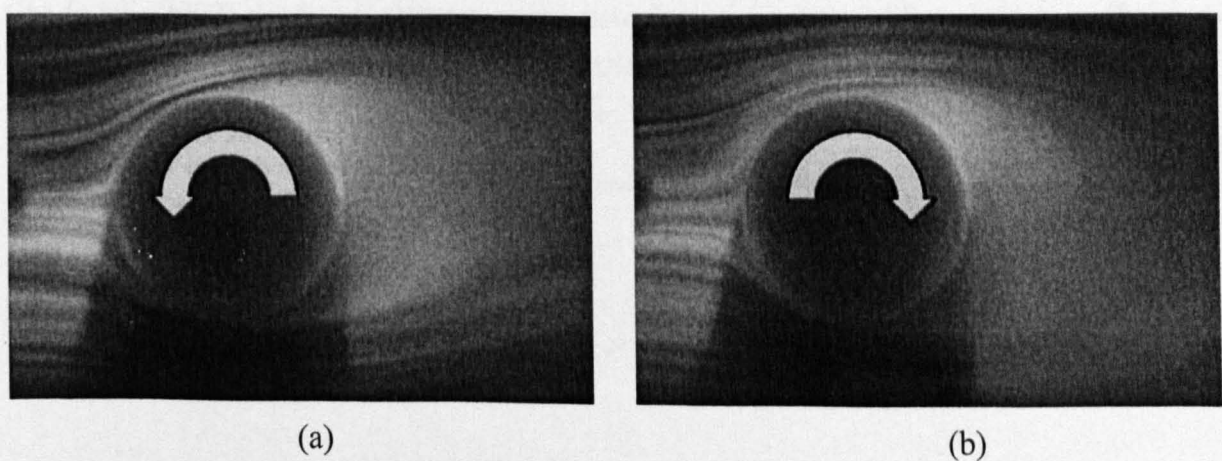
Figure 2.7 Flow visualisations for a tennis ball with (a) topspin and (b) backspin, from Pallis and Mehta (2000). The air flow is from left to right in each case.

Pallis and Mehta (2000) used an 11 inch (28 cm) novelty tennis ball to perform flow visualisation studies. With spin applied they produced clear evidence of non-symmetrical boundary layer separation leading to a Magnus force, which can be clearly seen by the offset wakes in Figure 2.7. Pallis and Mehta also measured the forces on a non-spinning ball. They found a value of around 0.6 for all wind speeds between 50 and 150 mph.

Mehta and Pallis (2001) found drag coefficients between 0.6 and 0.7 for new balls. The C_D value dropped at high Reynolds number, and this was attributed to the high wind speed "laying down" the nap on the ball. They tested used balls, and found that after 6 games C_D was about 6% higher than for a new ball, but after 9 games it was about 6% lower than for a new ball. This suggested that the cloth "fluffs up" on initial use, before becoming worn. They also tested a ball which had been used in the US Open and found drag coefficients about 0.1 lower than those seen elsewhere.
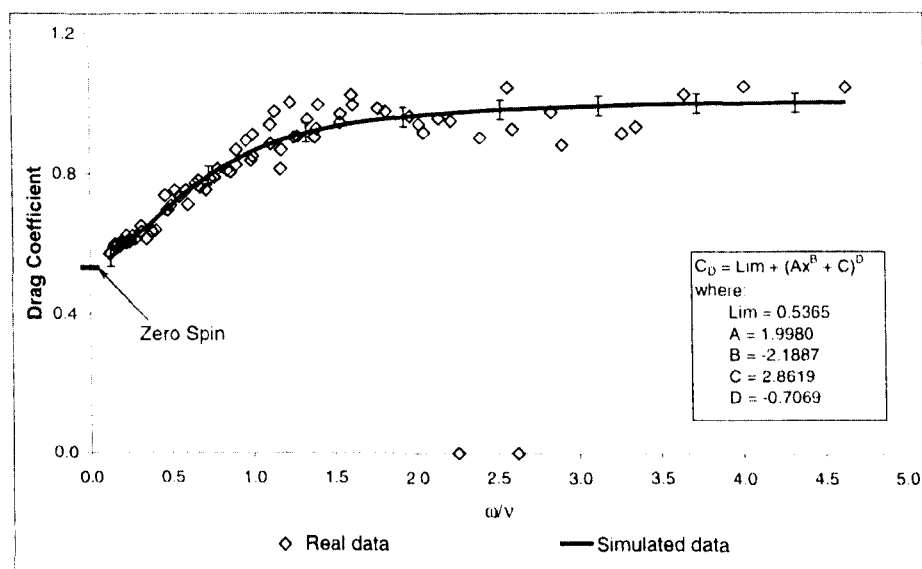
Figure 2.8 Drag coefficient versus spin ratio $\dfrac{\omega}{v}$, from Chadwick (2003).

Chadwick (2003) used two different wind tunnels and measured lift and drag coefficients. Figure 2.8 shows aggregated data for a variety of spins from zero (the static value of 0.5365) to 7300 rpm (760 rads^{-1}). An equation fitting this data was found to be

$$C_D = 0.5365 + \left(1.9980 \left(\frac{\omega}{v} \right)^{-2.1887} + 2.8619 \right)^{-0.7069}$$

with limiting values of $C_D = 0.5365$ and $C_D = 1.012$ at zero and infinite spin respectively.
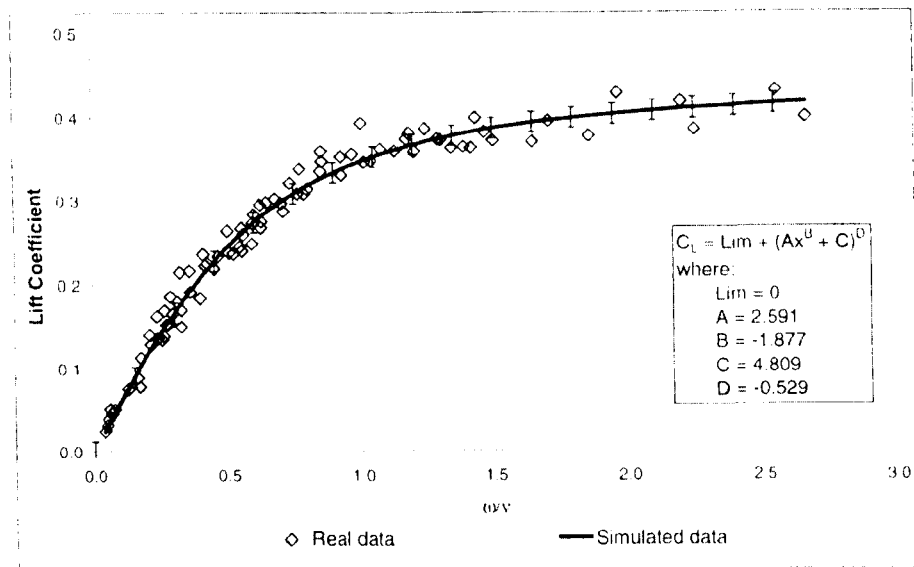
Figure 2.9 Lift coefficient versus spin ratio $\dfrac{\omega}{v}$, from Chadwick (2003).

Lift data measured at the same time produced the data shown above in Figure 2.9. The fit for this data was given by

$$C_L = \left(2.591 \left(\frac{\omega}{v} \right)^{-1.877} + 4.809 \right)^{-0.529}$$

It should be noted that for both the lift and drag data, Chadwick used a spin ratio $\left(\dfrac{\omega}{v} \right)$

where ω was defined as the equatorial velocity (*i.e.* the spin rate multiplied by the radius) rather than the conventional notation of spin rate used throughout this thesis.
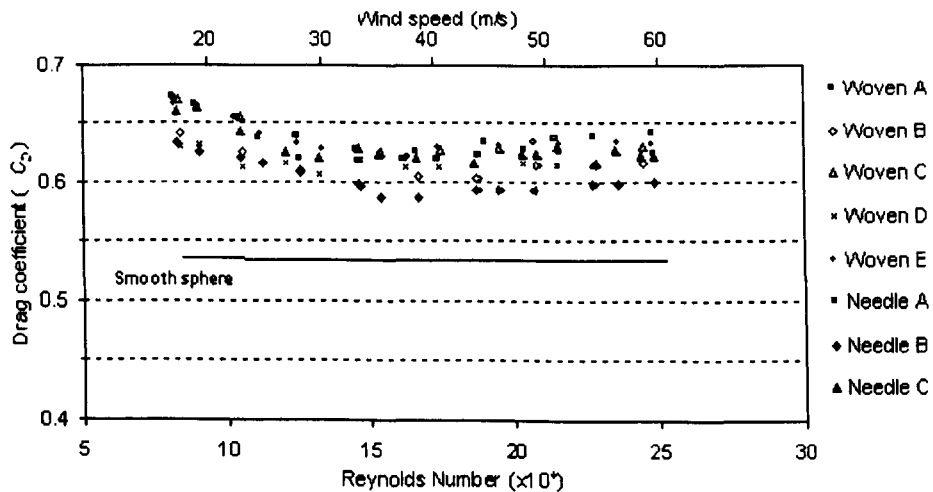
Figure 2.10 Drag coefficients for eight different non-spinning balls (Goodwill *et al.*, 2004).

Goodwill *et al.* (2004) mounted both stationary and spinning balls in a wind tunnel for speeds between 20 and 60 ms^{-1}. Drag coefficients are shown for eight different brands of ball in Figure 2.10. Most of the balls had very similar drag coefficients, except for the balls "Woven B" and "Needle B". It was not possible to show any significant difference between brands however. The drop in drag coefficient as the speed increased was attributed to the nap "laying down".

Figure 2.11 below shows drag and lift coefficients from Goodwill *et al.* for spinning balls at two different wind speeds. Data is shown for new balls and for balls which had been worn for varying numbers of impacts on a surface. They found that the drag coefficient increased with spin (or spin coefficient S, defined by dividing the circumferential speed by the wind tunnel speed) at the two Reynolds numbers tested. The balls subjected to 0 and 60 impacts showed a steady rise in C_D, from 0.65 to 0.69 at the lower wind speed. The more heavily worn balls actually show a decreased drag as spin is increased, although the amount is within the repeatability of the experiment. It is clear however that C_D for new balls is around 0.04 higher than for heavily worn balls for most spin rates. At the higher wind speed there is a general increasing trend for all balls, and again new balls exhibit a higher C_D than worn balls.

As would be expected, the lift coefficient is strongly dependent on spin, although again there was no difference with ball construction. There was little difference between new and worn balls except for a range $0.05 < S < 0.15$ – where increased number of impacts led to a lower lift coefficient - and this trend only showed at the lower wind speed.
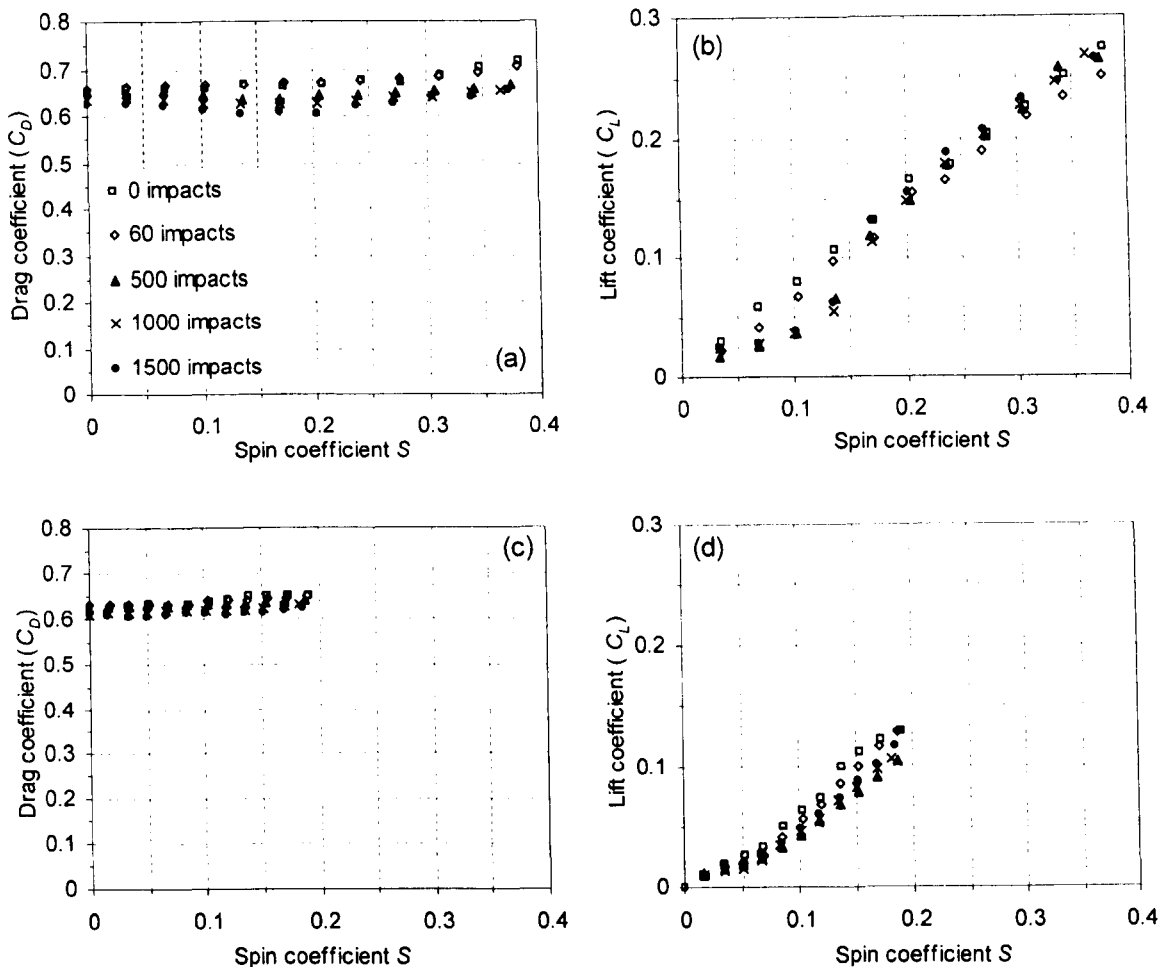
Figure 2.11 Aerodynamic coefficients found by Goodwill *et al.* (2004) for spinning balls; (a) and (b) show drag and lift coefficients respectively at a wind speed of 25 ms^{-1}, (c) and (d) show drag and lift coefficients respectively at a wind speed of 50 ms^{-1}. The same notation showing the number of impacts is used on each graph.

Summary

Tennis ball aerodynamics is an area in which there has been a large amount of recent work. A number of studies have produced drag coefficients, although lift coefficients are much harder to measure. There is a lack of data at high spin rates, which need a combination of a fast spinning ball and a wind tunnel which is accurate at low speeds. The data available does however make it possible to obtain realistic approximations of the court impact conditions, assuming some knowledge of the starting boundary conditions.

2.5 Player data

A major aim of this project was to be able to model impacts at a realistic range of speeds and spins. There is not a huge amount of data on speeds throughout trajectories and particularly on impact – often the only figures that are quoted are "serve speeds" which are maximum values measured with a radar gun.

Groppel *et al.* (1983) created an analytical model to predict the effect of angle of swing and orientation of the racket head on the spin imparted on a tennis ball. As an experimental validation of the model two male varsity players were filmed at 500 frames per second hitting balls with topspin and backspin. The six topspin shots had spin ranging from 36 to 195 rads^{-1}, and the two backspin shots were hit with 192 and 236 rads^{-1} of spin.

Elliott (1983) used two film cameras running at 200 and 300 frames per second to film twelve State ranked tournament players ages 12 years, 15 years and adult. He found that all the adult players hit the ball with a considerable amount of spin when asked to give a "hard first serve" - values of 11 to 19 rotations per second (70 to 120 rads^{-1}).

Elliott *et al.* (1986) filmed eight elite tennis players serving. For the male players, the ratio of the height of the ball at impact on the racket to the player's standing height was an average of 1.53. The balls dropped an average of 0.51 m from the top of the toss to the point of impact.

A collaborative project between NASA and Cislunar Aerospace, Inc. (Cislunar Aerospace, Inc. 2001) analysed a range of video footage from the 1997 and 1998 US Open tournaments, and provides an excellent source of data for professional tennis. Twenty nine first serves by Pete Sampras were analysed. The average speed of these serves was 120 mph. By the time the ball reached the court it had slowed to 87 mph. The impact on the court surface slowed the ball to 62 mph, and the drag while travelling from the service line to the baseline reduced the speed further to 54 mph. The spin generated by 11 professional men was also measured. The range of *average spins for each player* is shown in Table 2.1 for a variety of shots.

Table 2.1 Range of average spins measured by Cislunar (2001).

Type of shot	Min and max average spins measured rpm (rads^{-1})
Forehand topspin	1333 to 3331 (140 to 349)
Backhand topspin	1250 to 2332 (131 to 244)
Backhand backspin	2127 to 3124 (223 to 327)
First serve	1548 to 3167 (162 to 332)
Second serve	3370 to 4650 (353 to 487)

The technology of radar guns is mentioned by Dunlop (2000), who states that the accuracy of the guns tested was 1 km/hr (0.28 m/s), with 0.1 km/hr available using averaging

algorithms. He suggested the use of radar guns as a simple way to measure the "pace" (change in horizontal velocity component) and "bounce" (change in vertical velocity component) of a surface.

Summary

Somewhat surprisingly, more information is available on the spin a player gives to the ball than the speed with which it is hit. This spin is however important, as the values imparted by professional tennis players is extremely high – typically between 100 and 400 rads^{-1} for groundstrokes. Second serves can exceed these values, and even first serves (when the players were asked to hit the ball fast and flat) are of comparable spin rates. This suggests that any experimental impacts must include considerable spins to be realistic. Initial speeds off the racket are available, and so it is hoped aerodynamic modelling will make it possible to find court impact conditions.

2.6   Surface testing

Bell *et al.* (1985) presented a summary of various sports surface test methods. Values are quoted for "ball bounce resilience" on turf for different sports, where the vertical height a ball bounces to is recorded as a percentage of the drop height. Friction was measured by finding the distance a ball rolls along a surface before coming to rest. A rotating drum which drops a spinning ball was described as an alternative friction measurement (the distance between the first and subsequent bounce point defines the friction). The traction (described as applying to footwear "having studs, cleats or spikes to provide extra grip") was also discussed along with a variety of test methods using plates with attached studs to measure the turf shear resistance.

2.6.a   *ITF performance standards*

The three properties chosen as key characteristics of tennis court surfaces by the ITF (ITF, 1997) and their definitions are listed below:

- Surface pace - The speed of the court, which includes both speed and angle of the ball rebounding off the surface.

- Friction – As determined by measuring both Slip resistance and Traction.

- Energy Absorption – The ability of a surface to absorb energy (or shock).

Five more characteristics of a constructional nature are also described:

- Vertical ball bounce – The measure of the vertical ball bounce off a given surface.

- Permeability – The ability of a surface to allow water to pass through it.

- Slope – The gradient of a court which is designed to assist drainage of a surface.

- Evenness – The geometrical regularity of a surface.

- Consistency – The uniformity of the surface over the entire playing area.

Test methods are given for each of these characteristics. Of the eight, the following are most relevant to this project: surface pace, friction, energy absorption and vertical ball bounce.

2.6.b   *Surface pace rating*

The surface pace rating is intended to define both the speed and angle of the ball after rebounding off the surface. A ball is projected at 30 ± 2 ms^{-1} at $16 \pm 2°$ to the horizontal. The velocity components before and after impact as defined in Figure 2.12 below are measured.
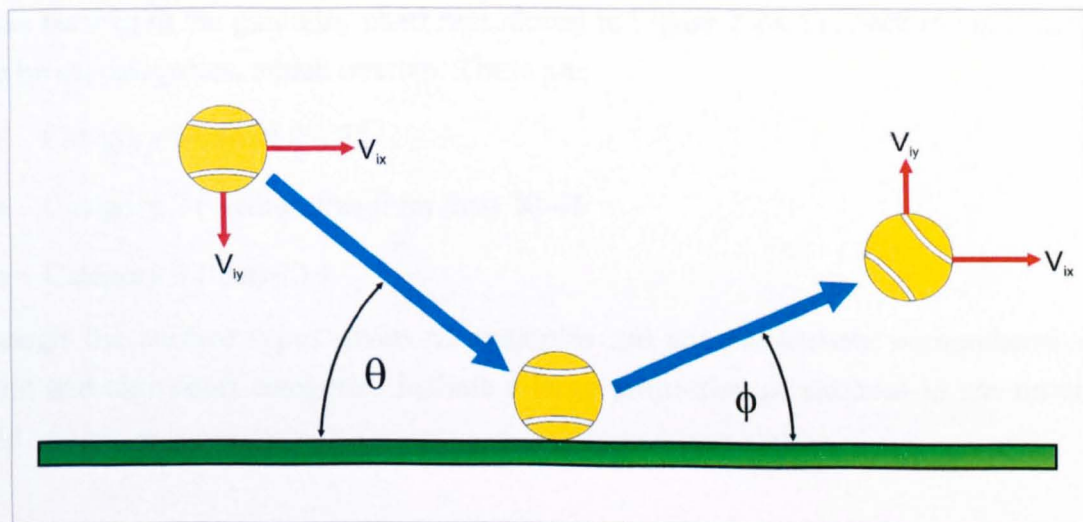
Figure 2.12 Definition of the velocity components used to calculate Surface Pace Rating (ITF, 1997).

The pace rating P is defined as $P = 100\left[1 - \dfrac{V_{ix} - V_{fx}}{V_{iy} + V_{fy}}\right] = 100\left[1 - \dfrac{\Delta V_x}{\Delta V_y}\right]$

Figure 2.13 Typical Surface Pace Ratings for new courts (ITF, 1997).

As can be seen in the guideline chart reproduced in Figure 2.13, the pace rating is split into three broad categories, which overlap. These are:

- Category 1 (slow) 0 – 35

- Category 2 (medium/medium fast) 30-45

- Category 3 (fast) 40 +

Although the surface types given as examples are not particularly comprehensive, the acrylic and clay court categories include a large proportion of surfaces in use around the world.
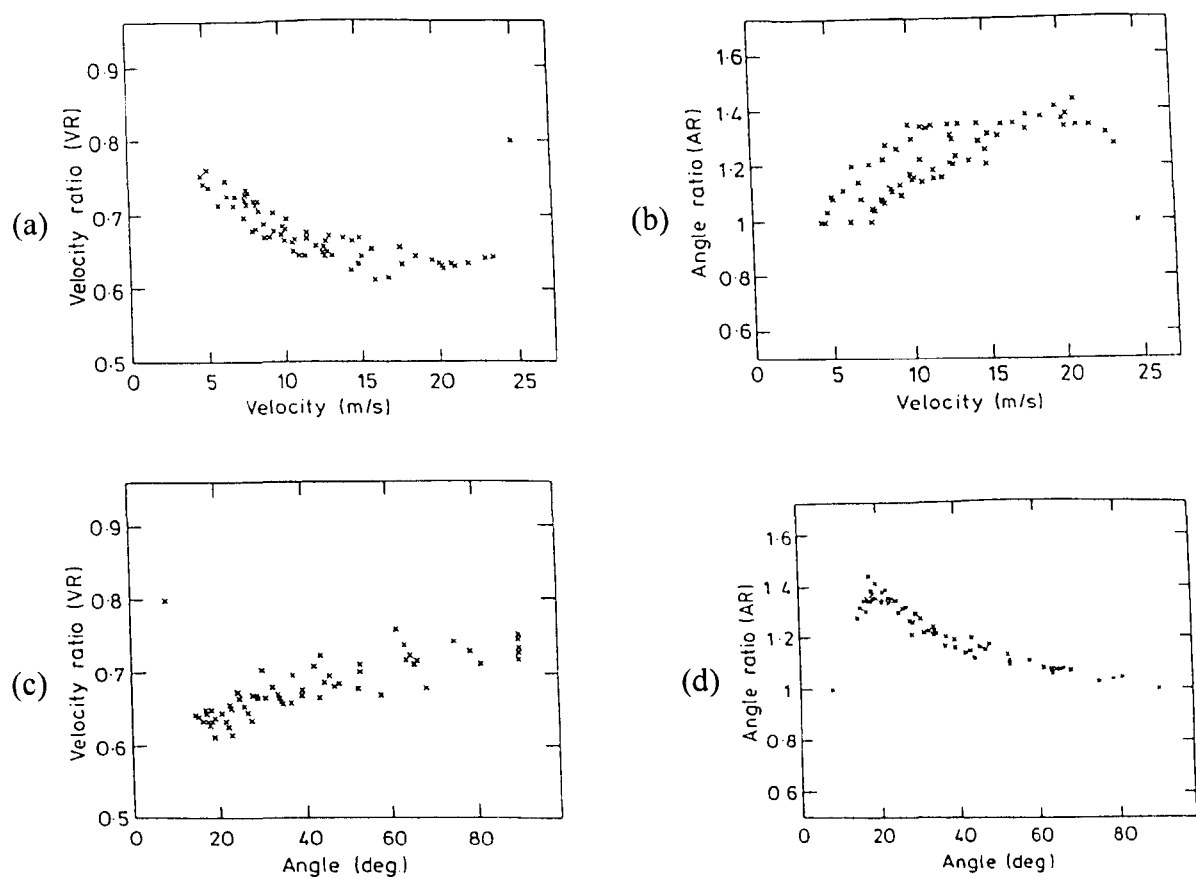
Figure 2.14 (a-d) Velocity and angle ratios plotted against (a-b) incoming speed, and (c-d) incoming angle, from Dunlop *et al.* (1992).

Before the ITF Pace test was established, Dunlop *et al.* (1992) stated that player perceptions of "pace" were a combination of horizontal and vertical velocity changes. In order to recreate a controlled simulation of a ball landing on an oblique surface, they filmed a ball landing on an inclined moving plane – by dropping balls off-centre onto a spinning wheel. Photo-diodes were used to ensure that the operator could tell if the ball landed in the required area. The landing position determined the angle of impact due to the tangent of the wheel circumference. Velocity and angle ratios are shown plotted against incoming speed and angle in Figure 2.14.
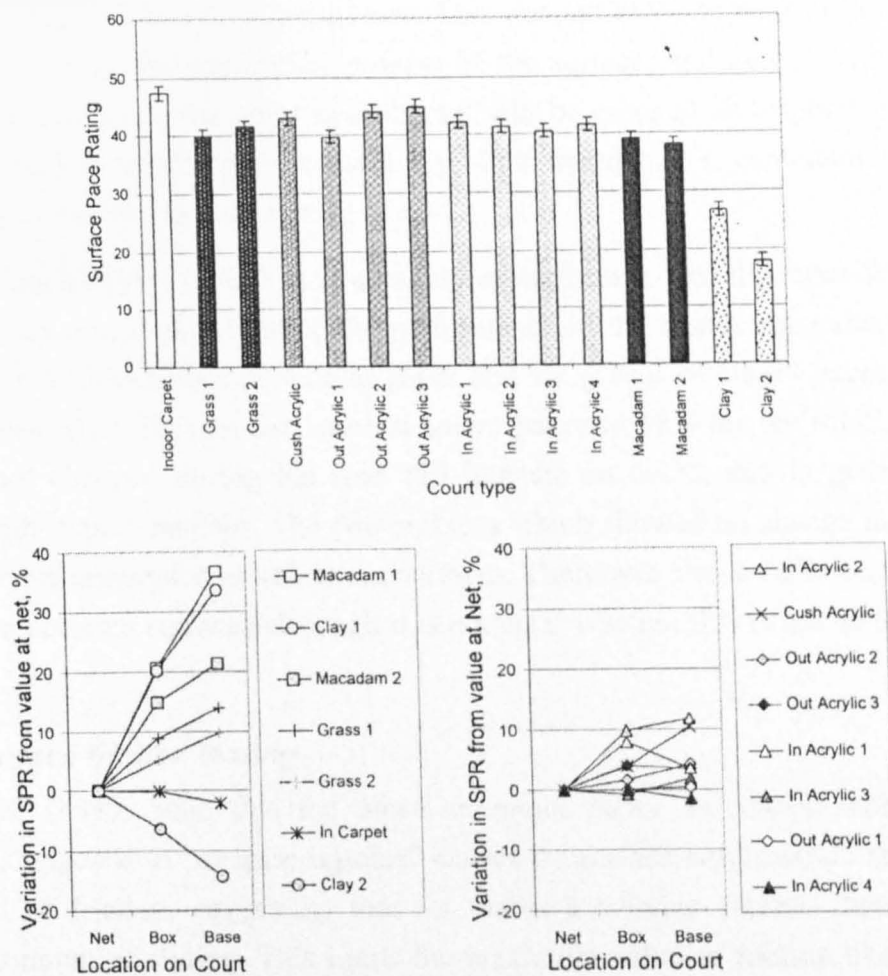
Figure 2.15 The variation of Surface Pace Rating with test position, for a variety of court types (Carré *et al.*, 2002). Also shown is the variation with court position.

Carré *et al.* (2002) performed Surface Pace Rating tests on fifteen different tennis courts around the UK, ranging from values of about 18 to 48. They measured the Pace at three different locations on the court: by the net (assumed to have little or no wear), in the service box (where wear is due to ball-surface interaction) and near the baseline (where player-surface interaction causes wear). Macadam and grass surfaces had an increase in pace both in the service box and at the baseline compared to by the net. An indoor carpet had very little change, and two clay courts had opposing behaviour - one was faster at either position away from the net, and one was slower. The various acrylic surfaces show differing amounts of change, but in almost all cases are between 0 and 10% faster away from the net.

Cox (2003) gave a summary of the Surface Pace Rating test including examples of some test values. During extremes of (English) weather in a grass court season, Pace Ratings from 34 in cool, damp conditions to 49 in hot, dry conditions were measured. Similarly, clay courts had typical Pace Ratings from high teens to around 25, and acrylic surfaces from 27 up to high forties – although the range 38-45 was most common. Cox also noted that acrylic courts have a noticeable change in pace during their early life, typically by 5 or

6 on a slow court, or 2 to 3 on a faster court. This was attributed to wear of the pronounced peaks formed during the application process of the surface, and agrees with the data of Carré *et al.* above, since the court near the net will be close to its original state. Acrylic courts were also noted for their consistency; Cox stated that a contractor can produce courts with a variability in Pace Rating of ±3.

Miller and Capel-Davies (2003) used a variety of surfaces to test the repeatability of SPR tests (in a study aimed at validating the performance of the Sestée apparatus). They used MDF wood, two thicknesses of writing paper and six grades of emery paper. Mean Pace Ratings ranged from 23.9 for the coarsest emery paper to 68.3 for the MDF. The impact point was not changed during the tests (10 impacts on each), and in general the pace increased with impact number. The two surfaces which showed no change in pace during the test were recommended as validation surfaces. There was also a variation in coefficient of restitution between surfaces although it is not clear whether this is due to the ball or the surface.

2.6.c   *Surface friction testing*

Dixon *et al.* (1999) state that the most important factor associated with "accidental injuries" (as opposed to "overuse injuries" caused by surface hardness) on sports surfaces is the level of friction, suggesting that for tennis a suitable surface should provide a controlled amount of sliding. This limits the maximum value of friction likely to be seen on a court.

Van Gheluwe and Deporte (1992) measured frictional forces and torques produced by good quality players hitting an open stance forehand. The players were asked to hit the ball while moving on a force plate covered with various playing surfaces. They found the friction was more affected by the surface than the choice of shoe.

As already mentioned, Brody (1984) dragged a weighted ball using a sprung force measurement. Hamilton (2000) used similar principles to measure the tension needed to pull along a sled whose bottom was covered in tennis ball cloth. These provide simple ways to measure dynamic coefficient of friction, but are rather user-dependent.

The ITF describe two tests designed to measure the friction of a surface (ITF, 1997). The first of these evaluates the rotational traction by measuring the torque needed to turn a rubber disc which has a substantial mass on it. The second uses a pendulum with a rubber foot which is released and allowed to impact along the surface. A sprung mechanism allows a specific contact length, and the height the pendulum reaches after sliding is recorded. These two tests are described in more detail in Chapter 5.

Haines (2002) developed a pendulum to measure friction between a tennis ball and court surface, which was commissioned by the ITF as a possible inexpensive alternative to the

Sestee Surface Pace Rating equipment. The theory given by Haines relates the loss of energy due to a ball sliding a distance d against a frictional force F. For a weight W (of the pendulum arm plus the ball) and the distance from the pivot to the centre of gravity is a, then the energy loss in relation to the angle θ the arm swings to is given by $Wa\cos\theta$. This energy loss is also equal to the work done by friction, or Fd. Equating these two energy losses and relating them to the vertical reaction force R by $F = \mu R$ leads to

$$\mu = \frac{Wa\cos\theta}{Rd}$$

If as Haines states, the variables w, a, R and d are all constants, this is of the form $\mu = K\cos\theta$, allowing a simple calculation to work out the coefficient of friction from the angle the pendulum swings to. Again, this test method is examined in more detail in Chapter 5.
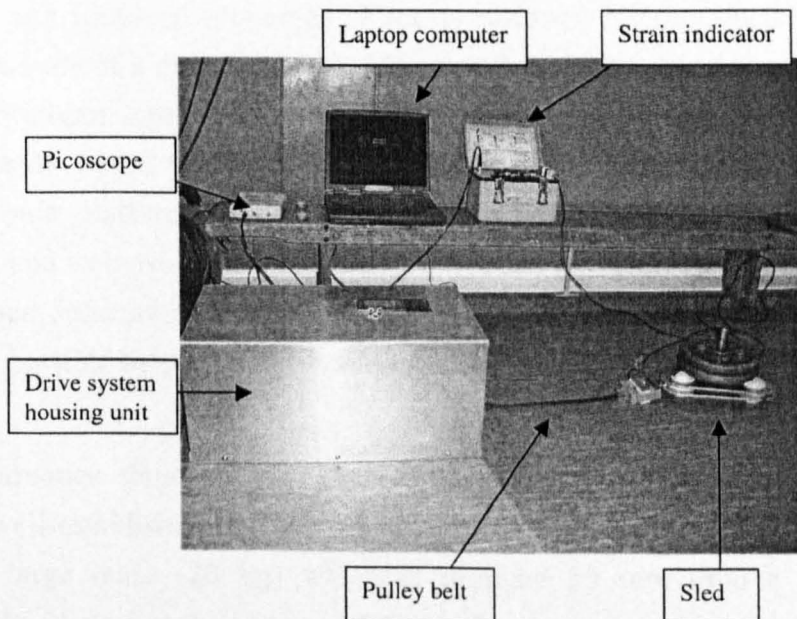
Figure 2.16 The friction rig tested by Teasdale (2003).

Teasdale (2003) performed testing using a bespoke friction rig which was designed to measure a dynamic coefficient of friction. This is shown in Figure 2.16 and contained a constant-speed motor which could be used to accurately pull a friction sled at specified speeds. A fibre-reinforced toothed belt pulled the sled along the surface. Three balls were secured in the sled and a weight applied to give a normal force. A load cell between the sled and rubber belt was used to measure the reaction force on a laptop, via a strain indicator box. Teasdale found that the ball mounting arrangement generally allowed six possible contact positions on each ball (opposite faces on three mutually perpendicular axes), although with hard balls such as hockey balls the contact area was reduced, allowing for more positions. In tests across four surfaces, Teasdale found that there was no

significant difference between friction coefficients for cushioned and uncushioned surfaces. There was a significant difference between coefficients of friction for "smooth" and "rough" surfaces - made with acrylic paint and with paint which was mixed with sand. He also found that the speed at which the sled was pulled had no consistent effect on friction on tennis surfaces for tennis, cricket or hockey balls. On an indoor wooden sports hall surface a hockey ball showed an increased friction with increased speed, although cricket and tennis balls did not.

Teasdale also tested friction with different normal loads on the sled. With loads between 50 and 250 N, he found that tennis and hockey balls did not show any change in frictional coefficient. Cricket balls seemed to show a trend of decreasing friction with increasing normal load, although the errors are significant.

2.6.d   Surface Impact testing (energy absorption)

Nigg (1990) performed a critical review of the test procedures commonly used to assess the cushioning and frictional properties of sports surfaces. He described six categories of cushioning tests: where a dropping mass falls onto a test foot containing sensors (such as the Berlin or Stuttgart Artificial Athlete), a dropping mass which itself contains impact sensors, drop tests where the sensors are underneath the surface (e.g. with the surface placed on a force platform), a drop test using an accelerometer to find stress-strain characteristics, and tests where subjects perform typical movements on a surface and either forces or surface deformations are measured. The dropping mass tests are of particular interest as it is possible they could give surface stiffness information useful in a ball impact model.

The ITF performance standards (ITF, 1997) specify only one test, the Berlin Artificial Athlete. This well-established test will be looked at more closely in Chapter 5, but in brief consists of a large mass (20 kg) which is dropped 55 mm onto a stiff spring. An instrumented shoe between the spring and the surface measures the peak force value seen, which is then compared to a control test value measured on a theoretically rigid surface such as concrete.

McMahon and Greene (1979) constructed a model of a runner where the leg was represented by a rack-and-pinion spring and damper, which was then assembled in series with a spring representing the surface. The stiffness values of various surfaces are quoted in Table 2.2. The model was used to predict contact time and step length. Although McMahon and Greene do not specify how the stiffness values were obtained, it is useful to consider the order of magnitude – the value for concrete or asphalt is around 100 times higher than typical values for ball stiffness.

Table 2.2 Stiffness values of running surfaces (reproduced from McMahon and Greene, 1979)

Material	Stiffness (kN/m)
Concrete / asphalt	4376
Packed cinders	2918
Board tracks	875
Experimental wooden track	195
Experimental wooden track	100

One standardised piece of equipment often used to assess the soil hardness is the Clegg Soil Impact Test (Clegg, 1976). This test drops an instrumented mass (0.5 kg or 4.5 kg, depending on the hardness of the surface being tested) down a guide tube and gives the peak deceleration. This equipment is easy to use but provides only a single measurement - the maximum value of (upwards) acceleration during impact. Rogers and Waddington (1990) listed nine specific measurements which were thought to fully define the impact absorption properties of a surface, and included such parameters as times, accelerations, peak forces and deformations.. They then went on to design apparatus using the Clegg tester and a vibration data analyser for obtaining a full acceleration-time profile. With the data downloaded onto computer, any number of useful properties can be calculated. Values are given for such features as impact time and rate of change of acceleration but no curves are shown. Conclusions drawn were that peak deceleration decreases with an increase in soil moisture or compaction.

A similar system was developed by Bregar and Moyer (1990). After experimenting with a computer-based data acquisition input card, they used a Brüel & Kjær standalone vibration analysis unit to record up to 50 acceleration profiles into non-volatile memory to analyse on computer later. A sampling rate of 20 kHz over a maximum time of 62.5 ms was found to be sufficient. Masses of 0.5 kg, 2.25 kg and 4.5 kg were tested, all from a drop height of 45.7 cm (18 inches). They found the system worked well but no experimental data is given.

Martin (1990) presented a theoretical analysis of impacts based on the Gadd severity index where $G = \int_{0}^{T} a^{2.5} dt$ for acceleration a measured for time t varying from 0 to T. The study was based on human safety, where values of G in excess of 1000 are considered to be unsafe. Martin found that as the drop height increased, the thickness of the surface became a more important factor in the magnitude of G.

Walker (1996) also mentioned the integrative severity index but suggests that a more useful figure is the tangent modulus of the load-deflection curve. This was measured at the point of peak force. He found that the standard weights used commonly in impact testing are too low and give results which are too similar across widely different surfaces and suggested using loads and areas which match human interaction as closely as possible (although the work is aimed at tests to reduce player injuries rather than ball performance). Tests on a standard hockey surface showed the effect of underlays of 12 mm and 20 mm thickness - as the thickness is increases, so does deflection while the force does not change much. Thus the stiffness and therefore perceived hardness reduces.

Davies and Karim (1995) developed an analytical model to predict the post-impact conditions of three kinds of impact test. These three tests were the Clegg impact tester using a vertically dropped mass, the Odin hammer which is essentially similar but which uses a hinged arm for the mass, and the Falling Weight Deflectometer which is a more complicated system, dropping a mass onto a sprung platform. The model was comprised of a spring of stiffness k and a dashpot with damping constant c. These two parameters were calculated for a contact area of radius r, using the soil properties of shear modulus G, Poisson's ratio v and mass density ρ:

$$k = \frac{4Gr}{1-v}$$

$$c = 3\frac{4r^2\sqrt{\rho G}}{1-v}$$

They found that the model worked well for the Odin hammer and FWD, but not as well for the Clegg tester. This was attributed to the higher stresses generated during impact which would affect the accuracy of some of the basic assumptions of the analysis.

Henderson et $al.$ (1990) used soil samples in boxes to establish a laboratory method for testing soil and turfgrass surfaces. A 9.1 kg missile was dropped from a height of 61 cm. It was found that the depth of soil in the box was important as the box and anvil appeared to affect the results for most samples; with less than 15 cm of soil, the peak deceleration and penetration depth varied with depth of the sample. However, the soils used would seem much softer than any tennis surface, as the peak deceleration was in the order of 20 to 50 gravities.
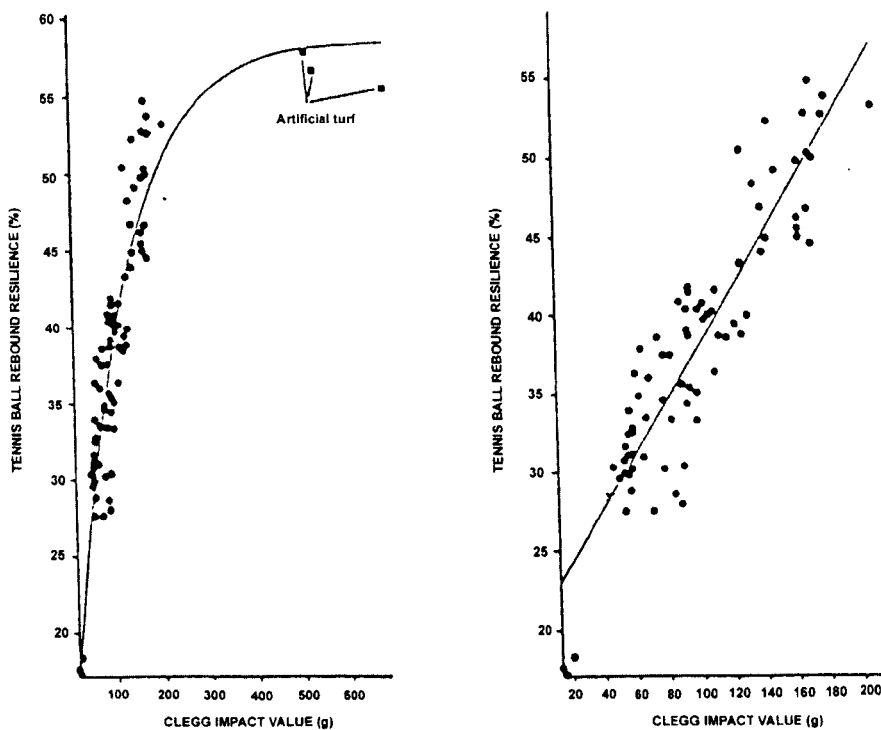
Figure 2.17 Tennis ball rebound resilience against Clegg Impact Value, for all surfaces and just for artificial turf (reproduced from Holmes and Bell, 1986).

Holmes and Bell (1986) dropped a 0.5 kg Clegg Impact Soil Tester on nine natural and one artificial turf playing courts (it is not clear whether these were actual courts or prepared sample areas). They also performed a 100 inch drop test using tennis balls on each surface. They found a strong relationship between Clegg Impact Value and rebound resilience (reproduced in Figure 2.17) which appeared to be linear for the natural turf. The artificial turf had only a slightly higher bounce despite a much higher Clegg Impact Value, suggesting that some asymptotic value had been reached where the surface was essentially rigid. The large range of ball bounce resilience seen suggests that some extremely soft surfaces were used. They conclude that small differences in hardness on a "hard" court will have little effect on rebound resilience. However, on a "soft" court, similar small differences in hardness will produce greater variations, contributing to the variability and inconsistency often seen on grass courts. Some of the courts tested produced ball bounce heights between 20% and 50% of the drop height, suggesting they were extremely soft.

Brody (1992) described a simple method of performing a comparative test of surface hardness. He attached two inexpensive resettable accelerometers to a baseball bat and dropped the bat from gradually increasing heights until the accelerometers tripped, showing that a specific value had been reached (in this case 138 g). The height varied by quite a large amount, from 0.08 m on the hardest surface (concrete) to 0.91 m on the softest (artificial grass). Without any data such as ball bounce height or impact force measurements, these numbers are somewhat difficult to interpret.

Dodd (2003) adapted a Clegg Impact Soil Tester in order to understand the influence of various parameters of surface stiffness properties. The key variables he chose were contact velocity, impact hammer mass, and hammer shape and surface area. Dodd found that the original Clegg device had errors of up to 20% in the impact velocity, and so a linear rail was used in an attempt to improve the accuracy. He concluded that the kinetic energy of impact was the dominant parameter in the loading part of the impact, but that the mass was more important during the unloading stage (and hence the hysteresis or energy loss). Dodd commented that it was not possible to match both the energy and mass to that of a sports ball impact. Dodd also created spring-damper models of athletic and cushioned tennis surfaces. The tennis surface was created using two springs, as it exhibited two behaviours - the stiffness increased due to a bottoming-out effect. The two springs in the model were of stiffness 180 N/mm and 2500 N/mm, with the softer spring switching off after the critical displacement of 1.6 mm. He suggested that the shape of the impact hammer should match that of the real situation in order to recreate the stresses and deformations.

Summary

The two surface properties which seem most likely to affect ball impacts are friction and stiffness. A form of friction is already commonly measured in terms of SPR, and a reasonable amount of data is available on values for various courts and their repeatability. A number of tests also attempt to measure the friction directly, although no attempt has been made to compare and correlate these to SPR values. Surface stiffness is also often measured in the sporting world, and several common test methods exist to find the shock absorption (often in terms of a peak force or deceleration). Most of these tests are designed to simulate the interaction of a human athlete on a surface, and it is therefore unclear how well the results can be applied to ball impacts where both the force and energy is much lower.

2.7   High speed ball impact testing

Haake (1994) used a modified baseball machine to project golf balls onto greens using rotating rubber wheels. The impacts were recorded using stroboscopic photography. He created a two-layer model to predict the impacts, where the top layer represented the grass, thatch and root layer while the second layer represented the soil underneath. He found that the greens could be split into two categories – the first where the ball slips throughout and retains backspin, and a second where the ball rolls matching a $v = \omega r$ relationship.

Dowell *et al.* (1987) projected balls at a wide range of angles (12.6° to 72.1°) at a mean velocity of 87 feet per second (26.5 ms^{-1}). They found the rebound angle was higher than the incident angle in all cases. The deviation between the two angles was lowest at either

extreme of angle, and increased in between, peaking at an incident angle of about 35°. The court used was a Laykol court, and no measure of friction is given.
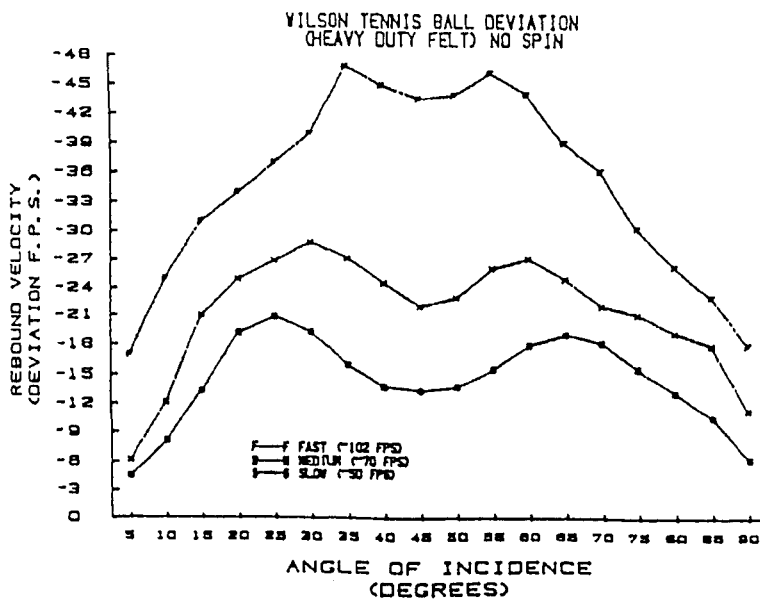
Figure 2.18 Change in velocity against incident angle for three different ball speeds (from Hope *et al.*, 1988).

Hope *et al.* (1988) performed a similar but extended study, projecting balls at about 50, 70 and 100 feet per second (15, 21 and 30 ms^{-1}). Impact angles ranged from 5 to 90 degrees. The change in velocity due to the impact is shown in Figure 2.18. An interesting bimodal distribution is shown for each speed, although the situation is rather complicated – different angles will produce completely different impacts because of the range of vertical velocity components seen (and their effects on COR), the slipping/rolling boundary and perhaps mechanisms of deformation. No attempt was made to explain the results.

As briefly mentioned earlier, Haake *et al.* (2000) performed a comparison test between normal pressurised and 6% oversized balls on both acrylic and clay surfaces. They found that in every case there was no difference between the rebound speeds of the two ball types. There was a suggestion that the oversized ball bounced with a steeper angle, but no indication of uncertainty is given and so the significance of the data is unclear.

Goodwill (2002) projected balls normally at a rigid surface between 4 and 30 ms^{-1}. He used four ball types (pressurised, pressureless, punctured and oversized) and found that they all had a similar coefficient of restitution of 0.8 at the lowest speed. As the impact speed increased, the COR dropped and differences between the balls became apparent. He found that the oversized ball rebounded slightly faster than the pressurised ball, and the pressureless ball slightly slower. The punctured ball rebounded significantly slower at all speeds. Goodwill then repeated these tests, impacting the balls on a force plate. At low impact speeds, the three non-punctured balls exhibited similar force-time characteristics,

with the punctured ball having a lower peak force and longer contact time. As the speed increased, all balls showed a very similar initial peak in the force. The pressurised and oversized balls remained similar throughout. The pressureless and punctured balls behaved in a more similar manner, both having a longer contact time and showing a late increase in force. Goodwill attributed this to these two non-pressurised balls "flipping back" to their original shape after compression.

Miller and Messner (2003) tested the normal impact performance of balls at speeds from 20 to 40 ms^{-1}, using an air cannon to fire the balls at a concrete block. Averaged over all balls, the coefficient of restitution dropped from about 0.75 at 7 ms^{-1} (to be expected, since the balls passed approval testing before use) to 0.40 at 40 ms^{-1}. Pressureless balls bounce slower than pressurised balls at 20 ms^{-1}, but the difference is negligible at 40 ms^{-1}. Data is shown for two manufacturers' balls which have the same rebound speed at 20 and 40 ms^{-1}, but have a different rebound speed in between. Miller and Messner comment that this difference is not statistically significant, but highlights how the differences between balls may depend on the speed.

Kirk (2003) performed a series of impact tests on four different acrylic surfaces in an attempt to understand the physical processes. He used acrylic paint to create surfaces on a rigid sheet of Perspex and on a cushioned substrate made from two sheets of thin plywood with a 6 mm rubber cushioning layer in between, giving what he termed "Smooth Hard" and "Smooth Cushioned" surfaces. Another two samples (using the same base materials) were made using the same paint mixed with 450 microns sized sand, giving "Rough Hard" and "Rough Cushioned" surfaces. He fired a ball using an air cannon – therefore without spin – at speeds between 12 and 50 ms^{-1}, and nominal angles of 12°, 20°, 32° and 40° to the horizontal. High speed video was used to film the impacts at 1500 frames per second. The main finding was that there were no differences between the hard and cushioned surfaces, for a given paint (and therefore friction). The friction did have a significant effect however. He also found that there was a critical angle where the impact changed between two phases, what he termed "under slipping" and "rolling".

Kirk also attempted to find a way to estimate how the moment of inertia of a tennis ball changes as it deforms. By combining the MOI of a truncated sphere with that of a circular disc (assumed to be the shape the portion in contact with the ground assumes), he calculated a reduction of about 8% compared to the undeformed ball. One major flaw in these calculations is that Kirk assumed the ball was a spherical shell made from a single homogenous material. Because the outer layer of cloth has a much lower mass density than the rubber layer inside it, the actual moment of inertia will be significantly lower.

Johnson (1983) used elastic theory to explain the counter-intuitive behaviour of a superball. These balls, made from a solid rubber material with high coefficients of

restitution and friction, can be projected onto a surface with backspin so that they rebound both in the opposite direction and with a reversal of spin direction. The reason for this behaviour is based in the way the contact area is divided into two areas, a central circular area with no slip (where the tangential force is below a limiting value), and a surrounding annular area containing "micro-slip". Cross (2002, 2003) developed this idea and attempted to measure the horizontal friction force (shown in Figure 2.19), which the micro-slip theory states will reverse in some cases. He bounced various balls on a piezoelectric force plate (measuring the vertical force) mounted on a wooden block, which was allowed to move in the horizontal direction on rollers. He also attached a piezo disc on the front of the wooden block to measure the horizontal force.
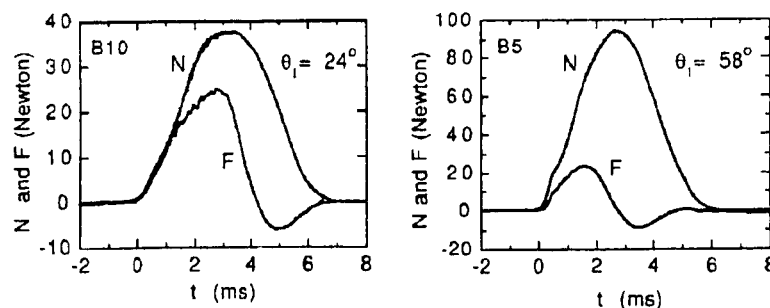
Figure 2.19 Vertical reaction force (N) and horizontal friction force (F) measured by Cross (2002) at two different impact angles for a tennis ball on a rough surface.

On a smooth surface the frictional force always acted against the direction of motion, suggesting a sliding motion throughout. When sandpaper was used to create a high friction surface, a reversal of the friction force was observed. Cross described this as a horizontal vibration of the ball, and remarked that the ball "bites" rather than rolling.

Summary

A relatively small amount of useful data is available on dynamic impacts, particularly of an oblique nature. Several studies are described which measured rebound speeds and angles, but did not attempt to explain the behaviour or physical processes of impacts. Kirk (2003) performed tests which suggested that a rubber underlay intended to reduce impact forces to players does not affect the way a ball bounces. He also found that whether a ball slipped or rolled throughout impact affects its behaviour, which meant that the range of incoming conditions chosen for this study should encompass both forms of impact.

2.8 Models of ball impacts

2.8.a Newtonian models

Two classic and commonly referenced studies of Newtonian studies of ball impacts are discussed, which have both been used by many authors as the starting point for their work.

The model equations have not been reproduced in any detail as they form the basis of Chapter 3 and will be discussed there.

Daish (1972) provides a comprehensive study of the mechanics behind the bounce of a ball, although one of his basic assumptions is that the ball is a rigid sphere. He suggests two main cases, where in the first the ball slides throughout impact and the second involves rolling. This second case will occur if the friction is sufficiently great. Equations are developed which give the limiting value of friction for rolling, but these are based on the assumption that the ball is a solid sphere and therefore will not necessarily apply to tennis.

Brody (1984) gave a theoretical analysis of generic ball impacts, including the effect of coefficients of restitution and friction. Although particular examples used were based on tennis shots, the analysis is quite comprehensive. Brody divided the impacts into two cases, where the ball slips throughout and where the ball begins to roll before the end of the impact. He observed that for a fairly slow court with friction of 0.6, the impact angle would have to be above 21 degrees for rolling to occur. He stated that this is unlikely as the vertical velocity component needed for this would suggest a shot hit 3.2 m high, although he does not take into account the effect of spin on either the trajectory (increasing the angle of impact) or the starting conditions for the impact (if the ball lands with topspin, less must be applied to reach the point of rolling). Brody also gave a range of values of coefficient of friction for tennis balls on various surfaces (ranging from wood at 0.25 to a synthetic carpet at 0.61) using half a ball containing a weight, dragged along the ground by a force meter.

2.8.b Analytical models

$[M=45.1g, K_1=4.9 \times 10^6 N/m, K_2=4.7 \times 10^6 N/m, C_1=250 N/(m/s)]$
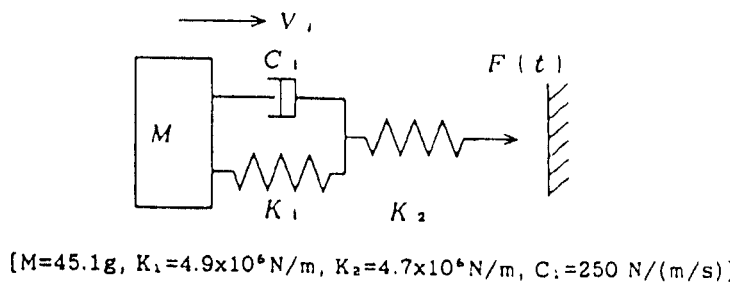
Figure 2.20 The spring-damper model used by Ujihashi (1994), including the spring and damper parameters.

A number of authors have constructed mechanical models of sports balls, particularly in the field of golf. These are reproduced as examples, although the exact nature of golf models is not reproduced in any detail. Ujihashi (2004) constructed a normal impact model consisting of two springs and a dashpot damper, as shown in Figure 2.20. This model matched the peak force well as well as the loading part of the force-time curve, but was not so accurate for the unloading portion.
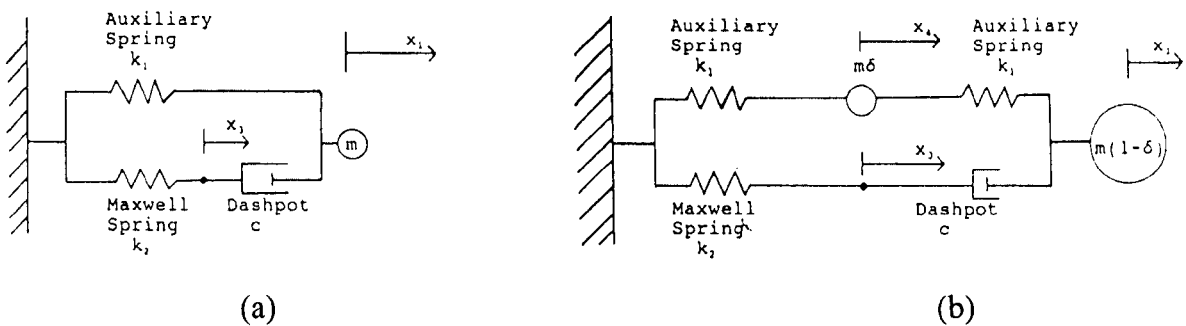
Figure 2.21 Spring damper models from Lieberman and Johnson (1994) for (a) solid and two-piece golf balls, and (b) wound balls.

Johnson and Lieberman (1994) gave a similar model to that of Ujihashi which they found matched experimental force-time data well for normal impacts of solid and two-piece golf balls, but was not adequate for wound balls. A more complicated arrangement was constructed which matched published results well. Lieberman and Johnson (1994) added a torsional component in order to model oblique impacts. Previously determined normal parameters were combined with "guessed values" for torsional parameters. Graphs of forces and accelerations of the various masses are given, but are not compared to any experimental data.

Johnson *et al.* (1973) studied the impact and flight of a football. They assumed the shape under deformation was a truncated sphere of the same radius as the original shape. The first approximation model assumed a constant internal pressure, but they later allowed the pressure (expressed as a gauge pressure P above atmospheric pressure P_A) to vary adiabatically such that $(P + P_A)V^{1.4} = const$. This increased pressure over a contact area of radius r led to a pressure reaction force of $\pi r^2 P$. Percival (1976) continued the work of Johnson *et al.* and introduced an impulsive force. This impulse is produced by the momentum change as material is brought to rest by striking the ground, and distributed around the edge of the contact area where the momentum change takes place. Percival found that this model gave a much better value of maximum contact area than that of Johnson *et al.* The values of rebound velocity and contact predicted are rather poor, but there is no other energy loss in the model such as material hysteresis or damping.
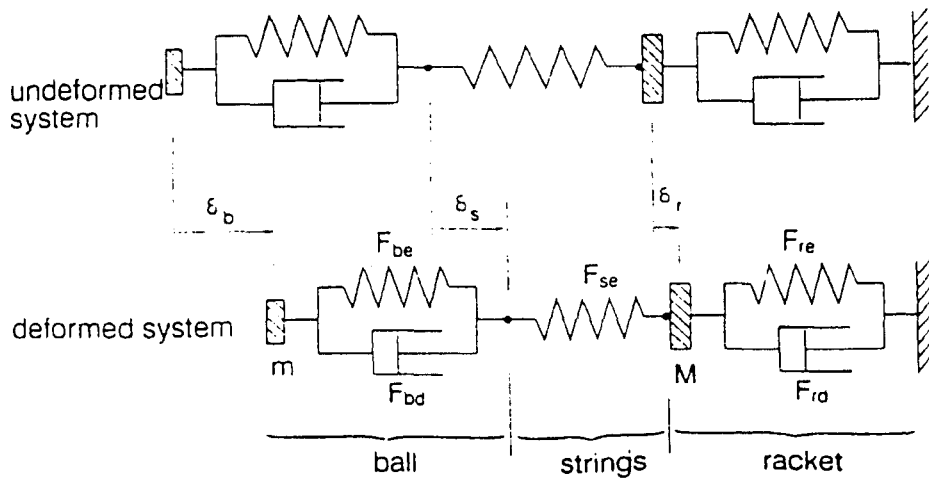
Figure 2.22 Spring-damper model of the ball, strings and racket by Leigh and Lu (1992).

Leigh and Lu (1992) created a model simulating the impact of a tennis ball on a racket which contained discrete components for the ball, the strings and the racket. The strings were represented by a spring, and the ball and racket each by a spring and damper in parallel. The three components were then assembled in series as shown in Figure 2.22. The spring and damper forces (F_{be} and F_{bd} respectively) were defined in terms of the ball deformation δ_b by

$$F_{be} = k_b \delta_b + n_b \delta_b^{\,3}$$

and

$$F_{bd} = c_b \dot{\delta}_b$$

The constants defining the ball stiffness were given as $k_b = 18.44$ kN/m and $n_b = 23860$ kN/m^3, and those defining the ball damping as $c_b = 6.66$ Ns/m. Model results were given for ball-racket impacts, but are not relevant to this study.

In some work using flexible beam theory to analyse the racket during impact, Cross (2000a) modelled a tennis ball as a spring element. He assumed the spring had a constant stiffness on loading and an unloading stiffness which varies with deflection. The force F at a deflection Y is given by

$$F = k_1 Y \qquad \text{(loading)}$$

and

$$F = k_2 Y^p \qquad \text{(unloading)}$$

and the parameter p can be defined to give an energy loss to match experimental values. Later in this work Cross gave values of $k_1 = 3 \times 10^4$ Nm^{-1} and $p = 2.55$.

(a)   (b)
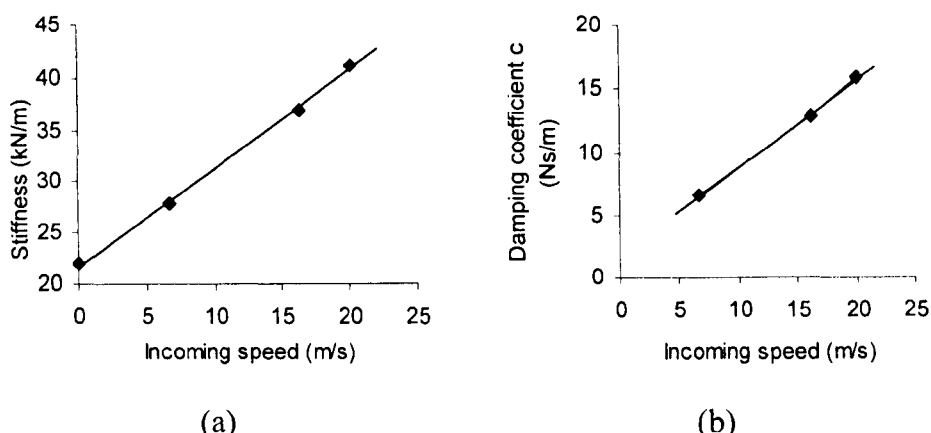
Figure 2.23 The variation of (a) tennis ball stiffness (including static stiffness) and (b) tennis ball damping coefficient against incoming speed, from Dignall and Haake (2000).

Dignall and Haake (2000) used a linear spring and dashpot damper in parallel to model a ball impact. By using contact times and rebound velocities for normal tests, they found linear relationships between impact speed and both stiffness and damping coefficients, as shown in Figure 2.23. This data was used to create an oblique model by adding a friction force, and this model matched one set of experimental data given.

Hubbard and Stronge (2001) used thin-wall shell theory to analyse the impact of a table-tennis ball. They divided the impact into three possible periods; where the shell flattened against the surface, where there was a buckling of the cap inside the shell, and at large deflections where there was an inverted buckling into a set of three or four lobes. High speed video showed signs of the first two of these stages. Strain energy equations were used which, because of the thin wall nature, cannot be applied accurately to tennis balls. Hubbard and Stronge also included the changing pressure in their equations, observing that the volume of the ball reduces by twice the volume of the cap which inverts during the buckling stage. This pressure has a small effect at low speeds, but becomes more important as the speed is increased. Model predictions have reasonably accurate contact times, but show far too low an energy loss, indicating the need for an alternative dissipative term.
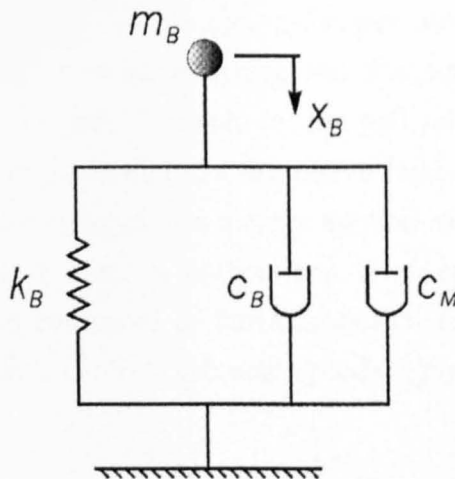
Figure 2.24 The "momentum-flux viscoelastic model" of Goodwill (2002).

Goodwill (2002) described a model which was used to predict impacts of balls on rackets. It consisted of a spring, and two sources of energy dissipation, a damper and a momentum flux component. The spring stiffness was adjusted to a higher value k_{SHELL} of 80 kN/m for the first 0.2 ms to simulate the large initial rise in force. After that a power law was used to find the stiffness k_B as a function of deflection, in the form $k_B = k_{B(0)} + A_K x_B^\alpha$. The damping coefficient C_B was also non-constant and was a function of contact diameter d_{CONT}. The ratio of the mass of ball still above the surface compared to the total mass was used to estimate the velocity of the ball shell as opposed to the centre of mass, leading to the equation $C_B = \dfrac{m_B}{m_1} A_C \left(d_{CONT}\right)^2 \dot{x}_B$. The momentum flux term described the impulsive force caused by material being brought to rest on the surface. This was calculated using the change in contact area over previous timesteps in the iteration, giving the mass of material change between the part of the spherical shell moving downwards and the part at rest on the surface. The four parameters of the model were found by an iterative process matching contact time and coefficient of restitution as closely as possible. These parameters are reproduced in Table 2.3.

Table 2.3 Model parameters reproduced from Goodwill (2002).

Ball type	$k_{B(0)}$ (kN/m)	A_K (kN/m^2)	α	A_C
Pressurised	21	16000	1.65	3.5
Pressureless	23	12500	1.70	4.0
Oversized	21	3600	1.30	3.2
Punctured	16	60000	2.00	5.8

Haake *et al.* (2003) extended the normal spring-damper model of Goodwill in order to apply it to oblique impacts. A non-linear spring and damper were used to represent the stiffness and energy loss in the ball. The spin on the ball (either applied or generated by frictional moments) caused non-symmetrical impulsive forces at the front and rear of the truncated sphere. This impulsive force was simply applied as single forces at the extreme front and back of the contact area. A comparison is given of horizontal and vertical displacements during impact compared to those measured experimentally and the model matches well, but no mention is given of rebound speeds, spins or angles.

Summary

Work in other sports suggests that some form of spring-damper modelling would give a reasonable solution for tennis ball impacts, and indeed there have been models created of varying complexity for tennis. All the existing tennis models have limitations however, most noticeably in the empirical nature of the coefficients used to define them. There would seem to be an opportunity to create a model more closely related to the physical nature of the impact, which would perhaps lend itself more accurately to an oblique extension of the model.

2.9 Overall literature summary

This literature review has shown that there is a definite need for research and understanding in the sport of tennis. A number of references have been quoted describing fears for the future of the game; a huge number more could have been reproduced.

Although many ball impact models have been created, none have successfully predicted the oblique impact of tennis balls. The Newtonian physics approach provides some good insights, but cannot match some of the quirks of normal tennis ball impacts, let alone oblique ones.

Not much data has been published on oblique impacts in general. It will be necessary to perform a series of oblique impact tests to find how the ball behaves under different circumstances (and of course providing valuable validation data for any model). Before this however, normal tests are necessary to provide a basic understanding of the dynamic behaviour of a ball.

Although there is not a vast array of data giving player performance statistics, there is enough information to determine how players typically hit the ball for various shots. An example of this is that the ball is rarely (if ever) hit completely flat, even on the fastest of first serves.

Aerodynamic knowledge has advanced greatly in recent years, providing good drag and lift coefficient data which enables trajectory simulations to be used. These can not only

provide information about how the ball reaches the surface (*i.e.* boundary conditions for a model), but also practical data about how to interpret the model predictions. For example, if ball B rebounds 10% faster than ball A but with 5% less topspin, how do the balls compare in the way they reach the opposing player?

There are a substantial number of accepted test methods for determining surface properties, not all of which will be relevant to the impact model created here. Surface friction and impact absorption tests must be evaluated to find their importance.

3 Fundamentals of Newtonian impact and modelling

3.1 Introduction

Before creating any sort of model, it is important to look at the basic physics behind what is happening. Consideration of the nature of the forces, deformations and so on are important to gain the understanding which is essential for a realistic model. This chapter discusses the mechanisms of impact and also looks at some of the mathematics behind impact. This leads to a rigid surface model which is based on some simple assumptions but can be used to provide some useful insights. Mechanisms of energy loss are discussed, together with deformations and their effect on the structural properties.

3.2 Normal impact on a rigid surface

Consider first a compressible hollow ball landing normally on a rigid surface. At the start of the impact it will have a maximum speed V_{in}. The impact will create a contact force opposing the motion - applied at the bottom of the ball - which will cause the structure to deform. Energy is stored in the material of the ball in the form of strain energy as a result of the deformation, which will be a combination of compression, bending and shear. In general the contained volume of the ball will decrease and thus the pressure of the air or other gas inside will increase (even if the ball is of the permanent pressure type, there is still a contained volume, initially at atmospheric pressure), although the actual deformed shape varies depending on a number of factors. This increase in gas pressure also stores energy.

The downwards speed of the ball centre of mass decreases due to the contact force, until it becomes zero. The bottom portion of the ball "spreads out" while momentum causes the rest to continue moving down. There will still be a restoring force upwards and so the ball continues to accelerate upwards until it leaves contact. At the end of the contact period the ball may still be in a compressed state. Regardless of this, the momentum of the rubber shell due to the expansion phase of the impact is likely to result in vibrational effects. Although Brown *et al.* (2000) found that this oscillation died out within 5 ms, it is another transfer of energy into a dissipated form.

If - as in the real world is always the case - the energy returned does not equal the energy stored, then the outgoing velocity will not be as high as the incoming velocity. In considering a general compressible ball, it is possible for permanent plastic deformation to occur as a mechanism for energy loss, but this obviously is not an important factor for the particular example of a tennis ball. What is important is the rubber used to construct the ball. When a material is tested for force-deflection properties, it can be described by two

stages, loading and unloading. If on unloading the force is less for a particular deflection than on loading, there will be an energy loss.
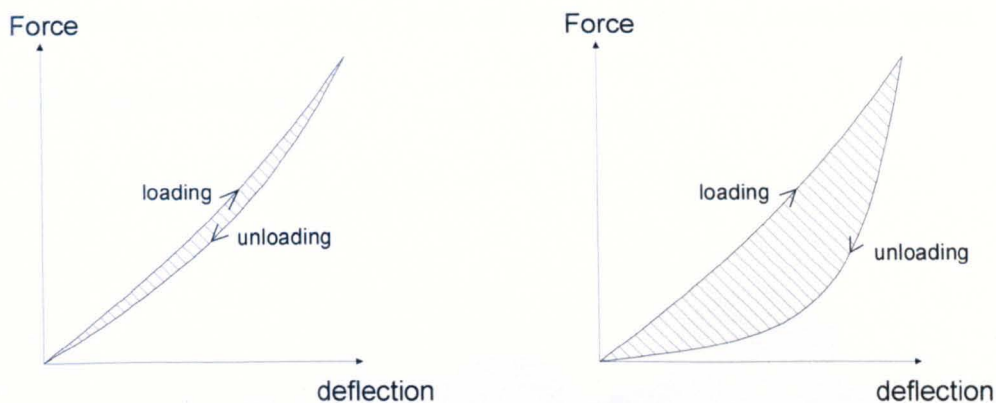
Figure 3.1 Force-deflection curves showing low and high energy losses, represented by the shaded areas.

Example force-deflection curves for small and large energy losses are shown in Figure 3.1, where the shaded area represents the difference between energy stored and returned. The area under the loading part of the curve is the energy stored, and the area under the unloading part the energy returned. The energy loss will come from a number of sources. The most intuitive is in the properties of the materials making up the ball, i.e. the rubber and the cloth. The cloth is a much softer material than the rubber and will not store much energy, but it is also poor at returning this energy. The rubber wall will undergo some compression and expansion but because of the nature of the relatively thin-walled spherical shell the majority of the ball deformation is from a different mechanism, as shown below.
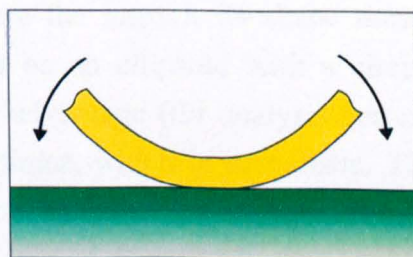
Figure 3.2 A cross-sectional view of the bottom of a ball during impact, showing the nature of the bending deflections.

Consider the cross-section shown in Figure 3.2. The dominant factor in the deformation is bending of the rubber wall around the edge of the contact area. Bending and return gives an energy absorption and loss in the same way as linear compression and expansion. There will be some dissipation of energy in the form of heat within both the rubber and the air.

It is theoretically possible for the stored energy to be totally returned to the ball, but even so for there to be a loss in speed. This could happen if significant vibrations are set up by the impact, so kinetic energy is transferred to oscillation. The vibration will be damped down fairly quickly without affecting the velocity of the centre of mass of the ball, by a

combination of the air compression-expansion and rubber bending-return as discussed above. This means that this damping then becomes a form of energy loss, dissipating the stored energy rather than converting it back to kinetic energy and increased speed.

3.2.a   *Deformation shapes*
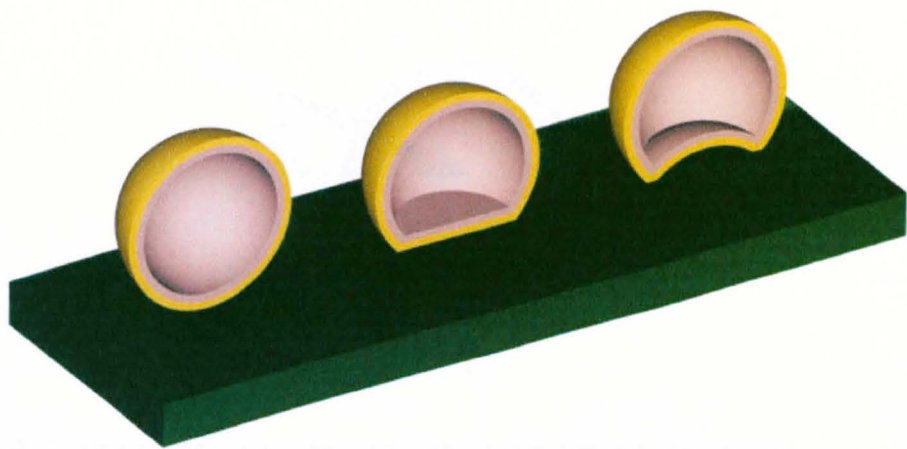
Figure 3.3   Possible ball deformation shapes, showing a sliced ball in each case; uncompressed, with a flattened bottom and buckled.

As the ball compresses during the impact, its shape must change from spherical. One simple possible shape would be an ellipsoid with a circular cross-section through any horizontal slice. This has the advantage (for analysis purposes) of being symmetrical but provides a point load at all times, which is unrealistic. The next most simple case is a truncated sphere where the portion below ground level is cut off, giving a flat contact area. This is shown in the central part of Figure 3.3. The problem here is that the volume of material in the shell is not conserved unless the spherical part changes radius (if the area is not in compression). Another possible case is the buckled third shape in Figure 3.3, where the portion below ground level is mirrored. This will give an annular contact area and a central circular area not in contact. Evidence for this shape can be seen by pressing half a ball by hand on to a rigid surface – the bottom section clearly "flips up" if the deformation is large enough.

Any deformation of the ball from its original spherical shell will alter both its centre of mass position relative to the undeformed top section, and its moment of inertia. This is important for two reasons. Firstly, nearly all analytical models use the centre of mass position to define displacements and apply loads. Any measurements relating to the

physical shape (whether they are measurements such as ball stiffness relative to displacement, or in the opposite direction comparing shapes predicted by the model with reality) need to be translated from centre of mass displacement variables. Secondly, the deformed shape is likely to have a significant effect on oblique impacts, where the position of the forces is important in terms of rotational moments.

3.3   Oblique impact on a rigid surface
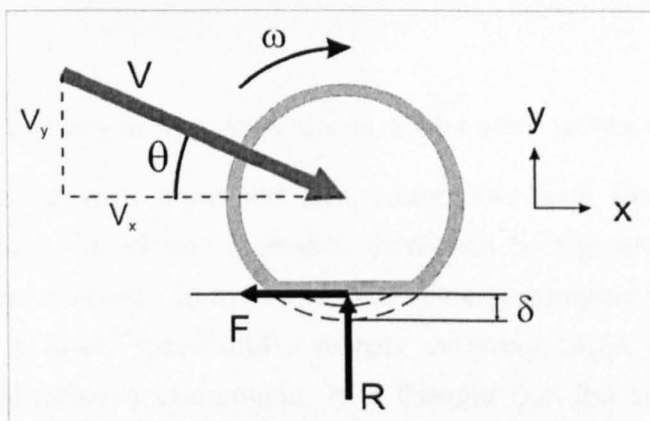
Figure 3.4 Forces acting on a cross-sectioned ball during an oblique impact.

The normal impact described above can be extended to oblique impact cases with the addition of a horizontal co-ordinate axis, and also spin. Consider the ball shown in Figure 3.4. One assumption commonly made is that the vertical properties of the ball are the same as for a normal impact having the same component of velocity perpendicular to the surface. This means that the vertical components of force, displacement etc can be considered independent of the horizontal ones (apart from obvious links such as normal and frictional force). In fact, under this assumption the vertical velocity, displacement and force components will be identical to those of a normal impact with the same incoming speed.

The vertical deformation produces a restoring reaction force R acting vertically upwards. For any non-normal impact, unless the contact time is instantaneously short, the bottom of the ball will slide along the surface, producing a retarding frictional force F. This frictional force will reduce the horizontal velocity component, and also provide a positive moment which will increase the topspin on the ball.

Low friction, higher horizontal speed

High friction, lower horizontal speed
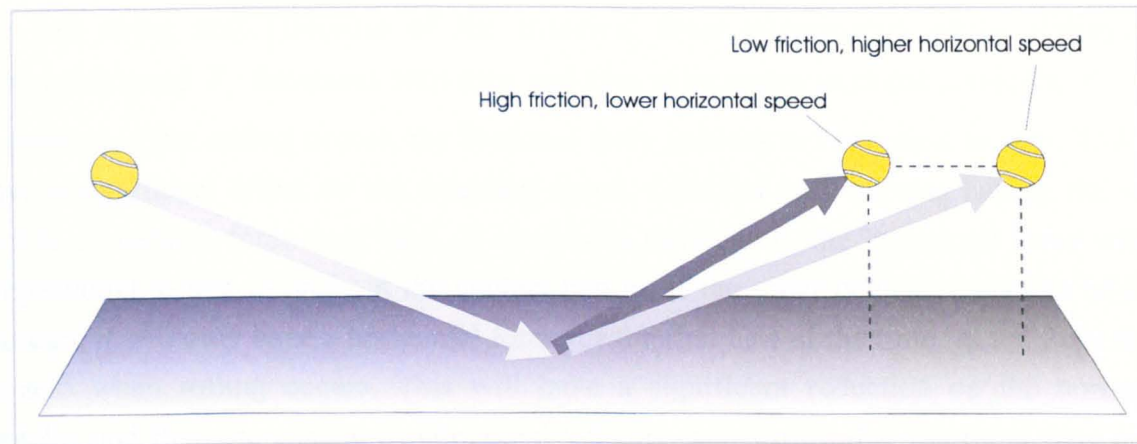
Figure 3.5 Higher friction leading to lower speed, for the same vertical velocity.

The main difference between slow and fast courts has been hypothesised to be the coefficient of friction. If the friction increases, there will be a greater horizontal impulse, and therefore a greater reduction in the horizontal velocity component as shown in Figure 3.5. This will mean a lower speed and a steeper outgoing angle, assuming there is no change in the vertical velocity component. It is thought that the horizontal speed is the most important factor in the perceived pace of a court, as it directly affects the time taken for the ball to reach the player. The higher friction will of course lead to a higher moment and therefore more spin after the impact, altering the trajectory.

3.4   Slipping and rolling

First, consider the case of a snooker ball (a highly rigid sphere) struck at the bottom of the ball to give it backspin. As it travels along the table, the ball is initially sliding rather than the typical rolling motion which might be expected. This sliding means that there is relative motion between the bottom of the ball and the cloth on the table, which provides a frictional force opposing the motion. This frictional force slows the ball's horizontal speed and also gives a rotational moment, reducing the backspin. At some point the backspin will be completely taken off the ball, and so the ball will start to gather topspin. Low values of topspin still give relative motion of the ball and the cloth, and it will still be in the slipping state. The horizontal speed will continue to reduce and the topspin increase because of the friction, until they "match" in the relationship $V = \omega r$. Depending on the amount of backspin applied and the friction between ball and surface, this whole process can take place extremely quickly.

Now consider a tennis ball landing obliquely with no spin. The frictional sliding force will gradually slow the ball and also add topspin. Depending on a number of factors such as angle of impact and coefficient of friction, the ball may start to roll along the surface before it leaves contact – it is of course perfectly possible for it to end the contact still in the slipping state. This rolling is characterised by the tangential velocity of the bottom of

the ball being zero. Because of the frictional force experienced whilst sliding, the horizontal speed V_x decreases with time and spin ω increases until the condition $V_x = \omega r$ is reached. After rolling occurs, the frictional force reduces to very close to zero. This can have a significant effect on the outgoing speed. Consider two impacts having the same profile of vertical force over time. If one slides throughout, the horizontal force will be proportional to this throughout the contact period. If the other begins to roll say halfway through, it will only have a horizontal force for the first half of the time, as the force drops to zero when rolling occurs. This will have a significant reduction on the horizontal impulse and thus the change in horizontal velocity, suggesting that the more time a ball spends rolling, the steeper it will bounce.

The examples above consider the cases where topspin is added until rolling occurs. It is theoretically possible for a ball to land with *greater* topspin than is needed for rolling. If this happens, the peripheral velocity of a point on the bottom of the ball will be in a direction opposing the horizontal velocity component, and the friction will be in an opposite direction to that previously discussed. However, it is seems very unlikely that this situation will occur, as the spins needed are large. For example, an impact at 30 ms^{-1} at 16° to the horizontal has a horizontal speed of 28.8 ms^{-1}. For a radius of 33 mm this gives an incoming rolling spin of over 870 rads^{-1}. Topspin slipping would require the player to impart a spin rate higher than this very high value.

3.5 Simple rigid body impact model

Consider a ball impacting obliquely on a rigid surface. It is possible to gain insights into its behaviour using rigid body theory. This relies on the assumption that the deformation of the ball is negligible, and so will not be valid if the vertical velocity component is large. The model is based on standard impulse equations in the horizontal, vertical and rotational directions:

x direction: $\int F dt = m \Delta V_x$ [3.1]

y direction: $\int R dt = m \Delta V_y$ [3.2]

Rotation: $\int M dt = \int -Fr dt = I \Delta \omega$ [3.3]

3.5.a Pace rating
The ITF Pace Rating is defined as (ITF, 1997):

$$Pace\ rating = 100 \left(1 - \frac{\Delta V_x}{\Delta V_y} \right)$$ [3.4]

Using [3.1] and [3.2], and assuming $F = \mu R$ throughout the impact (thus $\int F dt = \mu \int R dt$), this simplifies to

$$Pace\ rating = 100(1 - \mu)$$

3.5.b   Slipping/rolling limiting angle for non-spinning impacts

Defining $e = -\dfrac{V_{y_{out}}}{V_{y_{in}}}$ and using the relationship $V_{y_{in}} = -V_{in} \sin \theta$ (where θ is defined as the angle of velocity to the horizontal as shown in Figure 3.4), equation [3.2] gives

$$\int R dt = m(V_{y_{out}} - V_{y_{in}}) = mV_{in} \sin \theta (1 + e) \qquad [3.5]$$

Equating [3.1] and [3.2] by the expression $F = -\mu R$ gives $\int F dt = -\mu \int R dt$. Thus

$$\Delta V_x = -\mu \int R dt \qquad [3.6]$$

Substituting in from [3.5] gives

$$V_{x_{out}} - V_{in} \cos \theta = -V_{in} \mu \sin \theta (1 + e) \qquad [3.7]$$

For rolling spin, $V_x = \omega r$. Consider the case where the rolling condition is reached just at the end of the impact – it cannot happen earlier because of the assumption $F = -\mu R$. This gives $V_{x_{out}} = \omega_{out} r$ and therefore

$$\omega_{out} r = V_{in} [\cos \theta - \mu \sin \theta (1 + e)] \qquad [3.8]$$

Equating [3.3] and [3.5] by the expression $F = -\mu R$ thus $\int M dt = \mu r \int R dt$,

$$I \Delta \omega = \mu m r V_{in} \sin \theta (1 + e) \qquad [3.9]$$

assuming $\omega_{in} = 0$ (an impact with no incoming spin) and using the moment of inertia approximation for a thin-walled sphere $I = \dfrac{2}{3} mr^2$,

$$\frac{2}{3} mr\omega_{out} = \mu m V_{in} \sin \theta (1 + e) \qquad [3.10]$$

Substituting [3.8] into [3.10] gives,

$$\frac{2}{3} mV_{in} [\cos \theta - \mu \sin \theta (1 + e)] = \mu m V_{in} \sin \theta (1 + e)$$

$$\cos\theta - \mu\sin\theta(1+e) = \frac{3}{2}\mu\sin\theta(1+e)$$

$$\cos\theta - \frac{5}{2}\mu\sin\theta(1+e) = 0$$

Which rearranges to,

$$\tan\theta = \frac{2}{5\mu(1+e)} \qquad [3.11]$$

Equation [3.11] gives the limiting angle for impacts where the ball will slide throughout compared to those where there will be an element of rolling. This is important as the absence of friction in the rolling phase will have an effect on the outgoing velocity.

3.5.c   Limiting angle for impacts with incoming spin

The equations above can be adapted for the more general case where the incoming spin is non-zero. Following on from [3.9], if $\omega_{in} \neq 0$,

$$\frac{2}{3}mr(\omega_{out} - \omega_{in}) = \mu m V_{in}\sin\theta(1+e)$$

$$r\omega_{out} - r\omega_{in} = \frac{3}{2}\mu V_{in}\sin\theta(1+e)$$

sub [3.8] in: $V_{in}[\cos\theta - \mu\sin\theta(1+e)] - r\omega_{in} = \frac{3}{2}\mu V_{in}\sin\theta(1+e)$

$$V_{in}\cos\theta - r\omega_{in} = \frac{5}{2}\mu V_{in}\sin\theta(1+e)$$

If the speed and the angle are known, it is possible to rearrange to find the incoming spin which would promote rolling:

$$\omega_{in} = \frac{V_{in}}{r}\left[\cos\theta - \frac{5}{2}\mu\sin\theta(1+e)\right] \qquad [3.12]$$

3.5.d   Examples

Typical quoted values for the pace rating of a common acrylic surface are between 30 and 40 (ITF, 1997). The middle of this range corresponds to a frictional value of $\mu = 0.65$. The assumption was made that an extreme velocity was not used, so that a typical drop test COR could be used, i.e. $e = 0.75$. With these numbers, equation [3.11] gives a boundary angle of 19.4° to the horizontal. Any angle higher (i.e. steeper) than this will result in an impact containing some rolling.

Another condition worth investigating is that specified for the ITF pace rating tests, which is supposedly representative of a real shot. Firing a ball at 30 ms^{-1} at 16° to the horizontal is fairly close to the angle of 19.4° calculated above. Using these values together with $\mu = 0.65$ and $e = 0.75$ as before (a realistic COR, as this geometry gives a vertical incoming velocity of 8.3 ms^{-1}, not much higher than a 100 inch drop test), equation [3.12] gives the minimum topspin needed for rolling to occur as 160 rads^{-1}. This is certainly a figure which can be achieved by professional players.

Looking at equation [3.11], it is clear that increasing the value of μ will lower the boundary angle. Rearranging gives $\mu = \dfrac{2}{5\tan\theta(1+e)}$. For the pace rating conditions and $e = 0.75$, this gives a limiting friction of 0.80, suggesting that any surface with a pace rating of 20 or less will result in rolling.

3.6 Deformable surfaces

The descriptions above are based on an assumption that the surface is completely rigid. For many cases this many be an accurate assumption, but consideration must be given to the possibility of a surface which deforms.

In its simplest form surface deformation may affect the COR of a normal impact. The interaction between ball and ground is likely to affect the forces acting. Intuition may suggest that a softer surface leads to more energy loss, but this is not necessarily the case. The energy losses within the ball are due to its deformation; therefore a less stiff surface will reduce these losses by producing smaller ball deformations. This will of course store energy in the surface by deforming it rather than the ball – if it is an elastic enough material and returns a high enough proportion of the energy, the ball could rebound faster than on a rigid surface. It is important however that the time constant of the surface is not too dissimilar to that of the ball, or the recovery phase will take place after the ball has left.

Oblique impacts add a further complication. Previous work on impacts involving stiffer balls such as golf (Haake, 1994) and cricket (Carré et al., 1999) balls has found that the ground is deformed and pushed ahead of the ball. This forms a "ramp" up which the ball rolls, changing the angle of the velocity and also the forces acting. The ball will then rebound steeper than expected.

The important factor when the surface is deformable is the relative stiffness of the ball and surface. In the sport of golf, the ball is significantly stiffer than the surface – particularly when the weather is less than perfect and the turf is wet. Cricket research has found that the stiffness of the ball and surface are of the same order of magnitude. Compressing a tennis ball by hand and walking on a court (which is of course imposing a much larger force) suggests that for the majority of courts, the surface is significantly stiffer than the ball.

Whether this allows a rigid surface assumption in a model requires a more scientific approach to data collection, which will be investigated in a later chapter.

3.7   Developing the rigid body model

3.7.a   Finding velocities from the model

Previous steps have concentrated on using the relationships between the forces to work out slipping and rolling boundaries. The equations developed can be used to immediately find the outgoing conditions if an initial case of sliding throughout impact is considered. The COR e is defined by $e = -\dfrac{V_{y_{out}}}{V_{y_{in}}}$, giving $V_{y_{out}}$ if e is known. During sliding the relationship between friction and reaction force is $F = -\mu R$.

$$\int F dt = m\Delta V_x$$

but

$$\int F dt = -\mu \int R dt$$
$$= -m\mu\Delta V_y$$
$$= m\mu V_{y_{in}}(1+e)$$

therefore

$$V_{x_{out}} = V_{x_{in}} + \mu V_{y_{in}}(1+e)$$

Similarly, $M = Fr = -\mu r R$.

$$\int M dt = I\Delta\omega = -m\mu r\Delta V_y$$

$$\omega_{out} = \omega_{in} - \frac{3\mu V_{y_{in}}(1+e)}{2r}$$

$$\text{(assuming } I = \frac{2}{3}mr^2)$$

To progress any further it is necessary to make an hypothesis about the force profile. A sensible assumption is that the reaction force R is a half sine wave given by the equation $R = a\sin(bt)$. The coefficient a will thus be the peak force exerted on the ball. The other main feature of the waveform is the contact time T_C, giving $b = \dfrac{\pi}{T_C}$.

From the impulse equation,

$$\int_{t=0}^{t=T_C} R dt = m\left(V_{y_{out}} - V_{y_{in}}\right)$$
$$= -m V_{y_{in}}(1+e)$$

But $\qquad \int R dt = -\dfrac{a}{\omega}\cos(bt)$

thus $\qquad \dfrac{2a}{\omega} = -mV_{y_{in}}(1+e)$

giving $\qquad a = \dfrac{-mbV_{y_{in}}(1+e)}{2} = \dfrac{m\pi V_{y_{in}}(1+e)}{2T_C}$ $\qquad$ [3.13]

At a general time t, integrating the impulse equation allows the calculation of the vertical velocity V_y

$$-\dfrac{a}{\omega}\left[\cos(bt)-1\right] = m\left(V_y - V_{y_{in}}\right)$$

$$V_y = V_{y_{in}} - \dfrac{a}{mb}\left[\cos(bt)-1\right] \qquad [3.14]$$

Because $F = -\mu R$, a similar integration in the horizontal direction gives

$$V_x = V_{x_{in}} + \dfrac{\mu a}{mb}\left[\cos(bt)-1\right] \qquad [3.15]$$

Rotationally:

$$M = -Fr = \mu rR$$

$$\int M dt = I\Delta\omega$$

$$\mu r \int R dt = I\Delta\omega$$

$$-\dfrac{\mu ar}{\omega}\left[\cos(bt)-1\right] = I\Delta\omega = \dfrac{2}{3}mr^2(\omega - \omega_{in})$$

$$\omega = \omega_{in} - \dfrac{3\mu a}{2mrb}\left[\cos(bt)-1\right] \qquad [3.16]$$

At the time t_r where rolling starts, the condition $V_x = r\omega$ is satisfied. Therefore

$$V_{x_{in}} + \dfrac{\mu a}{mb}\left[\cos(bt_r)-1\right] = \omega_{in}r - \dfrac{3\mu a}{2mb}\left[\cos(bt_r)-1\right]$$

$$r\omega_{in} - V_{x_{in}} = \dfrac{5\mu a}{2mb}\left[\cos(bt_r)-1\right]$$

$$\cos(bt_r) = 1 + \dfrac{2mb}{5\mu a}\left(r\omega_{in} - V_{x_{in}}\right) \qquad [3.17]$$

The expressions derived here can be used to define a rigid body model which allows both sliding and rolling. If the equation for t_r is solvable and thus rolling occurs, the horizontal

speed and spin rate will remain the same for the range $t_r < t < T_c$. This is defined by the range

$$-2 < \frac{2mb}{5\mu a}\left(r\omega_{in} - V_{x_{in}}\right) < 0 \qquad [3.18]$$

The upper boundary of the expression above (i.e. $r\omega_{in} - V_{x_{in}} = 0$) defines an impact where the incoming spin matches that required for rolling. The lower boundary ($r\omega_{in} - V_{x_{in}} = 2$) describes an impact which just starts to roll at the end of contact, and by substituting in an expression for b/a from [3.1], equation [3.18] can be used to give limiting conditions in terms of incoming conditions as in the more general example earlier in the chapter.

Substituting the expression for $\cos(bt_r)$ back into the equations for V_x and ω leads to the values below which are valid for any impact which ends in rolling.

$$V_x = \frac{3V_{x_{in}} + 2r\omega_{in}}{5} \qquad [3.19]$$

$$\omega = \frac{3V_{x_{in}} + 2r\omega_{in}}{5r}$$

This model allows the investigation of the effect of incoming conditions. It is not on its own a solution to the modelling problem, as there are too many assumptions involved. The expressions developed here give outgoing conditions for velocity and spin both for impacts which slide throughout and for those which end in rolling. They are summarised in Table 3.1 below.

Table 3.1 Rigid body model equations for velocity and spin of impacts which are wholly sliding, or which contain some rolling.

Variable	General value at time t (assuming sliding)	Final value if sliding throughout	Final value if rolling occurs
V_x	$V_{x_{in}} + \frac{\mu a}{mb}\left[\cos(bt) - 1\right]$	$V_{x_{in}} + \mu V_{y_{in}}\left(1 + e\right)$	$\dfrac{3V_{x_{in}} + 2r\omega_{in}}{5}$
V_y	$V_{y_{in}} - \frac{a}{mb}\left[\cos(bt) - 1\right]$	$-eV_{y_{in}}$	
ω	$\omega_{in} - \frac{3\mu a}{2mrb}\left[\cos(bt) - 1\right]$	$\omega_{in} - \dfrac{3\mu V_{y_{in}}\left(1 + e\right)}{2r}$	$\dfrac{3V_{x_{in}} + 2r\omega_{in}}{5r}$

3.7.b   Applying model predictions to Surface Pace Rating

The definition of Surface Pace Rating is given in [3.4]. Looking at the equations in Table 3.1, if rolling occurs then the final value of the rebound velocities in both the horizontal and vertical directions will not depend on the coefficient of friction. In other words, increasing the friction will decrease the Pace Rating until rolling occurs, then any further increases in friction will not change the Pace. This limiting Pace value can be estimated using the equations above.

$$SPR = 100\left(1 - \frac{V_{x_{in}} - V_{x_{out}}}{V_{y_{out}} - V_{y_{in}}}\right)$$

$$= 100\left(1 - \frac{V_{x_{in}} - \left(\dfrac{3V_{x_{in}} + 2r\omega_{in}}{5}\right)}{-eV_{y_{in}} - V_{y_{in}}}\right)$$

$$= 100\left(1 - \frac{\dfrac{2}{5}\left(V_{x_{in}} - 2r\omega_{in}\right)}{-V_{y_{in}}\left(1 + e\right)}\right)$$

For the specific case (as in the Surface Pace tests) where the incoming spin is zero:

$$SPR = 100\left(1 - \frac{2V_{x_{in}}}{-5V_{y_{in}}\left(1 + e\right)}\right)$$

and as the incoming angle is defined by $\tan\theta = \dfrac{-V_{y_{in}}}{V_{x_{in}}}$ and applying the specific geometry

defined by the test specifications,

$$SPR = 100\left(1 - \frac{2}{5\left(1 + e\right)\tan 16°}\right)$$

For a typical COR of 0.75, this gives $SPR = 20.3$, suggesting that a Surface Pace value lower than this should never be measured.

3.7.c   Speed, spin and angle throughout impact

The equations in Table 3.1 can be used to see how changing the incoming conditions affects an impact. This gives an indication as to the importance of whether a ball slides or rolls. A range of conditions were used based on the pace rating test of a 30 ms^{-1} impact at 16° to the horizontal, without spin. A coefficient of friction of $\mu = 0.55$ was assumed.
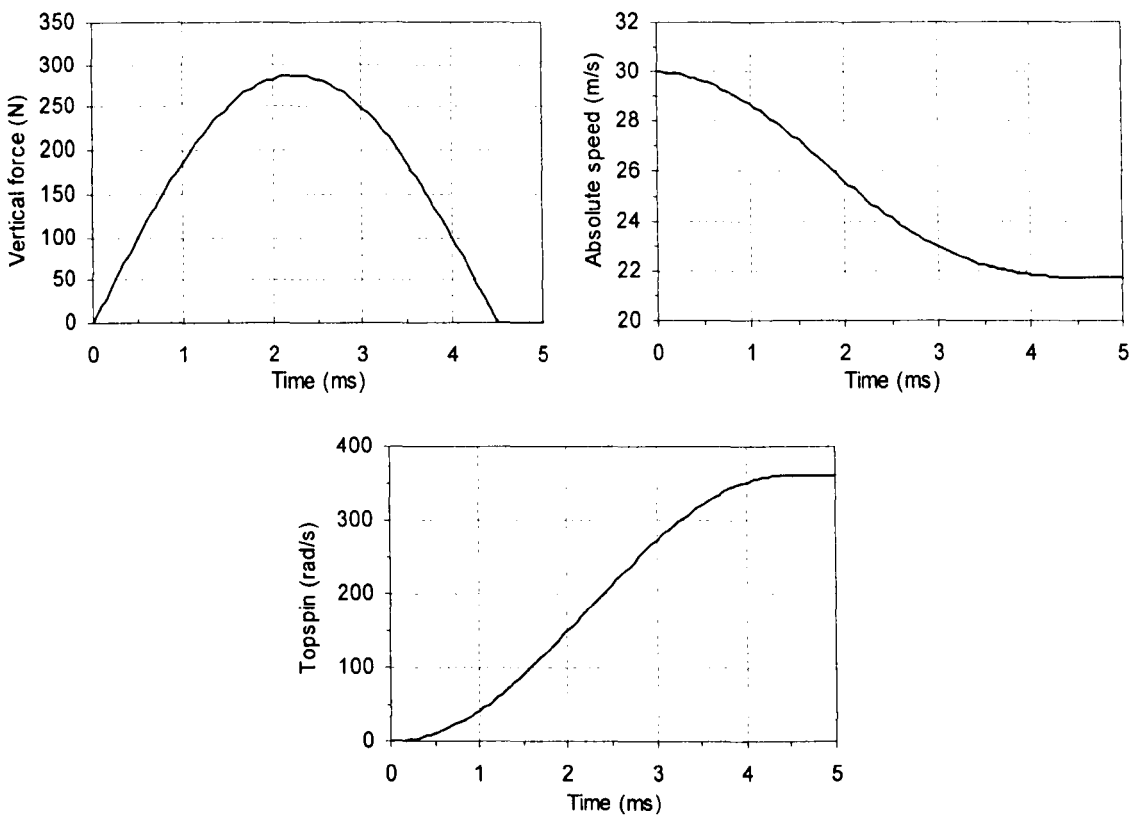
Figure 3.6 Force, speed and spin plotted during impact for a rigid body model.

Figure 3.6 shows force, speed and spin graphs through the impact. In order to plot these variables during contact, a contact time must be used. The value chosen was 4.5 ms, leading to a peak force of 288 N.

3.8   Rigid body model predictions - outgoing speeds, spins and angles

The equations in Table 3.1 were also used to investigate the importance of the different parameters of the model. The speed, spin and angle were varied in turn while keeping the other variables constant, based on an impact at 30 ms^{-1} at 16° to the horizontal on a surface with coefficient of friction $\mu = 0.55$.

3.8.a   The effect of speed

The first case considered is an impact with constant incoming angle and spin, looking at the effect of a variation in speed. If there is no incoming spin the initial speed will have no effect on whether the ball slides or rolls at the end of the impact. In this case, the outgoing speed and spin are both simple increasing functions of incoming speed, and the angle remains constant. In a real-life situation, increasing ball speed will change the COR and therefore have an effect on all the outgoing variables, but it is useful to remove this factor when assessing the effect of speed.

A more interesting situation is when the ball possesses a fixed value of incoming topspin. This will lead to a certain incoming speed which defines a boundary between wholly slipping impacts and those containing rolling, and this speed will depend on the value of spin.
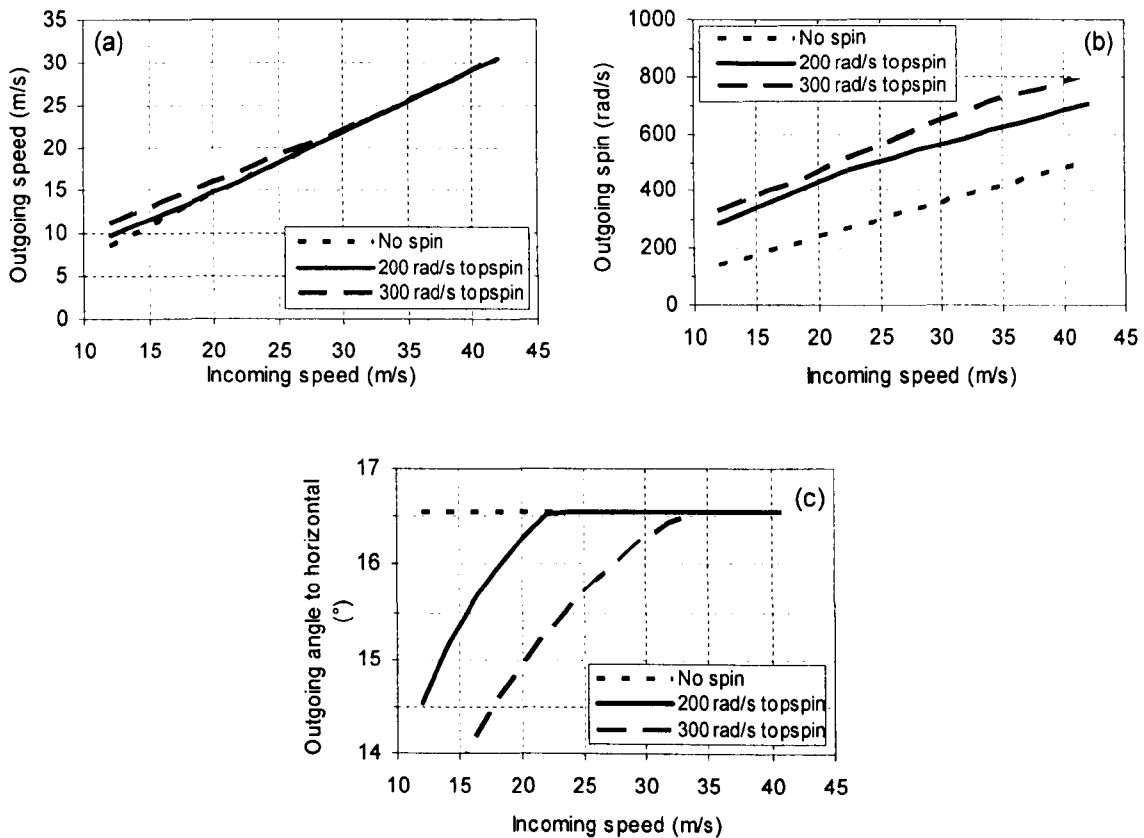
Figure 3.7 Rigid body model predictions showing the effect of changing the speed on an impact at 16° to the horizontal with $\mu = 0.55$.

These two cases are shown in Figure 3.7 for speeds between 12 and 42 ms^{-1} at an angle of 16°. Results were calculated for zero spin and also with 200 and 300 rads[-1] of incoming topspin. With these amounts of topspin there is a "boundary speed" of about 22 and 33 ms^{-1} respectively; above this speed the ball will always slide but below it the incoming topspin is enough to give rolling. The outgoing speed increases almost linearly, and there is very little difference between those impacts with spin and those without. As the speed increases, it will dominate the term $3V_{x_{in}} + 2r\omega_{in}$ if the incoming spin remains constant.

Figure 3.7 (b) shows the slight difference between sliding and rolling. For both situations the outgoing spin is a linear function of incoming speed and spin as can be seen from the equations in Table 3.1, but the gradients are different.

A graph of angle against speed is shown in Figure 3.7 (c). This shows a much clearer division between sliding and rolling. If the ball slides throughout, the angle must be the same whatever the incoming spin, as ω_{in} does not feature in the equations. This angle is

constant because all terms are functions of $V_{x_{in}}$ and $V_{y_{in}}$, and hence proportional to the incoming speed – in a more physical sense, the forces remain the same throughout. When rolling occurs, the outgoing horizontal speed is a function of ω_{in} – as the speed decreases the spin becomes more dominant and more time is spent rolling, therefore the angle decreases (as more time rolling means less horizontal impulse and therefore a larger horizontal velocity component).

3.8.b   The effect of spin
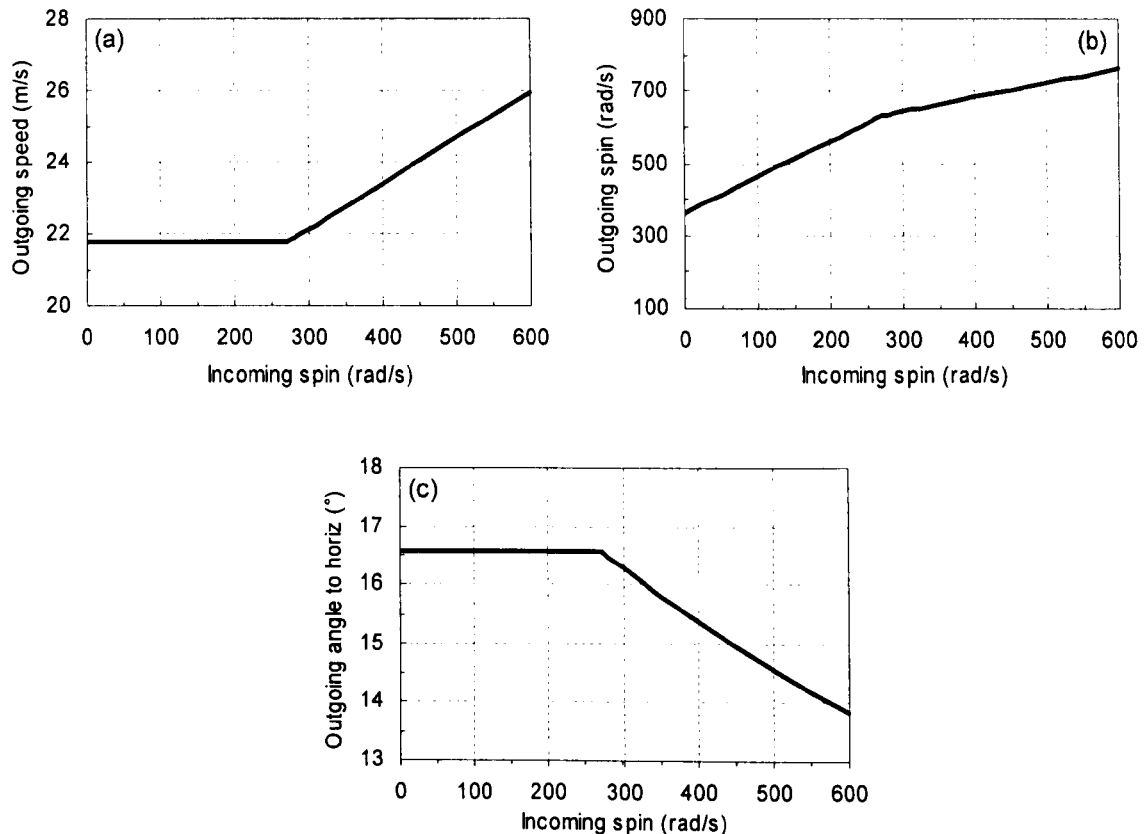
Figure 3.8 The effect of applied spin on outgoing (a) speed, (b) spin and (c) angle for a rigid body model of a ball impacting at 30 ms^{-1} at 16°.

The speed and angle will not change as long as the incoming spin remains within the range which gives sliding throughout. Equation [3.19] shows that the horizontal speed increases as a linear function of spin as the spin increases past the minimum value needed for rolling, therefore the absolute speed will also increase. The angle will decrease as the horizontal speed remains constant in all cases. Outgoing spin will increase linearly, but only 2/5 of each extra incoming unit of spin will be retained, whereas for wholly slipping impacts every unit of incoming spin adds to outgoing spin.

The result of these trends is shown schematically in Figure 3.8. This shows the model predictions for impacts at 30 ms^{-1} at 16° to the horizontal, with spin up to 600 rads^{-1} of topspin. Here the spin boundary for rolling to start is about 250 rads^{-1} of topspin. As

expected, spins below this give a constant speed and angle, and each extra unit of incoming spin is converted to outgoing spin. Above 250 rads⁻¹, the horizontal speed increases, and therefore the absolute speed. The vertical speed remains constant and so the angle decreases. The outgoing spin is still a linear function of incoming spin, but the decreased "conversion" of spin can be seen in the lower gradient in Figure 3.8 (b).

3.8.c   The effect of angle
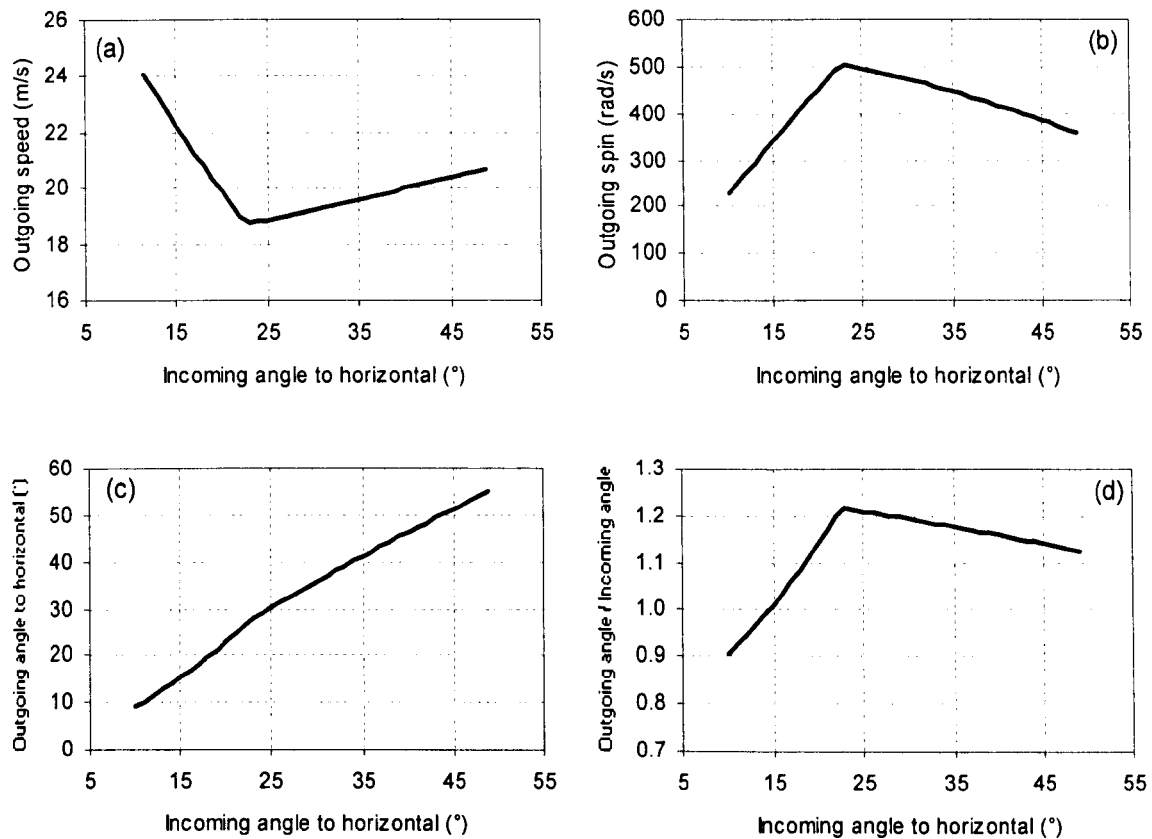
Figure 3.9 The effect of applied angle on outgoing (a) speed, (b) spin, (c) angle and (d) angle ratio, for a rigid body model of a ball impacting at 30 ms⁻¹.

Figure 3.9 shows how the impact is affected by a range of angles between 10 and 40 degrees. The equation $\tan\theta = \dfrac{2}{5\mu(1+e)}$ derived earlier gives a minimum angle for rolling to occur as 22.6°, and this can be clearly seen as discontinuities in the outgoing speed and spin graphs. The outgoing angle is affected less. This set of data is more difficult to predict from an intuitive viewpoint, because changing the incoming angle alters the ratio of horizontal and vertical speeds. A constant vertical COR will have a varying effect on the outcome depending on the size of $V_{y_{in}}$ relative to $V_{x_{in}}$. The outgoing angle is barely affected by the slipping or rolling condition, but the speed and spin trends change dramatically. As the incoming angle increases from its minimum value, the outgoing speed decreases until rolling occurs. The trend then reverses, and for further increases in angle

the speed increases. Similarly the outgoing spin increases with the angle until rolling, then decreases with higher angles.

3.8.d   The effect of friction

A range of coefficients of friction between 0 and 1 were applied, although the other incoming conditions were changed slightly to have an incoming spin of 300 rads^{-1} – chosen so that the slip/roll boundary would be approximately in the middle of the range of frictions used.
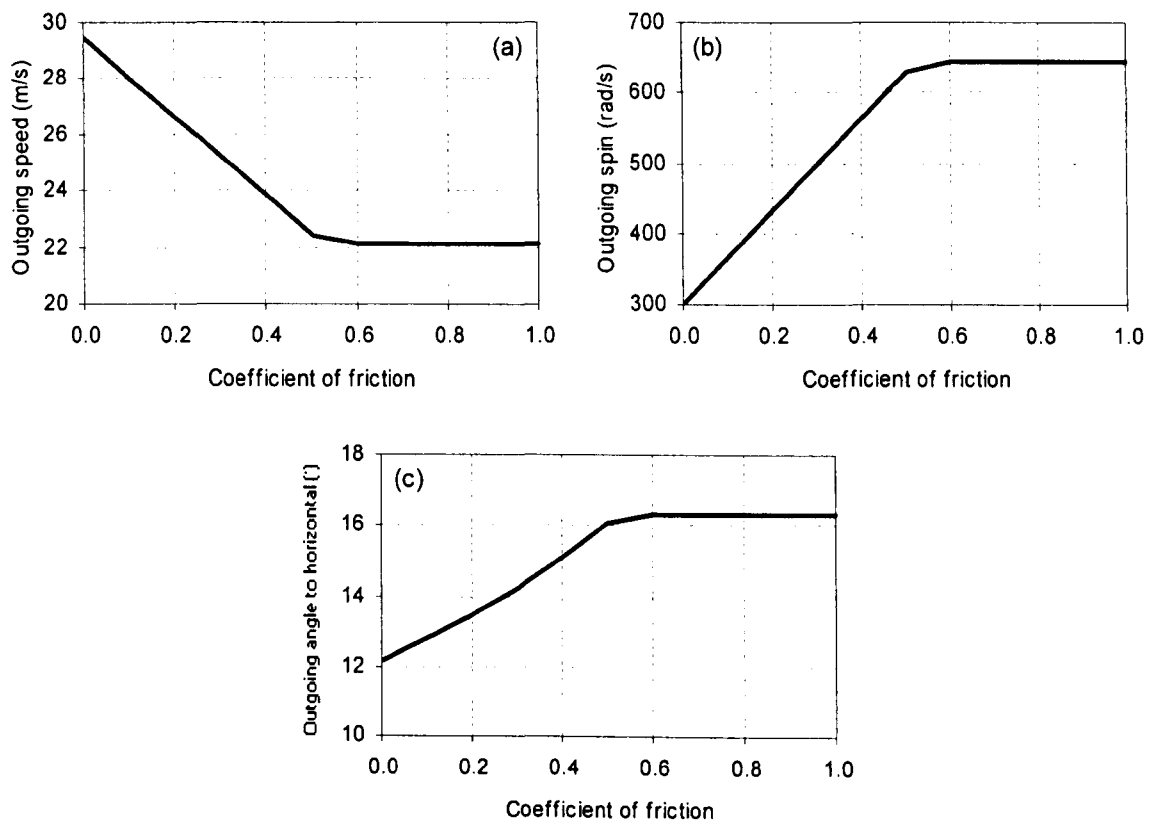
Figure 3.10 The effect of coefficient of friction on (a) outgoing speed, (b) outgoing spin and (c) outgoing angle, on a rigid body model of an impact at 16° with 300 rads^{-1} of topspin.

The effect of friction on outgoing conditions is shown in Figure 3.10. There are clear differences between slipping and rolling, but this is possibly the most intuitive parameter. In the slipping phase, as the friction is increased the speed drops, the spin increases as does the angle – the vertical velocity component stays constant and the horizontal velocity component reduces therefore the angle increases. Once rolling occurs, increasing the frictional coefficient further has no impact other than affect the time during the impact at which rolling happens.

3.9 Summary and conclusions

Consideration of a fairly crude rigid body model gives useful insight into the limits of surface and shot parameters which give an impact sliding throughout its duration. For example, the minimum topspin required for rolling for a 30 ms^{-1} at 16°to the horizontal on a surface with coefficient of friction of 0.65 is only 160 rads^{-1}. This suggests that rolling is likely to occur in a game, especially on slower surfaces, although this incoming velocity is not necessarily representative of a real shot. It is necessary to look more closely into the speeds and angles at which the ball lands on the court, which is the subject of the next chapter.

A refinement of the rigid body model was presented, based on the primary assumption of a sinusoidal shape to the force-time profile. This allows a prediction of how speeds and spins change during the impact period. From this model it appears that the slipping/rolling condition is extremely important, as trends in outgoing variables can change when the ball starts to roll.

4   The aerodynamics of a tennis shot

4.1   Introduction

The overall aim of this project is to model the impact of a tennis ball on a court surface. In order to know correct boundary conditions it is essential to know how the ball arrives on the surface. It would be extremely difficult to experimentally measure the shot of a top professional player in a tournament environment as it lands on the court, and so a trajectory model was used to predict the impact conditions given known initial speeds and spins. There is a reasonable amount of available data on ball speeds (particularly for services which have been regularly measured in recent years using radar guns), including average and maximum values. Although there is limited data as to the conditions at the point of impact on the court, a trajectory model based on initial speeds as the ball leaves the racket will give us a good approximation.

4.2   Aerodynamic forces
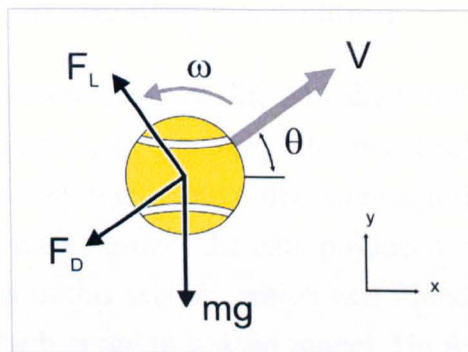
Figure 4.1 The forces acting on a spinning tennis ball during flight.

The equations of motion for an object travelling through a viscous fluid such as air are well-known. Consider the ball shown in Figure 4.1 travelling at speed V and backspin ω at an angle θ above the horizontal (using these directions as positive backspin causes a lift force upwards). Air resistance will provide a retarding drag force F_D on a ball governed by

$F_D = \frac{1}{2}\rho V^2 C_D A$ where ρ is the density of the air, v the ball speed, A its cross-sectional area and C_D the non-dimensional drag coefficient. A similar expression gives the lift force F_L as a function of lift coefficient C_L: $F_L = \frac{1}{2}\rho V^2 C_L A$. The challenge is to find values for the lift and drag coefficients, as both may vary with such factors as the speed and spin rate of the ball.

In order to find the trajectories, the forces are resolved to give components in terms of x and y co-ordinates.

Thus $\qquad V_x = V \cos\theta$

and $\qquad V_y = V \sin\theta$

$$m\frac{dV_x}{dt} = -F_D \cos\theta - F_L \sin\theta$$

$$m\frac{dV_y}{dt} = -mg - F_D \sin\theta + F_L \cos\theta \qquad [4.1]$$

The equations of motion above cannot be solved analytically, but a good solution can be found by advancing by a small time step Δt.

$$V_{x_{n+1}} = V_{x_n} - \frac{\Delta t}{m}\left(F_D \cos\theta + F_L \sin\theta\right) \qquad [4.2]$$

$$V_{y_{n+1}} = V_{y_n} + \frac{\Delta t}{m}\left(-mg - F_D \sin\theta + F_L \cos\theta\right) \qquad [4.3]$$

4.3   Measurements of lift and drag coefficients

Published data for the measurements of lift and drag coefficients of a tennis ball are discussed in detail in Chapter 2. In summary, the two coefficients depend on the speed through the air to a fairly small degree and much more significantly, the rate of spin of the ball. Due to the high spin rates needed, the data produced by Chadwick (2003) was used for most of the simulations in this section, which was found by mounting balls on a shaft spinning at an extremely high speed in a wind tunnel. He found empirical expressions for both coefficients which were independent of Reynolds number and thus purely a function of peripheral velocity ω and wind speed v, given by

$$C_D = 0.5365 + \left(1.9980\left(\frac{\omega}{v}\right)^{-2.1887} + 2.8619\right)^{-0.7069}$$

and $\qquad C_L = \left(2.591\left(\frac{\omega}{v}\right)^{-1.887} + 4.809\right)^{-0.529} \qquad [4.4]$

4.4   The effect of air resistance on a drop test

If an object drops under the influence of gravity and there are no other forces acting on it, the coefficient of restitution e (defined as the ratio of the rebound speed to the impact speed) is simply related to the drop height h_1 and the rebound height h_2 by the following expression:

$$e = \sqrt{\frac{h_2}{h_1}}$$

This would give the following acceptable range according to the ITF 100 inch drop test (which states the bound must lie between 53 and 58 inches):

$$e_{min} = \sqrt{\frac{53}{100}} \approx 0.73$$

and

$$e_{max} = \sqrt{\frac{58}{100}} \approx 0.76$$

However, the ball will be slowed both before and after bouncing by air resistance, and so for a given bounce height, the actual COR will be higher than calculated by the simple relationship above. A simple way to look at this is that for the ball to bounce to a certain height, if energy is lost to air resistance then less energy must be lost in the impact on the ground, hence a higher COR.

If the ball has cross-sectional area A and drag coefficient C_d, and the density of air is ρ, the equation of motion of the ball is shown below for conditions before and after impact (with the sign convention of positive being vertically upwards):

$$m\ddot{y} = \frac{1}{2}\rho C_d A \dot{y}^2 - mg \qquad (\dot{y} < 0) \qquad [4.5]$$

$$m\ddot{y} = -\frac{1}{2}\rho C_d A \dot{y}^2 - mg \qquad (\dot{y} > 0) \qquad [4.6]$$

Equations [4.5] and [4.6] were solved using a timestep iteration. For a ball with mass 57 grams, diameter 67 mm and constant drag coefficient $C_d = 0.53$ as found by Chadwick and Haake (2000), this gives an impact velocity of 6.88 ms^{-1} compared to 7.06 ms^{-1} neglecting drag. For a given rebound height, the COR can be varied and the iteration run until the height is achieved. The minimum and maximum COR values for the 53 and 58 inch limits using this method are 0.76 and 0.79, 4% higher than without considering drag (rebound speeds of 5.12 ms^{-1} and 5.46 ms^{-1}). This is not a huge error in itself but is significant – put into perspective, it is a similar figure to the difference between the minimum and maximum allowable COR values stipulated in the rules of tennis.

4.5   Applying aerodynamic theory to real shots

4.5.a   The effect of spin on trajectories
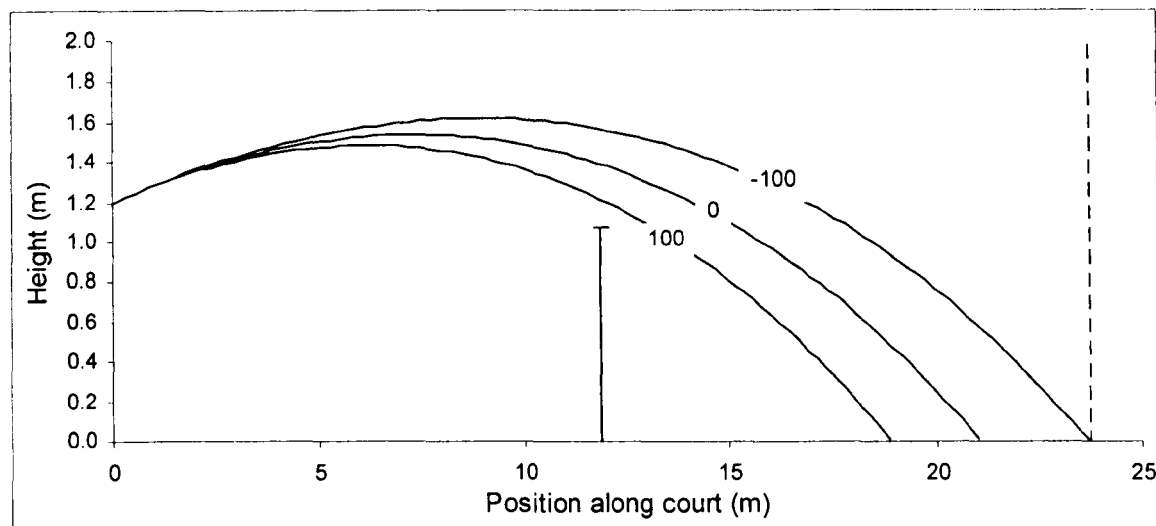
Figure 4.2 The effect of spin; the trajectory of a 70 mph groundstroke is shown for the shot hit flat and with 100 rads⁻¹ of both backspin and topspin.

Trajectories were calculated for a ball struck from the baseline at 30 ms^{-1} (70 mph), 5 degrees above horizontal. The initial height was 1.2 m. Figure 4.2 shows the trajectories for the shot hit without any spin, and with 100 rads^{-1} of both backspin (denoted as -100) and topspin (100). These are not necessarily realistic cases as a player will adjust the speed or angle to keep the ball reasonably close to the net, but they do show the effect spin can have on a shot. The value of spin used here is not actually a particularly large one; Cislunar (1997) measured average values for each of a range of professional men as 140 to 340 rads^{-1} of topspin and 223 to 327 rads^{-1} of backspin. Applying 100 rads^{-1} of topspin makes the ball land a little over two metres shorter than the shot without spin, and the same amount of backspin produces a shot which lands right on the baseline (just over 2.5 m further than the ball without spin). Of course, in game situations, a player is likely to use backspin when hitting the ball with considerably less power. The spin creates a lift force opposing gravity which allows the ball to travel further than it would without spin. This means the player can clear the net with a shot of lower speed which, combined with the shallower impact angle from the backspin trajectory, produces a lower bounce (making it hard for the opponent to return the ball with much pace).

4.5.b   Using the trajectory model to find impact conditions
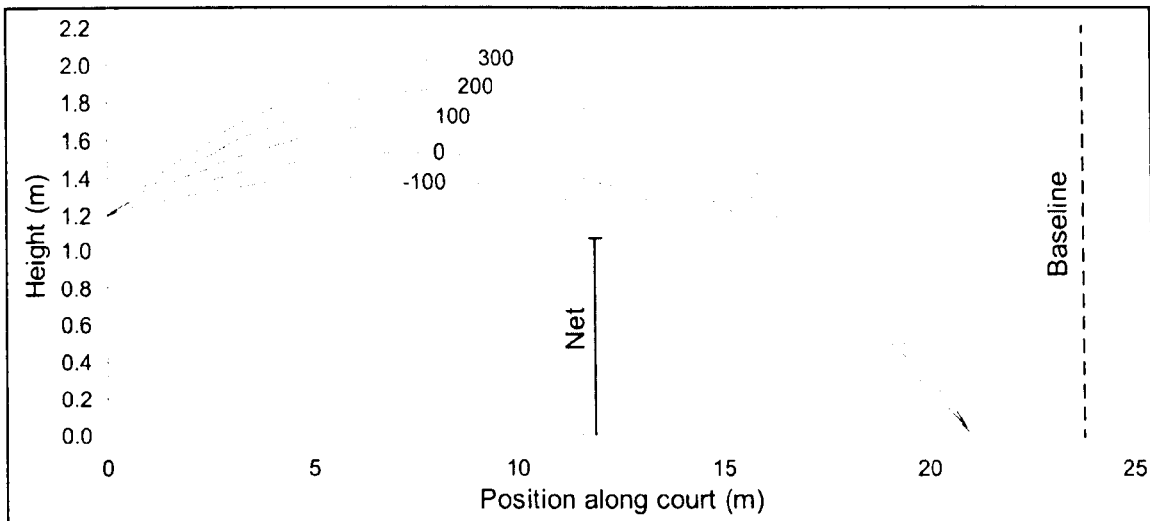
Figure 4.3 Trajectories for balls hit with the same speed but different spins, landing in the same position on the court. Each trajectory is labelled with the relevant topspin value for spin.

This set of calculations investigated the initial angles needed for a range of shots with a given speed to land in the same position on the court. Cislunar (2000) quote a typical speed for a professional groundstroke as being 70 mph. The impact position chosen was midway between the service line and the baseline, giving a reasonably deep shot. This gives the boundary condition $y = 0$ m when $x = 21.03$ m. The trajectory model was used to find the angle at which various 70 mph shots must be hit to land in the same place as the spin imparted on the ball varies. These shots are shown in Figure 4.3 which clearly demonstrates the effect that spin can have. Table 4.1 shows the initial angle as well as the impacting speed and angle for each spin. The data shows that the impact speed does not change greatly, but the spin has a big difference on the angle at which the ball reaches the court surface. Shots with 100 rads^{-1} of backspin are hit almost flat and land at 12.2° to the horizontal, whereas shots with 300 rads^{-1} of topspin are about 7° steeper both after being hit and landing.

Table 4.1 Impact speeds and angles for 70 mph shots with various spins landing at the same spot, midway between the service line and baseline.

Topspin (rads^{-1})	Launch angle (degrees)	Impact angle (degrees)	Impact speed (ms^{-1})
-100	3.4	12.2	20.8
0	4.9	13.8	21.2
100	6.7	15.9	20.8
200	8.4	18.2	20.1
300	10.0	20.3	19.3

The impact conditions were used to calculate minimum spins needed for the ball to roll. The rigid body model developed in Chapter 3 gave the spin boundary which for a constant speed of 21 ms^{-1} is a function of angle and coefficient of friction. This spin boundary is shown in Table 4.2 below for three different frictional values $\mu = 0.5$, $\mu = 0.6$ and $\mu = 0.7$. This corresponds to "pace ratings" of 50, 40 and 30 respectively, covering a wide range of courts. The shaded cells are those conditions where the spin is greater than that calculated as the slip/roll boundary. Even on the fastest of these surfaces, which is the most likely to retain slipping throughout, around 200 rads^{-1} or above of topspin will produce an impact which is rolling when it leaves the surface. When $\mu = 0.7$ (by no means an excessively high frictional value, clay courts commonly measure up to $\mu = 0.8$), less than 100 rads^{-1} is needed, meaning in practical terms that any topspin shot worthy of the name will cause the ball to roll.

Combining an aerodynamic model such as this with impact models discussed in a previous chapter makes this calculation much more realistic. The different trajectories can be incorporated, rather than ignoring the way that spin provided to the ball changes the way it lands.

Table 4.2 Rigid body model predictions for minimum spins needed for rolling to occur, using the impact angles found from trajectory modelling. Shaded cells are those for which the impact spin is greater than the minimum for rolling.

Impact topspin (rads^{-1})	Impact angle (degrees)	Calculated minimum spin needed for rolling (rads^{-1} topspin)		
		$\mu = 0.5$	$\mu = 0.6$	$\mu = 0.7$
-100	12.2	327	268	210
0	13.8	286	219	153
100	15.9	230	154	77
200	18.2	170	84	-3
300	20.3	113	17	-80

4.5.c   *Maximum impact speed on the court*

The extreme case of a "normal" shot is the serve. It is possible for such shots as a smash to happen with similarly high speeds, but these are much less common – every point starts with a serve! At the time of writing the fastest serve recorded was 149 mph (66.2 ms^{-1}) by Greg Rusedski at Indian Wells in 1998. There is no record of spins achieved by Rusedski but NASA and Cislunar Aerospace, Inc. (Cislunar Aerospace, Inc. 1997-2000) give estimates of first serve spin rates ranging between 162 and 332 rads^{-1}. This is the range of average values for 11 professional men, and therefore a mid-range value of 250 rads^{-1} was chosen as a typical value. Rusedski is 1.93 m tall, which using the ratio of 1.53 for impact height to standing height suggested by Elliott et al. (1986), gives an initial starting height for the ball of 2.95 m.

The window of a legal serve is formed by the boundaries of the net (giving the lowest angle) and the service line (giving the highest angle possible). Using the centre net height of three feet, this gives $y = 0.91$ at $x = 11.885$ for the first condition, and $y = 0$ at $x = 18.285$ for the second (in metres).

The initial conditions of speed and height were used to find the two angles giving trajectories passing through these points. For the ball to land on the service line it must be hit at 8.8 degrees below horizontal. A shot with the same speed and spin just clearing the net would need to be hit at an angle of 7.7 degrees below the horizontal. The ball would land 4.64 m into the service box, which is 72% of the way along its length. The second of these shots can be considered an extreme case of the vertical component of velocity. It lands with a speed normal to the court of -9.84 ms^{-1}.

This model also shows the value of spin. Even for a player of this above-average height, a flat serve would have to be hit incredibly accurately to reach 149 mph whilst still landing in the service box. In fact the serve landing on the service line has a height of 1.16 m when it passes the net. This means that the range of starting angles which will provide a legal serve form a "window" for the player to hit which is only 25 cm high.

4.6 Summary

There has not been a particularly large amount of work in the area of tennis ball aerodynamics, but recent research has provided good consistent measurements of the drag coefficient. A constant value of $C_D = 0.53$ was found by Chadwick and Haake (2000) for non-spinning balls. There has been much less work with spinning balls, as this is much more experimentally difficult. Stepanek (1988) gave an empirical formula for C_L as a function of the ball peripheral velocity. Chadwick (2003) found similar functions for both C_D and C_L, which give a value of $C_D = 0.54$ when there is no spin. Goodwill *et al.* (2004) measured both C_D and C_L for different spin rates and obtained similar results, although they found the values depended on Reynolds number.

Air resistance is often ignored when calculating the impact speed of a ball dropped under the influence of gravity. The square root of the ratio of the bound height to the drop height is commonly used to calculate a COR, but for the range of an approval drop test, this gives a COR value about 4% lower than if drag is applied.

A trajectory model was used to illustrate the large effect which spin has on the flight of a ball. For the same speed and angle of a 70 mph shot, a moderate spin rate of 100 rads^{-1} affects the landing position by several metres (in either direction, if topspin or backspin is used).

The model was also used to investigate the impact conditions for good length groundstrokes. With a constant incoming speed, the outgoing speed did not change significantly, but a range of spins from 100 rads^{-1} of backspin to 300 rads^{-1} of topspin produced an impact angle of between 12 and 20 degrees to the horizontal. Using these angles to improve the realism of previous calculations for the spins needed to cause the ball the roll provides interesting results. Even on fairly fast (i.e. low friction) surfaces, it is easily feasible for a professional player to hit a shot with enough spin to roll off the court. On slow surfaces such as clay, any shot with topspin will cause the ball to roll.

The current record for the fastest serve recorded (149 mph) gives a good limit to the absolute limit of vertical velocity component likely to be experienced in normal play. This was calculated to be 9.8 ms^{-1} for flat serves (i.e. without spin).

5   Surface testing

5.1   Introduction

The game of tennis is unusual for the variety of surfaces on which it can be played. It is commonly known and accepted that the surface properties play an important part in the game, and affect the behaviour of both players and equipment, as well as the tactics needed for success. This is demonstrated by the fact that many professional players are well known for their ability on one particular surface, and this defines their style of play. Indeed, the differences can be so extreme that there will be a huge difference between results in those times of the year traditionally associated with, for example, grass (or other fast surfaces) and clay court tournaments.

The challenge therefore is to identify and measure in an objective way those properties which can seem so self-evident to the spectator or player. It was also important to distinguish between the properties which affect the player and those which affect the ball, as their relative importance may well change dramatically.

5.2   Summary of existing ITF performance characteristics

The three performance characteristics which were identified by the ITF (1997) as being key factors in a tennis court surfaces are listed below with their quoted definitions:

- Surface Pace - *The "speed" of the court, which includes both speed and angle of the ball rebounding off the surface.*

- Friction - *As determined by measuring both Slip resistance and Traction.*

- Energy Absorption - *The ability of a surface to absorb energy (or shock).*

The first of these, surface pace, seems to sum up the intuitive perception of a court. As a first definition, players are most likely to describe a court as "fast" (e.g. grass) or "slow" (e.g. clay). The ITF came up with a mathematical formula for pace called Surface Pace Rating, based on the velocity changes which happen when a standard ball bounces on the court, which will be discussed later in the chapter. It has also been suggested that the change in horizontal velocity - effectively how soon the ball reaches the racket - is how a player measures the pace of a surface. The player is most likely to intuitively measure pace by the time he or she has to play a shot, but it is found that they also associate the pace with the angle at which the ball reaches them – for example, a "fast, skiddy, low-bouncing" surface as opposed to a "slow, high-bouncing" one. Some of this is due to the friction – a court with a high coefficient of friction will reduce the horizontal velocity much more than a low friction surface, but may produce the same vertical rebound velocity, increasing the angle of the trajectory. It must also be recognised however that the angle and height is

affected in other ways. For example, on a slow surface such as clay, players will hit the ball differently – slower and with more spin. Brody (1988) suggests that the difference between fast and slow surfaces should in theory only make 0.05 seconds difference to the time the receiver has, but that this is not representative of reality. In practise, the whole game is slowed down because if the ball reaches a player at a slower speed, it also leaves his racket at a slower speed for the same racket swing speed.

The friction measurements defined above as performance characteristics must be used carefully when the impact of ball on surface is considered, as the two methods are both aimed at measuring the friction between a shoe and the court. Slip resistance uses a swinging pendulum to slide a rubber foot along a court surface specimen for a certain distance, and finds the energy lost to friction by measuring the maximum height obtained after contact. The traction test measures the minimum force to cause rotational movement of a weighted circular disc, by gradually increasing the applied torque. This measurement is somewhat user-dependent.

Energy (or shock) absorption is primarily concerned with the effect of the surface on the biomechanics of the player. Although tennis courts need to be relatively "hard" in order to produce a bounce of a ball which enables the game to be played successfully, the shock transmitted to the player is particularly important in terms of comfort and injuries produced. The difference in forces produced by a running human and a bouncing tennis ball suggest that test methods aimed at measuring impact properties relevant to the player may not be useful when considering the ball.

Five other characteristics are also listed as important measurements: vertical ball bounce, permeability, slope, evenness and consistency. Of these five, the only one relevant to the problem of modelling ball impacts is the vertical ball bounce. It is however of potentially crucial importance, and will be discussed later in this chapter.

5.3 Surface Pace Rating

5.3.a Test method

At the time of writing, the concept of surface pace was of great interest in the world of tennis. A proposal was under development to bring into place a court surface classification scheme (ITF, 2000b). Under this scheme accredited laboratories would test a court and measure its pace, with the separate test equipment compared regularly. The test specification details how the surface sample should be fixed, and also the properties of the balls to be used. For the vast majority of tests, including surface classification, three special test balls should be used which satisfy a more stringent set of criteria than listed under the Rules of Tennis. These are reproduced from ITF (1997) and detailed in Table

5.1. If for some reason other balls (e.g. as played in a tournament) are to be used, four balls are used and the three most consistent values taken.

Table 5.1 Test ball specifications.

	Nominal value	Range for approval tests	Range for test balls
Ball mass	57.6 g	± 0.9 g	± 0.3 g
Ball diameter	67.5 mm	± 1.6 mm	± 0.40 mm
Forward deformation	6.48	± 0.89 mm	± 0.32 mm
100 inch rebound height	1.41 m	± 0.064 m	± 0.010 m
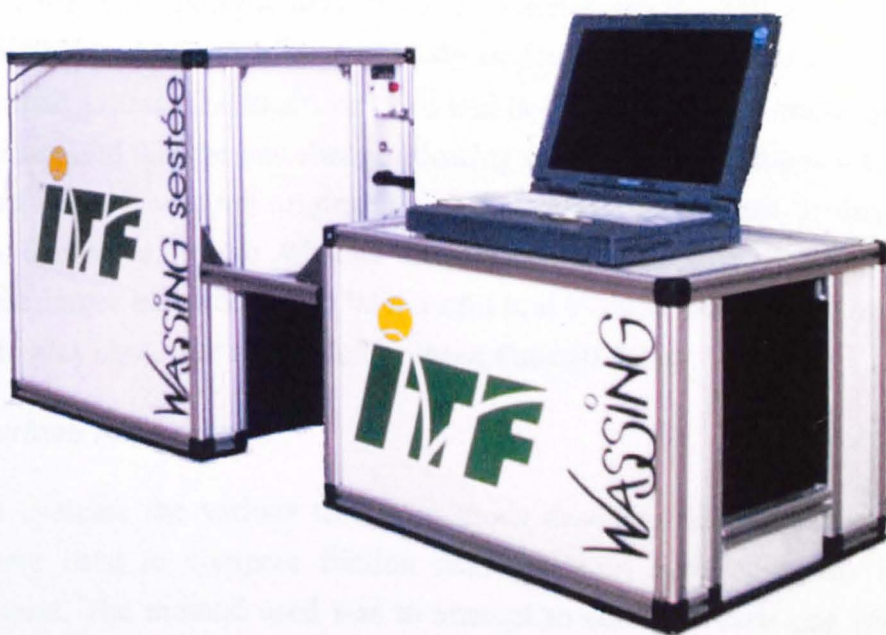
Figure 5.1 The equipment used to measure surface pace rating.

The standard piece of equipment used is shown in Figure 5.1. A ball is fired in from the left at 30 ± 2 ms^{-1}, at $16 \pm 2°$ to the horizontal. Although the method of projection is not specified in the test, the most common way of projecting the ball is using a compressed air cannon. This gives good positional accuracy and meets the requirement of imparting less than three revolutions per second of spin – in fact the spin is extremely close to zero. The ball passes through the smaller unit, impacts on the surface and then passes through the second unit. Each of the two sections contains an array of infra-red beams at both the entry

and exit. These beams are spaced closely enough together so that the timings of their being broken can be used together with the assumption of a spherical target object to give positional data with very good accuracy. The manufacturers of the system claim that the Sestée test apparatus measures the velocities to an accuracy of ± 0.01m/s and the angle within ± 0.1° (Wassing, 2004). Any speed measurements assume that the ball is travelling in a plane perpendicular to the array of infra-red beams. In practise the ball trajectory must be very close to this in order to pass through the four openings in the apparatus.

The three categories of SPR are defined as listed below. These categories overlap, allowing some leeway in the description of a court. Repeatability of the measurement is claimed to be ± 1.

- Category 1 (slow)   0 – 35
- Category 2 (medium/medium fast)   30 – 45
- Category 3 (fast)   40 +

One of the aims of the categorisation was to enable the "targeting" of balls to surfaces – initially *on a professional basis only*. A stiffer, faster-bouncing ball is intended for use on courts classified as slow and a larger, aerodynamically slower ball is intended for use on courts described as fast. The traditional ball will be used on medium/medium fast surfaces. It should be stressed that the law change allowing the two new ball types was on a two year experimental basis. It was not originally aimed at recreation players, as these do not need to concern themselves as to whether their game corresponds to official regulations. However, the larger ball would also be a useful tool to those learning the sport, as it gives more time to play shots due to the slower speed through the air.

5.3.b   Surface Pace results

In order to evaluate the various testing methods described in this chapter, a variety of surfaces were used to compare friction readings from each apparatus in a series of laboratory tests. The method used was to attempt to correlate each one with the Surface Pace Rating, which is an established test and widely used. The surfaces used ranged in Pace from 9 to 66 and included a variety of court surface samples as well as some extremes that would never be played on (for example a glazed ceramic tile was used to try and create an extremely fast surface). A good proportion of the surfaces were acrylic based, and this is reflected in the many values of pace between 30 and 50 - although the typical range for acrylic surfaces has been quoted as 30-40 (ITF, 1997). This predominance of medium speed surfaces can be seen in Figure 5.2 which shows the Pace values. The surface types are detailed in Table 5.2 below together with the Pace values.

The rigid body model developed in Chapter 3 suggested that the lowest possible Surface Pace is around 20, but three values are seen lower than this. One reason for this seeming discrepancy comes from surface deformation. The three surfaces with extremely low SPR values were all relatively soft rubber. The ball impact is likely to cause significant deformation, and the ball will effectively roll up the far side of a dip, increasing the rebound angle and thus decreasing the SPR. A similar effect happens on a clay court, where the ball "ploughs" the material in front of it and leaves a permanent deformation.
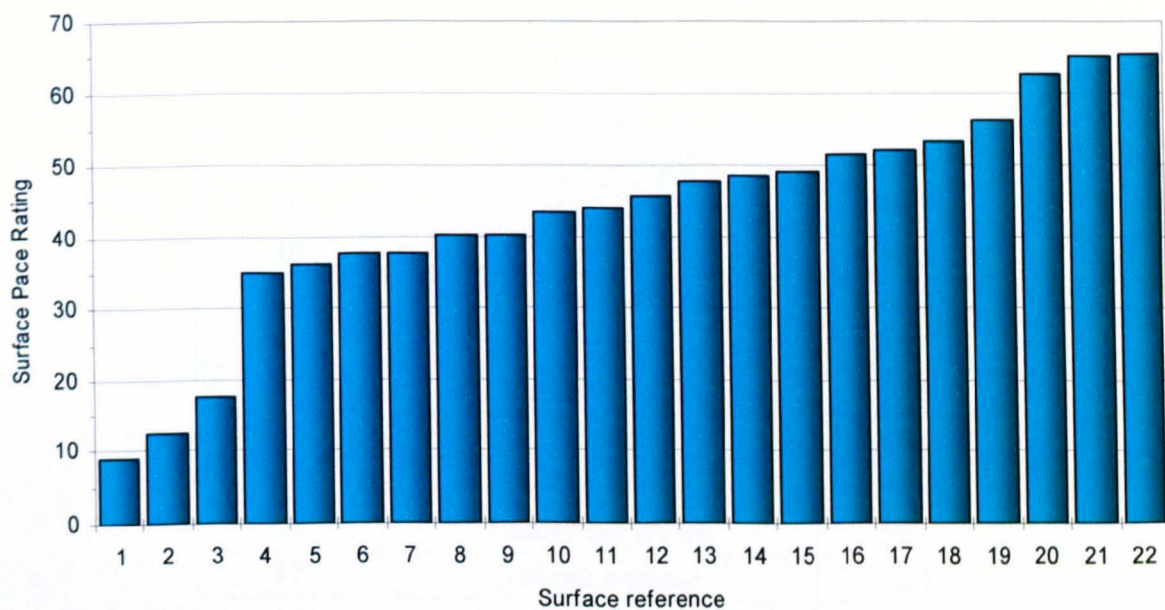
Figure 5.2 Surface Pace Ratings for a range of surface samples used to evaluate various friction tests, ranging from 9 to 65.

Table 5.2 Surface Pace Ratings for a range of surface samples used to evaluate various friction tests, together with the generic surface type in each case.

Ref no.	Surface reference	SPR
1	Rubber shockpad	9.1
2	Reformed rubber	12.4
3	Textured rubber	17.5
4	Acrylic	35.1
5	Acrylic	36.3
6	Acrylic	37.5
7	Acrylic	37.7
8	Concrete sample I	40.2
9	Acrylic	40.3
10	Acrylic	43.3
11	Concrete sample II	44.0
12	Acrylic	45.7
13	Rubber surface	47.9
14	Acrylic	48.6
15	Rubber surface	49.1
16	Textile carpet tile	51.4
17	Rubber surface	52.1
18	Rubber surface	53.3
19	Acrylic	56.0
20	Thin plastic sheet	62.5
21	Polished wood	65.0
22	Glazed ceramic tile	65.5

5.4 Surface friction testing

It has already been suggested that friction is an alternative measure of pace, and initial oblique testing indicated that it is of crucial importance. A number of different experimental methods for determining friction are discussed below. It is worth noting that all of these tests take place at a much lower speed than is experienced during an impact – typically in the order of one or two metres per second compared to a dynamic impact which could produce horizontal velocity components of twenty or thirty metres per second.

5.4.a   Friction sled

Figure 5.3 A sled used to measure friction between tennis ball cloth and a surface.

The simplest way to measure the friction between a ball and a court surface is to drag a friction sled – an example type used in a surface testing project by Hamilton (2000) is shown in Figure 5.3. A small sled is pulled horizontally by a wire which is taken round several pulleys so that masses can be hung to provide tension. The bottom of the sled can be covered with tennis ball cloth as in this case, or fastened to intact balls – for example used with a simple sled with a sprung force measurement by Brody (1984). The force applied to the sled is gradually increased until movement is seen. This can be done by using a linear force measurement, or by gradually increasing a suspended mass. Dividing the measured pulling force by the weight on the sled gives the static friction coefficient.

It is possible with this apparatus to attempt to measure the dynamic friction. Before the force is enough to overcome static friction, if the sled is given a small initial movement it will slide slowly but continually. This is however a rather user-dependent method, and gives no idea of how the friction varies with speed, so is not a practical method to gain an accurate measure of friction.

5.4.b   Pendulum tests

Slip resistance

An alternative way to measure friction is by using a swinging pendulum, which are available in a variety of forms. A foot is released and allowed to rotate under gravity. Energy is dissipated when the foot contacts the surface, and the energy loss is usually measured by finding the angle the arm swings to post-impact. There must be some compliance in the foot to allow contact to occur over a long enough sliding length to give meaningful results, but this makes it difficult to try and analyse the force equations and extract a proper coefficient of friction.

Figure 5.4 The TRRL pendulum used to measure friction.

The ITF Slip Resistance test uses a pendulum shown in Figure 5.4, which was originally designed for testing frictional properties of road surfaces by the Road Research Laboratory, part of the UK Government (it is also a standard test method of the UK Health & Safety Executive for measuring floor slipperiness). With this device, the height of the foot is adjusted to give a specific required sliding length of 125 mm by ensuring that it contacts the ground at either end of a calibration plate. This test is primarily aimed at measuring the linear friction between a player's shoe and the court, and so uses a rubber sample. There are therefore doubts as to how relevant the results would be to the impact of tennis balls.

Haines pendulum

Figure 5.5 The Haines pendulum for measuring friction, which uses a clamped ball.

An obvious improvement of the previous pendulum is to use either a sample of ball cloth or a ball itself. Haines (2002) developed a pendulum (Figure 5.5), commissioned by the ITF, which contains a captive ball and was designed to be an inexpensive alternative to the rather expensive surface pace rating equipment. The mounting for the ball is sprung in order to try to reproduce similar compressional forces to those seen when a ball lands on a court – otherwise there would be no way to allow a reasonable slide length without causing large ball deformations and high forces. Before use the clearance is adjusted so that the maximum compression produces a realistic level for normal force. The equipment avoids excessive cloth wear by allowing the ball to be rotated or replaced fairly easily.

The pendulum is calibrated by allowing it to swing freely without a ball present. The angle to which it moves a captive pointer gives a measure of the energy loss in the system. Then when a ball is used, the relative angle can be used to calculate the energy loss.

5.4.c   *Rotating friction*

Figure 5.6 Apparatus used to measure rotational friction.

Figure 5.6 shows the equipment specified by the ITF to measure the rotational frictional properties of a surface. Again, this test is concerned with the behaviour of players, and so a rubber layer is mounted on the test surface. A torque wrench is used to gradually increase the applied load on a weighted plate until rotational movement occurs. Using this apparatus is extremely user-dependent and repeatability is poor. Because of the rubber test surface, this test was thought to have no advantages over a linear test when considering the interaction of tennis balls and a court, and so it was not considered any further.

5.4.d   *Tortus*

Figure 5.7 The Tortus friction tester.

Figure 5.7 shows the Tortus automated friction tester. It is primarily designed for measuring the friction of floors for safety purposes (Mastrad Ltd, 2004), and as such attempts to replicate the interaction between a shoe and a surface. A constant vertical load

is applied and the machine moves along via a motor, measuring the horizontal frictional force. An average frictional value is given at the end of the motion.
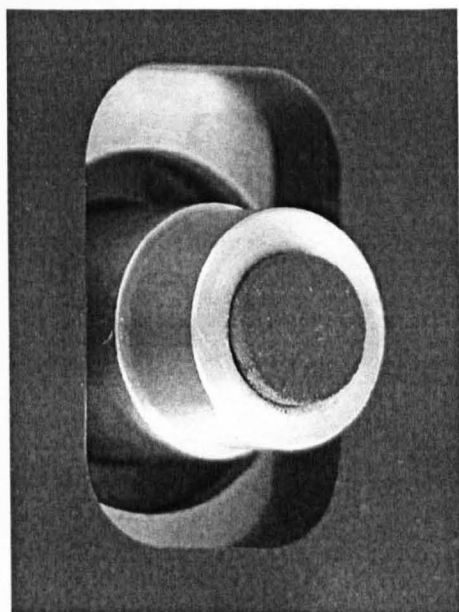
Figure 5.8 The underside of a Tortus, showing the rubber slider.

The main drawback of this machine as it is sold is that a rubber tip is fitted. This can be seen in Figure 5.8 – the photograph shows the underneath of the machine, with the foot and rubber tip sticking out. A small piece of cloth off a tennis ball was glued onto an alternate foot to see what effect this had, and a number of surfaces tested with both materials.
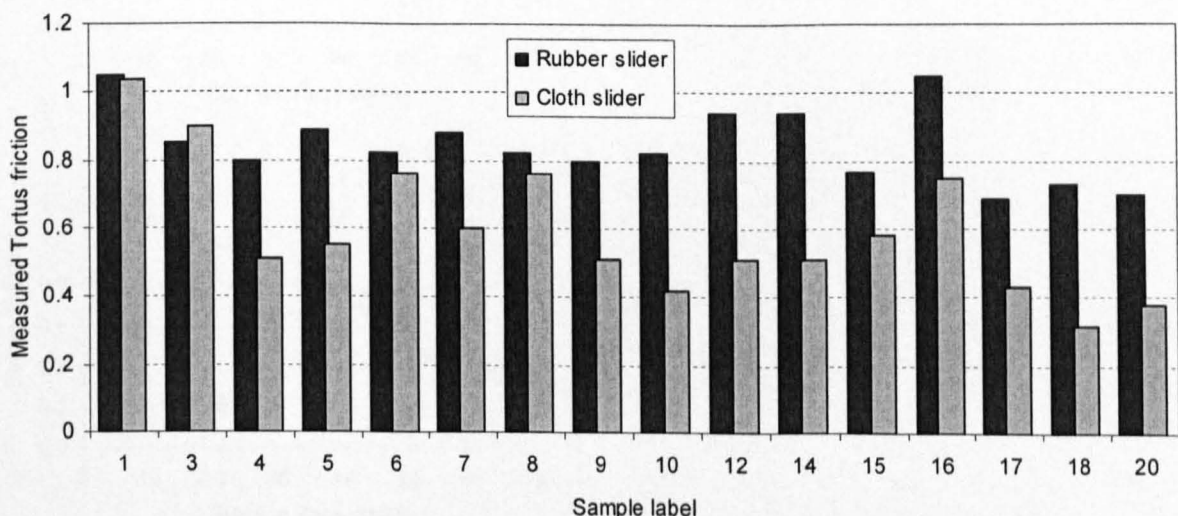
Figure 5.9 Tortus frictional values for both rubber and tennis ball cloth sliders.

Figure 5.9 shows the friction values for both slider material types. On three of the surfaces tested, the two materials gave similar coefficients of friction, but on the others there were large differences between 30% and 60%. Generally the rubber and polymeric surfaces gave the largest discrepancy, suggesting some sort of material interaction with the rubber slider.

5.4.e   *Surface testing results*

The surface samples used for the Surface Pace tests in section 5.3 were also used in an evaluation of the various friction tests described above. The surfaces came in a variety of forms, as not all were designed for playing tennis on. Some of the test methods need larger samples than others, and so it was not possible to perform all tests on all samples. The real tennis surfaces were however all large enough for each test.
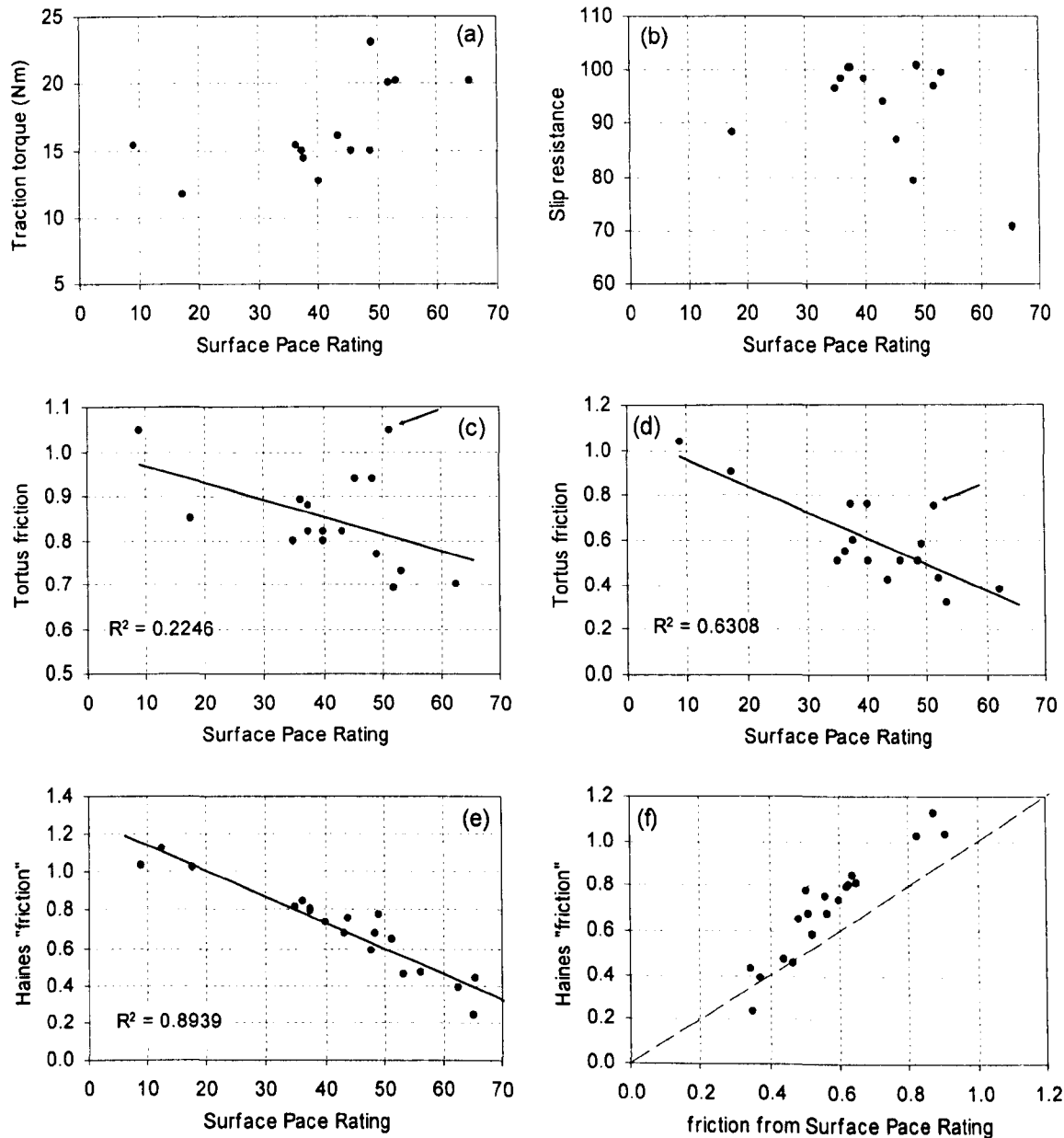
Figure 5.10 Correlations between various test methods and Surface Pace: (a) rotational traction, (b) slip resistance pendulum, (c) Tortus with rubber slider, (d) Tortus with tennis ball cloth slider and (e) Haines pendulum. (f) shows the Haines friction against SPR friction. The surface marked with an arrow in (c) and (d) is a textile carpet.

The first graph in Figure 5.10 shows the rotational traction device. It is immediately obvious that if there is any slight trend, it is in the opposite direction to that which might be expected – as surface pace goes up, friction goes down and therefore the torque needed to

turn the disc should reduce also. The slip resistance pendulum also produces no useful results – it is impossible to predict a meaningful trend.

The two tests which show more useful friction measurements are the Tortus and Haines pendulum. Both exhibit definite trends of decreasing friction with increasing surface pace. Replacing the rubber slider on the Tortus with a piece tennis ball cloth has a definite improvement on the results, which is reflected in the R^2 values of 0.22 and 0.63 with the rubber and cloth respectively. The largest error can be attributed to a physical cause. The data points marked with an arrow on both graphs is for a carpet surface. It seems likely that the relatively small tip digs into the carpet, producing a tractional component to the reaction force.

The Haines pendulum shows an even better linear correlation (with $R^2 = 0.89$). The value produced does not relate directly to the coefficient of friction obtained by rearranging the SPR formula ($\mu = 1 - \dfrac{SPR}{100}$), as can be seen in Figure 5.10 (f). The dashed line on the figure represents a 1:1 relationship. This suggests that the theory used in obtaining friction from the Haines values is incorrect, which is not a particular concern as this test is primarily designed as a comparative value as a rough guide to the playing performance. It is for example popular with court manufacturers who want to check the speed of a newly installed surface.

5.5   Surface stiffness testing

The third of the ITF's "key" properties is shock absorption. This is effectively a measurement of the surface stiffness. The higher the stiffness of the surface, the higher the shock, or force, transmitted. Of course, in practical terms a surface will not have a constant stiffness. This is particularly true of any surface which consists of one layer whose deflection reaches a significant proportion of the original thickness – the stiffness will increase dramatically as that layer is compressed. It is important to note that shock absorption as such is not a measure of energy return or efficiency, as a surface could be soft and therefore provide a softer reaction force, yet elastic enough to return a large amount of the stored energy.

There are a number of existing techniques for measuring the properties of material samples. However, one of the aims of the project was to gain the ability to characterise and model existing courts. This meant that there would be many cases where laboratory-based testing of samples would not be possible. The most practical way to gain data about the stiffness of an installed surface is using impact testing.

5.5.a   Berlin Athlete

Figure 5.11 The Berlin Artificial Athlete, used to test shock absorption properties of a surface.

The Berlin Artificial Athlete (shown in Figure 5.11) is an established and internationally accepted test method for shock absorption commonly used on athletic running tracks as well as a number of other sports surfaces. It is a biomechanical test which attempts to simulate the impact loading of a player running on a surface. It does this by dropping a 20 kg mass from a height of 55 mm onto a strong spring (stiffness 2000 kN/m). The spring transmits the load to the surface, where the peak force is measured by a force transducer. This peak force F_s is compared to the reference peak force seen dropping on a concrete sample F_c (which is used at the start of each test session as a calibration value), and expressed as a reduction percentage:

$$\text{Energy absorption (\%)} = 100 \left(1 - \frac{F_s}{F_c}\right) \qquad [5.2]$$

This test is of limited use when considering the interaction of tennis ball and surface because of the size of the mass used. Neglecting resistances, a mass allowed to drop from a height of 55 mm will achieve a speed of 1.04 ms^{-1}, providing an impact energy of 10.8 J. A typical tennis ball landing at 7 ms^{-1} will have an energy of only 1.4 J, an order of magnitude lower. The peak forces seen have an even larger discrepancy. A ball dropped from 100 inches onto a force plate provides a peak impact force of around 250 N, whereas an acrylic surface with little or no cushioning will usually generate a force measured by the Berlin Athlete of at least 5000 N. Although it is possible to use the Berlin Athlete data to find the relative hardness of surfaces, it would be dangerous to draw too many conclusions

about the stiffness given the differences. The test method seems to reduce the differences between surfaces which are quantitatively thought to be very dissimilar.
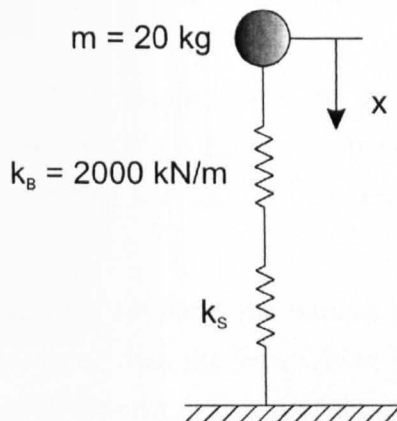
Figure 5.12 Two-spring model of the Berlin Artificial Athlete

If the rather large assumption is made that the surface acts as a linear spring with constant stiffness, it is possible to make an estimation of this surface stiffness. Consider two springs in series with a rigid ground as shown in Figure 5.12. The upper spring represents the Artificial Athlete and has a stiffness of $k_B = 2000$ kN/m, while the lower spring represents the surface, of stiffness k_s. The resultant stiffness of an equivalent spring k_{res} is given by

$$\frac{1}{k_{res}} = \frac{1}{2x10^6} + \frac{1}{k_s} \qquad [5.3]$$

For an impact of a 20 kg mass on an undamped spring of stiffness k_{res} the equation of motion is given by $m\ddot{x} + kx = 0$. This has a solution of the form $x = a\sin(bt)$, where $b = \sqrt{\frac{k_{res}}{m}}$. The equations for velocity and displacement are $\dot{x} = ab\cos(bt)$ and $\ddot{x} = -ab^2\cos(bt)$ respectively. Using the incoming boundary condition that $\dot{x} = V_{in}$ when $t = 0$ leads to an expression for the maximum force F_{max}:

$$F_{max} = V_{in}\sqrt{mk_{res}} \qquad [5.4]$$

The maximum force is returned directly from the Artificial Athlete. If [5.4] is rearranged to give k_{res} then substituted into [5.3], the surface stiffness can be found if the drop height of 55 mm is used to calculate an impact speed V_{in}.

$$k_s = \left(\frac{mV_{in}^2}{F_{max}^2} - \frac{1}{2x10^6}\right)^{-1}$$

Peak forces and force reductions relative to a measured force on concrete of 6110 N were measured (averaged over two tests of five drops each) by Hamilton (2000) and are

reproduced in Table 5.3 below. Also shown is a constant surface stiffness calculated using the equation above. This is not necessarily representative of the stiffness "seen" by a bouncing tennis ball because of the linear assumption, but it does give an indication of the very high stiffnesses of many of these surfaces. Even the artificial grass surface, which was deeper pile than usually used on tennis courts, produced a peak force of over 5000 N, which is an order of magnitude higher than the forces generated by a ball impact. This indicates that the results from this test cannot be used with any confidence in predicting ball behaviour.

Interesting data from this testing concerns the natural grass surfaces. The new grass area has a noticeably lower peak force than the area which had been played on and worn. This is thought to be mainly due to the compression of the ground by continual player impacts, as the mere presence of grass is unlikely to have such a softening effect.

A further issue with this test is that it provides only a peak force, giving no measure of the efficiency of a surface – whether it will return the energy supplied. This is a crucial factor when looking at the bounce of a ball, unless of course the surface is so hard it cannot store any energy!

Table 5.3 Berlin Artificial Athlete results for a range of surfaces, shown as peak forces, percentage force reduction and calculated surface stiffness.

Surface	Peak force (N)	Force Reduction (%)	Calculated surface stiffness k_s (kN/m)
Artificial grass	4186	31.5	1362
New grass (natural)	4464	26.9	1708
Shock pad	4922	19.4	2545
Textile carpet	5035	17.6	2830
Wood	5090	16.7	2986
Worn grass (natural)	5219	14.6	3398
Sand-filled artificial grass	5561	9.0	5011
Polymeric	5844	4.4	7492
Acrylic	6030	1.3	10537

The values given here are around twice as high as those given by McMahon and Greene (1979). They quote values of 4376 kN/m for concrete and asphalt and 2918 for packed cinders, and although there some discrepancy with the results presented here, both methods give stiffnesses of the same order of magnitude.

5.5.b Brody baseball bat test

An example of more basic impact testing was performed by Brody (1992), who described two simple tests to determine the surface hardness with a view to its cushioning. Both involved the acceleration of a dropped object. The first did so by measuring the acceleration or some function of acceleration of a body dropped from a fixed height. The second involved finding the maximum height from which a body can be dropped so as not to exceed a nominal fixed value of deceleration (for example 100g). Brody did this by attaching two inexpensive resettable accelerometers to a baseball bat and increased the drop height until the accelerometers indicated the nominal deceleration value had been

reached (in this case 138g). The heights ranged from 0.08 m on concrete, through several readings around 0.2 m for tennis court surfaces to 0.8 m for natural turf.

5.5.c   Clegg Impact tester

Figure 5.13 The Clegg Soil Impact Tester, showing the 0.5 kg mass and handset as well as the guide tube

The Clegg Soil Impact Tester is a commercially available instrument which consists of an accelerometer firmly attached to a 0.5 kg mass (a 4.5 kg mass is also available and is normally used for testing road surfaces). This mass is dropped down a guide tube which ensures an impact at a constant speed and provides a consistent normal impact with the ground. Under normal operation a handset is used which provides the peak value of the acceleration (measured in arbitrary units called Impact Values) produced by the impact on the ground. Both the mass and handset can be seen in Figure 5.13. The peak acceleration is generally used as a comparative value for the hardness of the ground (and as such is a similar method to Brody's baseball bat test described above), but by itself is of limited value to the modelling of impacts.

5.5.d   Adapting the Clegg - data acquisition hardware

The Clegg can be used to provide much more information by the addition of data sampling equipment. The drop hammer consists simply of an accelerometer attached to the mass, and so the signal can be used to capture the whole acceleration-time trace rather than using the handset to give just the maximum acceleration.

The analogue to digital converter used was the ADC-100 manufactured by Pico Technology. It allows sampling of two channels at 12-bit resolution with a variable input range between ±50 mV and ±20 V. It connects to a parallel printer port, thus enabling use with a laptop computer for field testing. Maximum sampling rate is about 100 kHz.

Because the ADC-100 does not have a suitably high input impedance (quoted as 1 MΩ), it was necessary to use a charge amplifier to preserve the signal. A commercial charge amplifier was considered, but because the accelerometer signal was already high enough and it was not necessary to use the amplifier with different accelerometers, a simple charge amplifier was constructed. This was configured to give a unity gain, effectively passing through the charge generated by the accelerometer to preserve the voltage, whilst having an input impedance in the order of 10^{12} ohms.

5.5.e   *Adapting the Clegg - data acquisition software*

Rather than use the oscilloscope style software provided with the ADC-100 which is functional but rather cumbersome, a specific application was developed in Microsoft Visual Basic. The aim was to speed up the experimental process and allow as many samples as possible to be gathered in a short space of time. This is important as it is often necessary to test different areas of a tennis court, and it is vital to make a number of measurements in each position. Consideration was also given to the fact that at some point in the future testing might be required after or even during games, so the procedure should be as quick and non-intrusive as possible. At the time of writing, the equipment had been used on several different projects, including testing on a number of professional cricket pitches immediately after the end of first-class matches. Here speed is essential, as the groundsman wishes to start work on the pitch as soon as possible. This testing was used as an example of what might be required on tennis courts in the future.
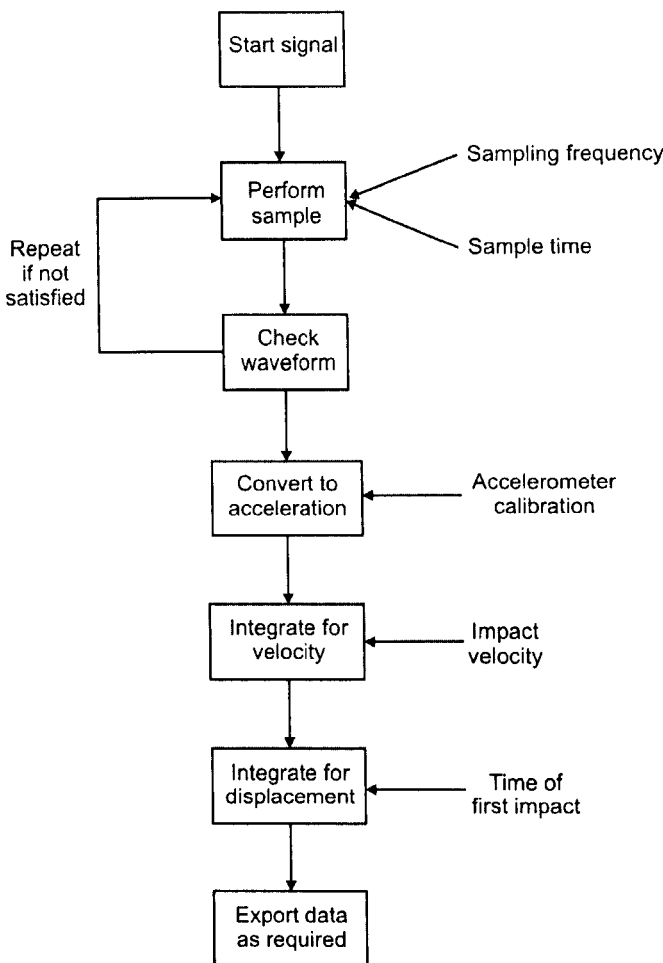
Figure 5.14 Flowchart of software requirements for sampling the signal from the Clegg Soil Impact Tester

A flowchart is shown in Figure 5.14 of the main software requirements. In order to start the sample, a manual trigger was needed. Because of the interface driver the program was based on, the sampling was limited to a data set of 32768 points. At a sampling frequency of 30 kHz this means a sample length of just over one second, or one and a half seconds for a frequency of 20 kHz. After testing, this was found to be more than long enough to capture the trace. After completing the data acquisition, the voltage trace is displayed on screen, allowing the operator to visually check the quality of the data. If no obvious problems can be seen, the voltage data is converted to an acceleration. This is done by knowing the sensitivity (i.e. calibration) of the accelerometer, which was provided by the manufacturer. The acceleration data is then integrated to give the velocity over time, knowing the impact speed, and integrated again to find displacement. Any or all of this data is then exported either to a text file on the computer, or directly into a spreadsheet.
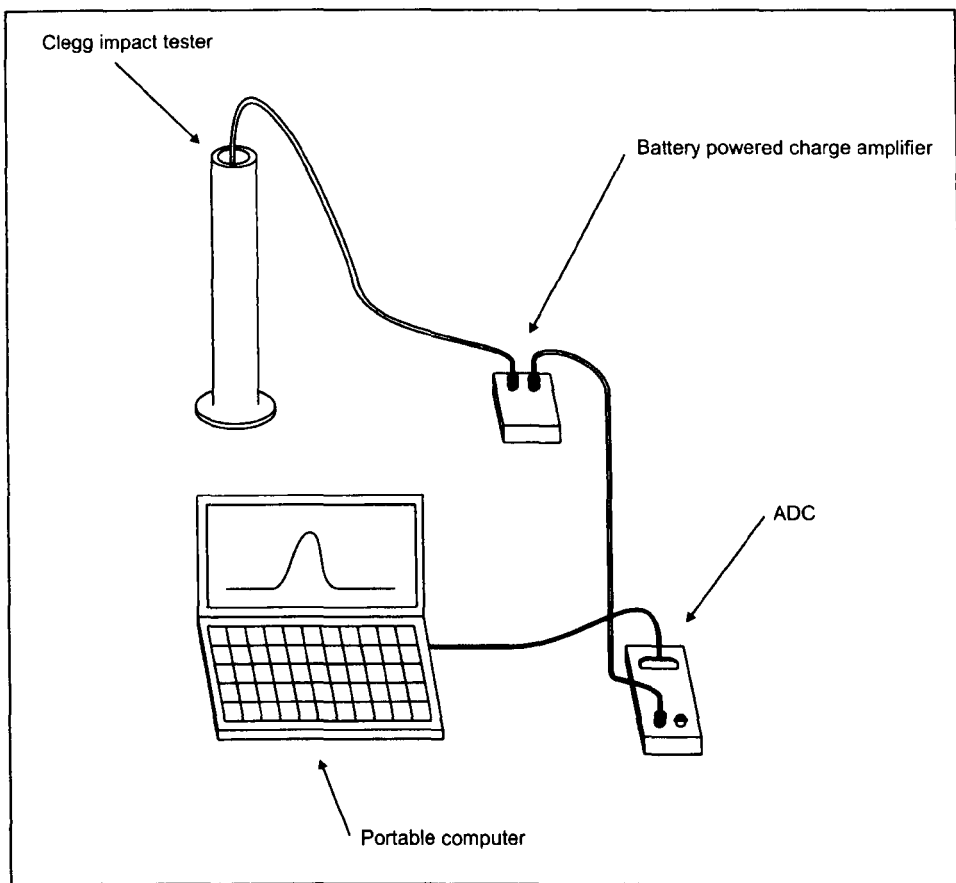
Figure 5.15 Schematic form of complete apparatus used to sample the accelerometer signal.

5.5.f   Calibration

Based on the capacitance of the accelerometer as provided by the manufacturer, the calibration factor from signal in mV to acceleration in gravities was 0.047. As this would be crucial in the signal processing (any errors would magnify as the data was integrated into velocity and displacement), it was verified experimentally.

The guide tube was raised on wooden blocks as shown in Figure 5.16 below, so that the hammer could be seen as it landed on the surface. High speed video was used to film the impact at 600 frames per second. The positions of markers drawn on the impact hammer were manually digitised to find displacement co-ordinates, and their rate of change used to give velocity values. These could then be compared to the captured and processed acceleration data to verify the calibration.

Examples of the displacement and velocity from a height of 0.3 m are shown in Figure 5.17 (a) and (b) below respectively. Also on the graphs are the same variables found using the sampled accelerometer signal for the same impact. It can be seen that the agreement is excellent, and therefore the sampled accelerometer signal is reliable. This procedure was repeated for heights of 0.4 and 0.5 m to ensure the calibration was consistent.
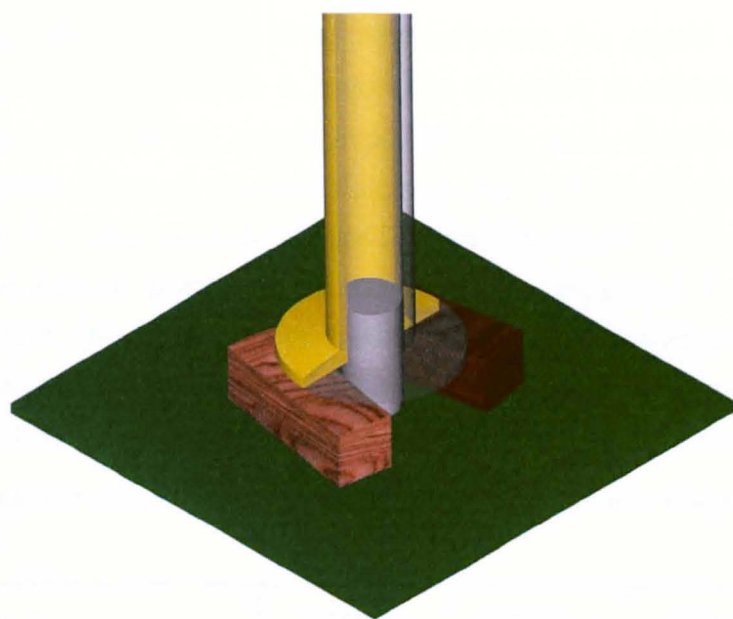
Figure 5.16 Filming the impact of the Clegg drop hammer to find the incoming velocity. The guide tube was raised on wooden blocks to allow the impact to be filmed.
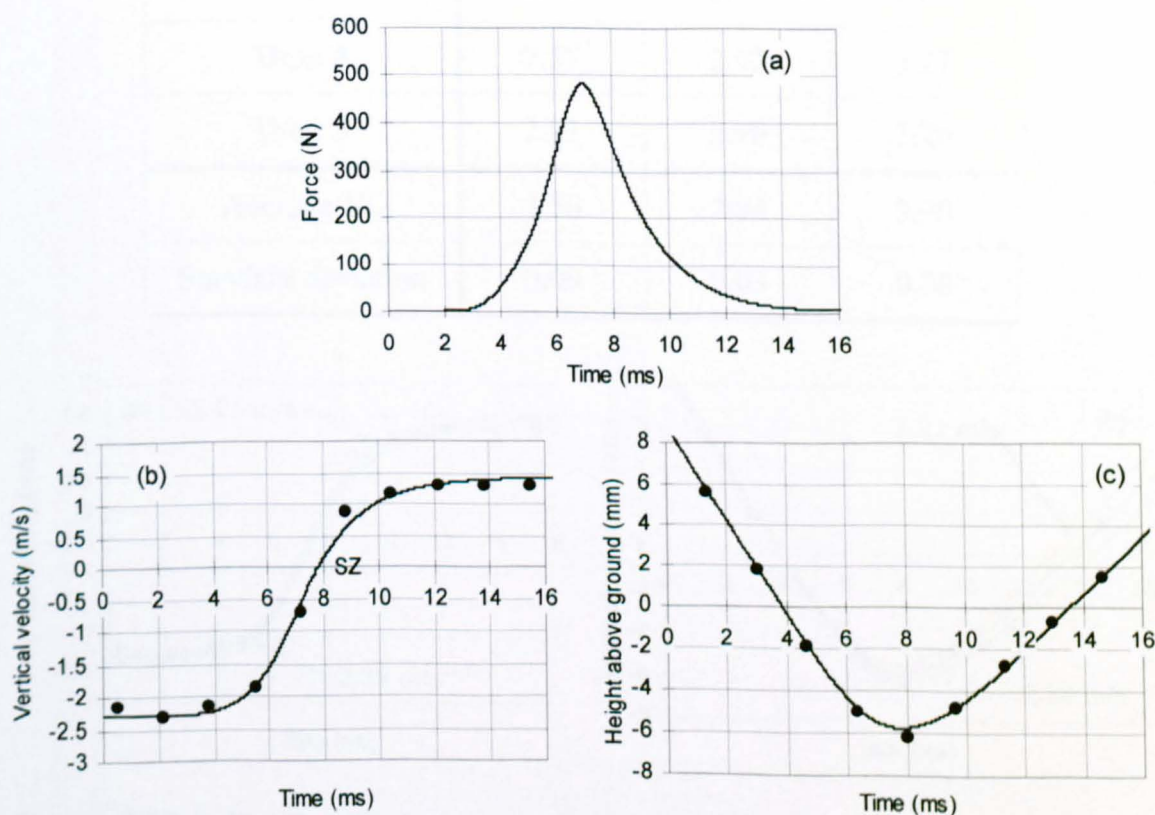
Figure 5.17 (a-c) (a) Force-time, (b) displacement-time , and (c) velocity-time for a drop of the Clegg hammer. Data from both high speed video footage (discrete data points) and from accelerometer signals (lines) is plotted.

Another important part of the data analysis procedure is knowing the incoming velocity. Any error in this value will not only offset the entire velocity-time profile, it will also

significantly affect the displacement data. Approximating the impact speed V_{in} from the drop height h is possible (although it is impossible to predict the effects of air resistance), but it was decided to check the speeds experimentally from various drop heights. The guide tube was again raised on wooden blocks as shown in Figure 5.16, and high speed video used to film five drops at each of three heights. The reference positions for dropping the hammer conventionally from 0.3 m, 0.4 m and 0.5 m were used, but the blocks added 69 mm to the heights (larger blocks were used than for the impact filmed and shown in Figure 5.17, which had an impact speed of 2.3 ms^{-1}). The resulting measured speeds are shown in Table 5.4. At all heights the standard deviation is under 0.1 ms^{-1}.

Table 5.4 Measured impact speeds for the Clegg impact hammer dropped at various heights (values in ms^{-1})

	0.369 m	0.469 m	0.569m
Drop 1	2.56	2.98	3.25
Drop 2	2.54	2.90	3.13
Drop 3	2.43	2.93	3.08
Drop 4	2.57	2.92	3.27
Drop 5	2.71	2.96	3.26
Average V_{in}	2.56	2.94	3.20
Standard deviation	0.09	0.03	0.08
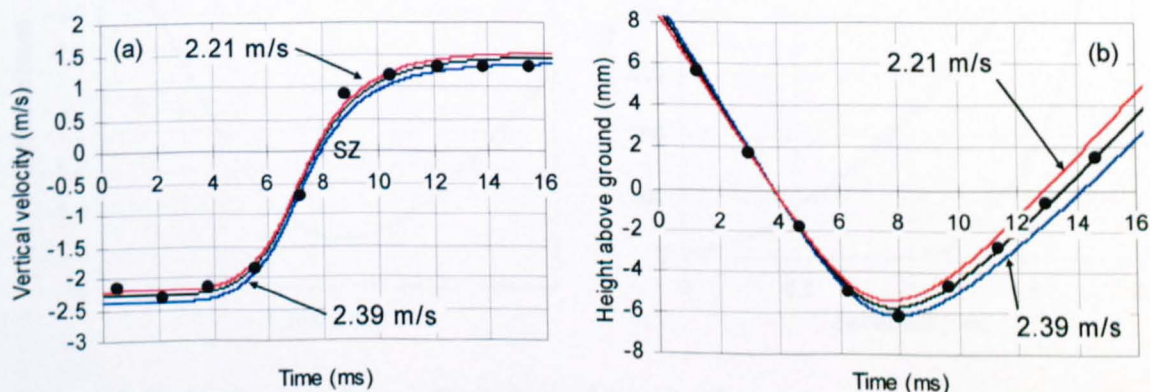
Figure 5.18 (a-b) The effect of a one standard deviation error in the velocity has on the integrated (a) velocity and (b) displacement curves for a Clegg drop at 0.3 m (nominal impact speed 2.3 ms^{-1}).

Figure 5.18 shows the difference by adding and subtracting 0.09 ms from the impact velocity for the drop in Figure 5.17. The change in speed simply acts as an offset to the velocity curve, but as the data is integrated through the impact, the "error" makes a larger

and larger difference to the displacement graph. This one standard deviation error would probably not be acceptable if accurate displacement values were needed (for example for a surface stiffness measurement for a model). The most likely cause for the differences in impact speed is a combination of error in the analysis stage (both human error and the fairly small number of data points available) and the clearance between the mass and the guide tube. This clearance must be large enough to stop air resistance being too great as the mass gets close to the ground, but this allows irregularities in its motion. The mass is released by holding the data cable and lining up various markers, which obviously will not give exactly the same release position and angle every time.

5.5.g   Clegg test results
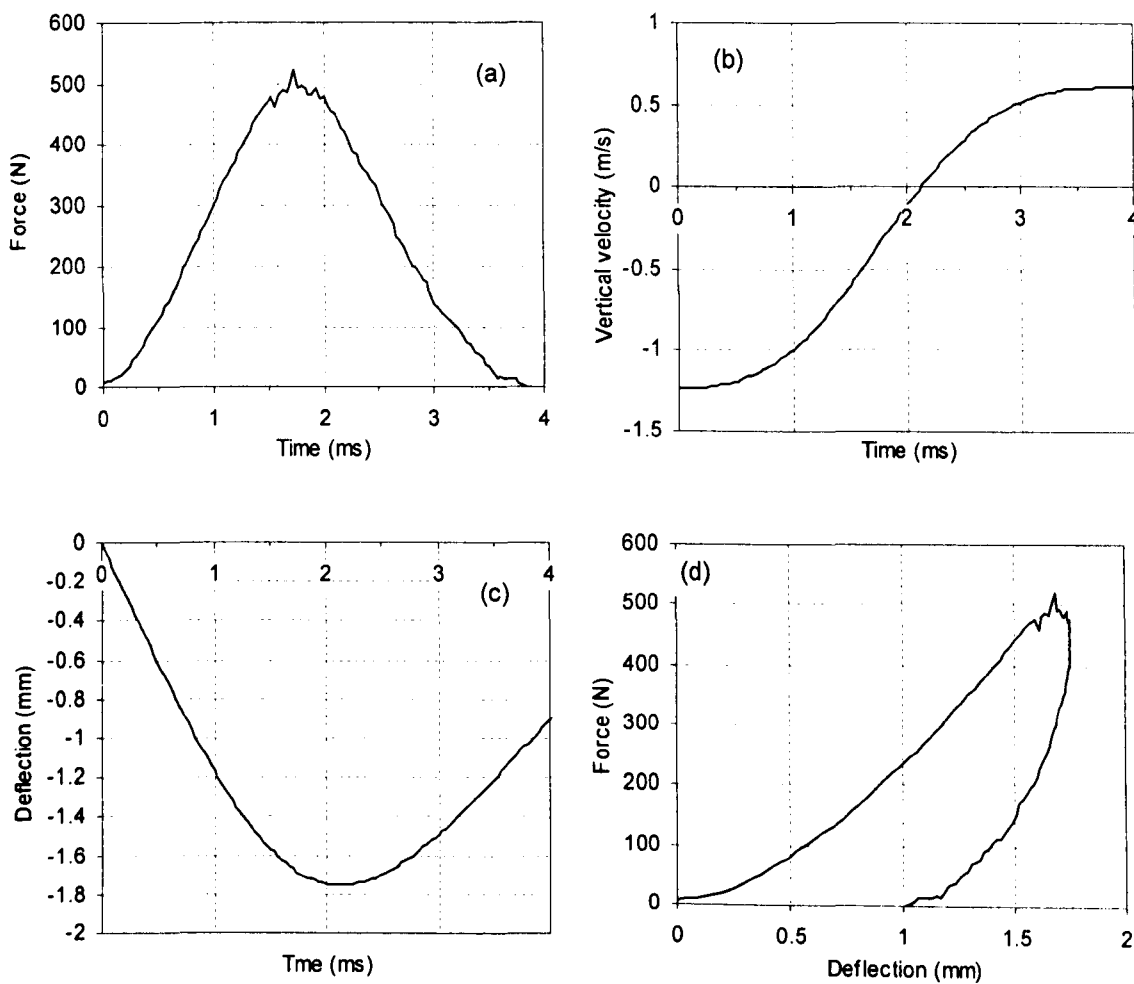
Figure 5.19 (a-d) Data from a Clegg impact on a textile carpet surface. Force, velocity and displacement against time, with force against displacement.

An example set of results is shown in Figure 5.19. This drop was from a height of 0.1 m on a textile carpet surface. The peak force is around 500 N, and the impact lasts around 3.75 ms. The incoming velocity is 1.2 ms⁻¹, and the outgoing velocity 0.6 ms⁻¹. A maximum surface deformation of 1.75 mm can be seen. The deformation stays below zero after the end of the impact, which means that the bottom of the hammer is still below the original

ground level. This could mean that either the surface undergoes permanent deformation, or more likely simply recovers slower than the hammer is rebounding.

The extremely small deflection and peak force of 500 N seen here (bearing in mind the very low drop height of just ten centimetres) again suggests that stiffnesses measured by this test method will be so high as to be able to be considered as rigid.
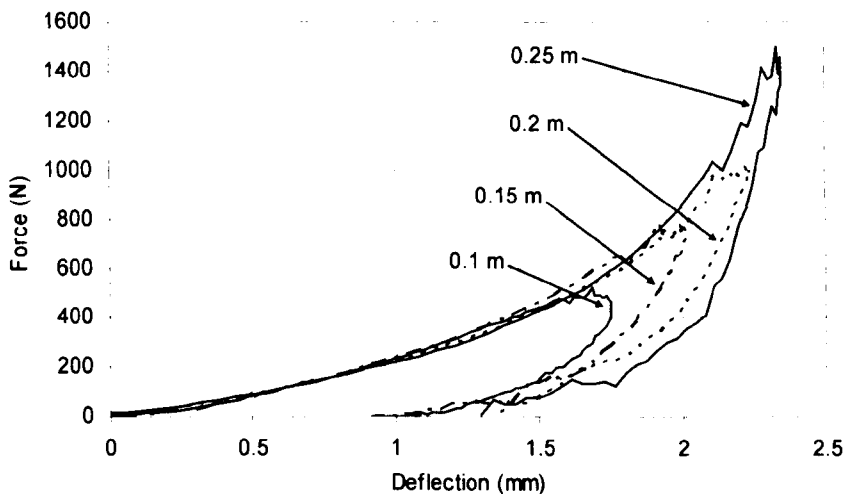
Figure 5.20 A comparison of force-deflection curves found by dropping the Clegg hammer from varying heights on a textile carpet.

Figure 5.20 shows force-deflection curves for drops on the same textile carpet surface from a range of heights from 0.1 to 0.25 m. It is an interesting result that the four curves follow the same loading path. This suggests that the stiffness (the gradient of the force-deflection curve) is a function of deflection, and does not directly change with impact speed – itself a function of drop height. A larger impact speed will of course lead to a larger deflection and increase the average stiffness throughout the impact, effectively progressing further up the loading curve.
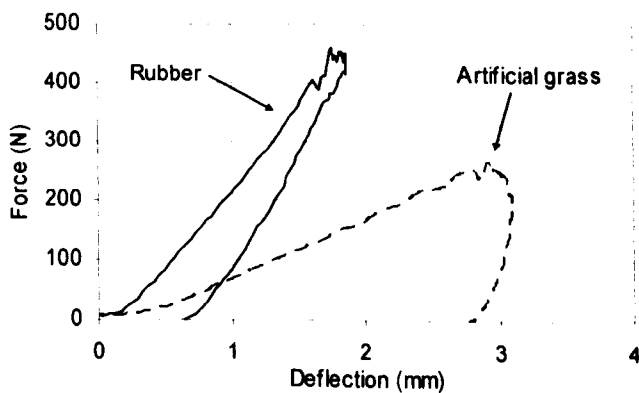
Figure 5.21 Force-deflection curves for drops from 0.1 m on rubber and artificial grass, surfaces with low and high energy losses.

Two obviously different surfaces are compared in Figure 5.21. This shows drops from heights of 0.1 m on rubber and artificial grass. Neither surface is representative of tennis courts but both provide reasonable deflection. The rubber (considerably softer than any shockpad used under a court) was a 25 mm thick sample and provided quite an elastic impact, as seen by the relatively small enclosed area in the force-deflection curve. A contrasting example is the artificial grass sample also shown. There is almost no force provided at all after the point of maximum deflection when the hammer returns upwards.

One problem with the Clegg test is that it is not designed for particularly hard surfaces, and on any realistic surface it must be dropped from a low height to avoid clipping the signal. There is a version available designed for harder surfaces with a 4.5 kg mass, but this will of course produce forces and deformations even further away from those produced by a ball impact.

5.6 Vertical ball bounce

The vertical bounce is another important test. It is widely used to ensure that the properties of a ball fall within a specified range, but can also be used to find the bounce properties of a court surface. Although in many situations the coefficient of restitution is the variable of interest, in practical terms it is usually easier to measure the rebound height a ball bounces to. This can be done using a standard video camera, whereas finding ball speeds requires high speed cameras (with the time consuming data processing this involves) or alternatively some sort of timing gates, which are expensive. Another method suggested is measuring the time between the first and second bounces, which can be achieved with a microphone (Brody, 1990).

Hamilton (2000) used a set of test balls to test the bounce properties of various surfaces. The bounce heights were measured using a video camera, with care taken to eliminate parallax errors. The results are shown in Table 5.5 as Relative Percentage Rebound values, expressed as a comparison to the measured heights on the concrete surface. COR values are also given, taking into account the effect of drag on the ball velocities before and after impact.

All the surfaces tested which might realistically be used as a tennis playing surface have RPR values within 1% of concrete. In each case, COR values were within one standard deviation of that for concrete, showing they could not be distinguished.

Table 5.5   Relative Percentage Rebound and COR values for a variety of surfaces (reproduced from Hamilton, 2000).

Surface	Mean RPR (%)	Mean COR
Artificial grass (no sand)	71.3	0.651
Textile carpet	90.9	0.736
Carpet tile	96.6	0.758
Ceramic tile	97.1	0.760
Concrete	100	0.772
Polymeric	100.3	0.773
Sand-filled artificial grass	100.7	0.775
Acrylic	100.7	0.775
Shock pad	102.2	0.780
Wood	103.3	0.784

5.7   Discussion

There are a number of established test methods which are used within tennis, and some of these are more relevant than others to this project. Many of them are more suited to player comfort and safety than ball bounce performance. All the data presented which measures surface stiffness properties suggests that even the most cushioned surface amongst those designed for playing tennis on is at least an order of magnitude stiffer than the ball, as they are designed to deform and give cushioning under the weight of a player. Further evidence for this is given by the ball bounce tests, where there is no significant difference between any of the tennis surfaces and the bounce on concrete (and indeed the very large slab of marble used by the ITF as a "rigid surface").

One consideration which should be noted is the effect of environmental conditions. The majority of the tests in this chapter were conducted in a controlled laboratory, where temperature and humidity were fixed. It is possible that both of these factors will have some influence on ball impact behaviour. Temperature is unlikely to affect the surface significantly, but will have more of an effect on the ball by altering the rubber material properties. Changing humidity may change the interaction of ball and surface by altering the coefficient of friction (since nylon can absorb significant quantities of water).

5.8 Summary

Work in previous chapters has identified the most important features of the bounce of a ball to be the coefficient of friction between the surface and the ball, and the coefficient of restitution (which depends on the properties of both the ball and the surface). The remaining surface properties are concerned more with either the interaction of the player and the surface or the constructional nature of the court.

There are a number of ways to measure the friction. Statically a weighted sled is quick and easy to use. The dynamic friction is harder to measure. Currently used tests utilising a pendulum or rotating disk concentrate on the friction between the ground and a test sample, usually rubber. This can of course be replaced by tennis ball cloth but this is not ideal because of effects of wear and cloth compression. A better method is to use a captive ball as in the Haines pendulum. Here the ball can quickly be replaced, or rotated to use an unworn part of the nap.

Coefficient of restitution depends on the ratio of energy returned to energy stored. For the speeds encountered, the kinetic energy of a ball is insufficient to generate enough deflection to store much energy in the surface. This suggests that for a tennis ball-surface impact, the surface is so much stiffer than the ball that it can be considered as rigid; both the Berlin Artificial Athlete and Clegg Impact Tester suggested the surface was at least one order of magnitude stiffer than the ball. This is born out by the rebound drop tests on various surfaces, where the tennis surfaces all had a bound height within 1% of the reference concrete value.

6 Quasi-static ball testing

6.1 Introduction

The overall aim of this study is to model the interaction of a tennis ball and a court surface. The previous chapter showed that for the vast majority of surfaces, the relative stiffnesses of ball and court mean that the court can be considered to be a rigid surface, contributing only a coefficient of friction. It is therefore important to get good measures of the stiffness and damping properties of the ball.

A feature of the modelling approach used was the way the ball properties were measured, and it is important to differentiate between material and structural properties. When using an approach such as Finite Element Analysis, properties must be defined for all the materials involved, and the problem definition converts these into a structure. An analytical model takes a more macroscopic view, and defines the stiffness and other properties of the structure itself. More simplistically, a whole tennis ball is tested rather than the component parts.

The aim of this chapter is to determine how the ball properties can be measured using quasi-static compression tests, so that these properties can be used in future chapters to develop a model of how the ball interacts with the court surface. Balls were measured at different compression speeds, to see how strain rate affected stiffness, and different types of balls tested to see the effect of construction. Holes were drilled in the balls to release the internal pressure, and the tests repeated to see the contribution of structural and pressure forces.

6.2 The effect of strain rate on ball compression

The most important property of the ball structure is the stiffness. Since the main component of a tennis ball is rubber, it would be reasonable to expect the stiffness to vary with both deformation and strain rate (i.e. impact speed). An investigation was therefore carried out to see how strain rate affected stiffness.

The ITF perform deformation tests as part of their ball approval process. In these tests, a ball is compressed on each of three mutually perpendicular axes in turn. The test (shown as a schematic in Figure 6.1) involves applying a load of 80 N, and holding this load for five seconds before reading the deflection (known as the "forward deformation"). The ball is then compressed to a deflection of an inch (25.4 mm), before being unloaded. A second deflection value is taken at a load of 80 N on the unloading cycle (known as the "return deformation") but before this reading the load is held for ten seconds. These time delays are included in an attempt to remove any strain-rate dependant properties, and give as close

as possible to a truly static stiffness measurement. There is also a requirement for both the forward and return deformations to be within 0.030 inches of each other across the three perpendicular axes, to ensure the ball is sufficiently homogeneous.
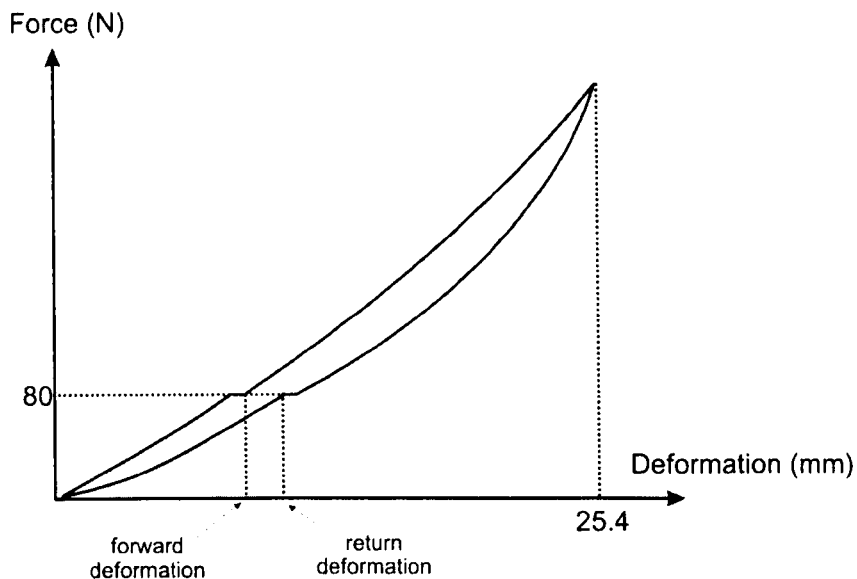
Figure 6.1 A schematic of the ITF compression test, required as part of the ball approval process.

In order to assess the visco-elastic effects, an Instron 5500 testing machine was used to compress a standard pressurised tennis ball to a maximum deflection of just over an inch, at various strain rates from 10 to 1000 mm/minute. This range included 200 mm/min, the rate used by the ITF for their deformation tests.
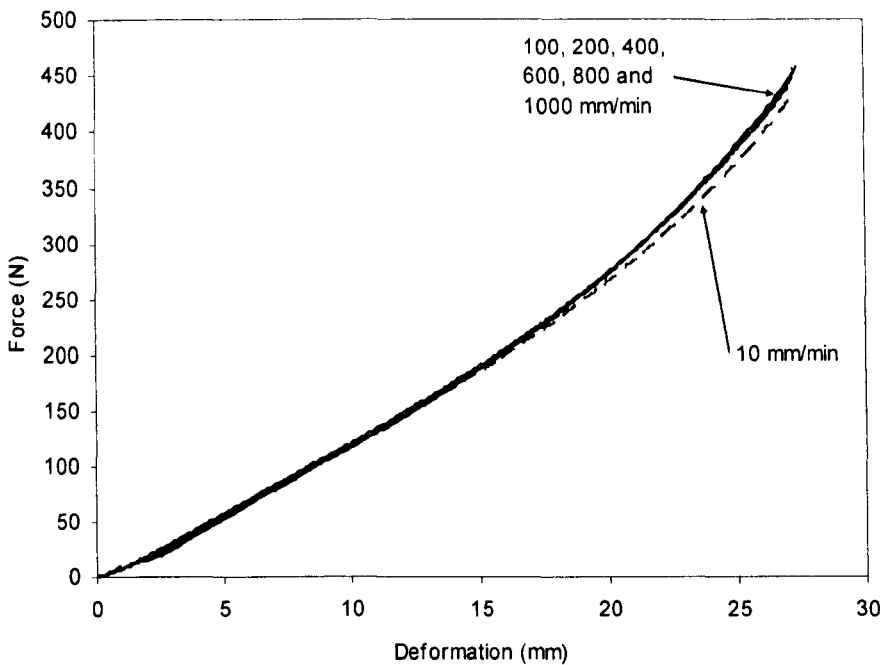
Figure 6.2 Force versus deflection for a tennis ball compressed at various strain rates from 10 to 1000 mm/min. Only the loading part of each curve is shown.

Figure 6.2 shows the force-deflection curves for the different strain rates. It can clearly be seen that for all rates above 10 mm/min - which is an extremely slow compression, taking several minutes to complete the test - the force (and thus the stiffness) is exactly the same at all deflections; so much so that it is impossible to separate and label the individual traces on the graph. The fastest rate of 1000 mm/min is equivalent to 16.7 mm/s and so is obviously far below that of a dynamic impact, but the fact that the stiffness barely changes over two orders of magnitude is encouraging for the use of quasi-static data in an impact. It is worth noting that a large deformation rate does not necessarily mean a large strain rate, since the speeds quoted are for the ball structure rather than a simple material sample.

6.3 The effect of ball construction and pressure

Knowing that strain rate was not important for the range available to the test machine, a rate of 200 mm/min was chosen to test several ball types. Pressurised and pressureless balls were compressed, and for the pressurised balls, both new and used balls were tested to see the effect of a few impacts on static compression. The new balls were given a full pre-compression cycle (three compressions to an inch on each of three perpendicular axes), and the used balls had been used for a set of oblique impact tests (described later in Chapter 9). These impact tests were recent enough that the pressure in the balls would not have dropped significantly from when the can was first opened, but would not have provided the same number of impacts as a full match. Figure 6.3 shows the new and old balls, and it is possible to see worn areas on the older ball, where the cloth has been

disturbed and the inked markings affected. All the balls had passed the ITF approval tests (the new balls the same day as the compression testing, and the used balls before their impact tests), ensuring they were representative samples.
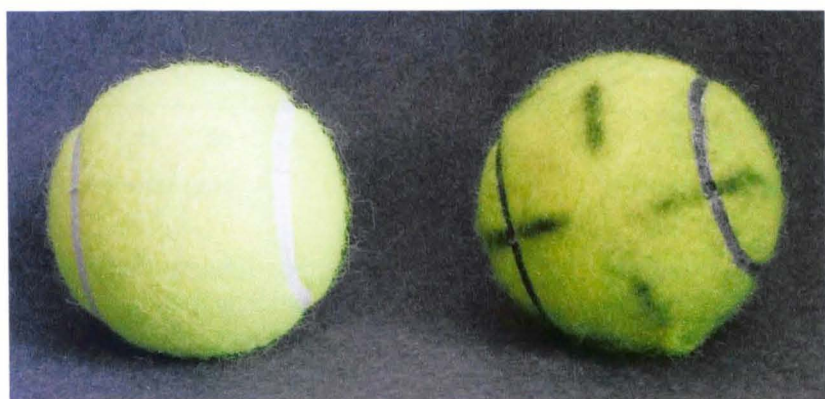
Figure 6.3 Photograph showing a comparison of new and used balls, as used in the compression tests.

Figure 6.4 Photograph showing the hole drilled in a tennis ball to test structural stiffness without internal pressure.

A reasonably large hole (about 10 mm) was then drilled in all the balls as shown in Figure 6.4, and the compression tests repeated. Ashcroft (2003) used a small tube to keep the hole open during compression (to ensure the ball did not become airtight and artificially increase stiffness due to pressure), but careful examination of the ball during compression showed that the hole remained open. This hole meant that only one compression axis could be used.
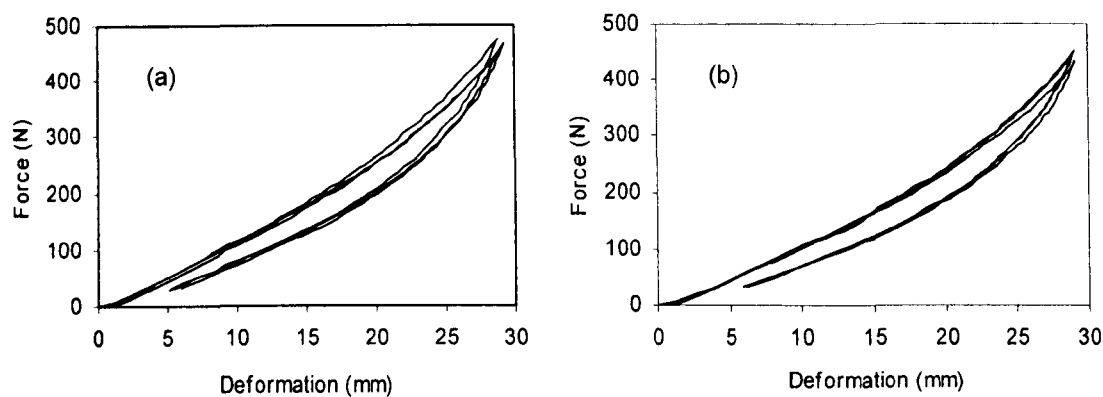
Figure 6.5 Force-deformation compression data for (a) new and (b) used pressurised balls. Three balls were tested in each case.

Figure 6.5 shows a comparison of the force-deformation data for the new and used pressurised balls. In each case three balls are shown on the graph, and it is clear there is no difference between the new and used balls. This data should not be used to infer too much about the effect of real gameplay on ball properties, as the typical lifespan of a ball in a professional match is likely to be of the order of 45 shots (Capel-Davies and Miller, 2003). However it is useful to have evidence that balls can be tested for stiffness after being used for a series of impact tests, without worrying about the effect of the impacts on the ball properties.
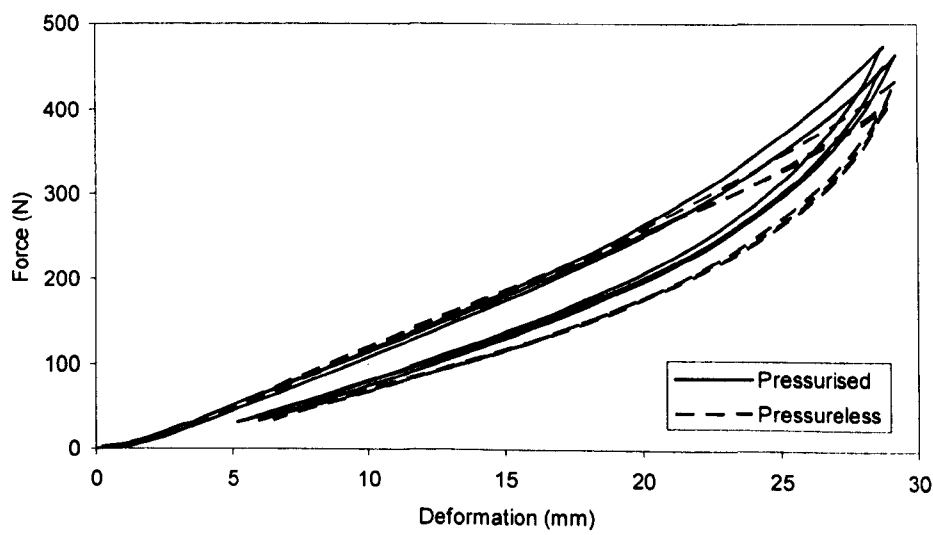
Figure 6.6 Comparison of force-deformation curves for (new) pressurised and pressureless balls; three of each type were tested.

Figure 6.6 shows deformation curves for pressurised and pressureless balls (new balls in each case). It can be seen that for most of the loading phase, the curves are very similar. At a deflection above about 20 mm, the pressurised ball seems to become slightly stiffer. This fits empirical experience that pressureless balls behave in a similar manner to pressurised

ones for low impact speeds (such as drop tests) but may bounce differently at higher speeds (to be discussed in a later chapter). There is also a difference on the unloading part of the cycle - the pressureless balls seem to have a lower force, suggesting a slightly increased energy loss.
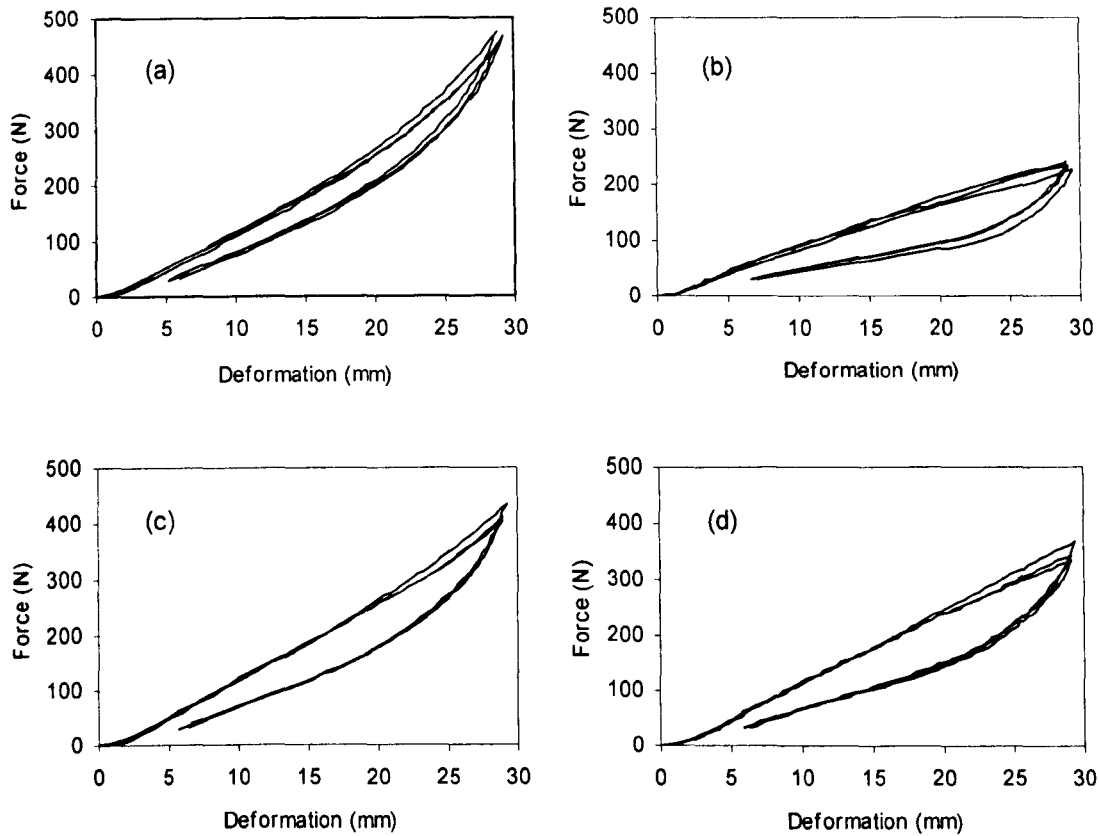
Figure 6.7 Force-deformation graphs for three each of (a) new pressurised, (b) drilled pressurised, (c) new pressureless and (d) drilled pressureless balls.

Figure 6.7 shows the effect of releasing the pressure on the ball stiffness. As would be expected, both balls are noticeably softer when there is no contained volume and the stiffness is provided purely by the structure of the ball. The softening effect is much less pronounced for the pressureless ball, which relies on a thicker wall and stiffer rubber for its strength rather than the internal air pressure.

There was no evidence of a sharp change in the stiffness due to buckling of the shell at any point, although the gradient of the pressureless graphs decreases slightly above about 10-15mm deformation.
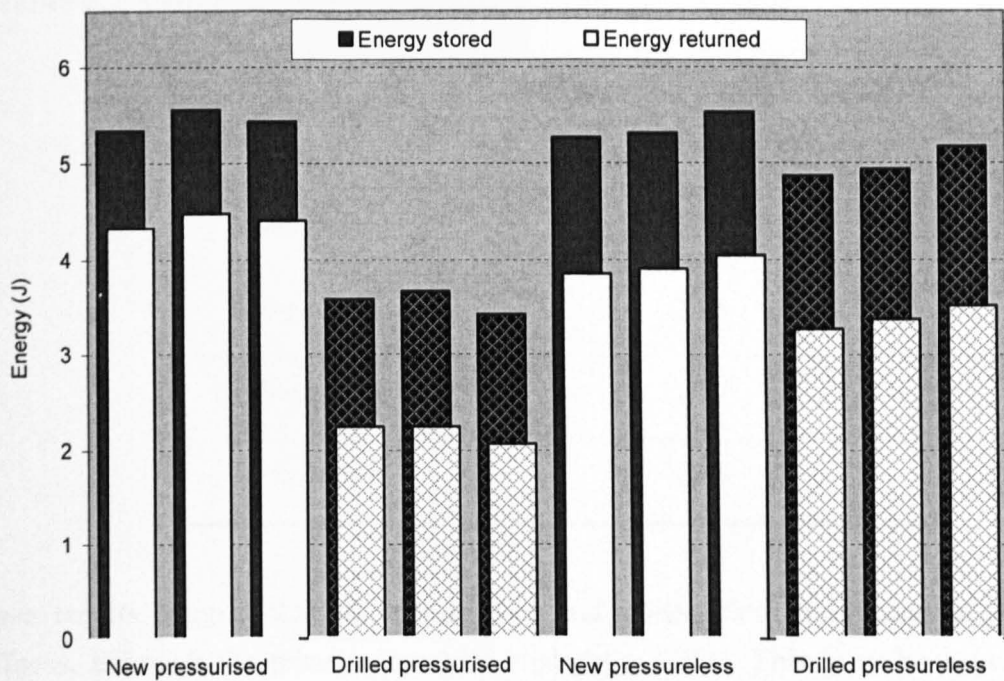
Figure 6.8 Energy stored and returned during compression, for new balls and those drilled to remove the effects of internal pressure.

In order to investigate the energies stored within the balls, the force-deflection curves were integrated using the trapezium rule. This data is shown in Figure 6.8. It is clear that pressurised and pressureless balls store similar amounts of energy on compression, although more is lost in the pressureless balls in hysteresis on restoration. Both balls store less energy without internal pressure, but the difference is much less for the pressureless balls.

6.4 Modelling the deformation

6.4.a *Original balls*

Polynomials were fitted to the loading curves of the various ball types, to find the stiffness at various loading levels. Of particular interest was the initial stiffness at zero compression. It can be seen from Figure 6.6 that the effect of the cloth makes it difficult to find the stiffness at zero deflection. The low stiffness for the very first part of the compression could give a misleading gradient to any fitted curve, as it was really the deflection due to the cloth, which is compressed before the rubber shell. The method used was to differentiate the trendline fitted, and use its gradient at a deflection value of two millimetres. This also minimised errors due to uncertainty in the starting deformation, as the gradient changed rapidly at low deflections if a high order polynomial was used. The measured stiffnesses are shown in Table 6.1.

Table 6.1 Measured stiffness at low deflection for four ball types.

Ball Type	Stiffness at 3 mm deflection (kN/m)
Pressurised	21.1
Pressureless	22.5
Oversized	18.7
Punctured	13.6

These results suggest that the pressurised and pressureless balls have a similar initial stiffness, although the pressureless ball is slightly stiffer. This is to be expected, as it is made to be harder to compensate for the lack of air pressure. The balls behave in a similar way at a drop test, which is a low speed dynamic test. Even at the speeds seen here the pressureless ball will lose effective stiffness from the lack of pressure, and so it must be structurally stronger. As expected, the punctured ball is much softer that the other three. A surprised is that the oversized ball has a much lower stiffness than the pressurised and pressureless balls., suggesting that the pressure compensates strongly during dynamic impacts for any weakness introduced by the thinner walls used to make it larger.

6.4.b   Drilled balls – loading

The force-deformation curves for the drilled balls lend themselves well to simple approximations, which are ideal for use in an impact model. In anticipation of a model based on using a point mass as a centre of mass deflection, the ball deformations were halved. Whatever shape the ball deforms to during compression, if the deformation is symmetrical then the centre of mass remains on the axis of symmetry and thus its deflection is always half the value of the ball deformation.
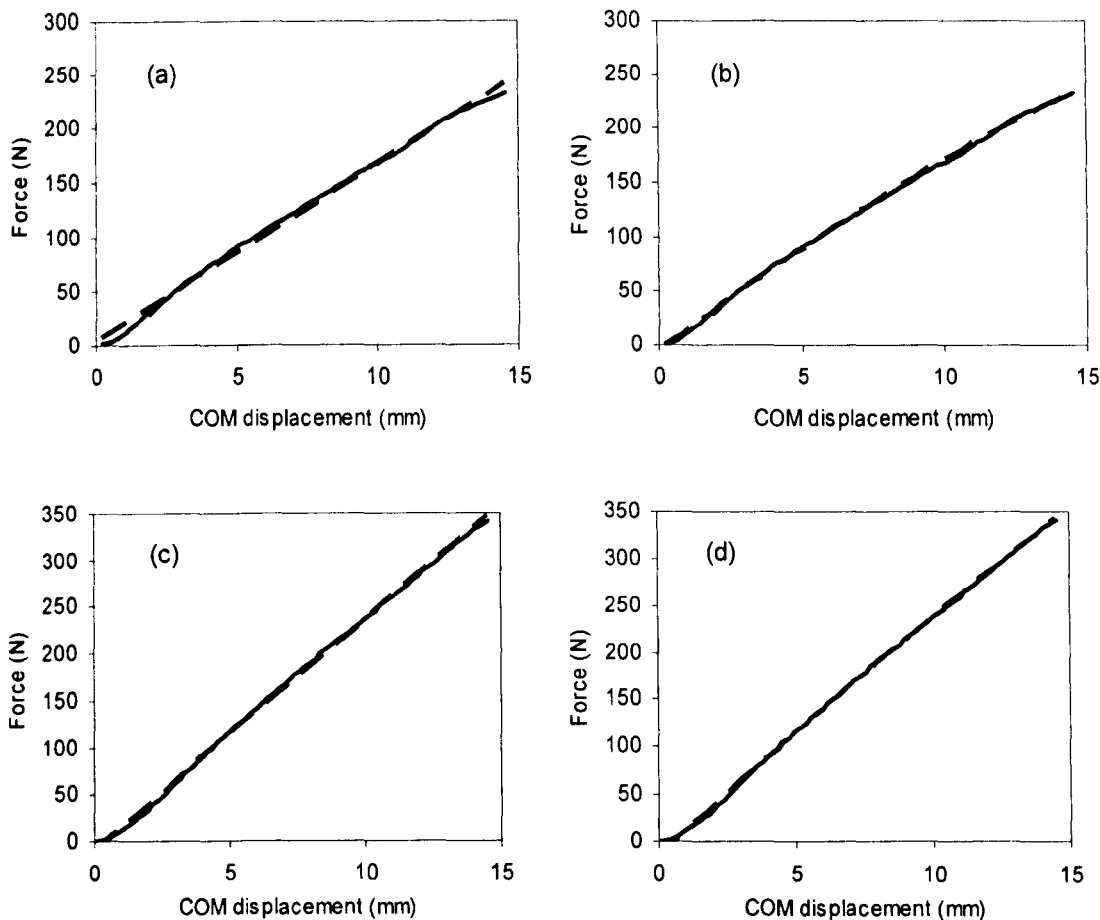
Figure 6.9 (a-d) Fitting (a) linear, and (b) quadratic curves to the loading part of the force-deformation data for a drilled pressurised ball; fitting (c) linear and (d) quadratic curves to the data for a drilled pressureless ball. In each case the solid line is experimental data and the dashed line is the fitted trendline.

Figure 6.9 (a-b) shows just the loading part of the curve for a pressurised ball, with both linear and quadratic fits. The linear fit is a reasonably good first approximation, and shows that the stiffness is fairly constant over a wide range of deflection, at 16.5 N/mm. A quadratic fit is even more accurate, giving a stiffness (found from differentiating the trendline equation) which decreases from 20.3 N/mm at zero deflection to 13.5 N/mm at a deflection of 12.7 mm (equivalent to a ball deformation of an inch). The equation relating force F to centre of mass deflection x is given (for deflections in metres) by

$$F = -26511x^2 + 20266x - 5.696$$ [6.1]

Figure 6.9 (c-d) shows the same fits to the loading curve for a pressureless ball. In this case the linear fit is even more accurate, giving a stiffness of 24.6 N/mm. The equation for the quadratic fit is given in equation [6.2]. Differentiated, it gives a stiffness of 27.7 N/mm at zero deformation and a lowered stiffness of 22.5 N/mm at a deformation of an inch – 37% and 66% higher stiffness than for the pressurised ball at the respective deformations.

$$F = -203309x^2 + 27685x - 18.129$$ [6.2]

6.4.c   Drilled balls - unloading

To be useful in an impact model, the hysteresis energy loss due to unloading must be simulated as well as the loading force. The method chosen was to choose a "shape factor" function which could be multiplied to the loading curve to give a reduced unloading curve. This must have a value of 1 at maximum deflection (and must never be greater than unity or this would lead to the unloading force being greater than the loading force). The first function tried used an exponential of the displacement unloaded as a proportion of the maximum displacement, i.e. $\dfrac{x_{max} - x}{x_{max}}$, leading to

$$F = F_{loading} \cdot e^{-k\left(1 - \frac{x}{x_{max}}\right)} \qquad\qquad [6.3]$$

This did not lead to the correct shape (although the numerical energy loss could be reproduced) and therefore the relationship was altered to use $\sqrt{\dfrac{x_{max} - x}{x_{max}}}$, leading to

$$F = F_{loading} \cdot e^{-k\sqrt{1 - \frac{x}{x_{max}}}} \qquad\qquad [6.4]$$
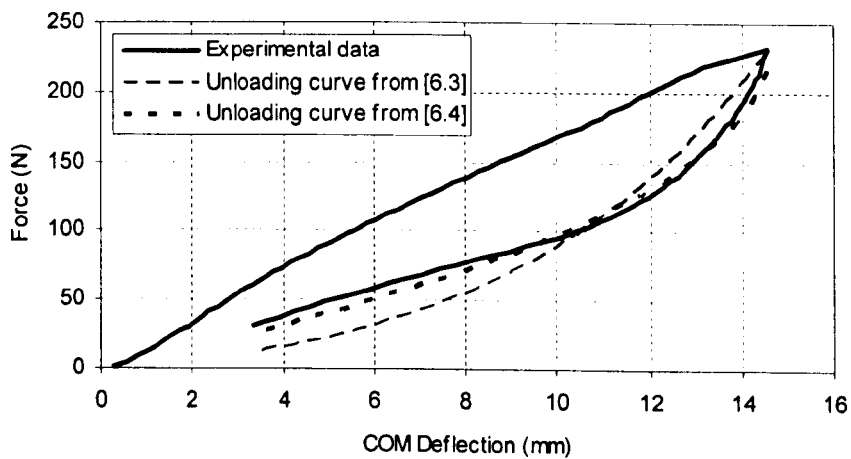
Figure 6.10 Modelling the unloading curve of a pressurised ball, showing shape factors from the two unloading equations defined in equations [6.3] and [6.4].
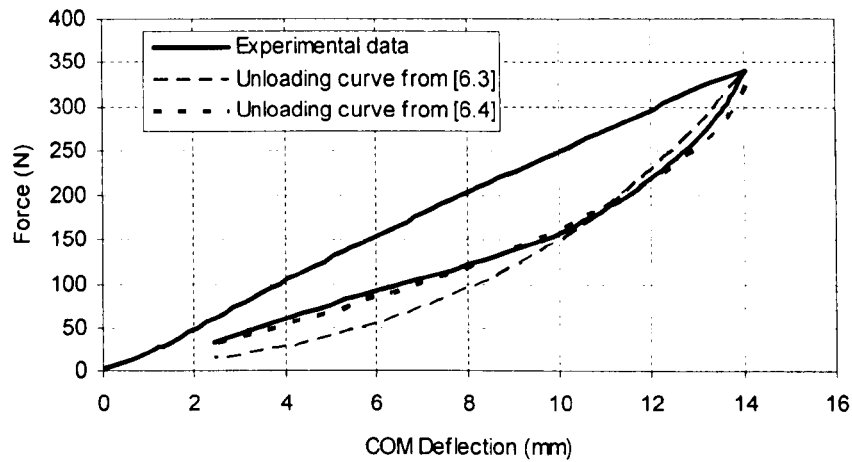
Figure 6.11 Modelling the unloading curve of a pressureless ball, showing shape factors from the two unloading equations defined in equations [6.3] and [6.4].

Figure 6.10 shows the loading curves produced by the two shape factor equations defined in [6.4] and [6.5]. It can clearly be seen that the second definition gives a much better fit. The same is shown in Figure 6.11 for a pressureless ball.

Unloading curves for different maximum deflections

(a)

(b)
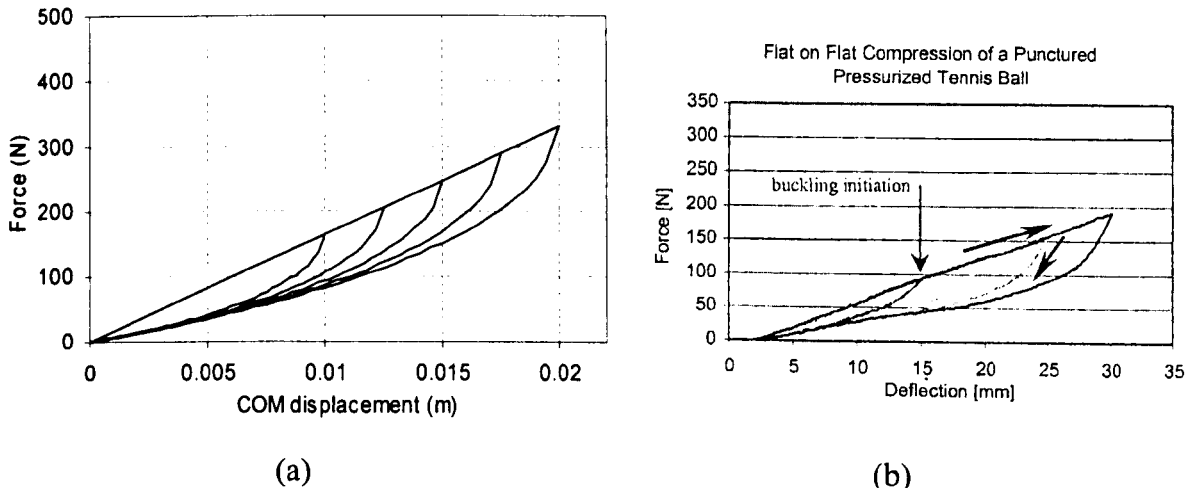
Figure 6.12 (a) The effect of shape factor on modelled unloading curves from various maximum loads, and (b) similar data reproduced from Ashcroft and Stronge (2003).

Figure 6.12 (a) shows unloading curves given the shape factor defined above when the ball is loaded to various values before being unloaded (using the linear loading approximation for simplicity). The unloading curves follow the trend of tending to the unloading curve of that for the highest load. This compares well to the experimental data reproduced from Ashcroft and Stronge (2003) in Figure 6.12 (b). The values of load against deflection do not match up for two reasons. The first of these is that the data of Ashcroft and Stronge uses actual ball deformation rather than centre of mass. The second is that the data plotted

in Figure 6.12 (a) assumes no cloth effects, whereas the data of Ashcroft and Stronge would need to be offset by 1 to 2 mm for a proper comparison.

6.5 Discussion

The definition of the ITF compression test calls for the machine to be zeroed when a preload of 80 N is measured. Such a preload is necessary to account for the variation in size between balls, and a relatively high load as this is needed because of the large initial deflections that occur due to the cloth deformation. This was reflected in the force-deflection curves seen here. A true zero is not only hard to define experimentally when setting up the apparatus, but gives initial deflections such as those shown by Ashcroft and Stronge in Figure 6.12 (b). This is why a deflection of 2 mm was used to define the "zero compression stiffness" in section 6.4.a.

The stiffnesses measured were in the order of 20 kN/m. The surface stiffness quoted by McMahon and Greene (1979) for asphalt or concrete was over 4000 kN/m. Values from 3000 kN/m and upwards were found using Berlin Artificial Athlete data in Chapter 5. All of this data suggests that a tennis ball has a stiffness two orders of magnitude lower than the court surface.

As in the previous chapter dealing with the experimental measurement of surface properties, the testing here was all performed in a controlled environment – actually in the same temperature and humidity controlled laboratory used by the ITF for ball approval testing. As mentioned in Chapter 2, Rose *et al.* (2000) found that static ball properties were not affected by temperature, and so this does not seem an important factor for the deformation testing discussed here.

6.6 Summary

In this chapter, the (quasi-) static properties of a tennis ball were examined. As would be expected given that all balls are manufactured to satisfy a standard set of tests, pressurised and pressureless balls behave the same in terms of stiffness and energy loss. When the internal pressure of these two types of balls is released however (to enable the pressure in the ball to be included in the model), they have very different stiffnesses – about 50% higher for the pressureless ball for a linear fit, which is a good first approximation in both cases. Quadratic approximations were found for the relationship between centre of mass deflection and force for both ball types, which could be useful modelling information if the volume and pressure were to be taken into account. A shape factor function was found which modelled the unloading shapes well.

Balls still containing pressure (since "punctured" balls still increase in pressure under compression, unlike the drilled balls), were also modelled by fitting polynomials to the

force-deflection curves. This allowed a "zero-compression" stiffness to be found by taking a tangent to the curve, although to take into account effects of cloth compression this was calculated at a nominal small deflection of 2 mm.

Compression tests were also performed at a variety of strain rates in an attempt to see how much difference this made to the stiffness. Somewhat surprisingly, all the deformation rates above 10 mm/min gave identical force-deflection curves (and even that very slow rate was very close to the others). This suggested that data taken at a relatively modest deformation rate can be useful in modelling, although dynamic experimentation is necessary to test this hypothesis.

7   Normal impact tests

7.1   Introduction

The rules of tennis give specific limits as to the bounce height of a ball when dropped onto a rigid surface from 100 inches. Normal impacts can also be used to investigate the interaction of ball and surface, finding the energy loss by measuring the coefficient of restitution (the ratio of rebound speed to impact speed). Because the ball is made of rubber, which is a non-linear viscoelastic material, it is to be expected that the energy loss will vary with strain rate (i.e. speed of impact). One of the main aims of this particular set of experiments was therefore to investigate how the properties of a ball change with speed. Several different ball types were bounced on a force plate at speeds from 3 to 20 ms^{-1} and the sampled force used to improve understanding of various dynamic properties of the ball, particularly stiffness.

7.2   Experimental apparatus
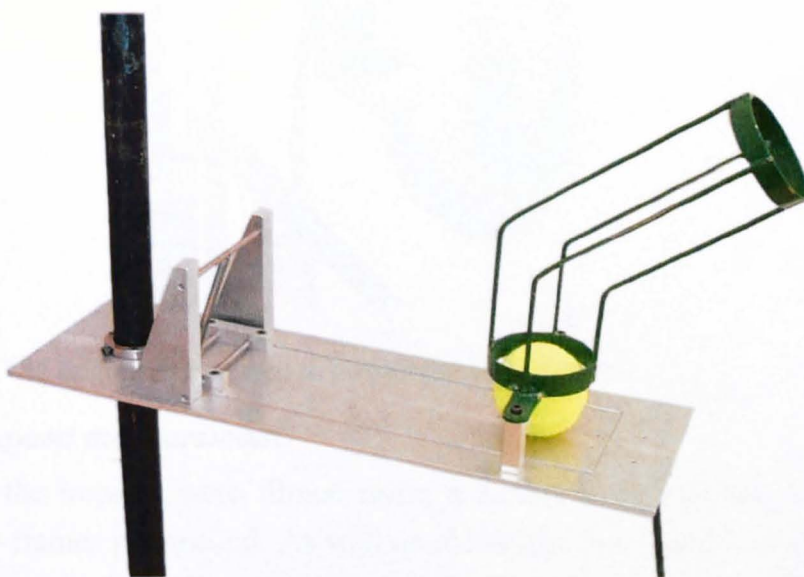
7.2.a   Balls used

Four ball types were chosen to illustrate a range of properties and provide an insight into the important parameters of construction. The first ball used was a standard pressurised ball, by far the most widely used type. The next was a pressureless ball. These contain air at atmospheric pressure but are made with a thicker rubber shell to compensate for the loss in stiffness which would provided by the air pressure. A modified pressurised ball with the pressure released by puncturing the rubber with a fine needle was thought to be a useful combination of the two. The final choice was a prototype oversize ball. The balls were 6% larger in diameter than standard balls, but contained the same internal pressure. The rubber walls were slightly reduced in thickness to keep the mass the same. The pressure of the two pressurised balls was measured after the tests. Ball properties are summarised in Table 7.1.

Although the tests described in this chapter (and the oblique impacts discussed later) were not performed in a controlled environment like the surface tests and quasi-station deformations, all the tests took place at a time of year that meant the temperature was between 20 and 25 degrees Centigrade. The data presented by Rose *et al.* (2000) suggested that for high speed dynamic impacts, a much wider temperature range than this had no significant effect on ball rebounds.

Table 7.1 An overview of the four different types of balls used.

Ball type	Gauge pressure	Shell thickness
Pressurised	0.069 MPa (10 p.s.i.)	3 mm
Pressureless	0 (Atmosphere)	4 mm
Oversize pressurised	0.069 MPa (10 p.s.i.)	2.8 mm
Punctured pressurised	0 (Atmosphere)	3 mm

7.2.b   *Ball release and projection*

Figure 7.1 The equipment used to accurately release balls without spin

Balls were projected normally onto a piezoelectric force plate at speeds between 4 and 20 ms^{-1}. At the lower speeds – up to about 7 ms^{-1} - the balls were dropped using a sprung trapdoor (shown in Figure 7.1). This gave good accuracy of the impact position and consistent speeds. It was designed to avoid imparting spin by using a spring to accelerate the trapdoor away from the ball faster than gravity. At the higher speeds they were fired horizontally from a modified Bola machine (Figure 7.2), which projects balls between two spinning solid rubber wheels and is sold as a cricket bowling machine. By setting both wheels at the same rotational speed, it was possible to ensure the balls were projected with

a low spin rate (which could be verified from the video footage). There was a range between 7 and 13 ms^{-1} where it was not practical to drop the ball using the trapdoor because of the extreme height which would be needed (not to mention the problem of achieving accuracy of impact), but was too slow to use the Bola effectively mounted horizontally because of problems achieving an accurate trajectory.
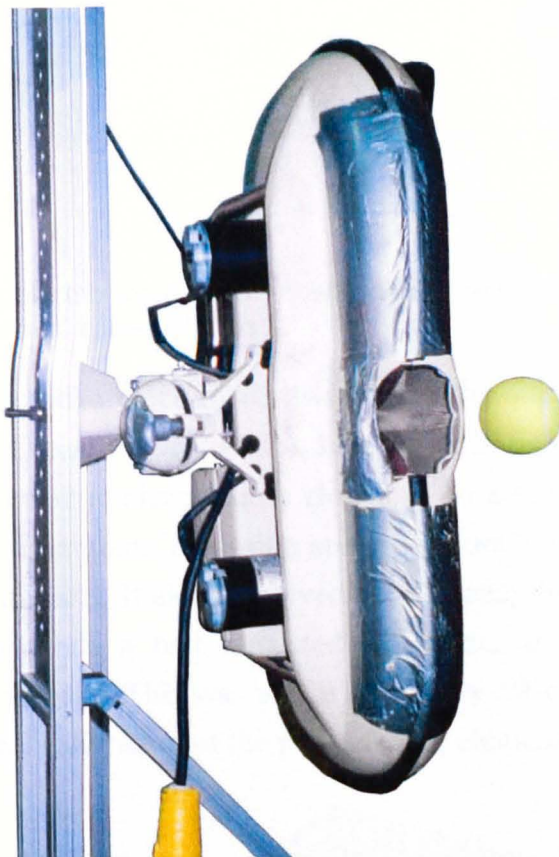
Figure 7.2 The Bola machine used to project the balls.

7.2.c   *Ball speed measurement*

At all speeds the impacts were filmed using a Kodak MotionCorder high speed video system, at 400 frames per second. As well as providing data which could be analysed for position and thus velocity (discussed in more detail later), this gave visual feedback as to the position of impact, and verified that there was little or no spin. At the higher speeds of 13 ms^{-1} and above, the incoming and outgoing ball speeds were measured using light beam timing gates. Because these gates were designed for high velocity use, they could not be used at the lower speeds (when the ball was dropped) and so the video data was manually analysed to find positional co-ordinates. Video data from several of the high speed impacts was used to ensure that values from this method agreed with those from the timing gates.

7.2.d   Piezoelectric force plate

(a)   (b)
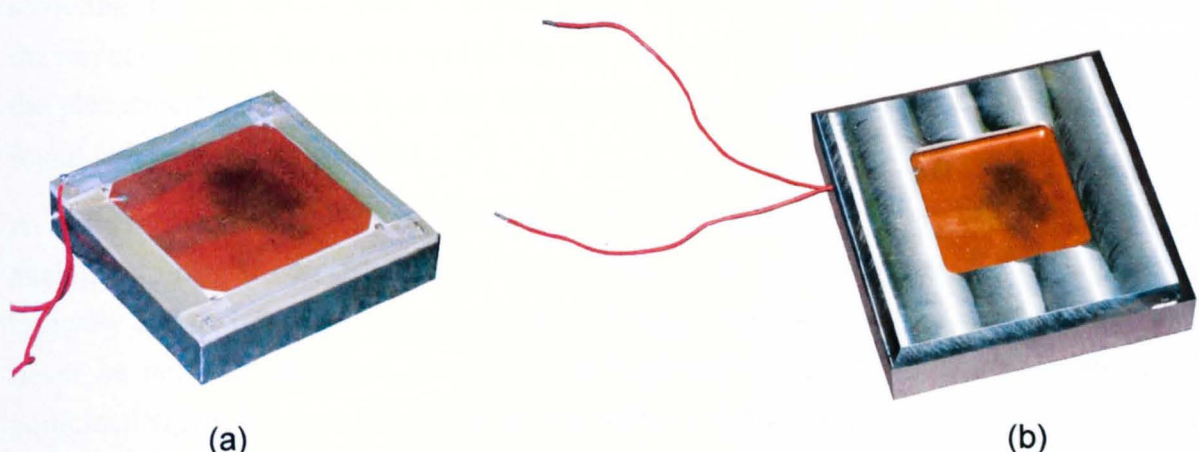
Figure 7.3 The piezoelectric force plate shown (a) as constructed and (b) in a protective aluminium mounting for high speed impacts.

The force plate was a bespoke piece of hardware manufactured by Cross and used in a number of experiments (Cross, 1999b, 2000b). It is shown in Figure 7.3 (a) and consists of an array of four square ceramic piezoelectric elements, on a steel base plate. This system was then fitted into the aluminium mounting seen in Figure 7.3 (b), which protected the wires from high speed impacts. It also improved the accuracy by reducing the target area and making it obvious when a ball impacted off-centre, as the ball would rebound sideways after striking an edge. This was useful as a badly off-centre impact would result in a significantly different calibration of the piezoelectric elements.
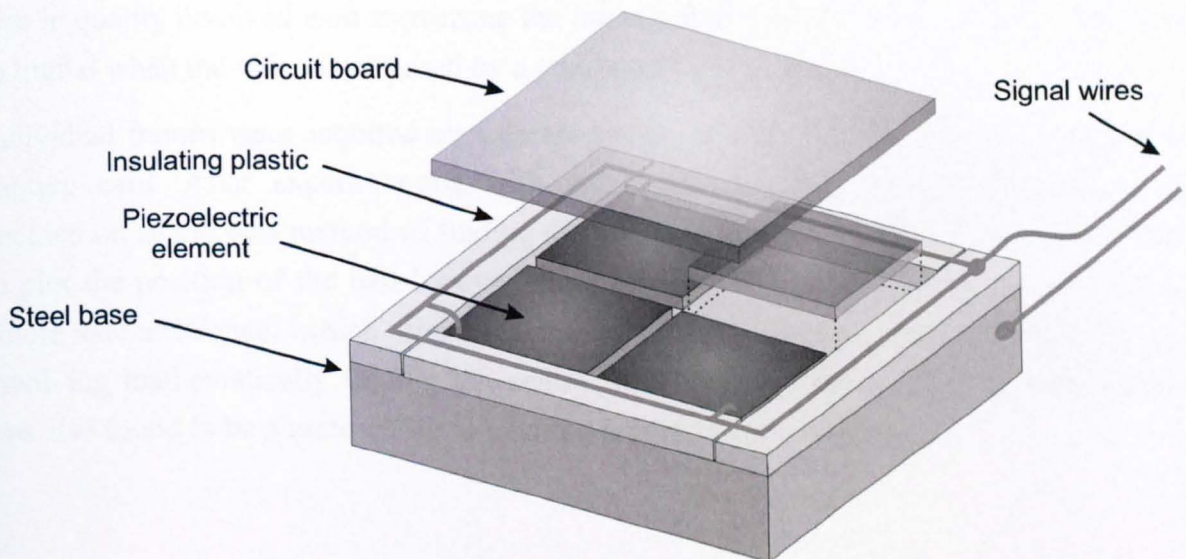
Figure 7.4 Exploded schematic of the force plate construction.

The four piezoelectric elements were aligned in the correct polarity, and attached to the steel base using conductive silver paste as shown diagrammatically in Figure 7.4. The first of the two connection wires was simply screwed to the base. The top surfaces were then

connected in parallel to the second signal wire using a carefully applied low temperature soldering iron. A square piece of circuit board was then attached on top. This evened out the impact force so that it was spread equally between the four elements, and also shielded the piezoelectric elements from any electrostatic charge generated by the ball (which was found to be a problem initially).

A 10x oscilloscope probe was used to connect the signal wires to a Picotech ADC-100 analogue-to-digital converter which sampled the force at a frequency of 60 kHz (giving typically 250 to 300 data points per impact). Because the four piezoelectric elements would never be perfectly matched, the impact and rebound speeds were used to calibrate the combined signal for each impact. This was done by integrating the force signal S over the duration of the impact (multiplied by the calibration c to give the force $F = cS$), and equating this total impulse to the momentum change of the ball as $\int F dt = \int cS dt = m\Delta V$. The maximum deviation seen was under 10% of the typical calibration.

7.2.e   Analysis of video data

This section describes an example of the process used to extract velocity information from the video footage. On triggering, the camera stores a number of frames in memory but these cannot be then saved directly in a digital format. The frames of interest are instead played back at a low speed (typically two frames per second) and either captured directly to computer, or more likely with experimental fieldwork are recorded onto an analogue video tape. This enables remote recording of a large amount of data but with an inevitable loss in quality involved with converting the information from digital to analogue, and back to digital when the video is acquired by a computer back in the lab.

Individual frames were acquired by a desktop computer and saved using a standard video capture card. After experimenting with automated tracking, manual digitisation was decided on as the best method of finding the ball position. A custom program was written to plot the position of the ball by overlaying a resizable circle. This effectively uses the whole circumference, which improves the accuracy compared to other methods (e.g. involving mathematically finding the centre from three points on the circumference). It was also found to be a more efficient tracking method in terms of time.
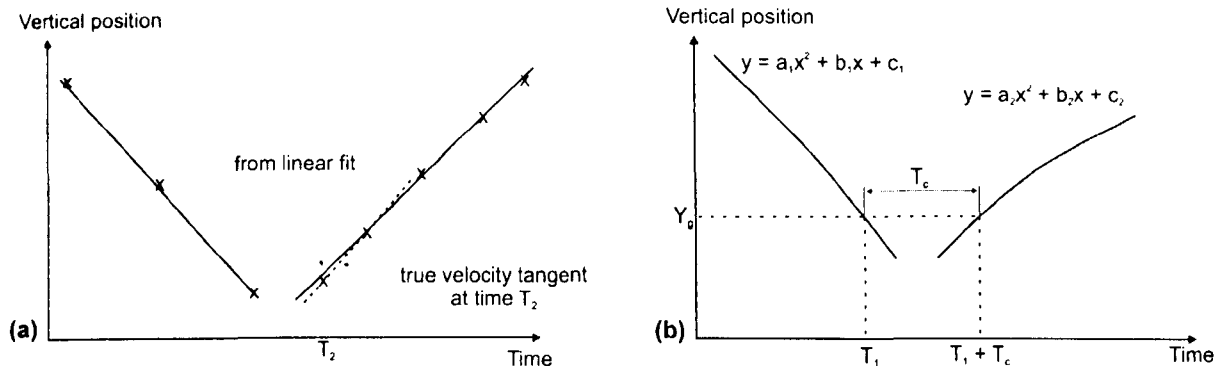
Figure 7.5 (a) possible errors in velocity using a linear fit to displacement data, and (b) using quadratic fits with contact time data to minimise these errors

There was a concern that for the slower impacting balls, gravity would have a significant effect on the speeds even during the short filming period. If a linear trendline is fitted to the displacement-time data but there is actually an acceleration downwards, this will underestimate both the speed before and after impact, as shown in exaggerated form in Figure 7.5 (a). The true tangent to the displacement curve will be steeper at the start and end of impact than a linear trendline fitted to all the data. To compensate for this error a quadratic trendline was used. If the vertical position of the ground was known, this would be a trivial task, but it was difficult to pick this out accurately from the video footage. Because the impact position was off-centre, any out of plane movement of the ball's trajectory moved the contact as seen by the camera. The oblique viewing angle also meant that it was not particularly accurate to simply use the frame with the highest deformation to ensure the ball was in contact since as the contact area widens, the lowest part of the ball seen by the camera moves.

The method adopted was to use the measured force data. This allows a reasonably accurate contact time to be determined. Consider Figure 7.5 (b). Let the quadratics (matched to the displacement-time data by a least-squares regression) for velocity before and after impact have equations $y_1 = a_1 t^2 + b_1 t + c_1$ and $y_2 = a_2 t^2 + b_2 t + c_2$ respectively. If T_1 is the time of the start of contact and T_C the length of contact, the value of T_1 can be found such that y_1 at $t = T_1$ is equal to y_2 at $t = T_1 + T_C$ - i.e. the ground level at the start of the impact matches that at the end of the impact. If these equations are equated, we find

$$a_1 T_1^2 + b_1 T_1 + c_1 = a_2 \left(T_1 + T_c\right)^2 + b_2 \left(T_1 + T_c\right) + c_2$$
$$= a_2 \left(T_1^2 + 2T_1 T_C + T_C^2\right) + b_2 \left(T_1 + T_c\right) + c_2$$

thus $\left(a_1 - a_2\right)T_1^2 + \left(b_1 - b_2 - 2a_2 T_C\right)T_1 + \left(c_1 - c_2 - a_2 T_C^2 - b_2 T_C\right) = 0$ [7.1]

Since T_C and the coefficients a, b and c are known, [7.1] is simply a quadratic in T_1. Solving this and substituting T_1 and $T_1 + T_C$ back into the initial equations giving y before and after impact gives the required speeds.

7.3   Sample force data
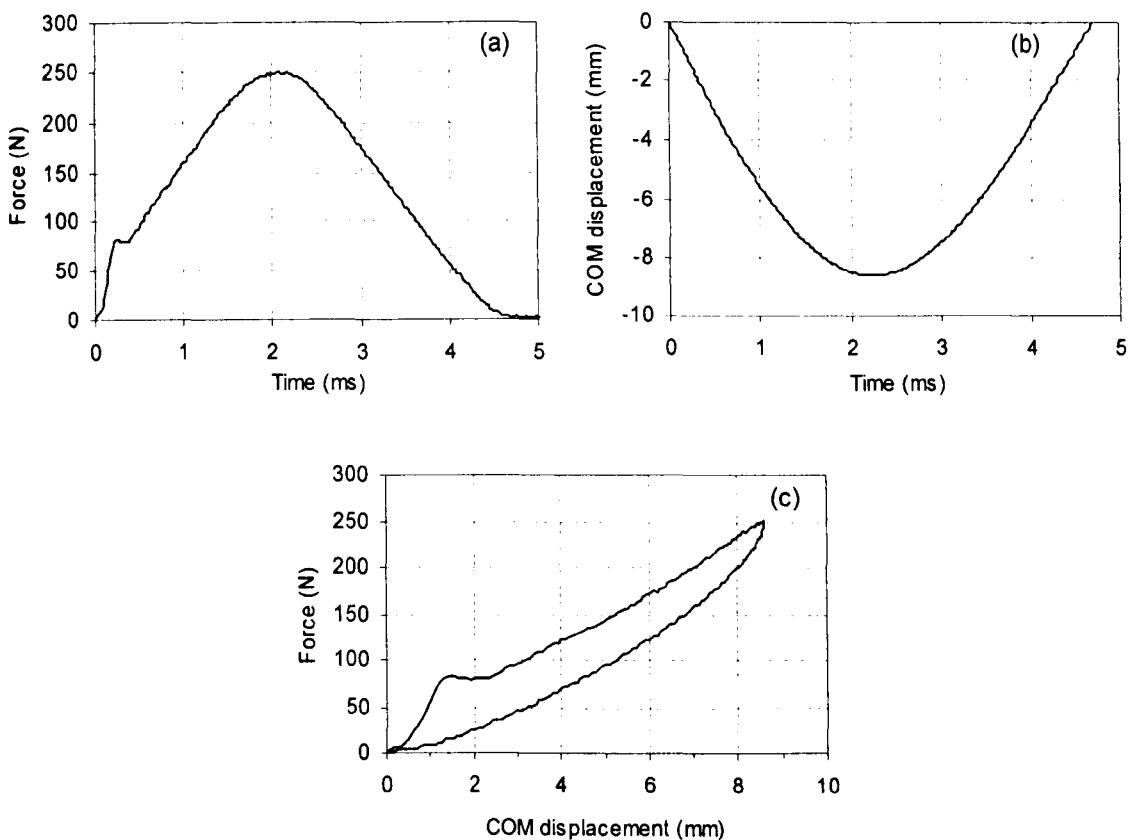
Figure 7.6 (a-c) (a) Force-time, (b) COM displacement-time and (c) force-displacement data, for a standard pressurised ball dropped from 100 inches.

Figure 7.6 (a) shows a typical force-time curve for a pressurised ball dropped from 2.54 m (100 inches). As the sampling was manually triggered at a random time between the ball being released and it impacting, a time offset was applied to the data to ensure the impact data started at time $t = 0$. There is a distinct shoulder about 0.25 ms after the start of the contact, but apart from this the curve is similar to a half sine wave.

If the force is divided by the mass to give acceleration and integrated, velocity can be calculated. Because the data was sampled at a reasonably high frequency and is fairly smooth, a simple trapezoidal integration rule was considered sufficiently accurate. The offset used here was the boundary condition of measured velocity V_{in} at time $t = 0$. A further integration gives displacement. Figure 7.6 (b) shows this displacement against time, which was given the boundary condition of zero displacement at $t = 0$. It should be remembered that this is displacement of the ball centre of mass, not the absolute deformation relative to the original sphere. This graph suggests that the ball is still slightly deformed after 4.5 ms, when it leaves contact with the surface of the force plate. There is a maximum centre of mass displacement of about 8.6 mm.

Figure 7.6 (c) plots the force-displacement curve for the structure. The negative displacement is shown here as a positive compression. The effective initial stiffness can be clearly seen to be higher than that later in the compression cycle. The secondary stiffness is almost constant as shown by the nearly linear force-compression relationship, suggesting that it does not change significantly throughout the loading. On unloading there is an enclosed area representing the hysteresis energy loss. This area is not particularly large, indicating qualitatively that the ball bounces fairly well, with a large proportion of its initial energy.

7.4   Comparison of force plate and video data

In order to verify the data from the force plate, an impact was filmed using a different high speed video system, at a higher frame rate. The frame rate of 400 Hz used previously was adequate for finding speeds before and after impact, but would only give two or three frames during contact. A Kodak 4540 system gave a frame rate of 9000 per second, providing typically 40 frames during a 4.5 ms contact period.
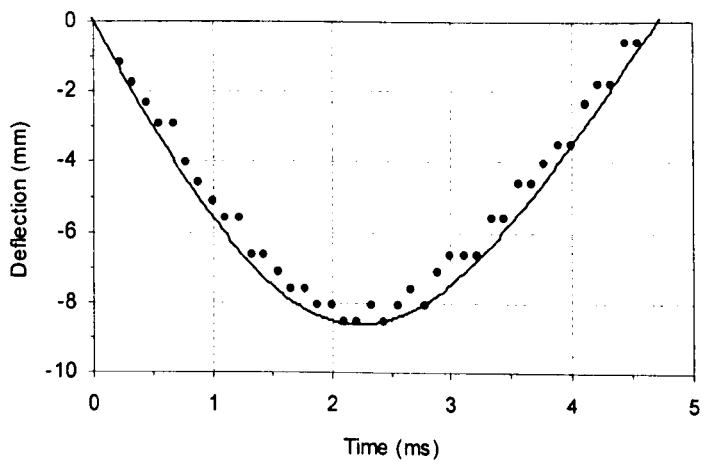
Figure 7.7 Comparison of high speed video measurements and integrated force plate data for ball COM deflection during normal impact.

Figure 7.7 shows the comparison between the ball centre of mass deflection calculated from the force signal and measured using high speed video. The video positional data was adjusted to take into account the effect of assumed deformations as discussed later in Chapter 8. It can be seen that there is very good agreement, suggesting that the assumption of deformation shape is a reasonable one and that the force plate data is accurate.

7.5   Results - velocities
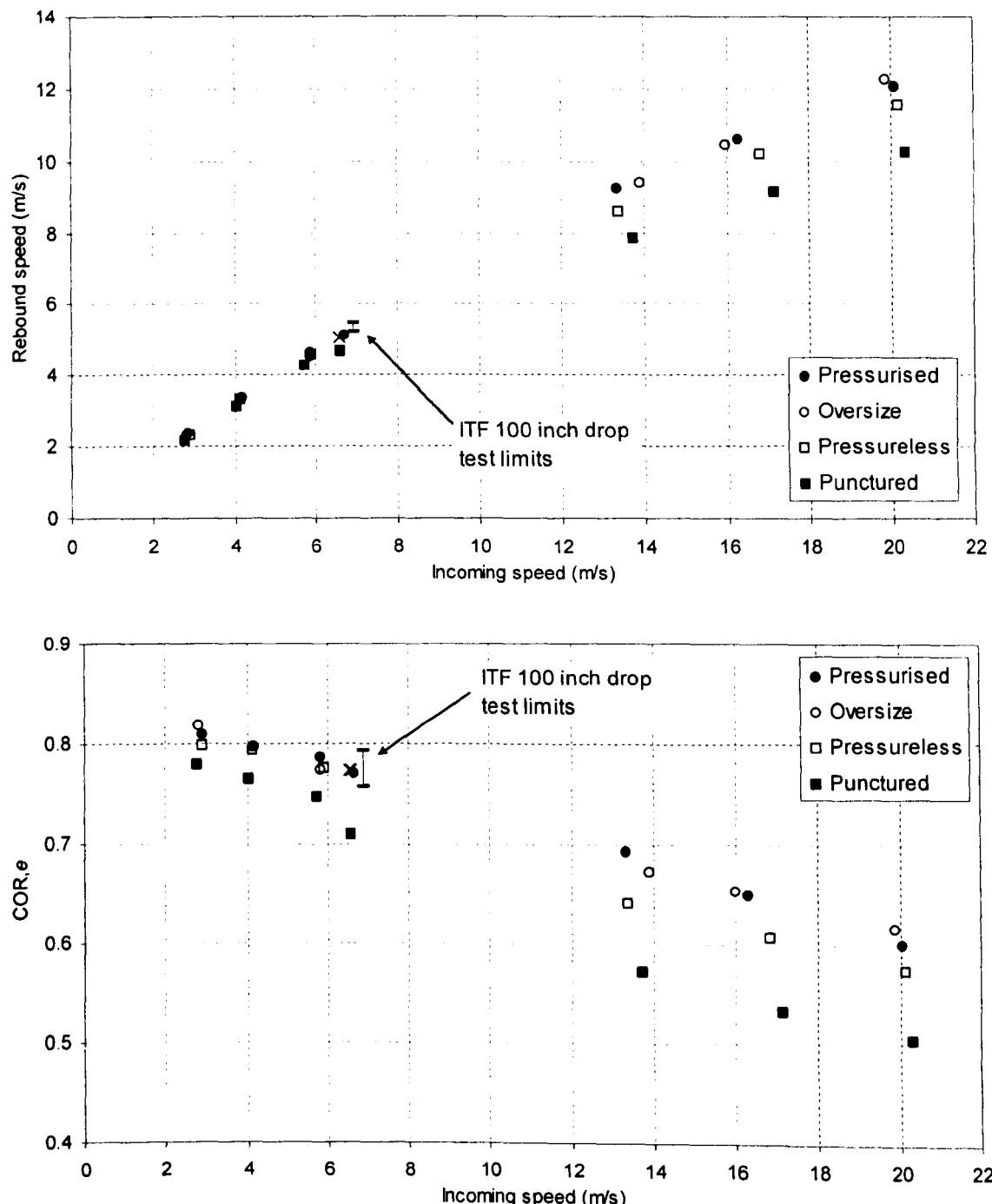
Figure 7.8 Rebound speed against incoming speed and COR against incoming speed, for four different ball types impacting normally at speeds between 4 and 20 ms^{-1}.

Figure 7.8 shows how rebound speed varies with impact speeds, for the four ball types – shown as both absolute speeds and COR values. At low impact speeds, the balls all behave in a similar manner, and even the punctured ball is fairly close to the other types in terms of rebound speed, although the difference is accentuated by looking at COR. This is because the small difference in absolute speed makes the graph points difficult to distinguish until they are normalised using COR.

It is to be expected that "off the shelf" balls will have very similar rebounds at low speeds. This is of course because balls are manufactured to achieve the specified bounce height range of the approval tests, which happens at a speed of just below 7 ms^{-1}. The construction of the normal and oversized pressurised balls does not seem to be different enough to cause significantly different rebounds even at the higher speeds. It is worth noting that the COR values at the 100 inch height lie in the 0.76-0.79 range found by taking aerodynamic drag into account, rather than the 0.73-0.76 range as would be expected using a simple energy conservation relationship.

As the speed is increased, the two pressurised balls maintain similar rebounds, but the pressureless ball has a lower COR. Pressureless balls compensate for the lack of internal pressure by having a thicker (and therefore stiffer) rubber shell, typically 4 mm compared to 3 mm for a conventional pressurised ball. As a ball is compressed, there are force components due to both the resistance of the structure to deformation and the internal pressure. Both of these are non-linear functions of deflection and so two balls with different wall thicknesses and internal pressures cannot have the same overall stiffness over a wide range of deflection. The permanent pressure balls undergo more deformation at higher speeds, and it is the deformation which provides most of the energy loss.

The deflated ball shares characteristics of the previous two balls. The pressure was released using a fine needle to puncture the rubber shell in various places around its circumference. The holes were small enough that unless a particularly large force was applied, the ball would retain the air and therefore there would be an increase in pressure as the volume was decreased. In this way the ball was similar to a permanent pressure ball. However, there was no extra structural stiffness from a thicker shell and so the deformations (and thus energy losses) will be larger than all other ball types at every impact speed. The difference in the COR compared to the pressurised balls does however increase with higher speeds, where the low stiffness allows extreme deformations.

7.6   Results - forces
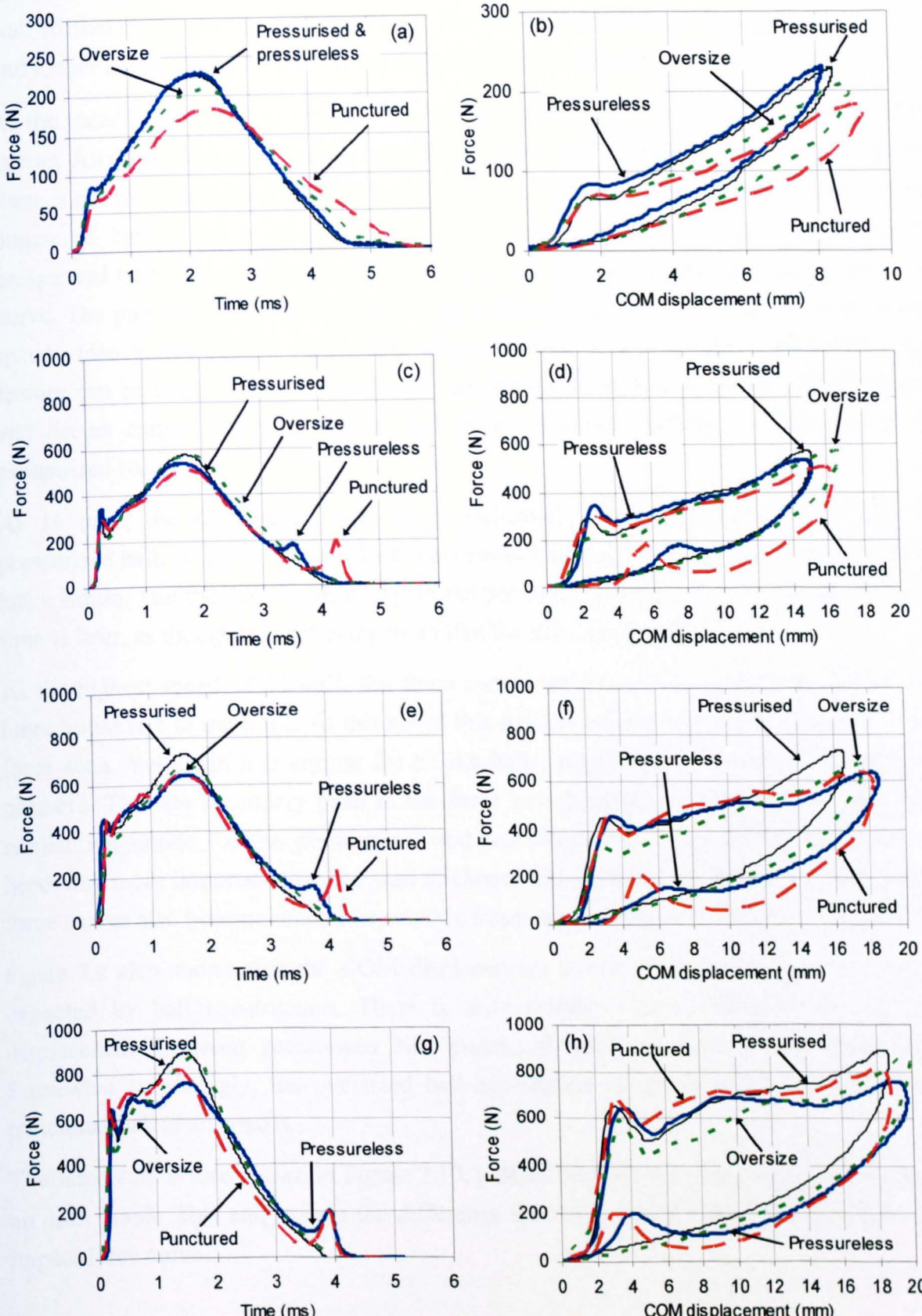
Figure 7.9 (a-h)   Force-time and force-displacement graphs for the various ball types at different speeds: (a,b) 5.8 ms^{-1}, (c,d) 13.5 ms^{-1}, (e,f) 16.5 ms^{-1} and (g,h) 20 ms^{-1}.

The force profiles of impacts at various speeds are shown in Figure 7.9. At low speeds, the pressurised and pressureless balls cannot be distinguished, suggesting that the increased wall stiffness balances the lower pressure. The punctured ball has a lower maximum force and longer contact time, both of which suggest a lower stiffness as would be expected.

As the speed is increased to 13 ms^{-1}, there is an immediate difference in the shapes of the curves. All three balls still have the same initial "shoulder" or peak in force. The maximum force is not too dissimilar for the different ball constructions, although the pressureless and punctured balls have a maximum force 7% and 12% lower respectively than the pressurised ball. The significant difference is at the tail end of the unloading part of the curve. The punctured ball shows a large and sudden extra peak. This can be seen on high speed video as the bottom of the ball "slapping back down" on the surface. The same feature can be seen on the pressureless force curve, although it is much less pronounced and occurs earlier. The pressureless ball retains a similar overall contact time to the pressurised ball.

At 16 ms^{-1}, the pressureless ball has a noticeably lower maximum force than the pressurised ball. Again all three balls have a similar initial rise in force. The punctured ball has a similar late increase in force. Again the pressureless ball has a smaller peak, but the time is later, as though it is behaving more like the punctured ball.

At the highest speed of 20 ms^{-1}, the force curves are beginning to be dominated by the large initial rise in the force. At this speed this peak is around two thirds of the maximum force seen. Yet again it is similar for all the balls, suggesting it is not a function of the pressure. The late secondary peak in the force now happens at a similar time and has a similar magnitude for the pressureless and punctured balls, suggesting the pressure is becoming more important than the wall thickness and stiffness. As the speed increases, the force curves also become much less smooth, implying vibration and irregular deformation.

Figure 7.9 also shows that the COM displacement is not affected as much as might be expected by ball construction. There is only around 1 mm difference in maximum displacement between pressurised and punctured balls at three of the four speeds. Somewhat surprisingly, the oversized ball has similar or greater displacement than the punctured ball at all speeds.

The same data is also shown in Figure 7.10, plotted with all the speeds for a particular ball on each graph. This emphasises the difference incoming speed makes to the shape of the impact force curve.
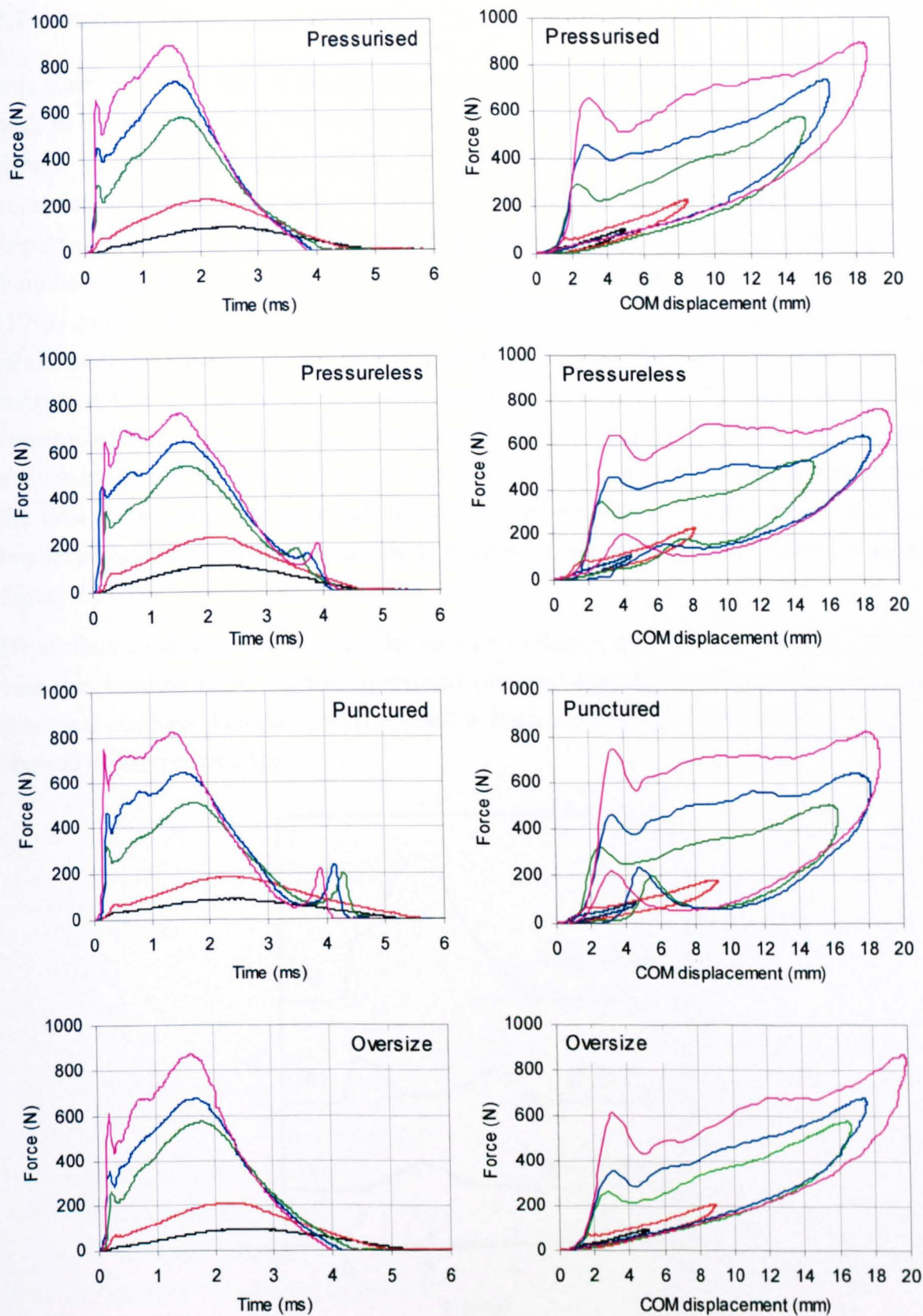
Figure 7.10 Force-time and force-displacement graphs per ball, plotting different speeds on the same graphs. In each case the data is for about 2.9 ms^{-1}, 5.8m s^{-1}, 13.5 m s^{-1}, 16.5m s^{-1} and 20 ms^{-1} in order of increasing peak force.

7.7 Discussion

It is clear from both the force-time and force-displacement graphs that there is an initial peak in the reaction force, which depending on impact speed can be the most noticeable feature of the impact. This effect does not seem to depend significantly on ball construction, but its value as a proportion of the overall maximum force increases with impact velocity. The force-displacement graphs show this peak as an initial peak stiffness. Various explanations have been suggested as to the reason for this initial peak. Thomson (1999) and Cross (1999b) both noted the dip after the initial peak in the force – which is much more noticeable on the force-displacement curves than the force-time ones) and suggested that it was due to a sudden change in stiffness of the ball. Cross (1999b) constructed a force platform which contained a small (13 mm) central piezo element above a much larger one, so that the contact force over a small area could be measured as well as the total force. By bouncing a ball directly on the smaller piezo as well as at a central impact point 20 mm away, he was able to produce centre and off-centre forces as shown in Figure 7.11.

He attributed the drop in stiffness after an initial sharp rise to internal buckling of the ball core (i.e. bending rather than compression) causing instability and reducing the effective structural stiffness. Dignall (1999) created a finite element model of the ball which also showed this same buckling.
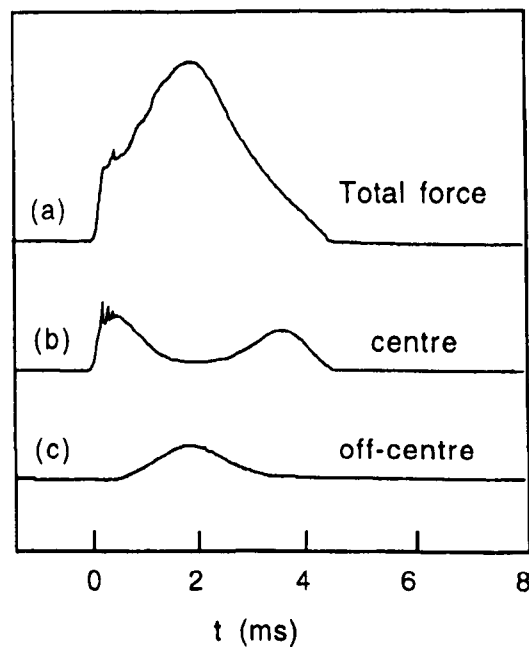
Figure 7.11 Experimentally measured impact force showing the total force and centre and off-centre measurements (reproduced from Cross, 1999).

An alternative mechanism for this initial peak in force is an impulsive force or "momentum flux", which has been used by several authors in ball impact models – described in more

detail in Chapter 2. This assumes the ball is split into two sections, one of which is the undeformed part of the ball above the surface, and the other which is either a flat area which does not move and stays in contact, or which buckles upwards. As the ball deformation increases, the material just above contact suddenly loses all its velocity, generating an impulsive reaction force.

One point which is worth noting is that this impulsive force mechanism proposes an alternative reason for the "inner and outer" forces noted by Cross. At the very start of the impact, the impulsive force will be a point force. As the ball deforms more and more, the sections of material coming to rest are gradually increasing circular slices until the deformation reaches the shell thickness. After this, the contact area for new material coming to rest and applying a force will be annular, at a gradually increasing radius, which will cause the measurable force in the central portion to drop – although there will still of course be a central force due to air pressure and other forces.

Another interesting feature of the initial peak in force is that there is a dip immediately after it. This becomes more prominent with increasing force and is more noticeable on the force-deflection curve than the force-time one. The most likely cause for this seems to be some element of buckling in the shell, momentarily reducing the effective stiffness.

7.8 Summary

This work confirmed the belief that incoming speed strongly affects the properties of a tennis ball; a significant change in COR can be seen by changing the impact speed (from about 0.8 at an impact speed of 3 ms^{-1} to about 0.6 at 20 ms^{-1}).

Ball construction also plays an important part in behaviour. All types of commercial balls have similar properties at low speeds because of the quasi-static nature of the approval tests (although the punctured ball is softer), but at higher speeds there are much more noticeable differences. The permanent pressure ball has a significantly lower COR than either of the two pressurised balls. The punctured ball bounces even slower, as would be expected.

All balls exhibit a sharp early rise in force giving a "shoulder" in the force-time curve. The value of this initial force becomes an increasing proportion of the overall maximum force as the impact speed is increased. The punctured and (to a lesser extent) pressureless balls also show an extra force in peak just before the end of the impact at higher speeds.

8 Normal impact model

8.1 Introduction

The previous chapter shows that when different balls are considered, even a normal impact is more complicated than might be expected. But although it was considered important to gain a full understanding of the impact, it was not thought necessary to create a model which simulated every last detail. The interest lay in predicting how a tennis ball would act in a game situation.

An important consideration was to create a model whose input conditions could be easily measured. The ideal situation given an unidentified tennis ball (perhaps a new design) would be to perform as few tests as simply and quickly as possible. Therefore a vital property of a model was the ease with which enough variables could be measured to allow prediction of its behaviour through a full range of conditions.

This chapter progresses through three models of varying complexity, before presenting one which satisfies the necessary criteria.

8.2 Calculating the centre of mass and moment of inertia for a deformed ball

8.2.a Overview

All the models presented here are based on simplifying the ball to a point mass, which means that the defining variables (displacement, velocity and acceleration or force) are calculated in terms of the centre of mass. It is useful – and in many cases vital – to be able to calculate the physical shape of the ball, either to simply find the external deformation or to derive more complex attributes such as circumferential contact area.

Several possible assumptions have already been mentioned for the deformed shape of the ball. None of these make it easy to analytically calculate the altered moment of inertia or centre of mass position of the new structure, and in all realistic cases it is impossible. Solutions were therefore found in software using the Monte Carlo method (written in Visual Basic). This involves discretising the ball into a large number n of point masses, by randomly generating coordinates until n have been found within the assumed physical volume of the deformed ball. The densities of the point masses in the rubber and cloth sections respectively can be calculated using the number of points in each part and the relative masses of the two materials (e.g. a 57g ball is typically 46g rubber and 11g cloth).

When a sufficient number of random points has been generated, the average centre of mass position y_{COM} can be calculated using

$$y_{COM} = \frac{1}{M} \sum_{i=1}^{n} y_i m_i$$

[8.1]

Once the centre of mass position is known, the deformed moment of inertia I can also be calculated:

$$I = \sum_{i=1}^{n} m_i r_i^2$$

[8.2]

where r_i is the radius about the spin axis.
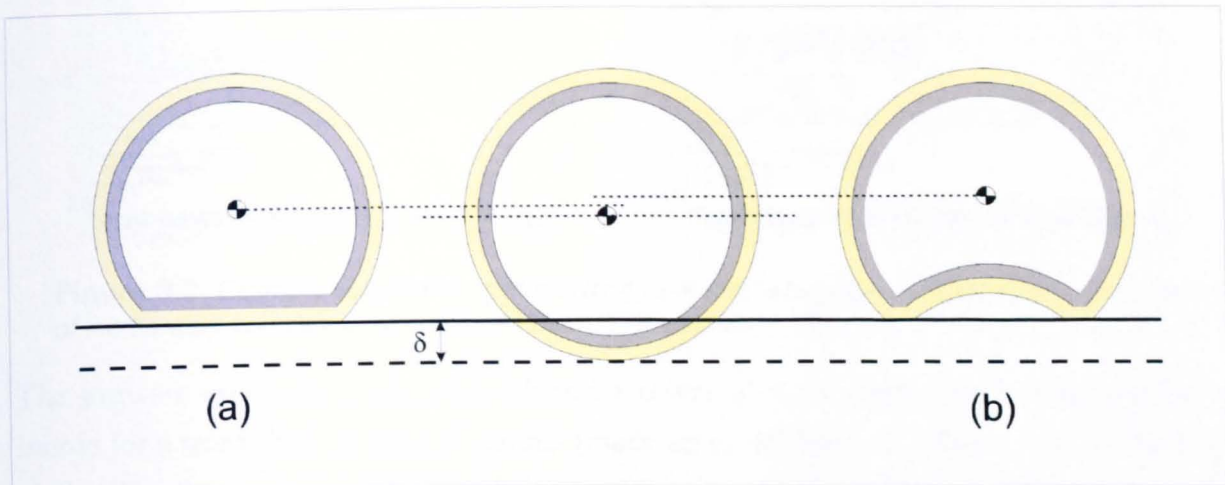
Figure 8.1   Assumed shapes for deformed ball with deflection d for (a) truncated and (b) buckled balls.

The centre of mass position and moment of inertia were calculated for two assumed ball deflections, where the majority of the ball remained an undeformed sphere in both cases. In the first shape, referred to as *truncated*, the ball deflection δ is created by simply flattening the rubber and cloth. In the second case, referred to as *buckled*, the material of the rubber and cloth is made to buckle inwards by reflecting it along an axis of symmetry. This will move the centre of mass position more and reduce the moment of inertia further, as the material which would be below the surface for an undeformed ball is displaced approximately twice the distance as for a truncated ball. The two assumed shapes are shown in Figure 8.1 relative to an undeformed ball.

8.2.b   Results
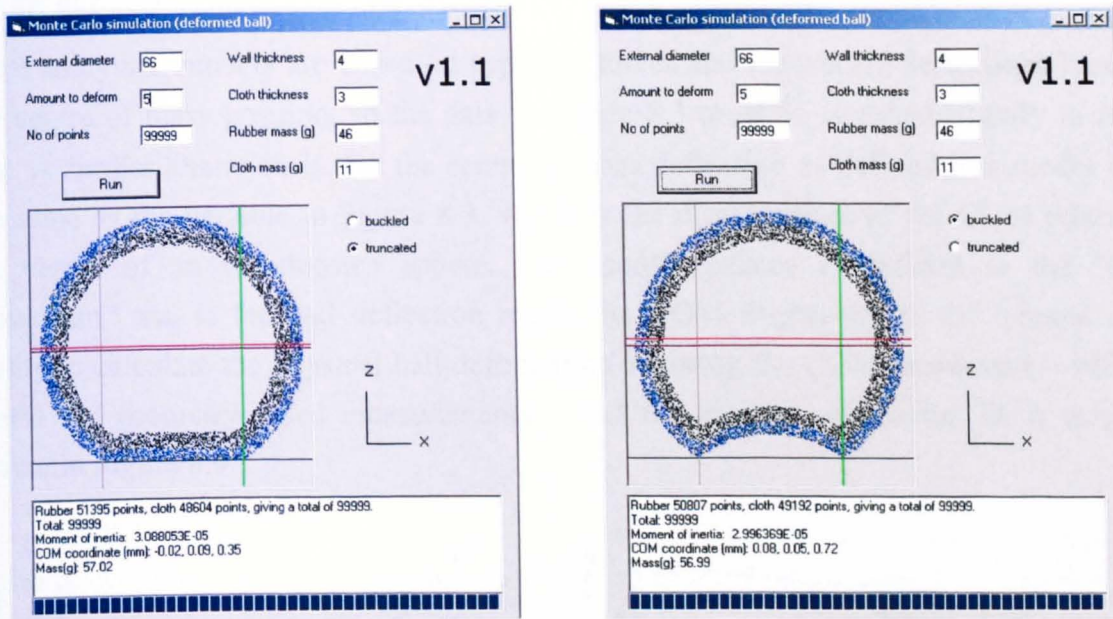
Figure 8.2 Example software output showing how centre of mass displacement and moment of inertia were calculated for deformed balls (with truncated and buckled shape assumptions).

The software was used to calculate values for centre of mass displacement and moment of inertia for a tennis ball of mass 57 grams (made up of 46 grams of rubber and 11 grams of cloth). The outside diameter of the ball was 66 mm, with the rubber and cloth layers each being 3 mm thick. 99 999 random points were used to define the ball structure. An example of the output is shown in Figure 8.2. Each coloured dot represents a randomly chosen point sitting within a slice 1 mm either side of the central axis.
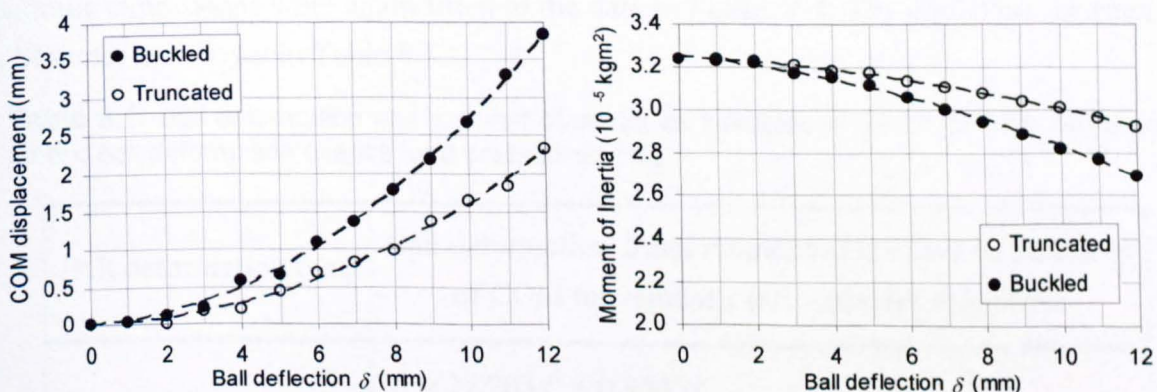
Figure 8.3 Displacement of centre of mass position and changed moment of inertia of a deformed pressurised tennis ball, plotted against ball deflection.

The effect of ball deflection on the centre of mass position and moment of inertia of the ball are shown in Figure 8.3. As this method relies on randomly generated points, the results will always be an approximation and thus a trendline was plotted (in all cases a quadratic). As would be expected, both variables are changed more by the buckled

assumption than the truncated one – about 1.5 times for the centre of mass and about twice for the moment of inertia.

Most analytical models are based on applying forces and measuring deflections based on the centre of mass position, so the data in Figure 8.3 must be changed slightly to reflect that. A further alteration is that the centre of mass deflection as defined in a model is not the same as the variable in Figure 8.3, which is the displacement of the COM relative to the centre of an undeformed sphere. The useful distance is defined as the "COM movement" and is the ball deflection minus the COM displacement. Of interest is the ability to calculate the physical ball deformation knowing the COM movement – which is useful for geometry-based measurements – and the moment of inertia. Both these are shown in Figure 8.4.
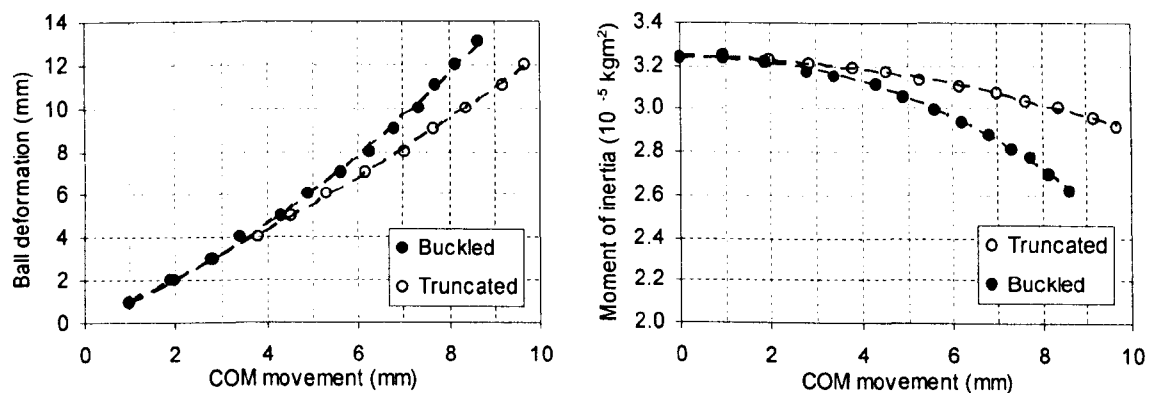
Figure 8.4 Ball deformation and moment of inertia as functions of centre of mass movement, for two assumed ball deformation shapes.

Quadratic expressions were again fitted to the data in Figure 8.4. The equations for each fit (in SI units) are shown in Table 8.1.

Table 8.1 Ball deformation and moment of inertia as functions of centre of mass movement, for two ball deformation shapes for a pressurised ball.

Ball deformation type	Ball deformation δ and moment of inertia I as functions of COM movement x (all variables in meters)
Truncated	$\delta = 27.203x^2 + 0.9645x$
	$I = 3.2428 \times 10^{-5} - 0.030558x^2 - 3.4082 \times 10^{-5}x$
Buckled	$\delta = 74.830x^2 + 0.841x$
	$I = 3.2295 \times 10^{-5} - 0.093891x^2 + 1.1426 \times 10^{-4}x$

The results above are of course only valid for a pressurised ball type. A pressureless ball will have different properties due to the altered distribution of material – it has the same cloth layer but a thicker rubber of lower density.
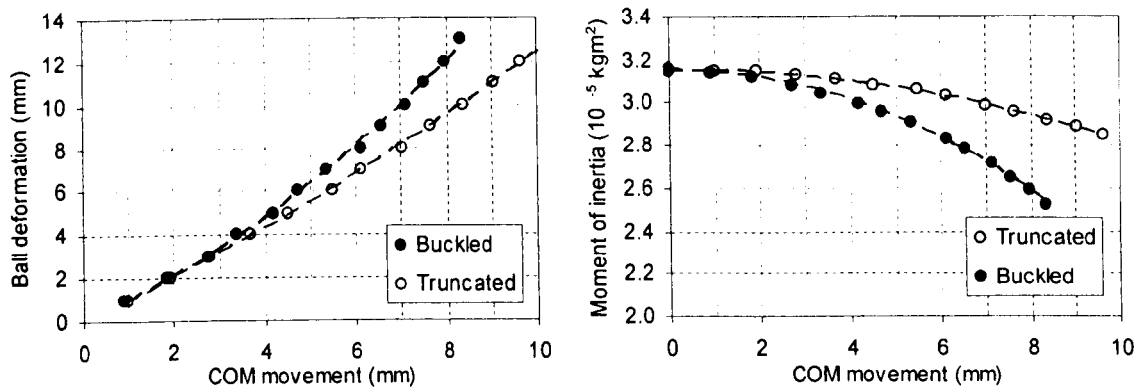
Figure 8.5 Physical ball deformation and moment of inertia predictions as functions of centre of mass displacement for a pressureless ball.

Figure 8.5 shows how the assumed deformation shapes affected the ball deformation and moment of inertia for a pressureless ball. The thicker shell had very little effect on the predicted ball deformation (especially for the truncated shape), but there was an effect on the moment of inertia. This is not a factor on the normal model presented in this chapter, but may be important for an oblique model in the way it changes rotational acceleration and therefore spin. The equations for the trendlines shown are in Table 8.2.

Table 8.2 Ball deformation and moment of inertia as functions of centre of mass movement, for two ball deformation shapes for a pressureless ball.

Ball deformation type	Ball deformation δ and moment of inertia I as functions of COM movement x (all variables in meters)
Truncated	$\delta = 28.031x^2 + 0.9634x$
	$I = 3.1541 \times 10^{-5} - 0.03264x^2 - 3.9665 \times 10^{-6}x$
Buckled	$\delta = 77.847x^2 + 0.878x$
	$I = 3.15 \times 10^{-5} - 0.0912x^2 + 2.51 \times 10^{-5}x$

8.2.c   *Discussion*
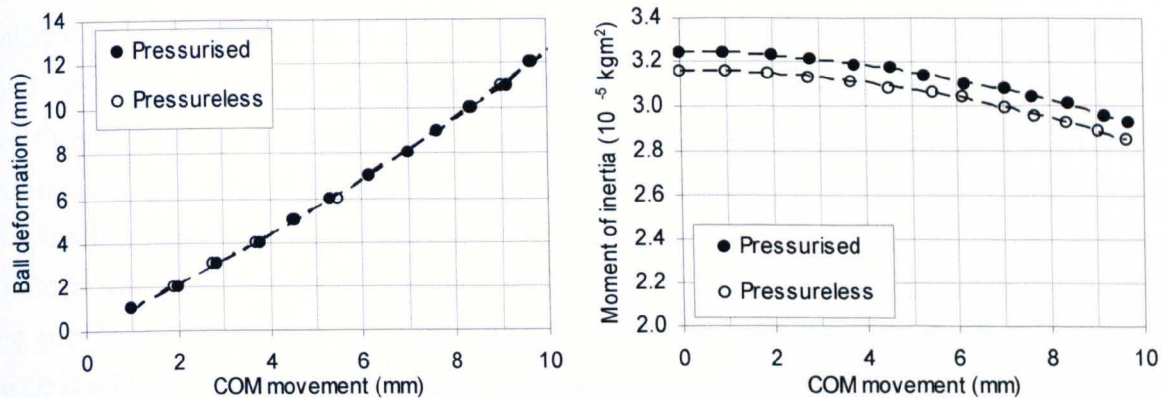
Figure 8.6 Comparing the deformation and centre of mass predictions for pressurised and pressureless ball types.

A comparison between the two ball types for just the truncated assumption is show in Figure 8.6. This demonstrates that the ball construction has no significant effect on the relationship between centre of mass displacement and external deformation, and therefore the same relationship could be used for all ball types – although this may not be the case if a different ball was used with a significant change in size or wall thickness.
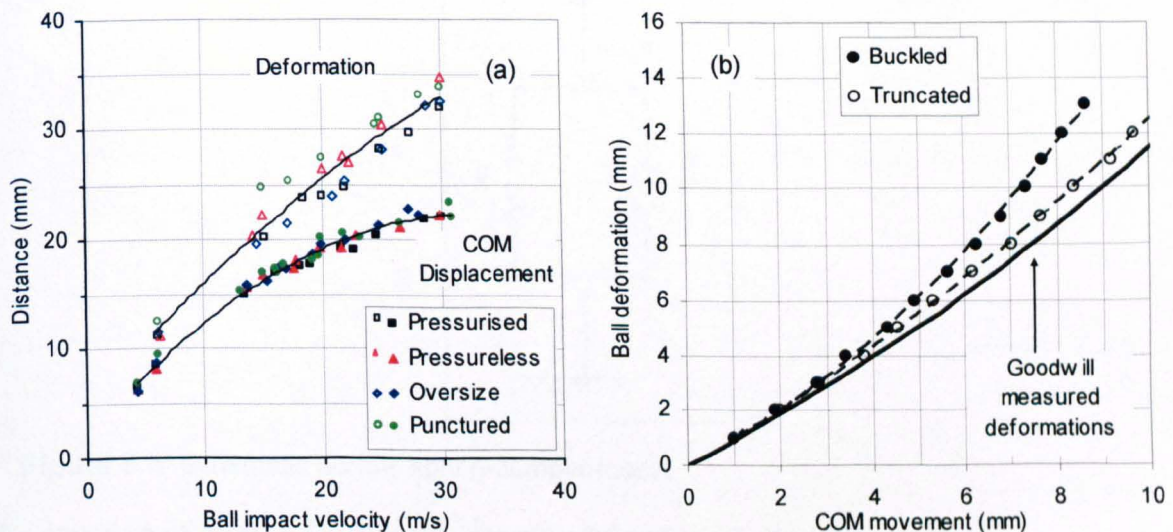
Figure 8.7 (a-b) (a) Measured ball deformation and integrated COM displacement (Goodwill, 2002), compared to (b) the predicted values.

Goodwill (2002) filmed normal impacts using high speed video. He measured the maximum ball deformation seen on the video, and used force plate data similar to Chapter 7 to calculate the maximum centre of mass displacement by integration. This data is shown in Figure 8.7 (a). The two trendlines shown (found for all ball types combined) were plotted against each other and shown with the data predicted here for centre of mass displacements in Figure 8.7 (b). There is very good agreement for the truncated

assumption, suggesting that this is a good relationship. It should be noted that the Goodwill curve shown is a small selection data which was mostly collected at a much higher impact velocity, and so the errors at the low velocities will be increased. More importantly, his data deals only in maximum values of measured deformation and COM displacement and are thus for a single instantaneous deformation shape – it will not necessarily be accurate throughout the course of an impact. The discrepancy between the predictions and Goodwill's measured values are a possible indication that the actual deformation shape is different from that assumed, although the fit is good. The frame rate used for the filming in the previous chapter was not high enough to monitor deformation shapes, although this issue is addressed while analysing the oblique impacts in Chapter 9.

8.3   One degree-of-freedom spring-damper model

8.3.a   Model overview

The simplest model and that which is considered first is shown in Figure 8.8. The ball is replaced by a point mass m, and has stiffness k and damping c. The deflection of the mass is x.
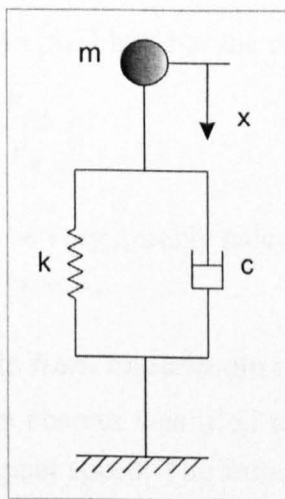
Figure 8.8 Schematic normal spring-damper model.

The equation of motion for this one degree-of-freedom system is

$$m\ddot{x} + c\dot{x} + kx = 0 \qquad [8.3]$$

Given the boundary condition of $x = 0$ at time $t = 0$, the solution to this equation is

$$x = ae^{-bt} \sin \omega t$$

Differentiating gives

$$\dot{x} = ae^{-bt} \left[\omega \cos \omega t - b \sin \omega t \right] \qquad [8.3]$$

and

$$\ddot{x} = ae^{-bt} \left[\left(b^2 - \omega^2 \right) \sin \omega t - 2b\omega \cos \omega t \right]$$

The boundary condition $x = 0$ at $t = T_C$ where T_c is the contact time gives $\omega = \dfrac{\pi}{T_C}$. Equating [8.3] to the incoming and outgoing velocities gives two more boundary conditions:

$$\dot{x}_{t=0} = V_{in} = a\omega$$

and $$\dot{x}_{t=T_C} = V_{out} = a\omega e^{-bT_C}$$

thus $$a = \frac{V_{in}}{\omega} = V_{in}\frac{T_C}{\pi}$$

and $$b = -\frac{1}{T_C}\ln\left(\frac{V_{out}}{a\omega}\right) = -\frac{1}{T_C}\ln\left(\frac{V_{out}}{V_{in}}\right)$$

Although the constants c and k are not necessary for the mathematical modelling, they are useful to give some physical understanding. As for an undamped model,

$$k = m\frac{\pi^2}{T_c^2}$$ [8.4]

Substituting both $\dot{x}$ and $\ddot{x}$ back into [8.3] leads to the expression

$$c = 2mb = -\frac{2m}{T_C}\ln\left(\frac{V_{out}}{V_{in}}\right)$$ [8.5]

Thus, the constants a, b and c can be very quickly calculated if the incoming and outgoing velocities and the contact time are known.

8.3.b   Finding model constants from experimental data

The data described in the previous chapter was used to investigate the model constants k and c, and how they vary with impact speed. The information needed to calculate k and c for each impact is simply the contact time and the COR. It is possible to estimate the contact time using high speed video but a filming rate of 10000 Hz would be necessary for a maximum possible 0.1 ms accuracy, and this still leaves the problem of visually interpreting the start and end of contact – it is extremely difficult to decide where contact begins even to within several frames. A much easier method is to use normal impact force data.

Normal impacts of a standard pressurised ball between 4 and 20 ms^{-1} were filmed using high-speed video. The contact times and speeds before and after impact were measured. This provided enough information to calculate k and c for each impact. The variation of these coefficients is shown in Figure 8.9, which suggests that both closely follow a linear relationship with impact speed. Also included is the statically measured stiffness. This was considered to be the stiffness at zero speed, and was measured using a quasi-static force-

deflection test. The initial loading tangent was used, and doubled since the ball centre of mass deflection would be half that measured by the loading rig (as discussed in Chapter 6).
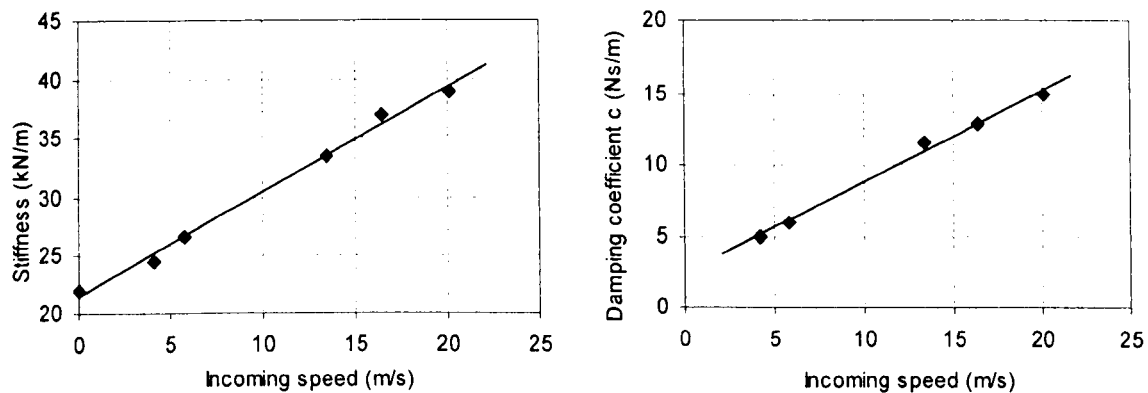
Figure 8.9 The variation of k and c for normal spring-damper model

The trendlines in Figure 8.9 can be used to give equations defining k and c as functions of impact speed, and are given below (in SI units so that damping is measured in N/m):

$$k = 21028 + 922 \ V_{in} \qquad\qquad\qquad [8.6]$$

$$c = 0.637 \ V_{in} + 2.41 \qquad\qquad\qquad [8.7]$$

8.3.c   *Model results*

The equations defining k and c were used to give appropriate spring and damper coefficients to model a drop test from 100 inches. With an assumed impact speed of 6.8 ms⁻¹, this gives $k = 27543 \, \text{N/m}$ and $c = 6.75 \, \text{Ns/m}$. Force, velocity and displacement graphs are shown in Figure 8.10. For this single degree of freedom model, the equations of motion have an exact analytical solution.
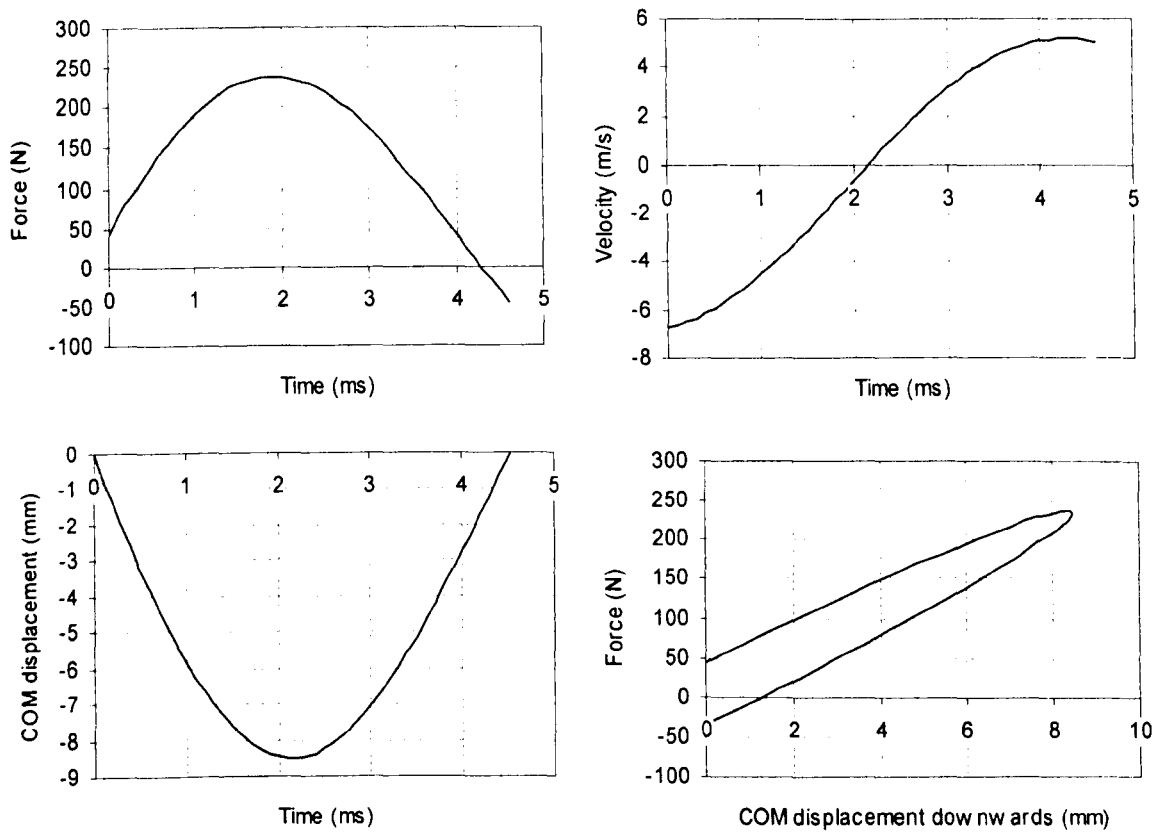
Figure 8.10 Model results for a single degree of freedom spring-damper model predicting an impact at 6.8 ms^{-1}

The model predictions are shown in Figure 8.10. It is immediately clear that there are two features which are physically unrealistic. The first of these is the initial starting force. At time $t = 0$, there is zero model compression and therefore no stiffness force, but there is also maximum velocity, which leads to a damping force which is instantaneous as the impact begins. The second is that the force becomes negative for the final 0.3 ms. This is again due to the damper, which produces a downwards force due to the upwards velocity at the end of contact. This is obviously unrealistic, as the ball cannot be subjected to a tensile force from the ground.

8.3.d Comparison with experimental data

In order to check the model, data from a pressurised ball drop-test was used (see previous chapter for experimental details). The model spring and damper coefficients were not taken directly from the data, but from the trendline equations in [8.6] and [8.7].
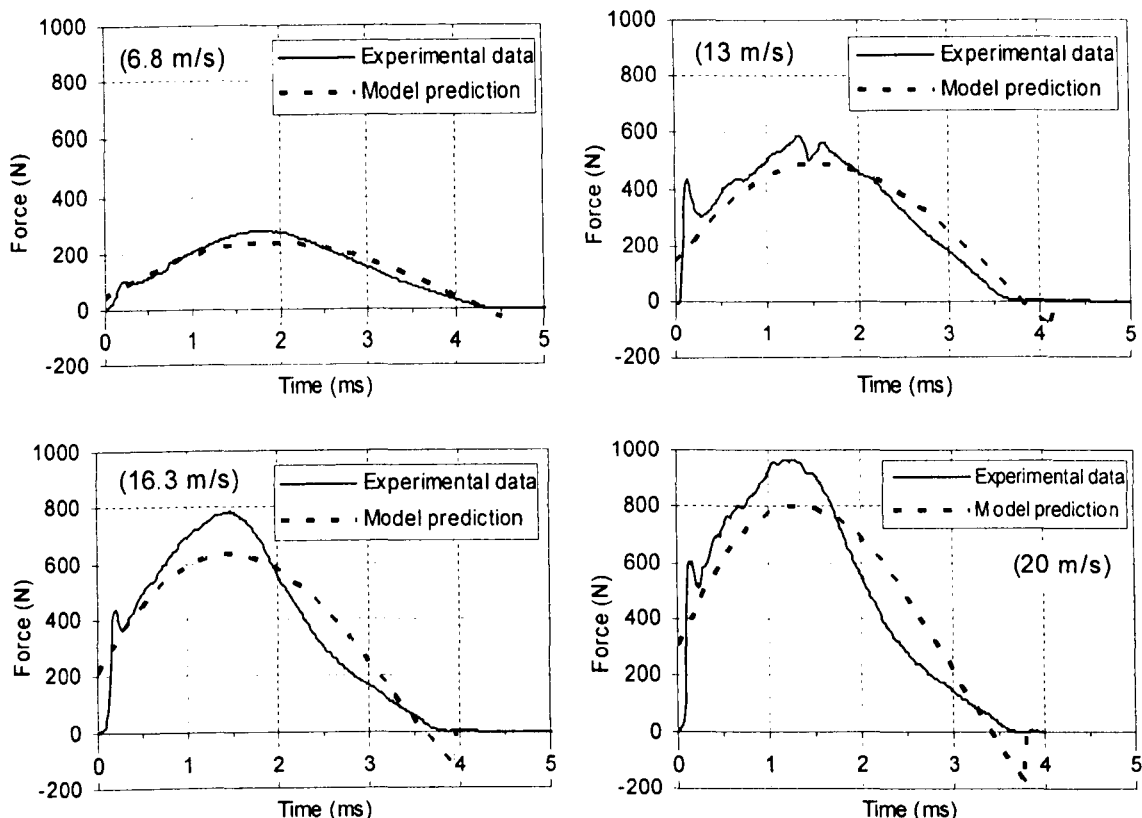
Figure 8.11 Comparison of model force-time predictions with experimental data at speeds between 6.8 and 20 ms⁻¹.

8.3.e   *Comparison of stiffness and damping for different ball types*

Data from the quasi-static data in Chapter 6 was used to find the "zero speed" stiffness for each ball type, and a combination of contact times and rebound speeds used to find the damping coefficients over a velocity range of 0 to 20 ms⁻¹. Figure 8.12 shows how the incoming speed affects the stiffness k and the damping c for (a) a pressureless ball, (b) a punctured ball, and (c) an oversize ball. Equations for the trendlines are shown in Table 8.3.

The data for all balls is shown in comparison in Figure 8.12 (d). It is interesting to consider the stiffness of the pressureless ball, remembering that it is an equivalent stiffness of the structure, taking into account both the rubber properties and the internal pressure. Statically it is the stiffest of all the balls because of the thicker rubber wall, but at an impact speed of 20 ms⁻¹ its stiffness is only slightly higher than that of the punctured ball. This suggests that at lower velocities when the deflections are small, the rubber shell is the most important factor. When the velocity is increased, the much larger ball deformation (and large reduction in volume) means that overall structural stiffness is dominated by the air pressure, to such an extent that the pressureless ball has a stiffness closer to the punctured ball than either of the pressurised ones. The punctured ball retains a surprisingly high stiffness, but has significantly higher damping than the other balls.

One feature worthy of note is that using the contact time gives a stiffness for the pressureless ball at 20 ms^{-1} which obviously does not follow the trend set by the other speeds (and in fact this data point was not used to find the trendline shown in Figure 8.12. This is caused by the late extra peak in the force, which extends the force-time curve later than would otherwise be the case. The same peak does not seem to affect the punctured ball stiffnesses, perhaps because it is evident at almost all impact speeds. Features of this nature mean that it would be impossible to extrapolate the data and predict the behaviour of the balls at higher velocities, as unknown irregularities in the force behaviour could change the behaviour significantly.

Table 8.3 Spring-damper model parameter equations for the four ball types.

Ball type	k (N/m)	c (Ns/m)
Pressurised	$k = 21028 + 922 \ V_{in}$	$c = 0.637 \ V_{in} + 2.41$
Pressureless	$k = 22289 + 542 \ V_{in}$	$c = 0.579 \ V_{in} + 3.12$
Oversized	$k = 17459 + 886 \ V_{in}$	$c = 0.543 \ V_{in} + 2.71$
Punctured	$k = 12483 + 988 \ V_{in}$	$c = 0.873 \ V_{in} + 1.19$
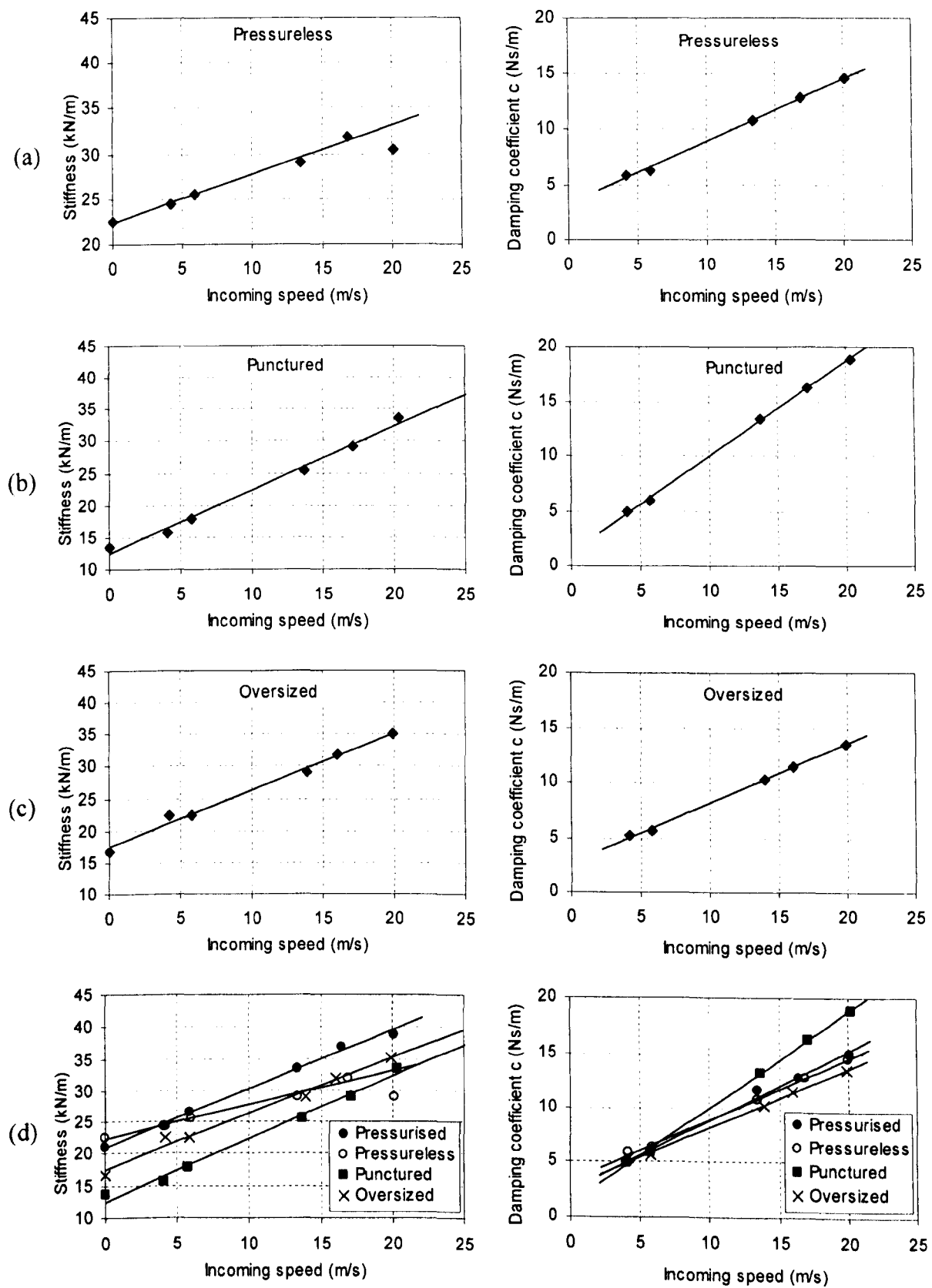
Figure 8.12 Variation of stiffness and damping with incoming speed for (a) pressureless, (b) punctured and (c) oversized balls, as well as (d) combined on a single graph together with pressurised data.

8.3.f   Model discussion

The Kelvin-Voigt model presented consists of a single spring and damper, whose values were constant for a particular impact but depended on the contact time of the impact and coefficient of restitution. Linear relationships were found between the spring and damper coefficients and the incoming velocity. It would seem dangerous however to extrapolate this linear regime to higher speeds, where the nature of the impact becomes more complicated – effects such as the initial shoulder in the force and the buckling of the shell are more significant.

It was found that pressureless balls have a similar stiffness to pressurised ones at low impact velocity, but significantly lower at high velocity. Punctured balls have the lowest stiffness at all velocities tested, but this was similar to the pressureless balls at the highest velocity tested. All the balls had similar damping coefficients at low velocity, but the punctured ball had significantly higher damping at high velocity than the pressurised and pressureless balls, which remained very similar at all speeds.

When forces and deformations during impact are considered, the model soon becomes inadequate. It is able to produce a high initial force at the start of the impact, but this is no more than a mathematical coincidence due to the peak incoming velocity producing a large damping force. This damper also produces a negative force at the end of the impact, which is another flaw in the model. A more significant problem is that all the model parameters are derived from experimental data which requires substantial (and complex) testing throughout the range of velocities at which the model could hope to be applied.

8.4 Impulsive force model

8.4.a   Model overview

It is clear that the model previously presented gives results which are superficially similar to actual ball impacts, but lacks the sophistication required to give accurate representations of reality. A different model was therefore created in an attempt to include all the important physical features.

The forces on the ball are listed below and each one will be discussed in detail. The deformation shape chosen was that of a truncated ball as discussed in section 8.2.

- Structural stiffness force

- Damping force

- Impulsive reaction force

8.4.b Structural stiffness force

Compression of the ball structure produces a structural force, whose properties depend on the rubber composition, its thickness and the internal pressure of the ball. Goodwill (2002) used a structural spring stiffness whose value k_B was a power law function of an initial stiffness $k_{B(0)}$ and ball COM deformation x raised to a power α:

$$k_B = k_{B(0)} + A_K x^\alpha \qquad\qquad [8.8]$$

The values Goodwill found for the constants are reproduced in Table 8.4 below for the four ball types. These values were found using a rather complicated iterative process involving contact times measured experimentally at a range of speeds up to 30 ms^{-1}.

Table 8.4 Spring stiffness parameters reproduced from Goodwill (2002).

Ball type	$k_{B(0)}$ (kN/m)	A_K (kN/m^2)	α
Pressurised	21	16000	1.65
Pressureless	23	12500	1.70
Oversized	21	3600	1.30
Punctured	16	60000	2.00

A slightly different method of calculating stiffness was adopted as one of the aims of this project was to create a model using as few experimental measurements as possible. The form of the equation used was chosen so that only one parameter needed to be found. Static stiffnesses at close to zero deflection were found in Chapter 6, and so the model stiffness should match these. The equation chosen was,

$$k = k_0 e^{Ax} \qquad\qquad [8.9]$$
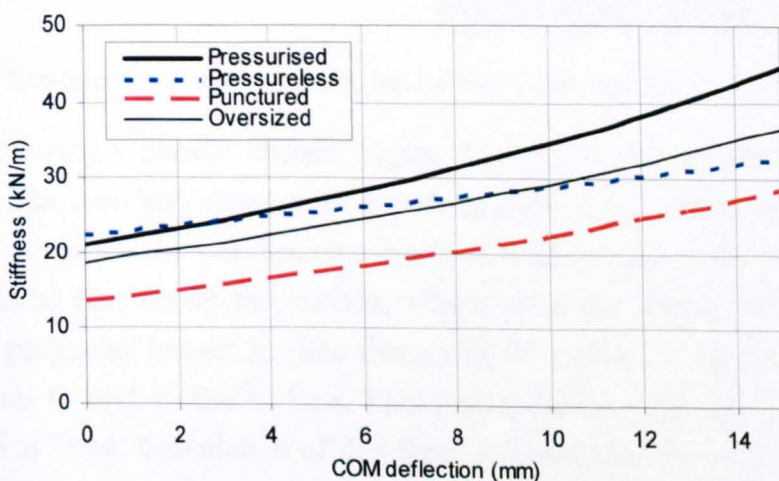
The value of k_0 was in each case the experimentally measured static stiffness at zero deflection, leaving just A to be determined. Initially A was chosen to match the static force-deflection curve as close as possible, but it was found that this gave a model which had too long a contact time and too low a peak force at all velocities – suggesting it was not stiff enough. Thus a higher value of A was found which matched the peak force and contact time for a single impact – that at 6.8 ms^{-1} for a 100 inch drop test.

Table 8.5 Spring stiffness parameters.

Ball type	k_0 (N/m)	A
Pressurised	21000	50
Pressureless	22500	25
Oversized	18700	45
Punctured	13600	50

Table 8.5 gives the values of k_0 and A that were found for the four ball types. The pressurised and pressureless balls have static stiffness values very close to those found by Goodwill, but both the oversized and punctured balls have a lower stiffness.

The model structural force given by the parameters in Table 8.5 are compared in Figure 8.13. It can be seen that at a low deflection, the pressurised and pressureless balls have a very similar stiffness, with the oversized ball also quite close. All four balls increase stiffness as the COM deflection increases – at values above 10 mm, the oversized ball becomes stiffer than the pressureless one. The pressureless ball stiffness seems to be approaching similar values to that of the punctured ball at high deflections.

Figure 8.13 Comparison of force-deflection data for model parameters of different ball types.

When used in the model, this structural stiffness was changed slightly to include the effect of the cloth. When a ball is bounced on a force plate, there is an initial period where the cloth compresses for very little force. This can be seen in the experimental data in Chapter 7, in the force-time plots as an initial very gentle rise in the force, and in the force-deflection plots as an initial compression before the force suddenly peaks. This was modelled by allowing an initial period of 0.2 ms where the stiffness was set to zero.

8.4.c   *Impulsive force*

The experimental data presented in Chapter 7 suggested that ball impacts produce a sharp initial rise in force which is strongly dependent on impact speed, but not on ball construction. The idea of an impulsive reaction force or "momentum flux" has been used by various authors. Percival (1976) used the idea of elements impacting on the surface to add an impulsive force to a model of a football. Hubbard and Stronge (2001) included a similar force in a model of a table-tennis ball impact. Goodwill (2002) used the idea of an impulsive force to create a model of a normal impact between a ball and a rigid surface which was then applied to the interaction with a racket stringbed, but the data used was rather empirical and difficult to relate to the physical situation.
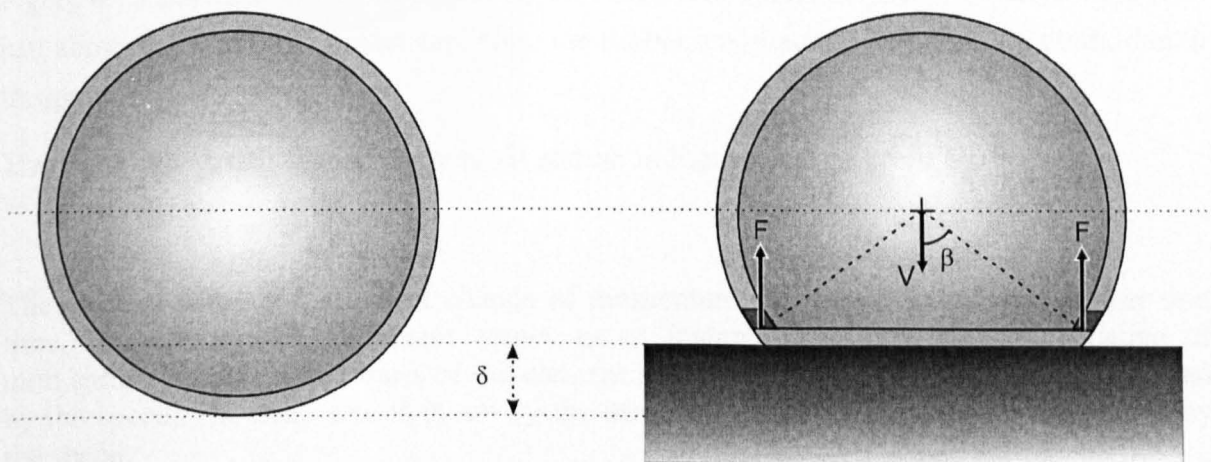
Figure 8.14 The geometry and forces caused by impulsive reaction on a truncated ball.

Consider a ball during a normal impact. Figure 8.14 (a) shows an undeformed ball, and Figure 8.14 (b) the assumed shape with a deformation y. At this point the ball can be considered as two parts – the flat disc or cap which is in contact with the surface, and the remaining spherical part above the surface, which is all moving down (all at the same speed). At this particular instant in time there will be a ring or annulus of cloth and of rubber that comes to rest on the surface. This instantaneous velocity change provides an impulsive reaction force. Calculation of this force is simplified by the assumption that the small elements of mass change from a downwards velocity to being at rest.
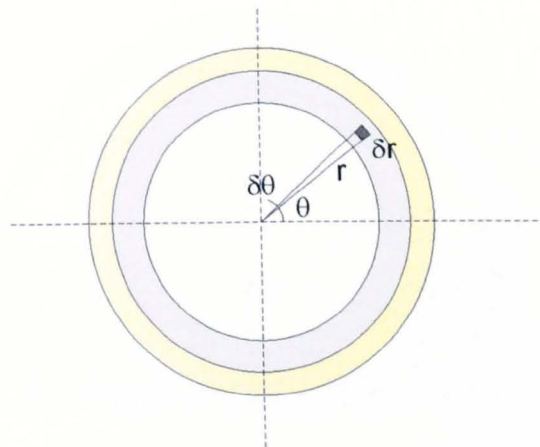
Figure 8.15 The geometry of the contact area cross-section, showing an integration element.

Figure 8.15 shows a horizontal cross-section of the rubber and cloth in the ball at a position just above the flattened contact cap. Note the rubber annulus is wider than the cloth, due to the geometry.

The area of the small shaded element δA shown in Figure 8.15 is given by:

$$\delta A = r\,\delta r\,\delta\theta$$

The force is equal to the rate of change of momentum, or change in momentum per unit time. Because the mass element comes to an instantaneous rest, this rate change of momentum is equal to the mass of the element hitting the surface per unit time multiplied by the speed. The mass rate is given by the area multiplied by the density, multiplied by the speed.

$$\delta F = \delta M V^2$$
$$= \rho \delta A V^2$$

$$F = \iint \rho V^2 r\,dr\,d\theta$$

This integral applies in turn for both the cloth and the rubber. If the inner and outer limits of radius are r_i and r_o, this gives:

$$F = \rho \int_{r_i}^{r_o} \int_0^{2\pi} r V_y^2 \, d\theta\,dr$$
$$= \rho \pi V_y^2 \left(r_o^2 - r_i^2 \right) \qquad\qquad [8.10]$$
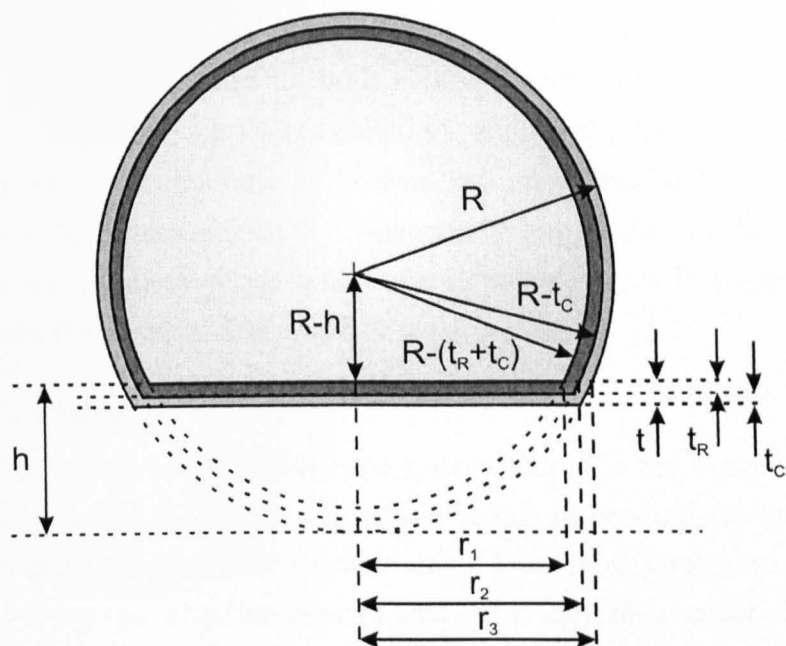
Figure 8.16 Calculating inner and outer radii for the contact areas during impact.

In order to calculate the integral limits r_i and r_o, consider the geometry shown in Figure 8.16, where the rubber and cloth layers have thickness t_R and t_C respectively. The contact plane used to calculate the radii is at a distance h above the undeformed base of the ball. The outer radius for the rubber contact area will be the same as the inner radius for the cloth contact area, r_2. The inner radius for the rubber contact area is r_1 and the outer radius for the cloth contact area r_3.

For small deflections, the cross-sectional contact area will be circular rather than annular. For h less than 3 mm, both r_1 and r_2 will be zero. Between 3 and 6 mm, r_1 will be zero. This larger circular area (created at higher incoming velocities) will lead to an initial peak in force as shown in all tennis ball impact measurements. Above 6 mm, the integral area will be of an annulus as shown in Figure 8.15. This leads to the term $\left(r_o^2 - r_i^2 \right)$ being constant (since cross-sectional areas of parallel slices of a spherical shell are constant), and the force simply being proportional to the square of velocity. The values for the three radii are shown in Table 8.6.

Table 8.6 Summary of the contact area radius equations.

Deflection	r_1	r_2	r_3
$0 < h < 3$ mm	0	0	
3 mm $< h < 6$ mm	0	$\sqrt{\left(R - t_C\right)^2 - \left(R - h\right)^2}$	$\sqrt{R^2 - \left(R - h\right)^2}$
$h > 6$ mm	$\sqrt{\left(R - t_R - t_C\right)^2 - \left(R - h\right)^2}$		

It is important to note that the velocity used is that of the ball shell rather than the centre of mass. This difference was noted by both Hubbard and Stronge (2001) and Goodwill (2002). The physical ball velocity was defined by multiplying the centre of mass velocity by a scale factor which was the ratio of the total ball mass divided by the mass of the ball above the surface. This does not have a particularly large effect on the impulsive force however, as during the early phase where the impulsive force is highest there is little difference between the physical and centre of mass velocities.

8.4.d   Damping force

The "damping force" represents viscoelastic energy losses in the rubber of the ball. The assumption was made that the energy lost would be due to bending around the edge of the contact area and compression of the circular area.. A damping coefficient c was therefore defined as being proportional to the contact area – but only the contact area of the rubber section, as there will be almost no energy loss in bending the cloth layer. If the area of material instantaneously coming into contact is an annulus of inner radius r_i and outer radius r_o as used to calculate the impulsive force, the average contact diameter d is given by

$$d = 2.\frac{(r_i + r_o)}{2} = r_i + r_o$$

Since the contact area is proportional to the square of the diameter, the damping coefficient was defined using a constant C_0 to give

$$F_D = C_0 \left(r_i + r_o \right)^2 V$$

This model parameter could not be measured directly from the ball, and therefore a value of COR had to be used to calculate it. Again the 100 inch drop test was used, and a damping coefficient chosen to match a rebound value for each ball type.

Goodwill (2002) found a similar relationship relating contact diameter d_{CONT} to ball deformation δ_{BALL} using high speed video, which is reproduced in [8.11]. This relationship was valid only for the compression phase of the impact, as there was too much scatter in the data for the rebound phase. A significant factor in this is the high impact speeds used by Goodwill – up to 30 ms^{-1}. These speeds will cause much more irregular deformation shapes, exaggerating both the oscillations and late force peak shown in the force data in Chapter 7.

$$d_{CONT} = -1.66 \times 10^{-5} \delta_{BALL}{}^4 + 1.27 \times 10^4 \delta_{BALL}{}^3 - 4.13 \times 10^2 \delta_{BALL}{}^2 + 7.6 \delta_{BALL}$$

$$[8.11]$$

This gives the diameter of the contact area between the ball and surface, but not necessarily of the diameter of the disc or annulus where the bending causing damping is actually taking place. A comparison of the contact diameter calculated using this equation and compared to that used in the model is shown in Figure 8.17, demonstrating a very close relationship. The model data here is for an impact at 20 ms^{-1}.
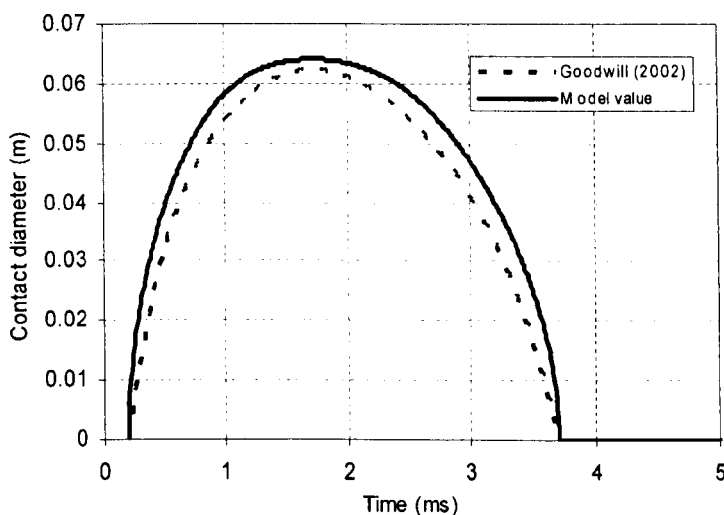
Figure 8.17 Contact diameter used for the damping force, as used in the model and compared to the experimental values of Goodwill (2002).

The values found for the parameter C_0 are shown in Table 8.7. The results are difficult to interpret in isolation; what seems important is the relationship between stiffness and damping – for example, the oversized ball has the lowest damping coefficient but also lower stiffness than the pressurised ball, which combine to give the same COR.

Table 8.7 Model damping parameters for the various ball types.

Ball type	C_0 (Ns/m^3)
Pressurised	4000
Pressureless	3800
Oversized	3500
Punctured	4500

8.4.e *Solving the model*
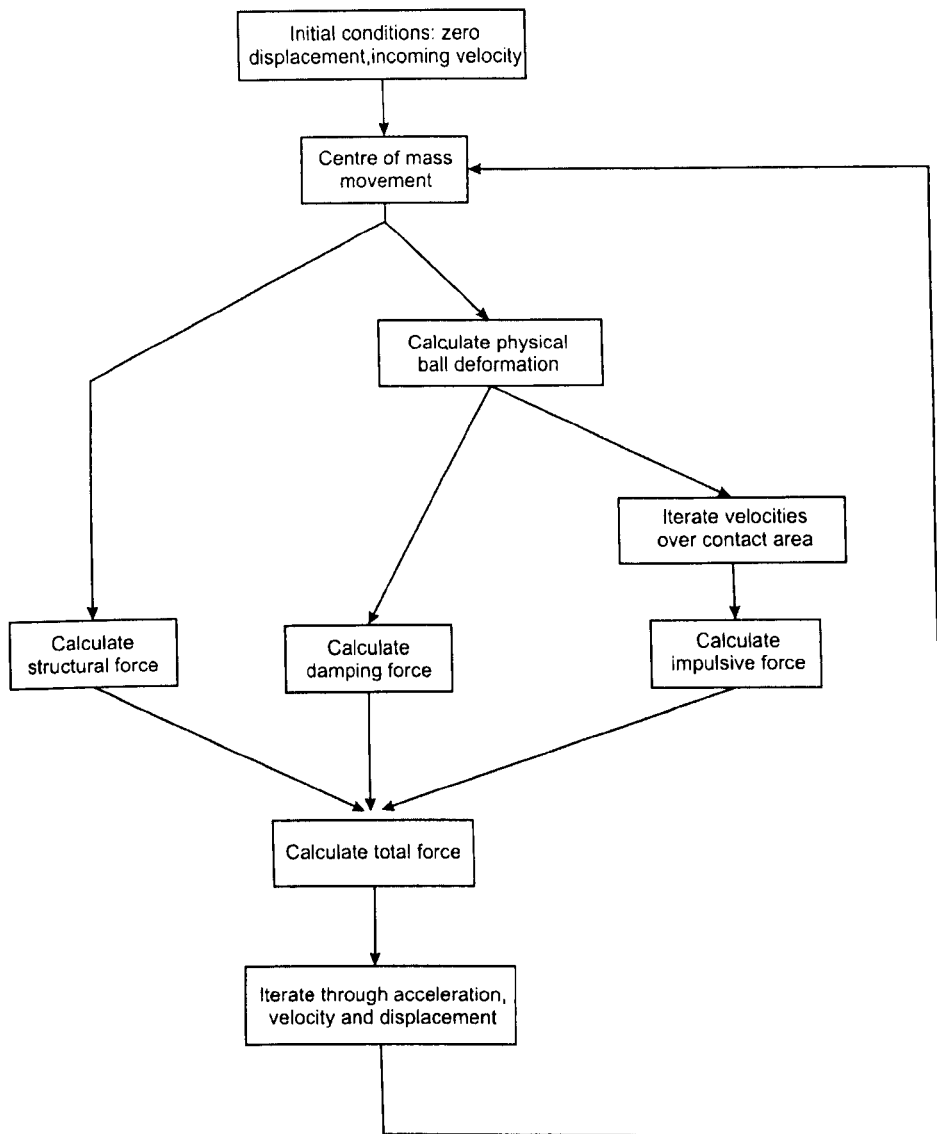
Figure 8.18 Flowchart of the model iteration process.

The model solving process is summarised in a flowchart in Figure 8.18. A spreadsheet was used to progress the model in an iterative way, using formulae of the form $x_{n+1} = x_n + v_n \delta t$. Amongst the initial parameters were the total mass of the ball and the amount of this made up by rubber and cloth – to calculate the density of each as used in the impulsive force component as well as various geometry calculations such as the mass of the ball still moving towards the surface. Boundary conditions such as initial displacement of zero and initial centre of mass velocity being that of ball impact speed were also used, but the only other parameters needed were the coefficients for the various force equations.

The structural force could be calculated directly from the centre of mass displacement x, but the other two force components needed this displacement to be converted to a physical

ball deformation as they were calculated using the ball geometry. These three forces, the variables used to calculate them and the defining functions are summarised in Table 8.8. The forces were then combined and the model advanced by a timestep δt.

Table 8.8 Summary of model force components.

Force component	Governing variables	Defining function	Parameters needed
Structural stiffness	Centre of mass displacement x	$k = k_0 e^{Ax}$ $F_S = k_B x$	k_0, and A
Impulsive reaction	Physical ball deformation	$F = \rho \int_{r_i}^{r_o} \int_0^{2\pi} rV_y^2 \, d\theta dr$ $= \rho\pi V_y^2 \left(r_o^2 - r_i^2 \right)$	Cloth and rubber density ρ
Damping	Physical ball deformation	$F_D = C_0 \left(r_i + r_o \right)^2 V$	C_0

8.4.f   Model results
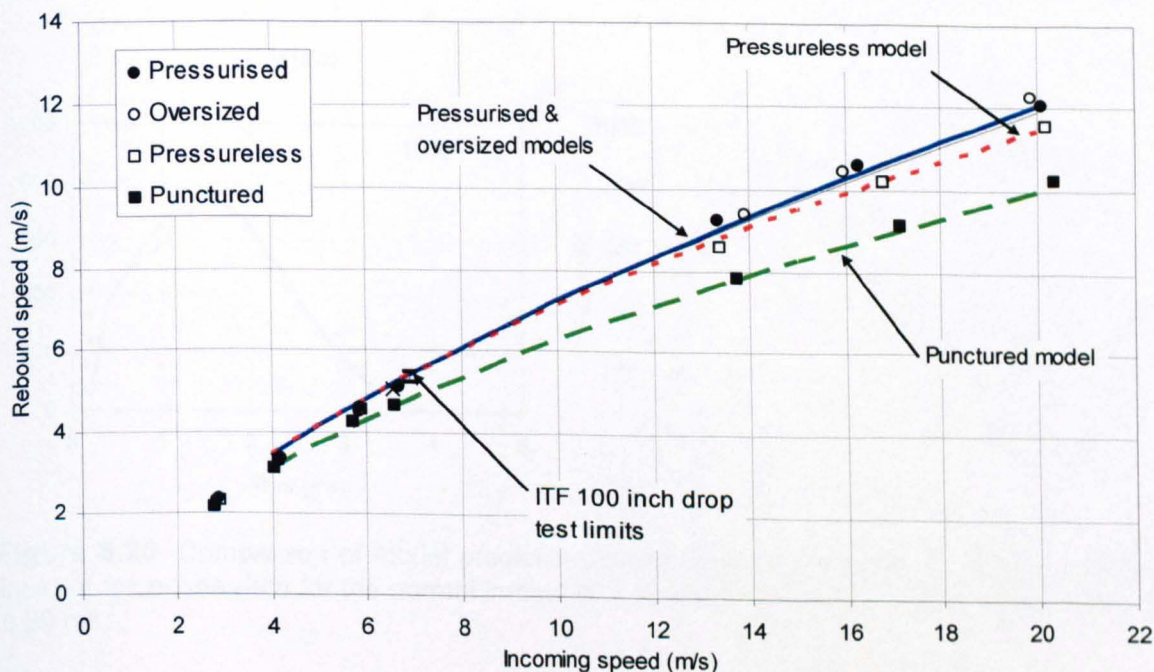
Figure 8.19 Experimental and model predicted rebound velocities.

The model was used to calculate predictions for rebound speed for various ball types, and the results are shown in Figure 8.19. The match between experimental and model data is extremely good, and clearly differentiates between the different ball constructions. The

pressurised and oversized model data are shown as separate lines, but they cannot be distinguished.

Force data for a pressurised ball is show in Figure 8.20 below, for speeds between 5.8 and 20 ms^{-1}. The initial peak force is predicted well by the impulsive force portion of the model. One difference between the experimental data and model predictions is the drop in stiffness immediately after the initial peak, which may be caused by buckling of the ball. This effect is seen to a greater extent as the impact speed increases.

Model and experimental forces are also shown for punctured, pressureless and oversized balls in Figure 8.21, Figure 8.22 and Figure 8.23 respectively. Again the force matches up well although it fails to predict the late second peak seen to some degree with the pressureless ball and particularly with the punctured ball (and thought to be due to buckling caused by the lack of internal pressure in these two ball types).
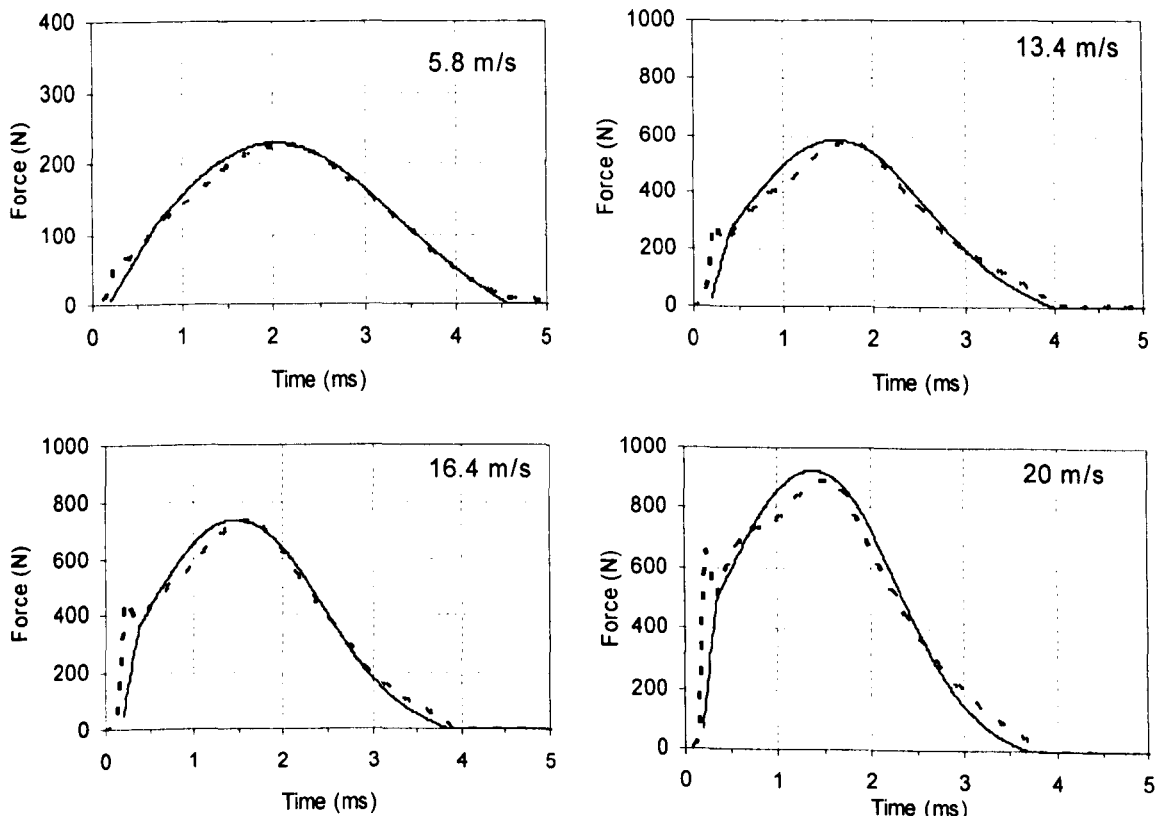
Figure 8.20 Comparison of model predictions (solid lines) and experimental values (dashed lines) of force-time data for the normal impact of a pressurised ball at various speeds from 5.8 to 20 ms^{-1}.
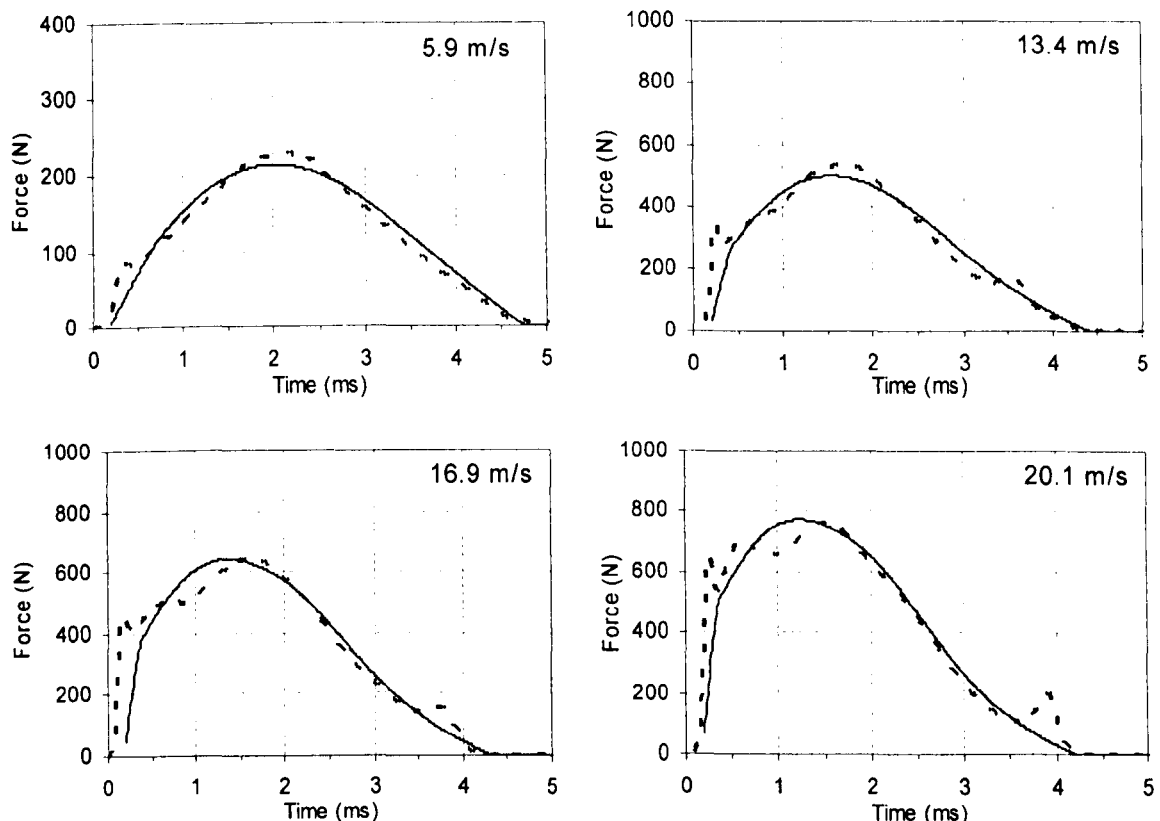
Figure 8.21 Comparison of model predictions and experimental values of force-time data for the normal impact of a pressureless ball at various speeds from 5.9 to 20.1 ms^{-1}.
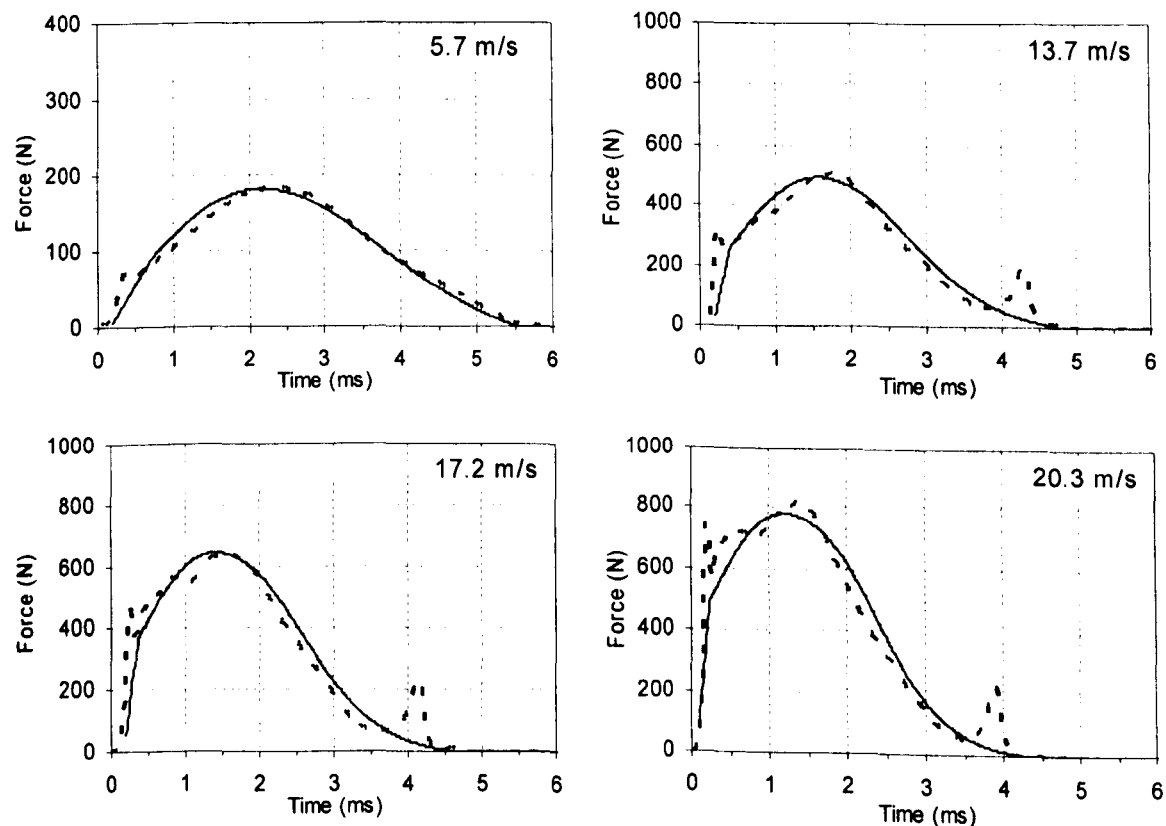
Figure 8.22 Comparison of model predictions and experimental values of force-time data for the normal impact of a punctured ball at various speeds from 5.7 to 20.3 ms^{-1}.
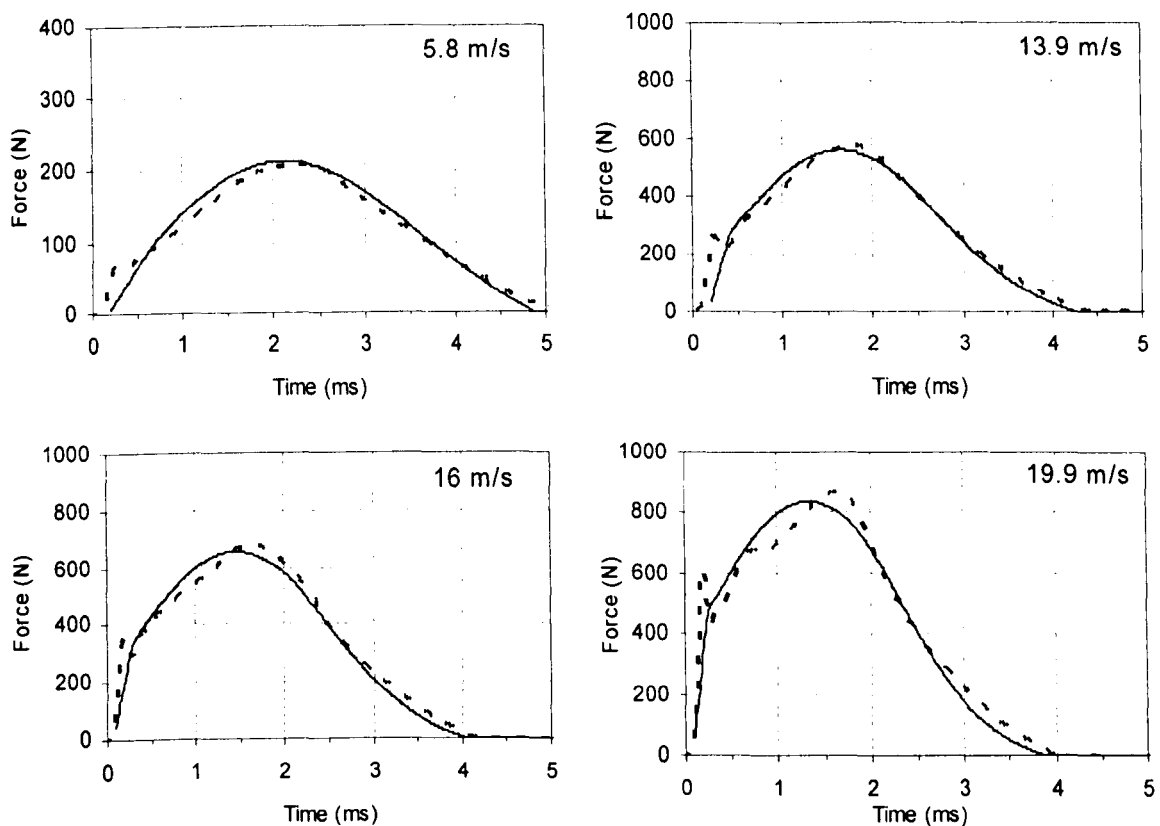
Figure 8.23 Comparison of model predictions and experimental values of force-time data for the normal impact of a oversized ball at various speeds from 5.8 to 19.9 ms^{-1}.

8.5   Discussion

The second model presented is a far superior representation of a tennis ball impact. Not only does it give a much more accurate depiction of the forces on the ball, it does so in a way which attempts to recognise and predict the various physical processes involved. The forms of the various equations used in the model were carefully chosen to be as "real" as possible, rather than abstract coefficients (which are often found by circular use of the data to be predicted). The only experimental data used to find the model parameters was static properties and force data from a single dynamic impact at fairly low speed (6.8 ms^{-1} from a 100 inch drop test). It must be recognised that if a radically different design of ball was introduced whose behaviour changed unpredictably compared to the various current balls, it is possible that this model might not model the various forces adequately to be accurate over a range of velocities. For example, a single value at 6.8 ms^{-1} is used to find the damping, and so a ball made from (for example) a different material may not obey the same damping laws at different speeds.
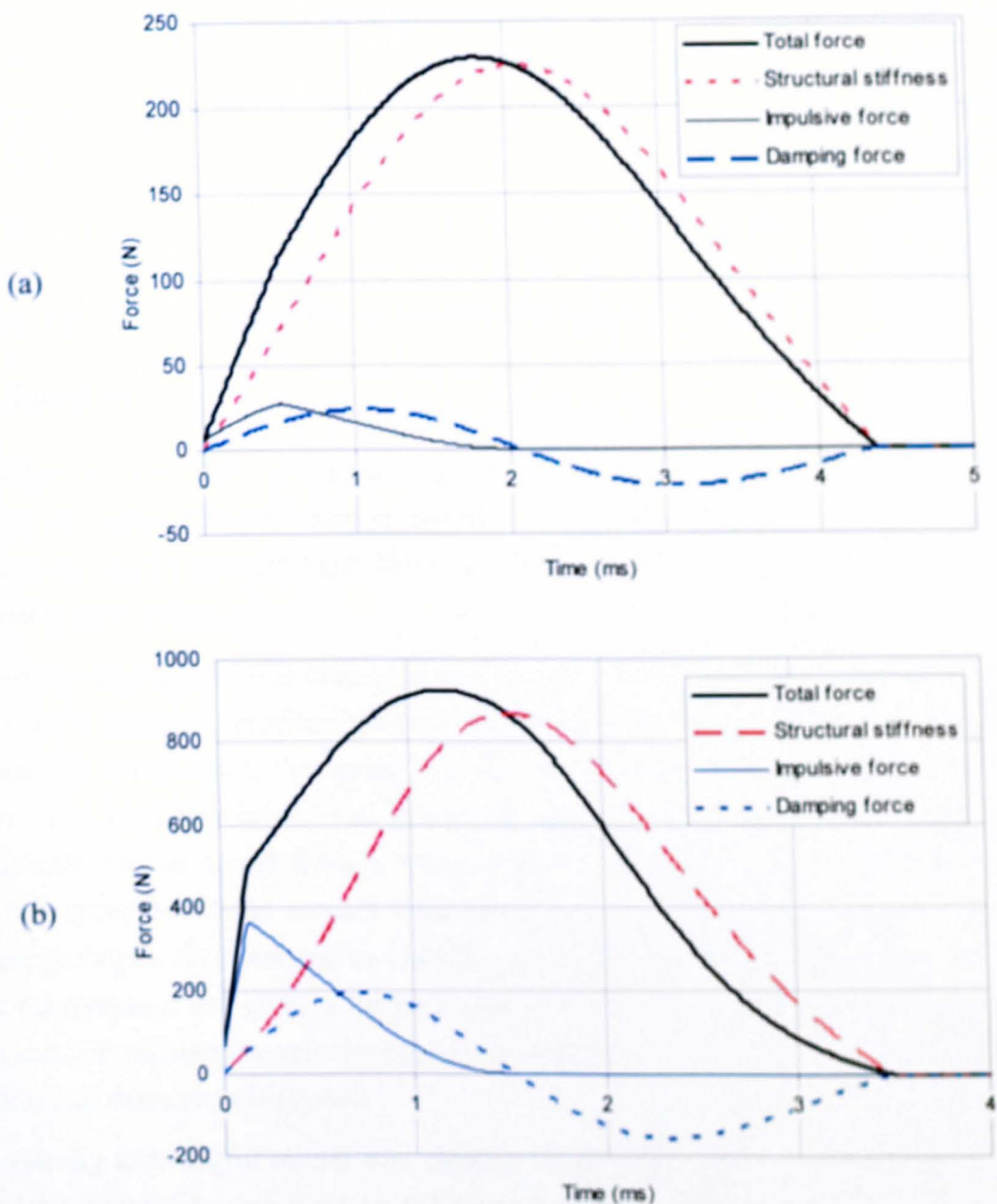
Figure 8.24 Various force components for a normal impact model of a pressurised ball at (a) 5.8 ms^{-1} and (b) 20 ms^{-1}.

The three different mechanisms contributing to the total force are shown in Figure 8.24, which plots the forces for a pressurised ball impacting at 5.8 and 20 ms^{-1}. At the lower speed the impact is dominated by the structural stiffness. The impulsive force has little effect on the qualitative look of the overall curve, and the damping is also a fairly minor effect.

When the speed is increased, the structural and damping forces are still reasonably symmetrical, but the impulsive force produces the early rise in force which gives the total force curve its distinctive shape. This is highest during the first part of the impact as the cross-section coming to rest has the widest area towards the bottom of the spherical shell,

as well as the velocity change being at its highest. As the "momentum flux" decreases, the force reduces and reach zero at the point where the centre of mass downwards velocity becomes zero. As the centre of mass moves back upwards, there can be no more impulsive force as the mass elements are leaving the surface and cannot impart a tensile force.

Goodwill (2002) produced a similar initial force peak by introducing an artificially increased stiffness during the first part of the impact. This method has the obvious disadvantage that it is impossible to measure this increased stiffness experimentally.

8.6 Summary

A method is described for calculating the centre of mass displacement and changed moment of inertia of a deformed tennis ball. These variables were calculated for the two deformation shapes thought most likely, and best fit polynomials used to derive functions estimating their values.

A spring-damper model was created whose input conditions could be measured in a simple way. Over a range of velocities which is more than adequate for the normal component of any realistic tennis shot, the spring and damper coefficients k and c both follow linear trends. The mathematics of the governing equations of the model mean that these coefficients can be found from a rebound test where the COR (i.e. the incoming and outgoing speeds) and the contact time are measured. Thus a minimum of two tests is needed, perhaps a drop test and an impact at the highest speed expected to be of interest. A static compression test gives a further value of stiffness equivalent to zero impact speed. More tests throughout the velocity range will obviously improve the quality of the fit of the stiffness and damping with speed.

A physically meaningful model was created which was based on measurable parameters. Quasi-static test data was used to define the structural stiffness of a ball as well as the energy loss due to hysteresis unloading. A truncated deformation hypothesis enabled calculation of the centre of mass position and the moment of inertia (although this is not needed for a normal model). This also led to relationships defining the change in internal pressure of the ball and therefore the pressure force during an impact. The final force on the ball was the damping force, which was based on the contact area to simulate the energy lost in bending of the rubber shell wall. A summary of the model parameters for the various ball types is given in Table 8.9 below.

Table 8.9 Model parameters for the various ball types.

Ball type	k_0 (N/m)	A (m^{-1})	C_0 (Ns/m^3)
Pressurised	21000	50	4000
Pressureless	22500	25	3800
Oversized	18700	45	3500
Punctured	13600	50	4500

9 Oblique impact tests

9.1 Introduction

The previous chapter provided a normal impact model which satisfied a number of requirements, and suggested that the normal behaviour of a tennis ball could be predicted. The aim of the work described in this chapter was therefore to examine the experimental characteristics of oblique impacts on a rigid surface. This would not only provide data to verify any oblique impact models created, but would also give insight into the physics of how a ball bounces.

For a given tennis ball, there are three fundamental properties which define its motion at a particular instant: the speed and the angle (which could be grouped as the velocity) and the spin. The first set of experiments was performed to find and understand the effect of each property. One of the speed, angle and spin was varied in turn whilst keeping the other two constant. One of the main aims was to see if there was a noticeable difference between slipping and rolling impacts.

Two further sets of experiments were then performed to understand the effects of ball construction and court friction. Two alternative ball types (punctured pressurised and pressureless) were used together with surfaces of extreme friction (the slowest acrylic available, and a highly polished wooden surface).

Finally, the effect of incoming angle on ball deformation was investigated by firing balls to impact with the same vertical velocity component, but different angles (and therefore different absolute speeds).

9.2   Experimental setup

9.2.a   *General setup*
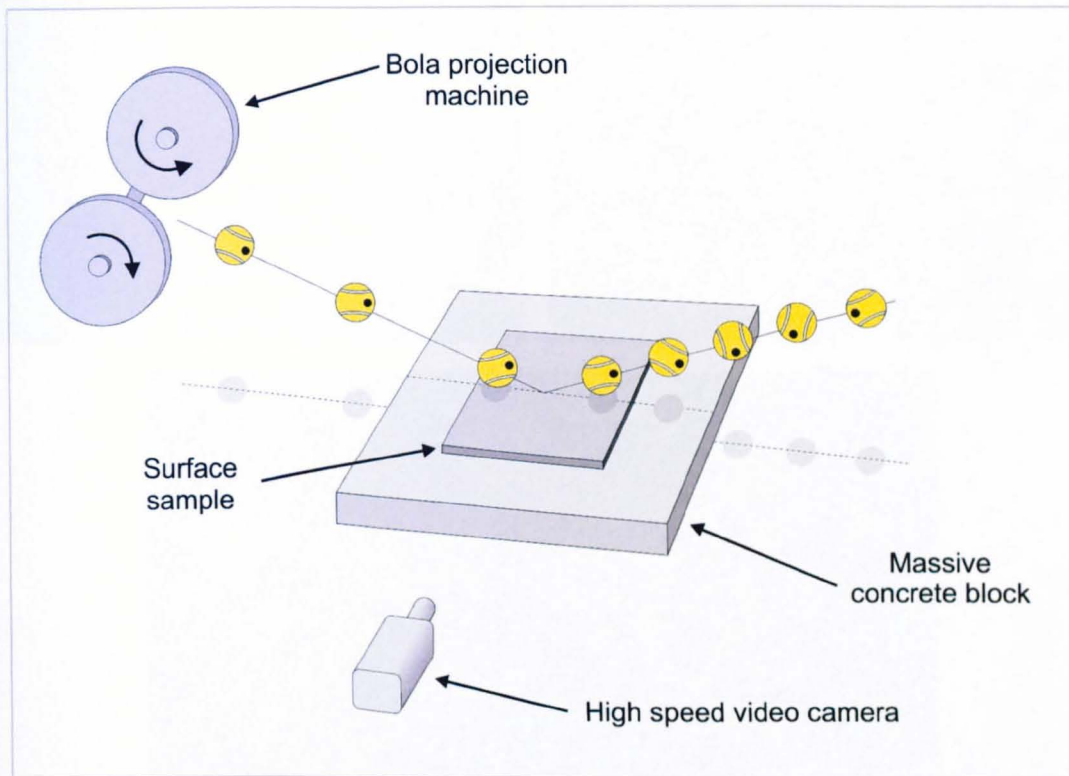
Figure 9.1 Experimental set-up for high speed filming of oblique impacts.

The equipment used is shown in Figure 9.1. In each set of tests, three standard pressurised balls were used after pre-compression, for one impact per ball under each of the conditions. The surface was firmly fixed to a large concrete block to allow no possibility of deformation and subsequent energy loss.

In all cases except for the final set of tests, the balls were projected using a Bola machine consisting of two spinning wheels as for the previous experimental work on normal impacts. The wheels were orientated in the vertical plane and could be independently controlled, so a difference in their speed provided either topspin or backspin as required. A high speed video camera (running at 240 to 400 frames per second for most tests, and 7000 frames per second for others) was used to film the impacts, and the results analysed using an in-house piece of software.

Figure 9.2 The three surfaces used for the oblique testing: (a) slow acrylic surface (with sand included in the paint), (b) medium acrylic surface and (c) fast wooden surface.

The various parameters are summarised below in Table 9.1. For the first set of tests, the same ball type and surface was used throughout. Each of the spin, speed and angle was varied in turn while keeping the other two properties constant. For the second set of tests, two different surfaces were chosen to give as wide a range of friction as possible. These were a deliberately high-friction acrylic surface, and a highly polished smooth wooden board to give low friction – shown in Figure 9.2 (a) and (c) respectively. The acrylic was made by painting directly onto a Perspex sheet, and mixing quantities of sand into the acrylic paint.

The range of all three impact variables was deliberately chosen to encompass and extend the range produce by players. This would ensure that the different physical situations such as slipping and rolling would be reproduced, and their effects hopefully exaggerated.

Literature previously mentioned suggests that players usually hit the ball with an *average* spin of 100 to 200 rads^{-1}, suggesting that some shots will contain significantly higher spin rates. The decision was made to use the maximum possible range of spins provided by the Bola, which can provide up to around 600 rads^{-1} of either topspin or backspin.

Realistic speed and angle values were more difficult to achieve. Experimental practicalities made it impossible to achieve the shallow angles required to match those seen in a match.

Rather than project the ball more slowly to give a low vertical velocity, the decision was made to keep the speed high to give realistic deformation shapes.

The third set of tests involved different ball constructions. Commercial pressureless balls were chosen as an off-the-shelf type. Standard pressurised balls (as previously used) were punctured with a fine needle, so that the ball still retained a fixed pressure of one atmosphere.

Table 9.1 Summary of the various parameters for oblique impact tests. The parameter of interest in each test is shaded.

	Surface	Ball type	V_{in} (m/s)	θ_{in} (degrees to horiz)	ω_{in} (rads^{-1})
Varying spin, speed & angle	Medium	Pressurised	30	24	-600 to 600
			25 to 60	24	0
			30	24 to 52	0
Changing surface	Fast ($\mu = 0.3$)	Pressurised	30	24	-600 to 600
	Medium ($\mu = 0.55$)				
	Slow ($\mu = 0.61$)				
Changing ball type	Medium	Pressurised	30	24	-600 to 600
		Pressureless			
		Punctured			

9.2.b   *Ball markings*
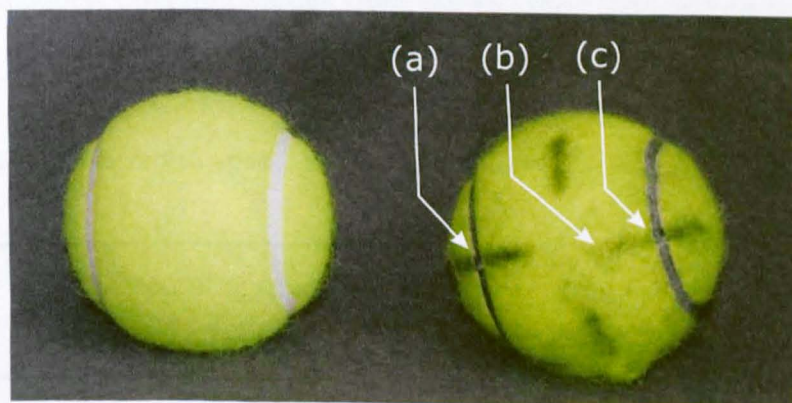
Figure 9.3 A new unmarked ball (left) and one after a series of impact tests (right). The markings can still be seen, but the wear on the ball is apparent.

The balls were marked with black ink so that the relative angular position of the ball in each frame could be determined. A line was drawn around the seam and regular marks drawn on the felt to intersect. As well as increasing the visibility, having most of the

marking located on the indented seam minimised any chance of the ink affecting the frictional properties of the ball, however small these would be. Markings on the cloth itself were seen to wear off much faster than those on the seam. The ball shown in Figure 9.3 shows how the markings have worn off somewhat after a series of impacts. The markings on the right-hand side of the ball as pictured clearly do not show the same level of contrast as those on the left-hand side. The two intersections marked (a) and (c) could still be used, but (b) has become too faint to be seen accurately without re-marking – this point would not be chosen during analysis. Figure 9.3 also shows how the cloth is quickly affected by a relatively small number of impacts. It was found from experimentation that the cloth wear was caused by the friction with the Bola wheels rather than interaction with the surface, but there is no way to impart spin on the ball without producing such wear.

9.2.c   240/400 fps filming

When changing the spin, speed and angle for the first set of tests, the discrete positions achievable in each range gave a total of 39, 21 and 18 impacts respectively. The surface used was a non-cushioned acrylic sample which was firmly fixed to a massive concrete slab. This sample was chosen to give a realistic tennis surface but one which could be considered rigid, to prevent surface deformation. If deformation did occur, its extent and therefore its effect on the impact would change with speed and angle, making it harder to interpret the results. An independent Surface Pace Rating (defined as $100\left(1 - \dfrac{\Delta V_x}{\Delta V_y}\right)$ by the ITF as discussed in Chapter 3) test on a sample of the same acrylic material gave a value of 45, which according to simple rigid body theory is equivalent to a frictional value of $\mu = 0.55$. This is the highest value in the suggested range for the ITF "Medium/Medium-Fast" surface category, covering values from 30-45. The "Fast" category is suggested as values from 40 upwards. This overlap means that this particular surface could be placed in either category.

Table 9.2 Nominal incoming speed, angle and spin values for the three parts of the first set of experiments.

	Incoming speed V_{in} (ms^{-1})	Incoming angle θ_{in} (degrees to horiz.)	Incoming spin ω_{in} (rads^{-1})
Varying spin	30	24	-600 to 600
Varying speed	25 to 60	24	0
Varying angle	30	24 to 52	0

Table 9.2 shows the intended values for incoming speed, angle and spin for the different experiments. In practice the two "static" variables could not be kept totally constant, and their variations and the effect this had on the results is discussed in each section.
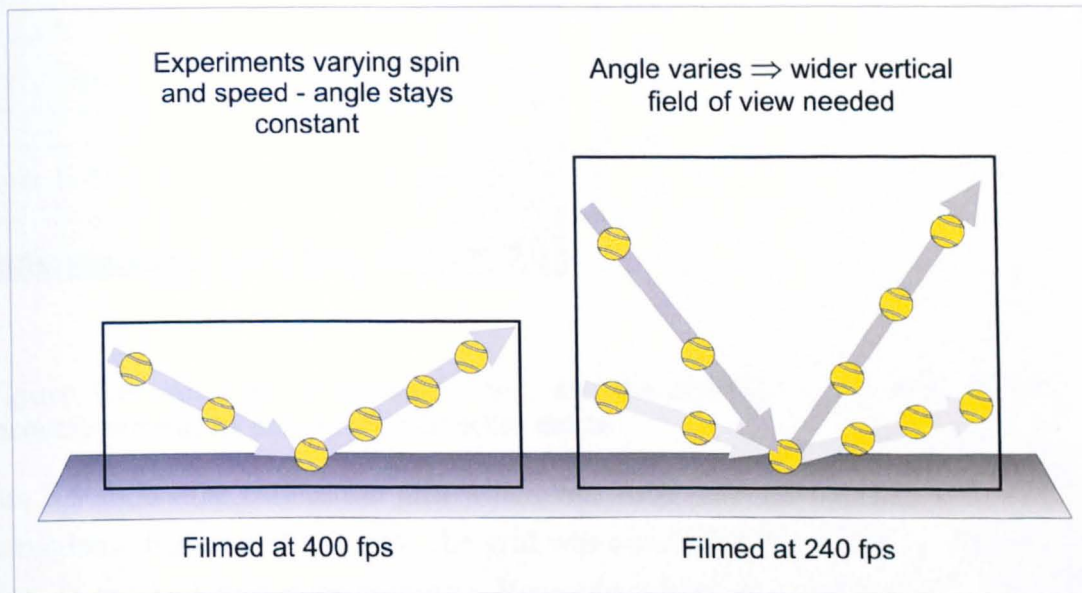
Figure 9.4 Different frame aspect ratios needed for different impact angles.

The impacts were filmed using a Kodak Motioncorder high speed video system running at 400 frames per second for the changing spin and changing speed experiments, and 240 frames per second for the changing angle experiment. This difference was because the higher angles used in the latter experiment meant a much wider vertical field of view was needed, and the design of the camera meant that it could then capture at a lower maximum frame rate (see Figure 9.4). Impacts where the ball did not land close to the centre of the video frame were immediately rejected and repeated in order to keep the angle as accurate as possible, although once the Bola had been set up for each set of impacts it was very consistent.

9.2.d   *7000 fps filming*

The remaining tests were performed using a Phantom v4 camera (which was not available for all the testing) at 7000 frames per second. This meant it was possible to measure the deformation over a large number of frames (typically 30-35) during an impact, and see the deformation shapes.

9.3   Experimental analysis
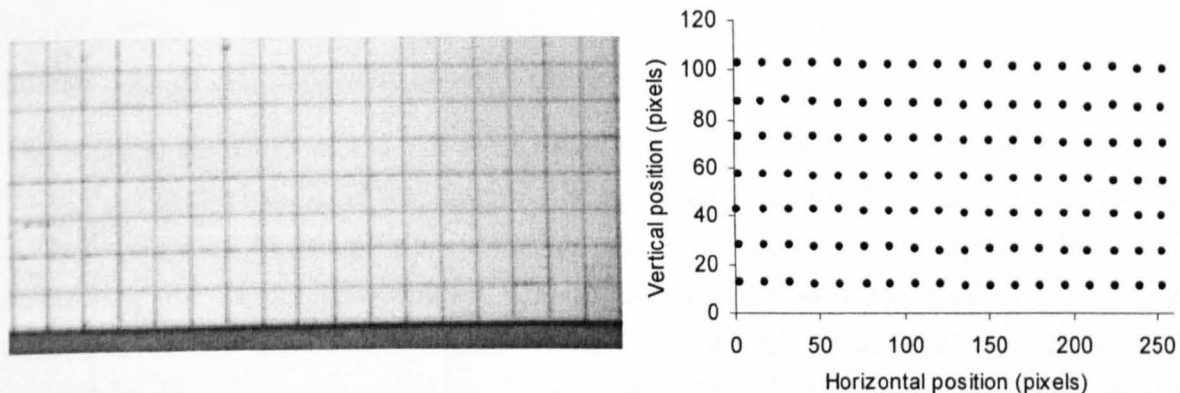
Figure 9.5 An example calibration grid, with the positional coordinate data after being manually sampled by clicking on intersection points.

Figure 9.5 shows the calibration grid which was used – in this case for the different ball constructions (filmed at 7000 fps). The grid was carefully placed in line with the plane of motion of the ball to ensure accuracy. Repeated testing ensured that the ball remained extremely close to this plane. Points marked at the intersection of the gridlines were used to convert positional data measured in pixels on the computer to displacement in millimetres. This also compensated for any angular rotation of the camera, which can be seen here in the gradient of the lines (again the raw positional data as shown is measured downwards from the top of the image, which is why the skew in the grid points seems to be the opposite direction to the video frame). As long a focal length lens as possible was used to put a reasonable distance between the camera and impact position, which virtually eliminated lens distortion effects. This is apparent in Figure 9.5, which shows no noticeable pincushion or barrel distortion. To verify this, pixel-to-physical calibration ratios were calculated for each row and column of points in turn. For the columns, this gave 18 calibration values, with a standard deviation of less than 0.3% of the average, and all values within 0.52% of the average. For the rows, this gave 7 values, with a standard deviation of 0.13% of the average, and all values within 0.24% of the average.
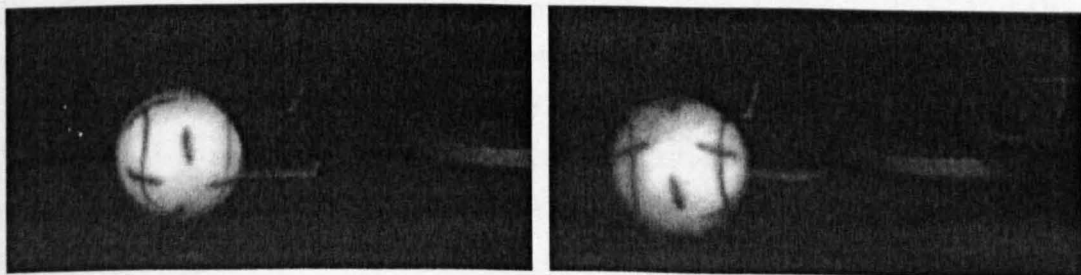
Figure 9.6 Two sample frames from oblique impacts filmed at 7000 fps, for (a) the first impact, and (b) the last impact of a specific ball, showing the wear effects on the markers used to measure speeds and spins.

Two example frames from the video footage for the first and last impact of one of the balls are shown in Figure 9.6. The effect of cloth wear on the markings can clearly be seen as a blurring effect, but it is also apparent that good accuracy could be maintained if "sharp" intersections of markings were chosen - i.e. points (a) or (c) in Figure 9.3 rather than (b).

The position and angle of the ball were found in the analysis software by fitting a circle to the outline of the ball. This was found to be more accurate and consistent than alternative methods such as clicking three points on the ball circumference and mathematically calculating the centre co-ordinates. Unless the lighting is very good (and extremely consistent across the whole field of view), it is difficult to always mark these points accurately. The circle was resized to fit the size of the ball, and meant that it was possible to get good positional data in situations where the lighting was not perfect. The angular position was then found by clicking a particular point, usually the intersection of the markings drawn on the ball. This point was chosen to be at as high a radius as possible looking at the two-dimensional picture, so as to minimise angular error. The images could also be used to verify by eye that there was only spin about a single axis, i.e. purely topspin or backspin with no element of sidespin.
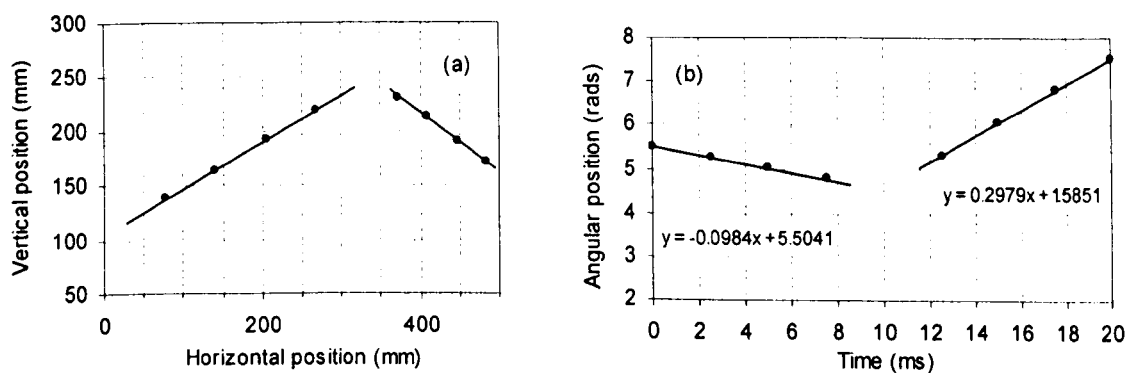
Figure 9.7 Examples of (a) raw positional data and (b) raw angular data, for an impact with backspin filmed at 400 frames per second.

On almost all impacts filmed at 240 or 400 frames per second, positional and angle data was found for four frames before and four frames after impact. Those where the ball was in contact with the surface were not used. Figure 9.7 (a) shows an example of positional data, with each dot representing the position of the ball every 2.5 ms. It should be noted that the data is exported from the software such that a positive vertical position is measured downwards. The height of the ball above the ground was not important – the frame rate was not high enough to provide any useful information during contact, so only data for speeds and spins before and after impact were measured. The velocity components were calculated using the horizontal and vertical positions relative to time rather than to each other, assuming a linear fit – which will of course be a good assumption given the fairly high speeds and the short space of time used. The angular data is plotted against time in

Figure 9.7 (b). The reference points used to find the angle were not necessarily the same before and after impact, so the relative vertical position of the two parts of the graph is meaningless. The gradient of the linear trendline gives the spin – in this case 18.1 rads^{-1} of backspin before impact and 386.3 rads^{-1} of topspin after impact (the time is shown in milliseconds hence the gradient must be multiplied by 1000 to give spin rates per second).
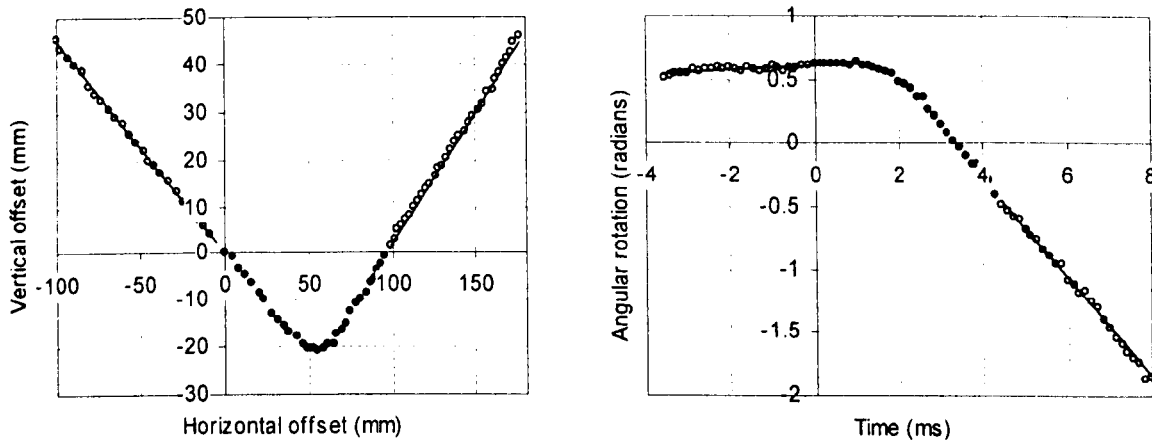
Figure 9.8 (a) positional, and (b) angular displacement data for an oblique impact filmed at 7000 fps.

An example of positional and angular data for an impact filmed at the higher frame rate of 7000 frames per second is shown in Figure 9.8. Because the resolution of this camera is not as high (256x128 pixels compared to 640x320 pixels for the Motioncorder), the positions in all frames were measured to keep errors as low as possible. The effect of the lower resolution can be seen in slightly larger scatter in the data compared to Figure 9.7. The displacement data is offset so that the origin of the graph corresponds to what visually appeared to be that start of contact with the surface, although this is difficult to determine absolutely. Linear trendlines are shown on the graphs for the periods before and after contact, which were used to calculate the positional and angular velocities – in this case a small amount of backspin before the impact, and a much larger amount of topspin after.

9.4   Results - The effect of changing spin (constant speed and angle)
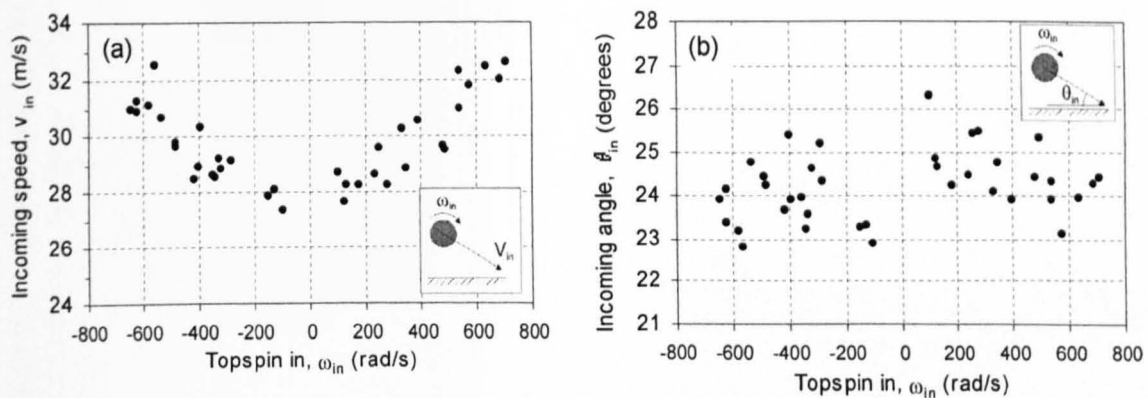
Figure 9.9 Variation of (a) incoming speed and (b) incoming angle with incoming spin, for impacts nominally at 30 ms^{-1} at 24° to the horizontal.

The spins used ranged from approximately 600 rads^{-1} backspin to 600 rads^{-1} topspin. The intention was to project the balls with a constant speed and at a constant angle. However, this was impossible to achieve and there was a systematic error caused by the changing spin. Even over a fairly short distance the lift force caused by these fairly large spin rates will affect the trajectory, and the differing speeds of the two wheels of the Bola also skew the angle. Figure 9.9 (a) shows that the incoming speed changes with incoming spin, giving a range of about ±2 ms^{-1} either side of the intended value of 30 ms^{-1}. This suggests that the relative speed of the wheels is not perfectly calibrated to provide consistent speeds as the spin is varied by large amounts. An aerodynamic model was used to assess the effect of different applied spins on ball trajectories. According to this model, 600 rads^{-1} of top or back spin (applied to a ball fired at 30 ms^{-1} at 24 degrees to the horizontal from a start height of one metre) made the ball land approximately 8 cm earlier or later respectively, but barely changed the speed. This suggests that the speed variation seen was due to the equipment.

Figure 9.9 (b) shows there was scatter in the angle, although the variation was not as great as for the speed. The angles for those impacts with incoming backspin were on average were an average of 24 ± 1.5° and appear randomly scattered. When incoming topspin was applied there was a slight trend for increasing spin to produce a lower incoming angle, which varied from about 25.5° with no spin to 24° with 700 rads^{-1} of topspin.

9.4.a   Speed results
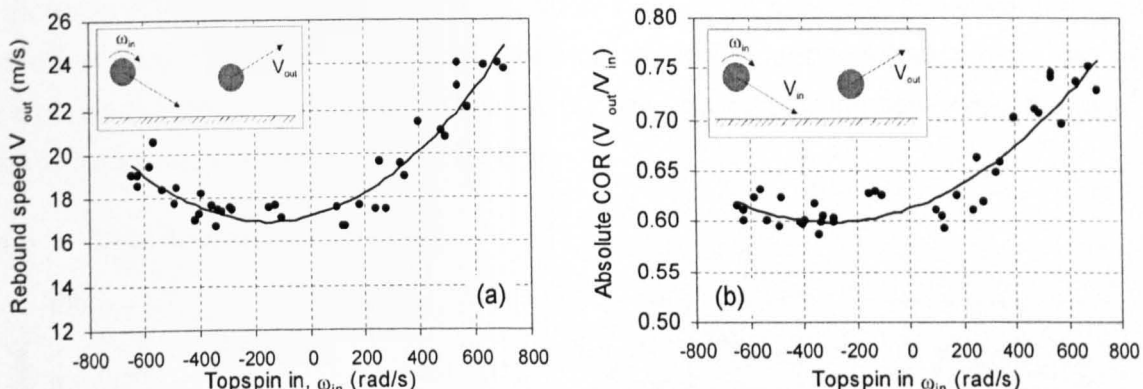
Figure 9.10 (a) outgoing speed and (b) absolute COR against incoming spin.

Figure 9.10 (a) shows how the outgoing speed varies with incoming spin. There is some evidence of a trend, but this is much more informative when the speed is normalised by dividing by the incoming speed, thus removing the systematic bias produced by the Bola projection machine. Figure 9.10 (b) shows that the speed ratio V_{out}/V_{in} or "absolute COR" is fairly constant for impacts with incoming backspin, and then increases in a roughly linear fashion when topspin is applied. This is because as the incoming topspin increases, the ball reaches rolling conditions at an earlier stage of the impact. After rolling starts, the vertical reaction force no longer produces a horizontal frictional force. Therefore more topspin means a smaller horizontal impulse and a lower horizontal rebound velocity – and hence lower absolute speed.
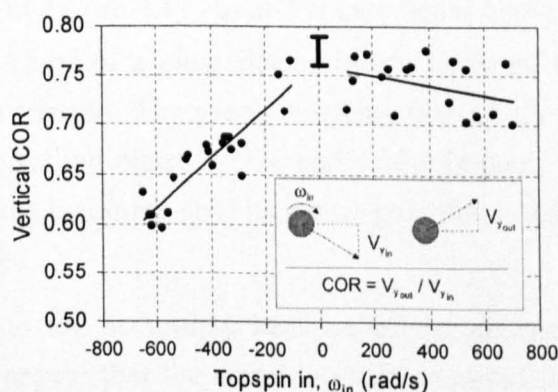
Figure 9.11 Vertical COR against incoming spin. The 100 inch drop test limits are also shown.

The vertical COR e_y (defined by $e_y = -\dfrac{V_{y_{out}}}{V_{y_{in}}}$) is shown against incoming spin in Figure 9.11. This graph clearly shows that the COR significantly changes with incoming backspin. This explains the slightly increased rebound speed at larger incoming backspin which was displayed in Figure 9.10 (b) – horizontal velocity components will dominate and hence the change is not very big. There is a slight downward trend of vertical COR

when more topspin is applied, but this can be attributed to the bias in the incoming speed, as shown in Figure 9.9 (a). As shown in Chapter 7, the COR would be expected to decrease as the incoming speed increased. At the vertical velocity component seen here, the COR for a purely normal impact would be around 0.7, suggesting that impacts with 200 rads^{-1} of applied backspin match this most closely.

9.4.b   *Spin results*
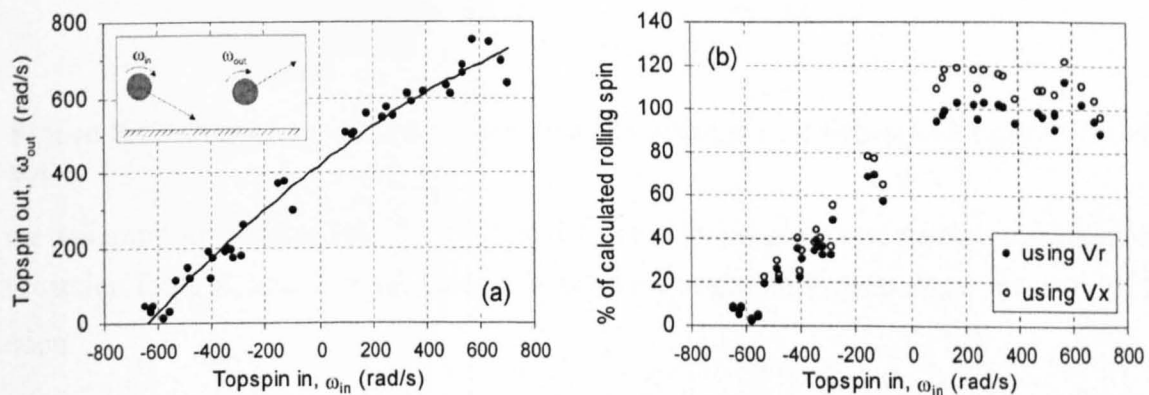
Figure 9.12   (a) Outgoing spin against incoming spin, and (b) rolling spin ratio against incoming spin.

Figure 9.12 (a) shows how the outgoing spin varies with incoming spin. There is an increasing trend which seems to fit a gentle curve. An alternative measure which can be used is the rolling spin ratio, calculated by dividing the actual rebound topspin by the topspin necessary to meet the definition of rolling based on the rebound speed given by $\omega = V/r$. This is shown in Figure 9.12 (b) and is calculated using both horizontal speed V_x and absolute speed V_r. There is a clear discontinuity between the balls impacting with backspin and those with topspin. The graph suggests that all the impacts given incoming topspin have entered the rolling phase by the end of the impact. The actual outgoing spin continues to increase as the incoming spin increases past that needed for rolling, because of the greater outgoing speed.

Although it is difficult to tell accurately because of the absence of data between ±100 rads^{-1} topspin, it would appear that the incoming spin required for the ball to start rolling by the end of the impact is somewhere between zero and 200 rads^{-1} of topspin.
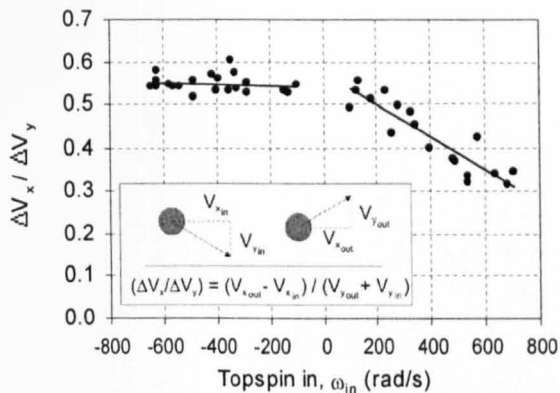
Figure 9.13 Change in horizontal speed divided by change in vertical speed, against incoming spin.

If the assumption is made that the frictional force F is proportional throughout impact to the reaction force R, and $F = \mu R$, then it is possible to get an experimental measure of the friction:

$$\mu = \frac{\Delta V_x}{\Delta V_y}$$

[9.1]

The relationship $\Delta V_x / \Delta V_y$ is plotted against incoming spin in Figure 9.13. It is clear that this expression gives a consistent measure of friction for all the impacts with backspin. There is again a clear discontinuity at about zero incoming spin. The graph suggests that as the ball is given more incoming topspin, the ball rolls rather than slips for an increasing proportion of the contact time. This means that the change in horizontal velocity is reduced, and so the expression in [9.1] decreases. The graph does show however that as long as the ball slides throughout impact, $\Delta V_x / \Delta V_y$ is a fairly consistent figure (if the ball rolls, the expression $F = \mu R$ no longer holds, so $\Delta V_x / \Delta V_y$ no longer represents a measure of friction). The value of friction predicted by this data is $\mu = 0.55$, which corresponds to a Pace Rating of 45 and matches almost exactly that measured by an SPR test, despite the impact angle being considerably higher than the 16° used in that test.

9.4.c   Angle results
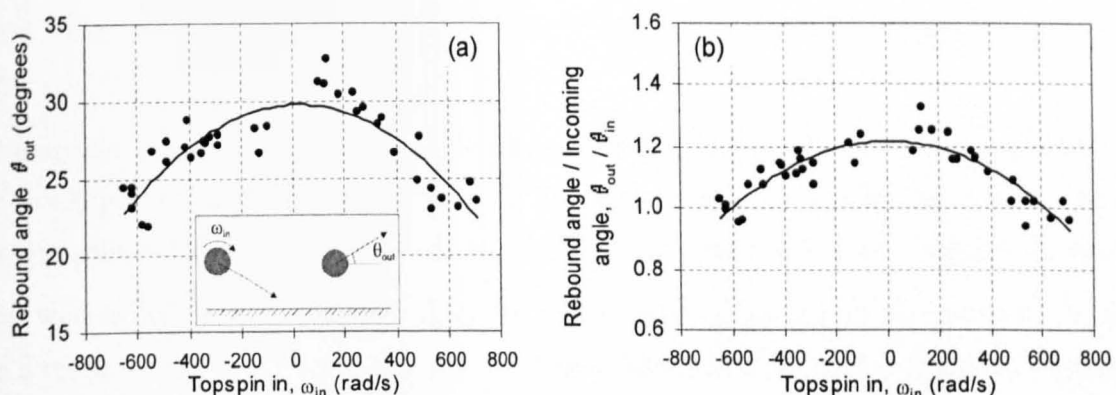
Figure 9.14 Outgoing (a) angle, and (b) angle ratio against incoming spin.

Figure 9.14 shows the outgoing angle against the incoming spin – both as an absolute value and a ratio compared to the incoming angle, which brings the data for backspin and topspin closer together. It can be seen that the highest angle is obtained at roughly zero incoming spin, and the angle decreases as either topspin or backspin is applied. This is the result of two separate physical processes, explained by the force-time schematics in Figure 9.15.
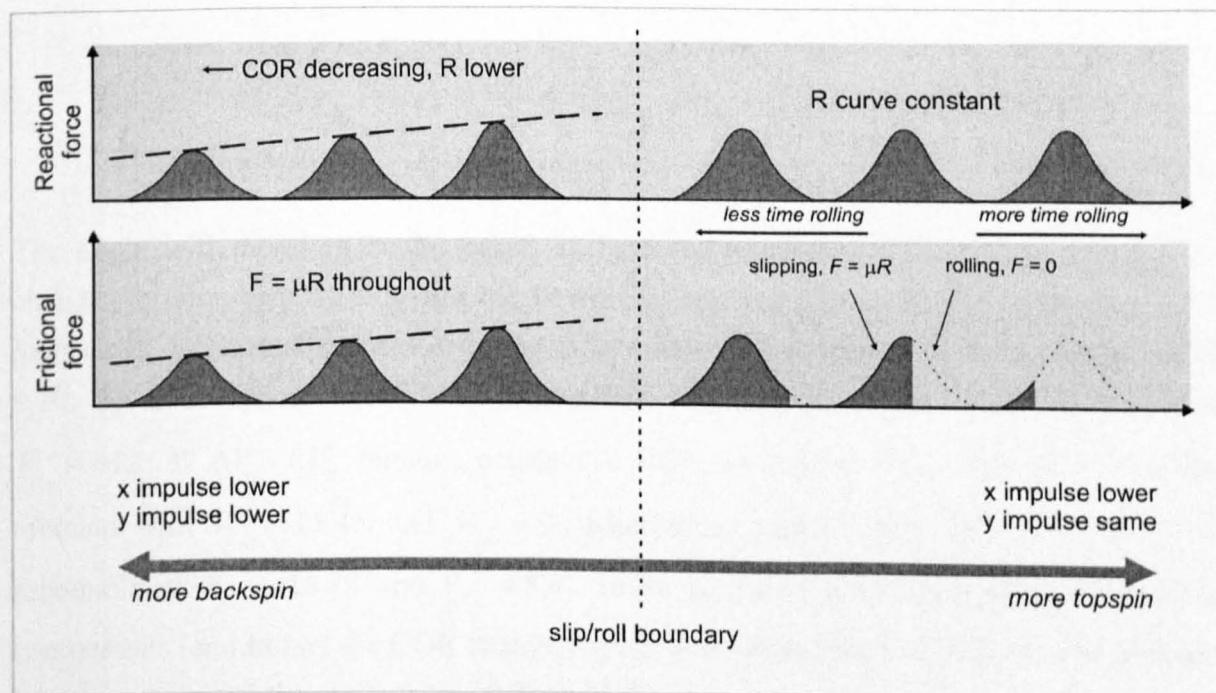
Figure 9.15 Schematic profiles for reaction and friction forces.

Firstly, consider the right-hand side of Figure 9.15 – the balls impacting with topspin. As has been shown, for all these impacts the ball starts off slipping but is rolling by the time it leaves the surface. As the incoming spin increases, a greater proportion of the contact time is spent rolling. During the slipping period, $F = \mu R$ but when rolling occurs F drops to very close to zero. Therefore with more topspin the horizontal impulse given by the

integral $\int Fdt$ decreases. As shown in Figure 9.11, the COR and hence the change in vertical velocity stays almost constant. Given these two factors the rebound angle will reduce.

Now consider impacts with backspin, as shown on the left-hand side of Figure 9.15. As more backspin is applied, the vertical COR reduces (as shown in the COR against incoming spin in Figure 9.11). Because the friction and hence $\Delta V_x / \Delta V_y$ remains constant, ΔV_x as well as ΔV_y will be reduced. Because of the signs of the incoming components, this gives a reduced $V_{y_{out}}$ but an increased $V_{x_{out}}$. This is illustrated by rearranging the frictional relationship as in equation [9.2] below. If μ stays the same (which is to be expected, since it is a physical property of the surface) and e decreases, $V_{x_{out}}$ will increase since $V_{y_{in}}$ is negative.

$$\mu = \frac{\Delta V_x}{\Delta V_y}$$

$$= \frac{V_{x_{in}} - V_{x_{out}}}{V_{y_{out}} - V_{y_{in}}}$$

$$= \frac{V_{x_{in}} - V_{x_{out}}}{-V_{y_{in}}(1+e)}$$

$$V_{x_{out}} = V_{x_{in}} + V_{y_{in}}\mu(1+e) \qquad\qquad [9.2]$$

The angle will therefore be increased as backspin increases (and is quite sensitive to changes in components) although the speed will not change significantly because of the increase in one component and decrease in the other. This is shown by the results in Figure 9.10. As a numerical example of this effect, consider an impact with $V_{x_{in}} = 27$ and $V_{y_{in}} = -12$. If $\Delta V_x / \Delta V_y$ remains constant at 0.55, an impact with COR of 0.75 would rebound with $V_{x_{out}} = 15.45$ and $V_{y_{out}} = 9$, whereas an impact with COR of 0.70 would rebound with $V_{x_{out}} = 15.78$ and $V_{y_{out}} = 8.4$. These are fairly small changes in the velocity components (and in fact the COR changes by far more than this over the range of backspin tested), but change the angle from 30.2° to 28.0°.
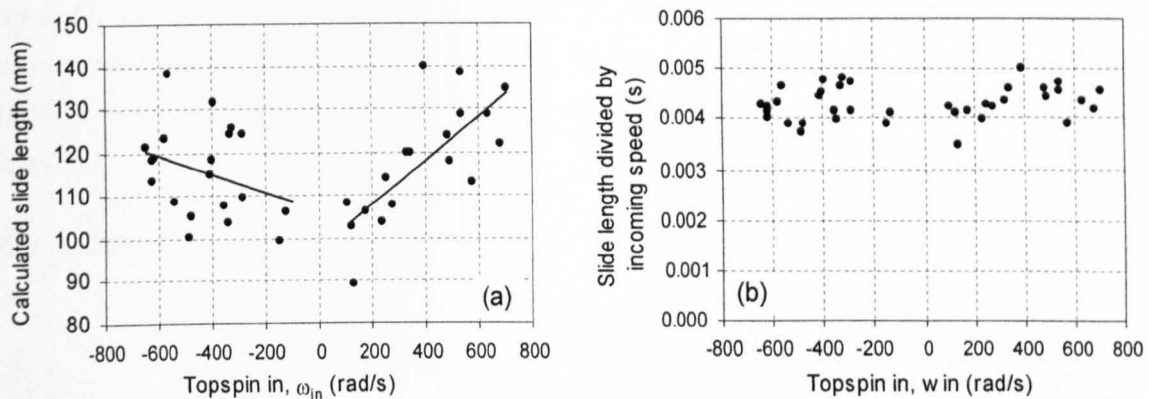
Figure 9.16 Calculated slide length for oblique impacts with various spins, shown as (a) an absolute value, and (b) divided by the incoming speed.

Figure 9.16 shows the slide length – the horizontal distance between the start and end of the contact. This was found by extrapolating a straight line from the positional data to an interception with the ground level. It is clear that the slide length increases as the spin moves away from zero. However, if the ratio of slide length to incoming horizontal speed is used, the value is fairly constant. This suggests that the slide length depends only on horizontal speed, and is not affected by spin – and is an indication that the contact time does not significantly change with spin.

9.5 Results - the effect of changing speed (constant angle and spin)
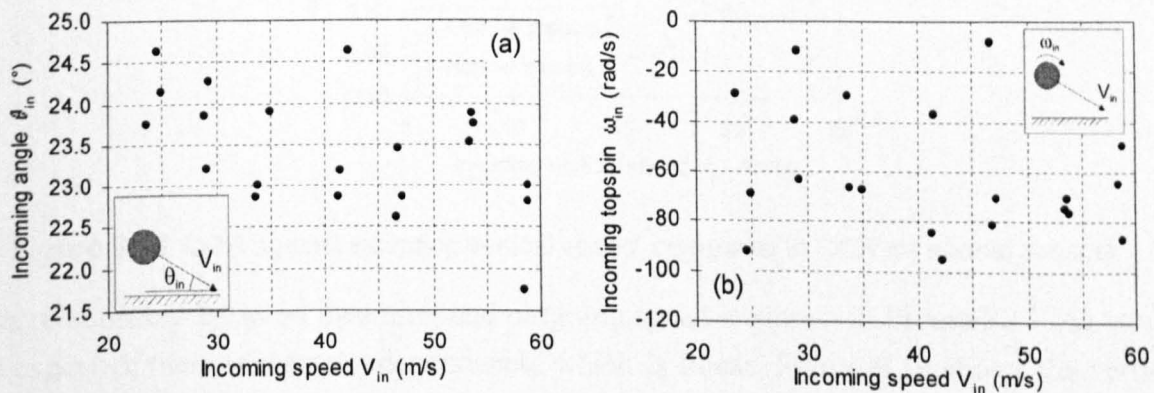
Figure 9.17 The variation of (a) incoming angle V_{in}, and (b) incoming spin ω_{in}, with incoming speed.

As with the changing spin experiment, there was an element of scatter in the incoming angle and spin, the two properties intended to be constant. Figure 9.17 shows the change in (a) incoming angle and (b) incoming spin as the velocity was increased. The angle has a clear reduction with increasing incoming speed as is to be expected – for motion between a fixed start and end point, a higher speed will lead to a straighter trajectory and therefore a shallower angle. This change in angle is not particularly high however, dropping from about 24° at 25 ms^{-1} to about 22° at 60 ms^{-1}. The spin is randomly scattered, averaging

around 60 rads^{-1} of backspin. Ideally the balls would have been projected without spin (zero incoming spin would mean that speed should not affect slipping/rolling conditions), but this was not as important as the main criterion of keeping the spin constant, which was achieved.

9.5.a   Speed results
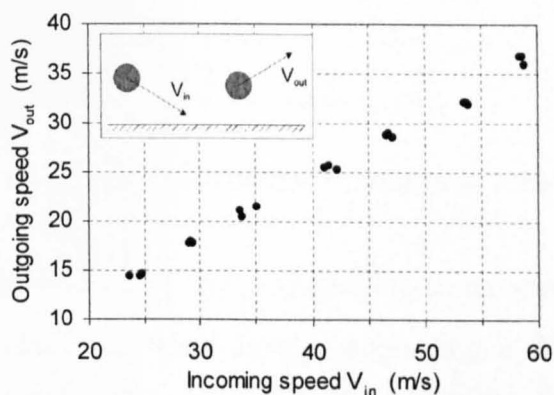
Figure 9.18 Outgoing speed V_{out} against incoming speed V_{in}.
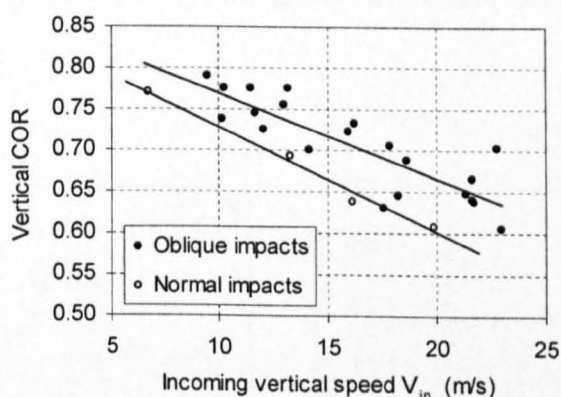
Figure 9.19 COR against incoming vertical speed, compared to COR for normal impacts.

The relationship between incoming and outgoing speed is shown in Figure 9.18. As would be expected, there is a strong dependence, which is linear. Figure 9.19 shows the vertical COR plotted against the vertical incoming speed. The COR drops from about 0.8 to 0.6 over the velocity range. Also included on this figure is the COR measured from purely normal impacts. For the same incoming vertical velocity component (including 7 ms^{-1} where the approval tests are performed), the oblique impacts have a higher COR in each case.
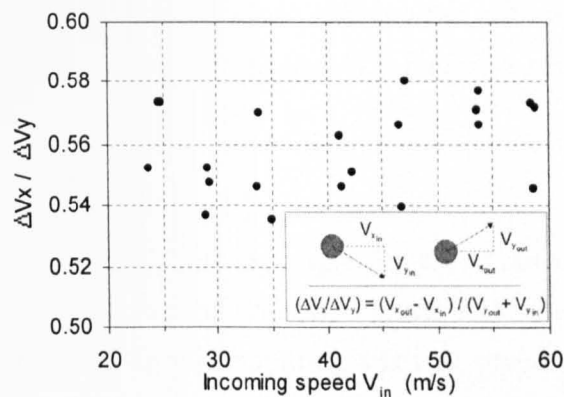
Figure 9.20 Change in horizontal speed divided by change in vertical speed, against incoming speed.

Figure 9.20 plots the expression $\Delta V_x / \Delta V_y$ against incoming speed. Although there is an amount of scatter, the relation is fairly steady, suggesting a frictional measurement of about 0.56. This ties in extremely well with the measured SPR of 45, which gives $\Delta V_x / \Delta V_y = 0.55$. This constant value of $\Delta V_x / \Delta V_y$ suggests that the impacts all slide throughout – or that any periods of rolling are short and do not affect the outgoing conditions.

9.5.b   *Spin results*
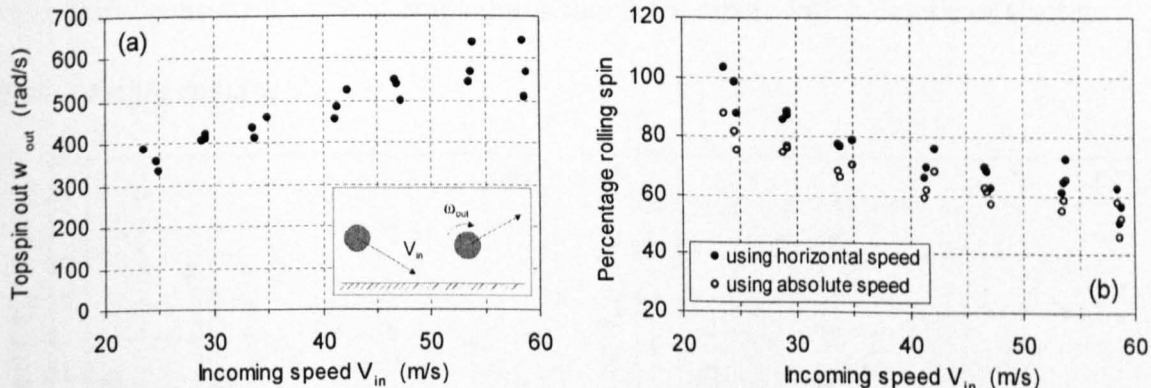
Figure 9.21   (a) Topspin out, and (b) Topspin out as a percentage of rolling spin, against incoming speed.

The outgoing spin is plotted against incoming speed in Figure 9.21 (a). This graph simply shows the spin increasing with speed as would be expected (a higher speed leads to a larger reaction force, hence a larger frictional force and rotational moment), but in Figure 9.21 (b) the spin is plotted as a percentage of rolling spin, calculated from the outgoing speed using $\omega = \dfrac{v}{r}$ as before. At the lowest impact speed it seems the ball may be rolling (or at least close to rolling) by the end of impact, but as the speed increases we move further away from the rolling condition and the ball slips throughout impact. A possible reason for this

can be seen by considering the equation below defining the minimum angle for rolling θ_{min} in terms of coefficient of friction μ and vertical coefficient of restitution e:

$$\tan\theta_{min} = \frac{2}{5\mu(1+e)} \qquad\qquad [9.3]$$

Equation [9.3] gives the theoretical limiting angle for which an impact with no incoming spin will just start to roll at the end of contact. Figure 9.19 showed that the value of e dropped from around 0.8 to 0.6 as the incoming vertical speed increased from 10 to 20 ms^{-1}. For a value of $\mu = 0.55$, this would raise the angle boundary from 22° to 24.4°. Figure 9.17 (a) shows that the observed incoming angle decreased from 24.5° to 22.5°. According to this theory, as the incoming speed increases from 10 to 20 ms^{-1}, the impact changes from slipping/rolling to purely slipping. It is impossible to see this from the data in Figure 9.21 (a), but Figure 9.21 (b) does suggest that the lowest speed impacts may be rolling if the horizontal speed is used to calculate rolling spin. The fact that the proportion of rolling spin drops as soon as the incoming speed increases suggests that even for these impacts, rolling is only just attained by the end of the impact. This means that the horizontal impulse is barely affected by the rolling, as the reaction force will be very low for the short period when rolling happens. Therefore $\Delta V_x / \Delta V_y$ is probably a good measure of friction throughout this set of tests. This expression is shown in Figure 9.20 and gives a fairly consistent value averaging to about 0.56, albeit with a degree of scatter.

9.5.c   Angle results
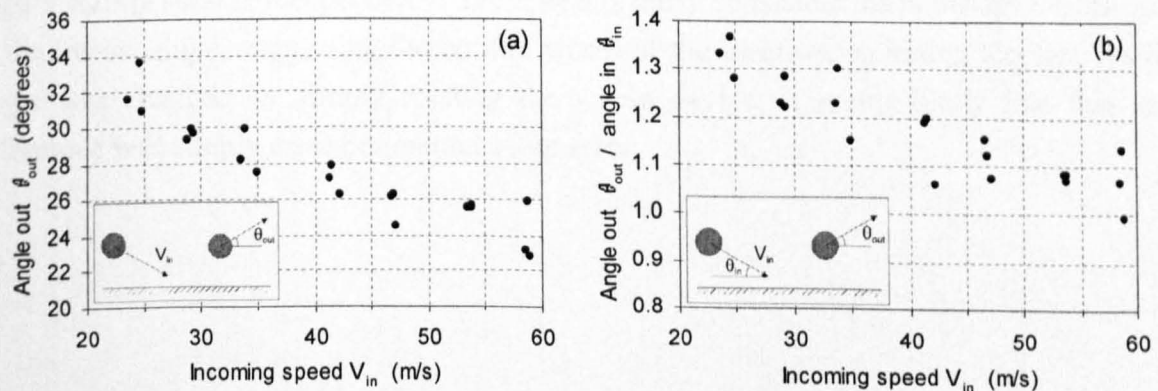
Figure 9.22 (a) outgoing angle θ_{out}, and (b) angle ratio $\theta_{out} / \theta_{in}$ against incoming speed V_{in}.

Figure 9.22 (a) shows how the outgoing angle decreases as the incoming speed increases. This effect is increased slightly by the bias in incoming angle, which also reduces as the speed increases. However, Figure 9.22 (b) plots the angle ratio ($\theta_{out} / \theta_{in}$) and the trend is still obvious. The reason for this is the reduction in vertical COR which happens due to the increased vertical incoming speed. As previously discussed in section 9.4.c, this decreases

the outgoing vertical speed and increases the outgoing horizontal speed, lowering the angle.

9.6   Results - the effect of changing angle (constant speed and spin)

This experiment was much more difficult to set up than the two with varying speeds and spins - in both of the earlier sets of tests the Bola could be more or less left in one position and the desired variable changed by settings on the machine. Changing the angle meant moving the relative position of the Bola and the target, and consequent fine-tuning to keep the impact in the correct place. Therefore only six separate angles were used, with three impacts at each angle.
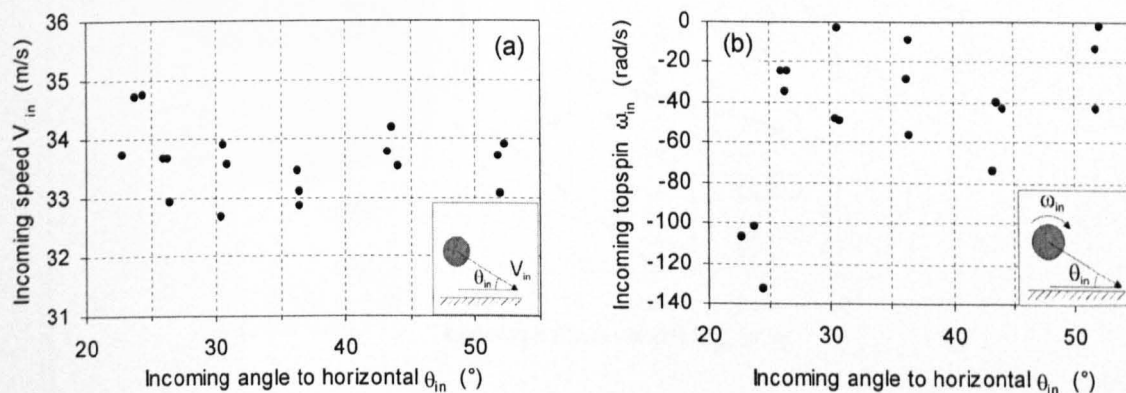
Figure 9.23 The effect of incoming angle on (a) incoming speed and (b) incoming spin.

The variation of incoming speed and spin (ideally both constant) with angle is shown in Figure 9.23 (a) and (b) respectively. The speed is fairly consistent, as is the spin. Both vary at the lowest angle, suggesting the bottom wheel of the Bola was spinning too fast. As the angle was changed by simply rotating the whole device, it seems likely that this spin difference was simply an experimental setup error.

9.6.a   *Speed results*
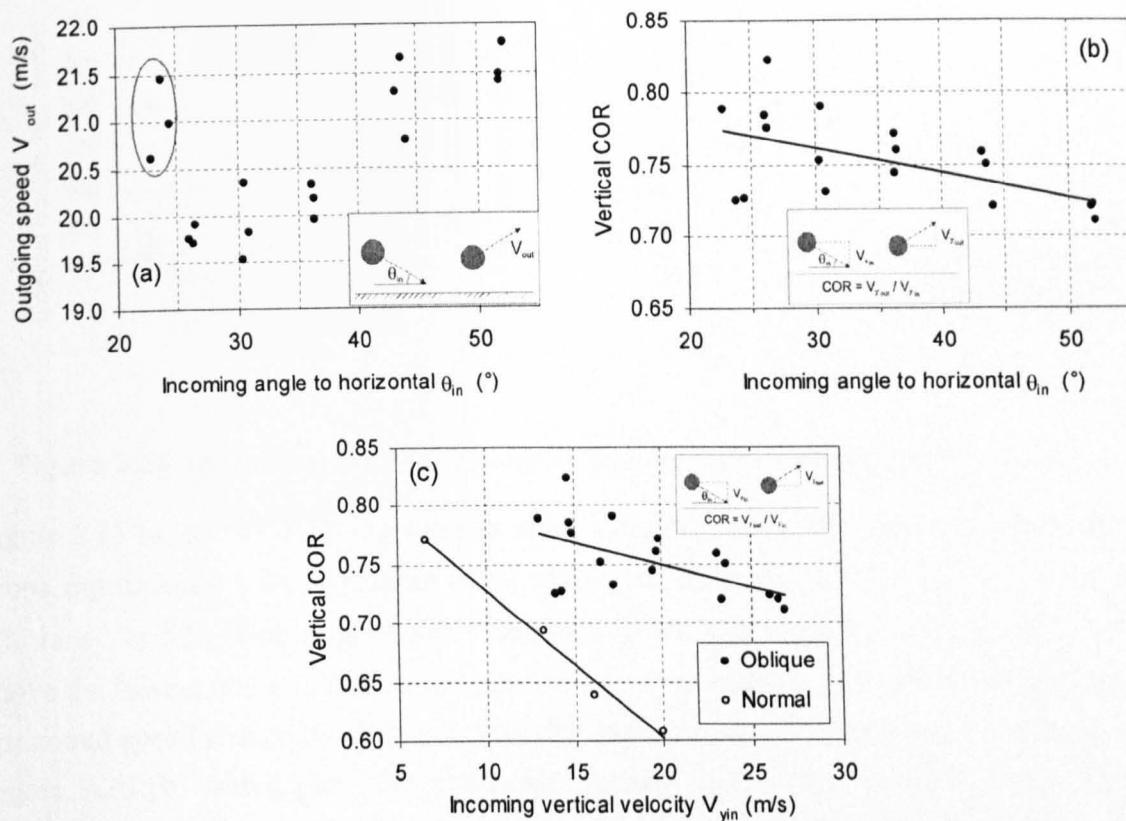
Figure 9.24 (a) Outgoing speed vs. incoming angle, (b) COR vs. incoming angle, and (c) COR against incoming vertical speed (including normal impacts for comparison).

The effect of incoming angle on outgoing speed is shown in Figure 9.24 (a), and the vertical COR in Figure 9.24 (b). The rebound speed increases with steeper angles apart from the very lowest angle, which is significantly faster than the one above it. Although the vertical COR decreases with increasing angle (and therefore incoming vertical speed) as would be expected, Figure 9.24 (c) shows that it remains higher than for normal impacts having the same vertical velocity. The difference widens significantly as the angle becomes steeper.

Using a value of $\mu = 0.55$ (as measured by the SPR friction tests) and a typical COR value of $e = 0.75$, the theoretical equation [9.3] developed in Chapter 3 gives a minimum angle of 22.6°, above which rolling will occur. It is possible therefore that this explains the discontinuity in the speed in Figure 9.24 (a), and suggests that all the impacts apart from those ringed contain some rolling. As the angle to the horizontal increases, the incoming vertical velocity will also increase and the horizontal velocity will decrease. The former will increase the reaction force and hence the frictional moment and rate of spin application. The latter will decrease the spin needed for rolling to occur as defined by

$\omega = \dfrac{v}{r}$. Both bring about the onset of rolling earlier in the impact.

9.6.b   *Spin results*
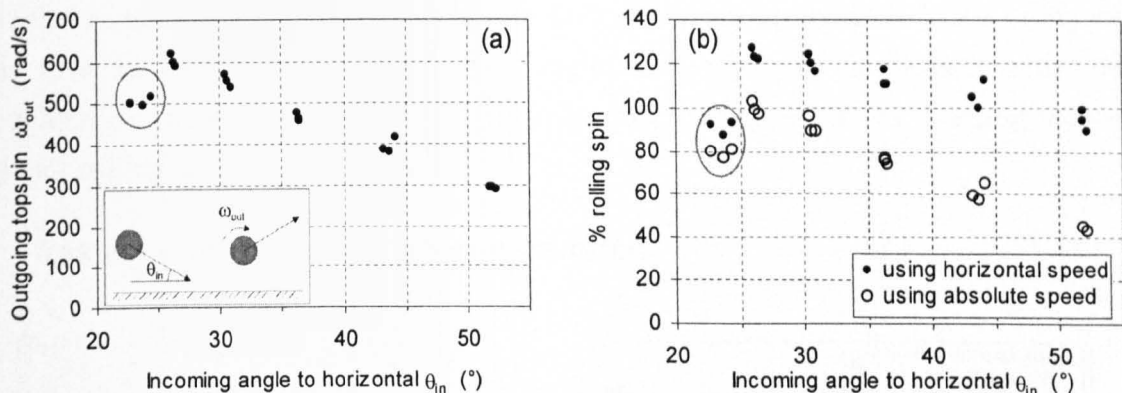
Figure 9.25 (a) Topspin out, and (b) percentage rolling spin, against incoming angle.

Figure 9.25 (a) shows outgoing topspin plotted against incoming angle. The outgoing spin drops significantly with increasing angle of impact, from about 600 rads^{-1} at 25°, to about 300 rads^{-1} at 52°. This might seem surprising given the statement above that all angles above the lowest one will end in rolling, but of course both the incoming and the outgoing horizontal speed reduce by almost half as the angle increases. This is taken into account in Figure 9.25 (b) which plots the percentage rolling spin, which is much closer to being constant. It should be noted that the lower outgoing spin for the impacts ringed (whether absolute value or percentage of rolling spin) should not be taken as absolute evidence of the angle needed for rolling to occur, as the impacts at the lower angle impacted with significantly more backspin (100 rads^{-1} compared to an average of 40 rads^{-1} for other angles). This difference does not totally account for the lower values of outgoing spin ringed in Figure 9.25 (a), but does explain the sharp discrepancy.

9.6.c   *Angle results*
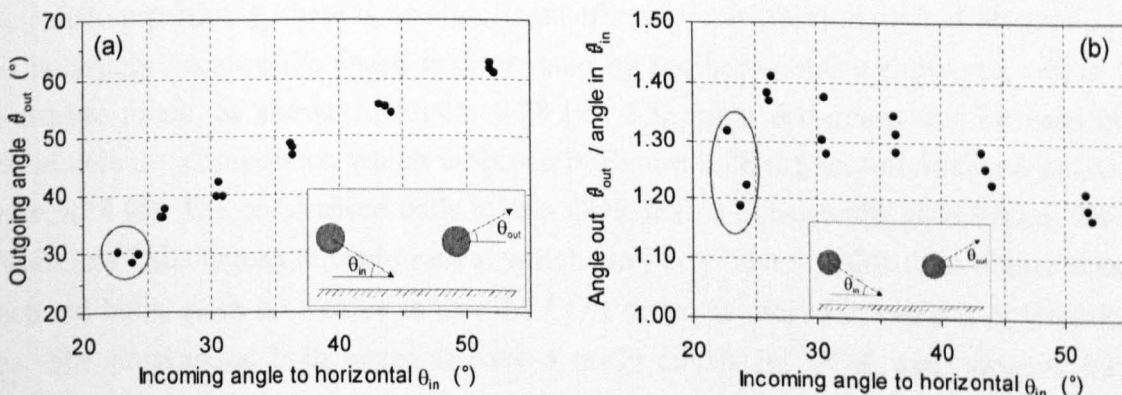
Figure 9.26 (a) Outgoing angle, and (b) angle ratio, against incoming angle.

The outgoing angle is shown plotted against the incoming angle in Figure 9.26 (a). A steeper incoming angle leads to a steeper outgoing angle, but it is difficult to draw many

further conclusions. Figure 9.26 (b) shows the angle ratio (θ_{out}/θ_{in}) and the trend appears to be that as the angle is increased this ratio decreases, thus an increase in incoming angle leads to a smaller increase in outgoing angle. The effect of an impact which slips throughout can be clearly seen in that the angle ratio is highest at the limiting incoming angle for rolling, and drops either side.

9.7   Results – the effect of ball construction
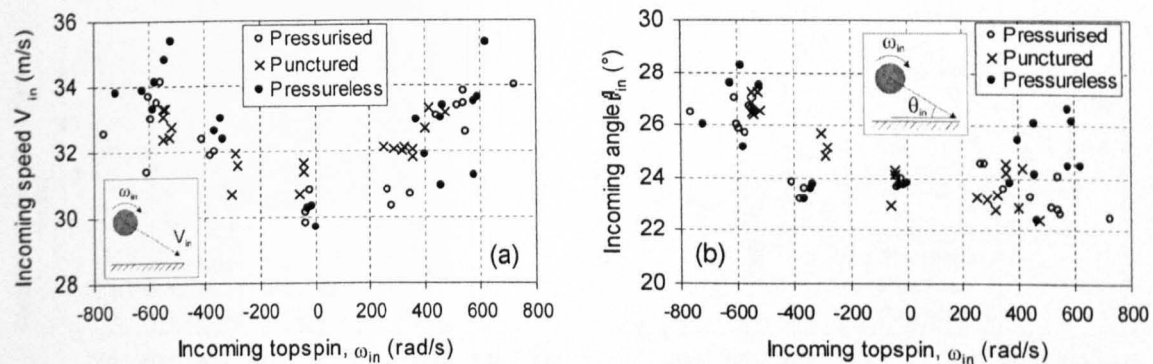
Figure 9.27 Variation of (a) incoming speed and (b) incoming angle with incoming spin, for impacts nominally at 30 ms^{-1} at 24° to the horizontal for three different ball types.

There was again a variation of impact speed and angle with spin when the first set of tests was repeated with different ball types, as can be seen in Figure 9.27. The speed showed the same trend of increasing from the set value when either topspin or backspin was applied, and the same happened with all three balls. The angle remained roughly clustered around 24° (albeit with a fair degree of scatter) apart from the impacts with large amounts of incoming backspin, which had a noticeably higher angle.

Figure 9.28 (a) below shows a comparison of outgoing ball speed for the three ball types. Somewhat surprisingly, there is no significant effect of construction on ball rebound speed. This is largely because the speed is dominated by the horizontal component, which does not change much, as shown in Figure 9.28 (b). The main difference can be seen in the vertical velocity component, which is shown in Figure 9.28 (c), and normalised to COR in Figure 9.28 (d). The pressurised balls have a COR that is consistently 0.05 higher than the pressureless balls across the spin range, which similarly have a COR 0.05 higher than the punctured balls. Also noticeable is that the COR drops as more backspin is applied for all balls. The pressurised balls seem to have a fairly consistent COR with topspin, but the other two construction types both drop. These speed results suggest that all balls would reach the player at the same time (since horizontal speed is the dominant factor) albeit at a different height, but of course that assumes they have been hit at the same speed - and the speed of the ball off the racket is likely to follow the same trends as the COR data.
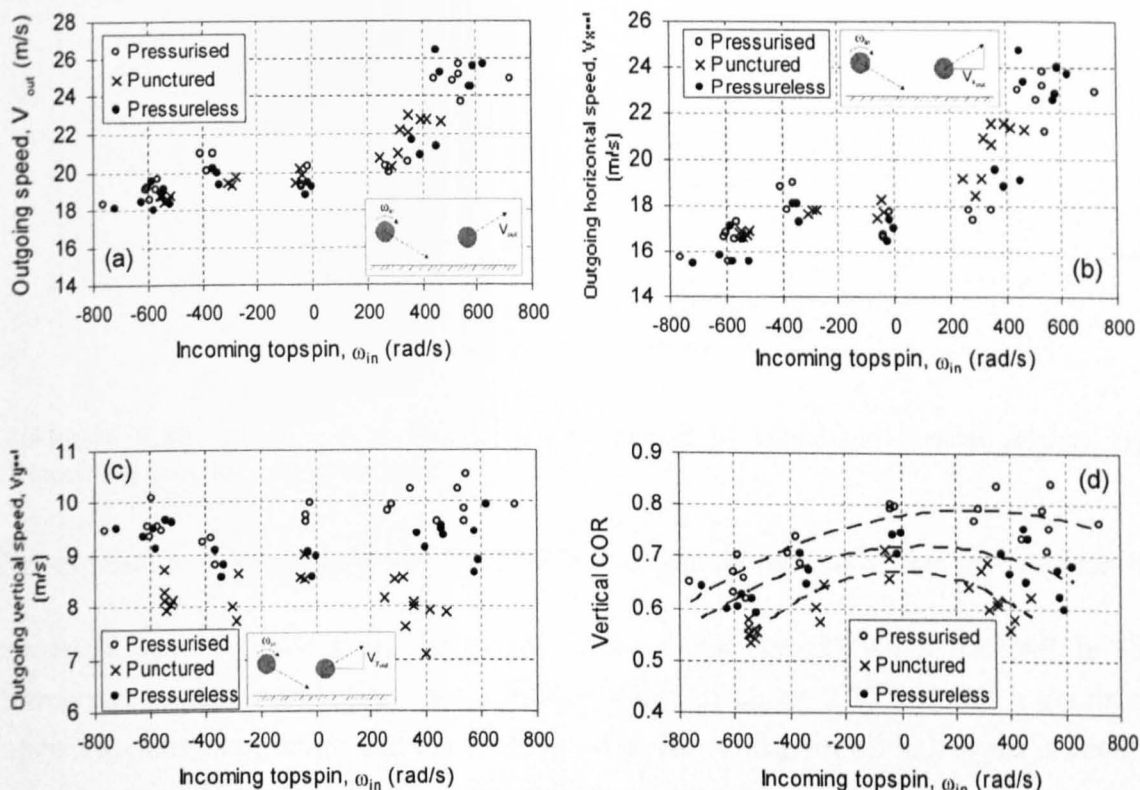
Figure 9.28 (a-d) The effect of ball construction on rebound speeds. (a) absolute speed, (b) horizontal speed, (c) vertical speed and (d) COR are shown.
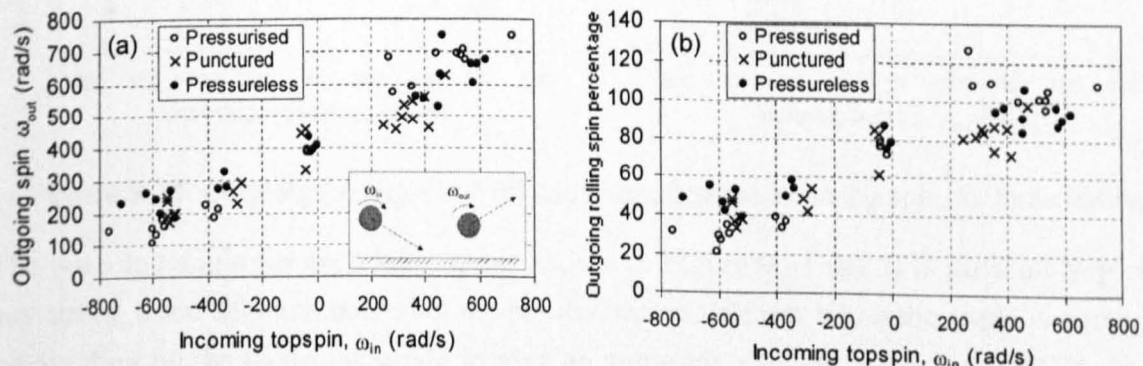
Figure 9.29 Outgoing spin against incoming spin, for three ball types, expressed as (a) an absolute value, and (b) a percentage of the calculated rolling spin.

Figure 9.29 shows the outgoing spin, expressed as both an absolute value and as a proportion of the absolute rolling spin. In both cases there is no significant difference between the ball constructions. Increased topspin before impact led to increased topspin after impact. The rolling spin percentage seems to level off, suggesting that rolling is occurring with incoming topspin, but this is not conclusive.
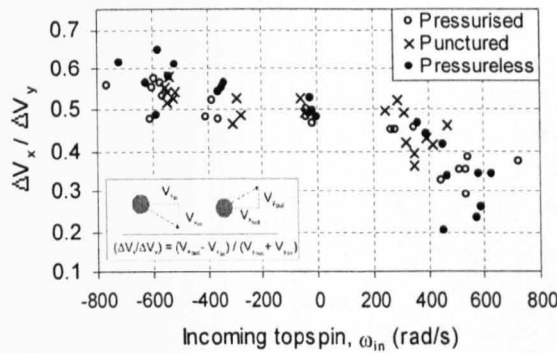
Figure 9.30 Change in horizontal velocity divided by change in vertical velocity, against incoming spin, for three ball types.

The expression $\dfrac{\Delta V_x}{\Delta V_y}$ is shown in Figure 9.30. As found previously, this gives a reasonably

consistent value (showing no difference between ball types) when the ball is sliding throughout impact, suggesting here a friction value of about 0.50 to 0.55. It decreases as topspin applies, suggesting that the limiting value for rolling for all ball types is about zero incoming spin. There is also an increase with large amounts of applied backspin.
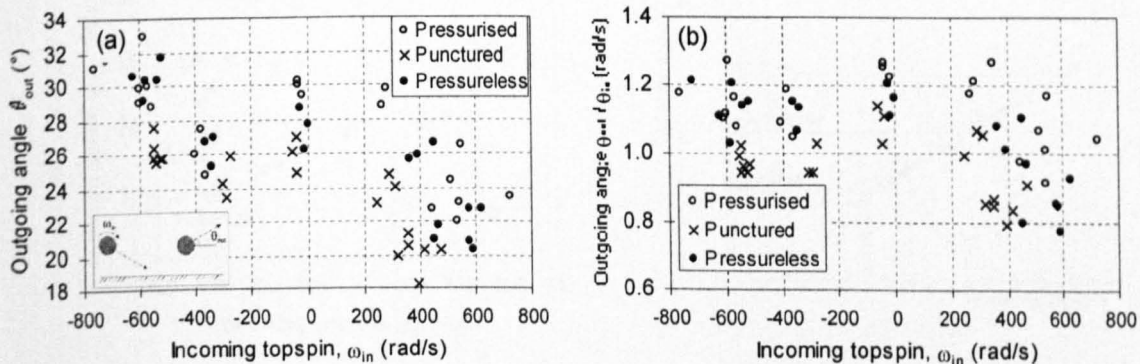
Figure 9.31 Outgoing (a) angle and (b) angle ratio against incoming spin, for three ball types.

The outgoing angle for each ball type is shown in Figure 9.31 (a). It is difficult to pick out any strong trend between balls, but the results become clearer when the angle is normalised by dividing by the incoming angle to give an angle ratio θ_{out}/θ_{in} as in Figure 9.31 (b). It is clear that the punctured ball always has a lower angle ratio than the other two balls. The pressurised and pressureless balls have a similar angle ratio for those impacts with incoming backspin, but the pressurised ball bounces higher when there is incoming topspin.

9.8   Results – the effect of surface type
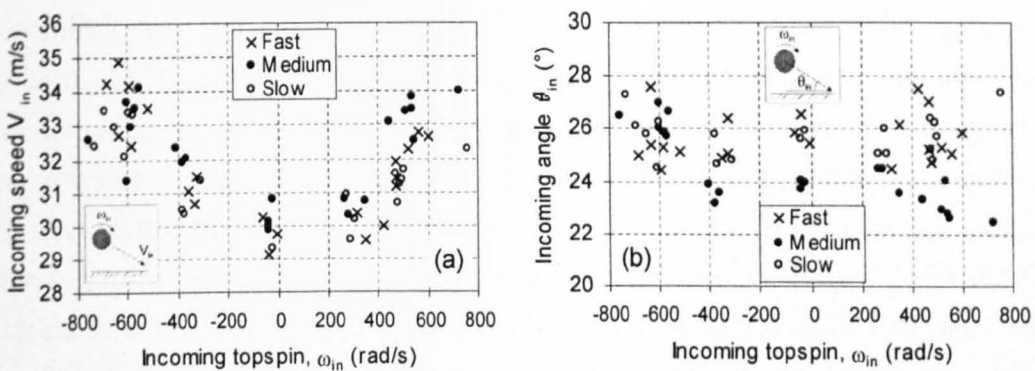
Figure 9.32 Variation of (a) incoming speed and (b) incoming angle with incoming spin, for impacts nominally at 30 ms^{-1} at 24° to the horizontal for three different surfaces.

Figure 9.32 shows how the impact speed and angle varied with different value of applied spin. The same trends are seen for each surface, although the values are not exactly the same – because all the tests were performed on each surface in turn and so the individual wheel speeds could not be totally consistent between surfaces.
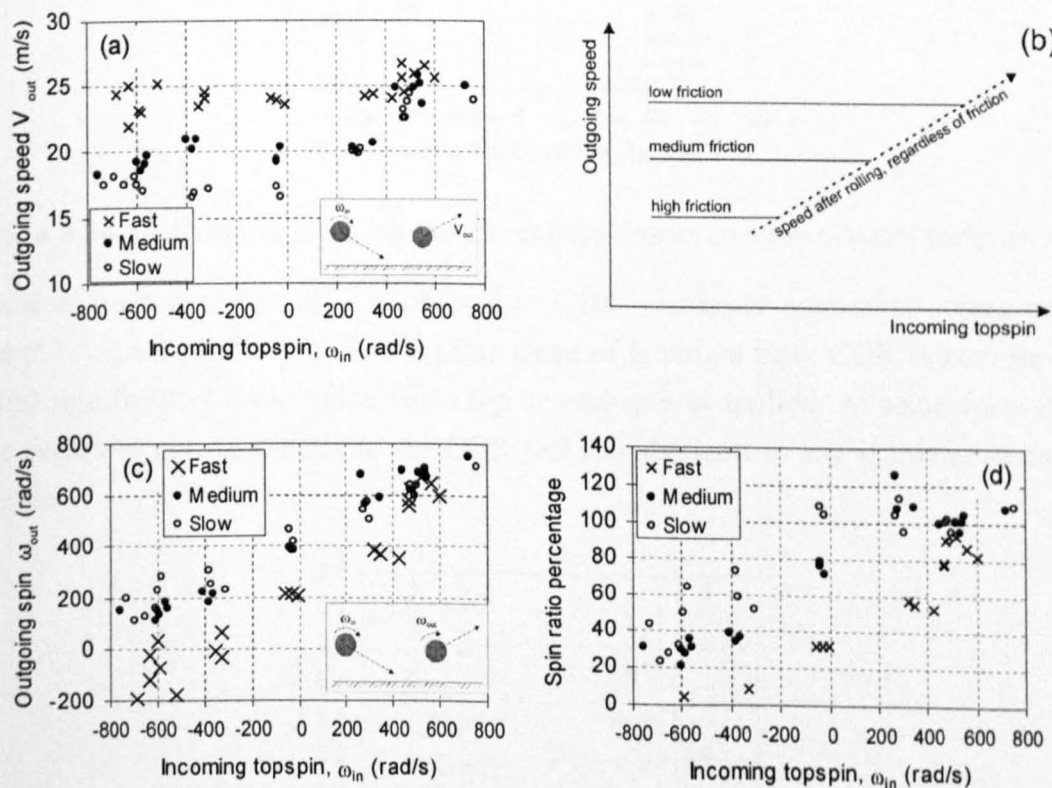
Figure 9.33 (a) Experimental and (b) stylistic data for outgoing speed versus spin; (c-d) outgoing spin expressed as absolute and relative to rolling values.

The effect of surface type on outgoing speed is shown in Figure 9.33 (a). As would be expected, the choice of surface (and therefore surface friction) has a significant effect on speed. With no spin or backspin, the low, medium and high friction surfaces produce

consistent speeds of about 24, 20 and 17 ms^{-1}. These differences become much less apparent as the balls are projected with topspin. As each ball type reaches the spin needed for rolling, they join the same speed trendline - shown stylistically in Figure 9.33 (b). This is born out by the spin data in Figure 9.33 (c-d). The slow and medium surfaces have similar outgoing spins, consistently above those for the fast surface apart from those impacts with high incoming topspin. Plotting the data as a rolling spin percentage shows more evidence for the slipping/rolling boundary in each case. The data suggests that the slipping rolling boundaries are between 0 and 100 rads^{-1} of backspin for the slow surface, around 200 rads^{-1} of topspin for the medium surface and around 600 rads^{-1} of topspin for the fast surface (which just reaches 100% rolling spin at the maximum applied incoming spin).
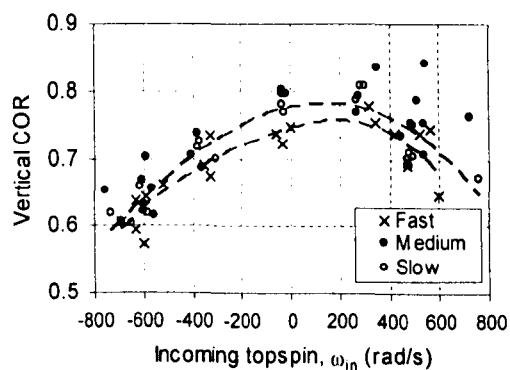
Figure 9.34 COR against incoming spin, for oblique impact on three different surfaces.

The vertical outgoing velocity – expressed as COR - is fairly consistent across surfaces (Figure 9.34). Each surface shows the same trend of having a peak COR at zero incoming spin, and significantly lower value when top or backspin is applied. At some spins the fast surface seems to give a slightly lower COR but it is difficult to say if this is statistically significant.
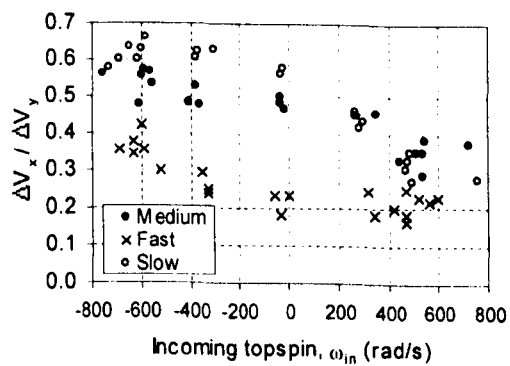
Figure 9.35 Change in horizontal velocity divided by change in vertical velocity, for oblique impact on three different surfaces.

Since the expression $\dfrac{\Delta V_x}{\Delta V_y}$ can be approximated to the friction (as discussion earlier), the

different surfaces would be expected to produce different values. In all three cases (see Figure 9.35), applying less backspin (i.e. more topspin) produces a slowly decreasing value of the expression until the spin boundary for rolling is reached.
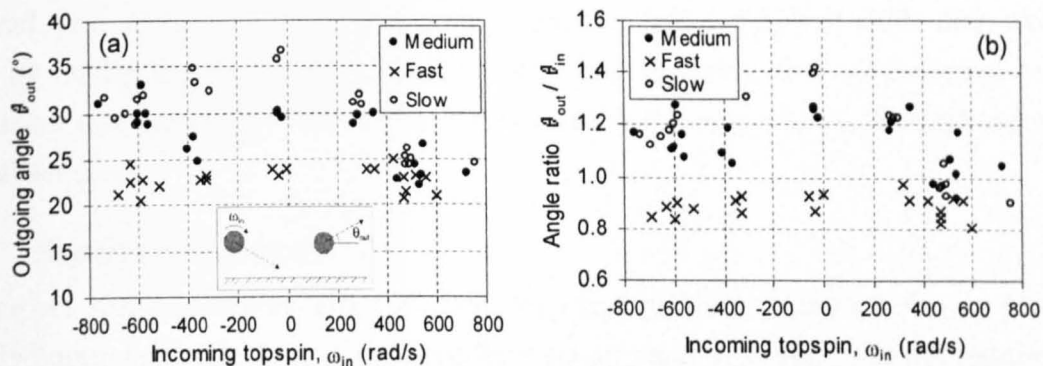
Figure 9.36 (a) Outgoing angle and (b) angle ratio for impacts on three different surfaces.

The effect of surface friction on angle is difficult to analyse until the angle is normalised by dividing by the incoming angle (Figure 9.36). For low to moderate amounts of top and backspin, the fast surface always leads to the most shallow angles, and the slow surface to the steepest. This does not however mean that the ball will necessarily bounce through any higher, but that for a fairly similar value of COR (and hence vertical speed), the surfaces will have different horizontal speeds. This can be seen in the velocity plots in Figure 9.37. The different spins for each surface are not distinguished.
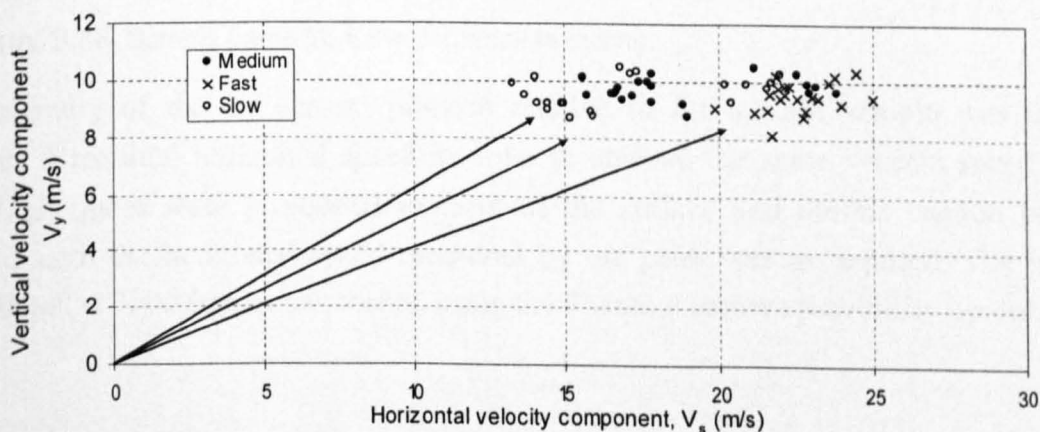
Figure 9.37 Vertical against horizontal outgoing velocities for oblique impacts on different surfaces, depicting typical velocity vectors for each surface type.

9.9   Deformation tests

9.9.a   Introduction

Results presented in this chapter suggest that horizontal and vertical velocity components cannot be totally separated. Many authors have assumed that a model can be created by assuming a normal model with the correct velocity component, and adding a horizontal frictional term. Data here found that oblique impacts had a different COR than would be found by taking the incoming vertical velocity and applying that to a normal test. An experiment was therefore performed to try to identify the physical mechanism behind this COR difference.

9.9.b   Experimental setup

The impact speed of a standard 100 inch drop test (6.8 ms^{-1}) was chosen as the target velocity component. The balls were fired from an air cannon as spin was not required, and this method achieves a higher accuracy than using rotating wheels. This accuracy was particularly important as the impact was filmed extremely close up (a sample frame is shown in Figure 9.38) in order to be able to measure deformations, meaning that fewer frames were available before and after impact to calculate velocities. The errors in the velocities will therefore be higher than for previous experiments.

Figure 9.38 Sample frame from the deformation testing.

The geometry of the air cannon position relative to the surface sample was used to calculate a required horizontal speed in order to achieve the same vertical speed of 6.8 ms^{-1}. Light gates were positioned in front of the surface and the air cannon pressure adjusted until the horizontal speed measured by the gates was as required. The impacts were filmed at 7000 frames per second using the Phantom camera previously described.

9.9.c   Results – speeds
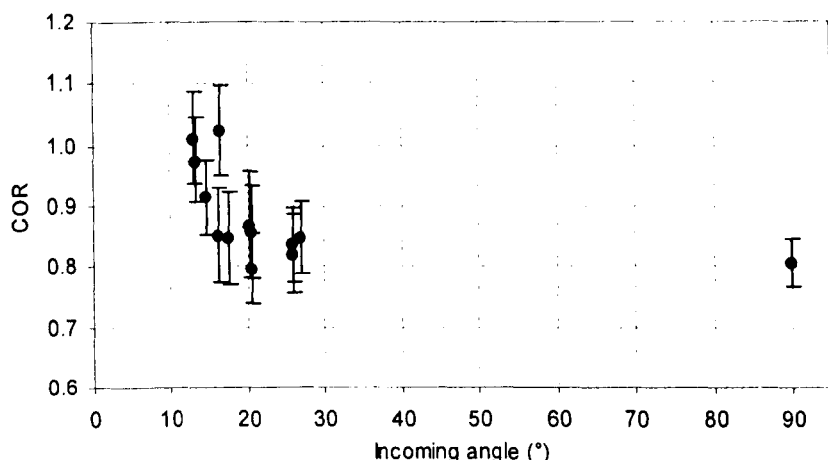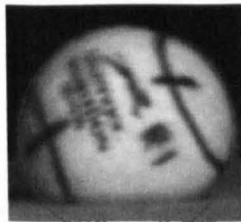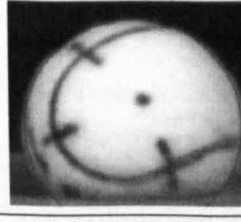
Figure 9.39 COR data for impacts at various angles with the same normal velocity component.

The COR for each impact is shown in Figure 9.39, together with the effect one standard deviation either way on the measured velocity makes to the COR. This shows that there seems to be a sudden decrease in COR as the angle is raised above 20 degrees, although the errors are large. These errors were calculated by finding the standard deviation of the incoming and outgoing speeds for each impact, and finding the maximum possible change on the COR (e.g. adding one outgoing SD to the outgoing speed and subtracting the corresponding incoming SD from the incoming speed would give the max COR). This is a reflection on the problems with measuring speed from a relatively small number of data points over a short time period. It can be seen that the steeper the angle, the smaller the error – because the speed reduces and thus the ball remains in the field of view longer.

9.9.d   Results – deformation shapes

Examples of the deformed shapes of the ball are shown in Table 9.3. For each angle a single frame is reproduced at the point of maximum deflection. It is immediately clear that for this vertical impact velocity, all the impacts keep roughly the same deformation shape, and the part of the ball seen above the surface stays close to a truncated sphere. This spherical shape is not perfect, as a small amount of bulging can be seen outside the circular line drawn. This will lead to an error in any assumption of mass distribution, moving the centre of mass and changing the moment of inertia slightly. This error will however be acceptably small, as the images shown are at maximum deflection and therefore the "worst case" frames, and even in these images the bulging shown is not a large feature.

Table 9.3 Comparison of deflection shapes for oblique impacts at various angles.

Impact angle to horizontal (degrees)	Shape at maximum deformation
14	
17	
21	
26	
(normal impact)	

9.9.e   Results – positional data
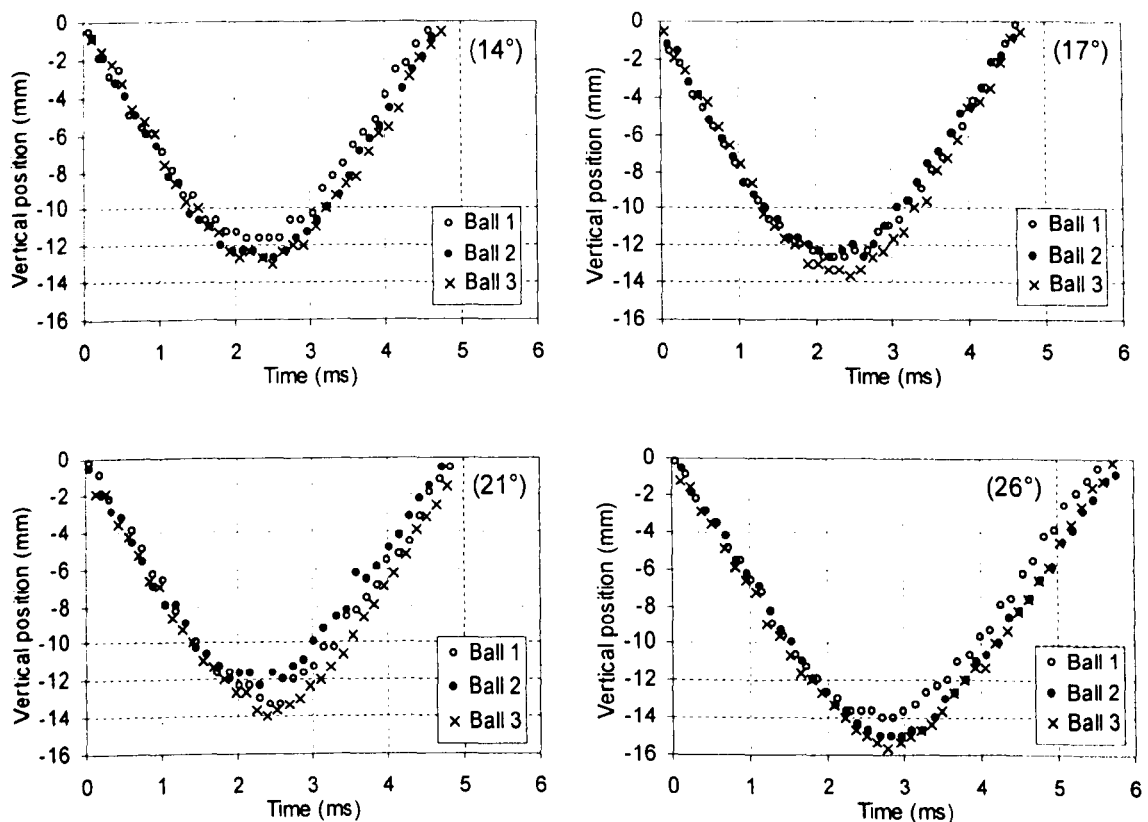
Figure 9.40 (a-d) Vertical displacement against time for three balls at each angle.

Vertical positional data is shown in Figure 9.40 (a-d). It can be seen that there is a degree of scatter in the data, but it is not consistent in terms of which ball deforms more. The size of the ball on the video footage means that the analysis error is as low as possible.
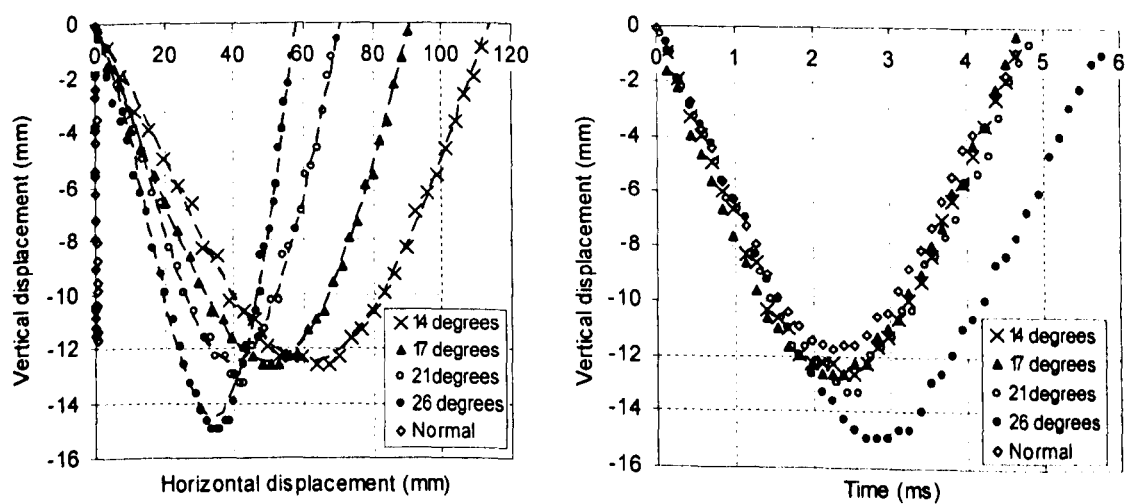
Figure 9.41 Comparison of vertical displacements for oblique impacts – one ball shown at various angles with the same vertical velocity component, plotted against (a) horizontal displacement, and (b) time.

The "middle" ball from each graph in Figure 9.40 was used to compare the positional data at each angle as shown in Figure 9.41. The ball projected at the steepest angle of 26 degrees has a deformation of a little under two millimetres more than all the other impacts, which were reasonably similar. This is particularly noticeable when the vertical displacement is plotted relative to time as in Figure 9.41.

To investigate this further, the equation developed in Chapter 3 was used to estimate the minimum angle needed for rolling to occur. It was found that the steepest angle of 27° was the only one where the impact angle exceeded the required minimum angle for rolling. It is unclear if this is relevant however, as the rolling will only happen towards the end of the impact period.

9.10 Discussion

9.10.a   The effect of impact conditions on "friction" measurements

Throughout this chapter, the relationship $\Delta V_x / \Delta V_y$ has been used as an experimental measure of the friction between ball and surface during impact. A combined set of data from the first part of this chapter (balls on a single surface varying spin, speed and angle in turn) was used to look at this calculated variable over a variety of impact conditions.
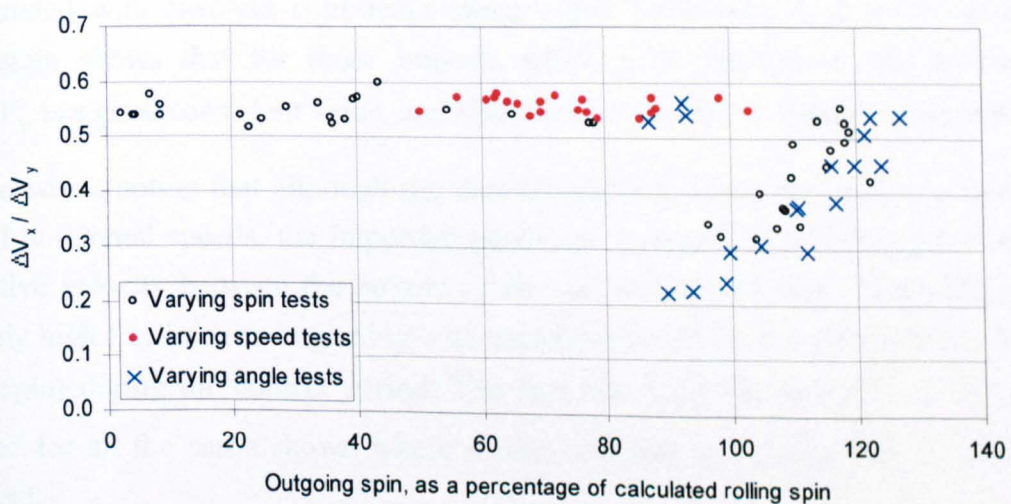
Figure 9.42   Change in horizontal velocity divided by change in vertical velocity, plotted against calculated rolling spin. The data is split into the three sets where the spin, speed and angle were varied in turn.

Figure 9.42 shows $\Delta V_x / \Delta V_y$ plotted against calculated rolling spin. This shows a clear difference between those impacts which were sliding throughout (where the "friction measurement" is fairly consistent) and those which contained some rolling.
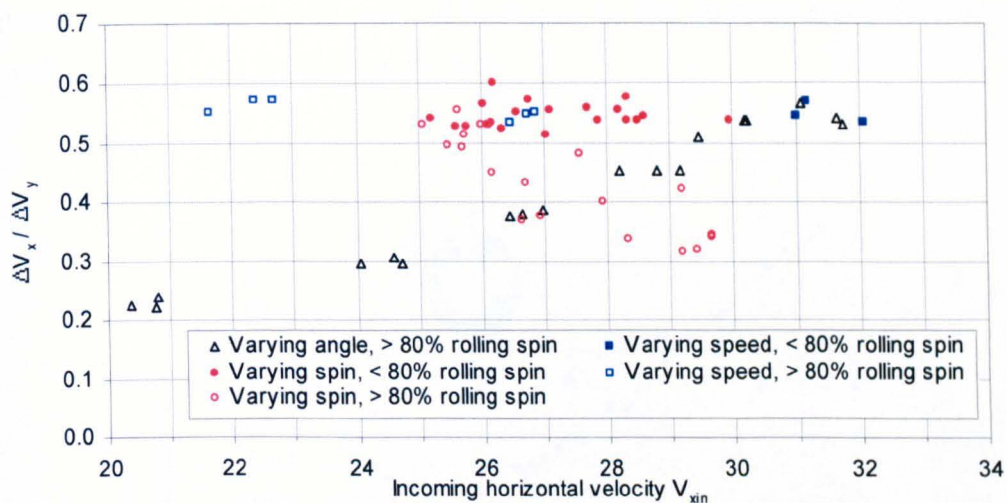
Figure 9.43 Change in horizontal velocity divided by change in vertical velocity, plotted against incoming horizontal velocity.

Figure 9.43 shows the same data plotted against incoming horizontal velocity. In this graph the same shape of symbol is used for each impact series (varying spin, speed or angle) but a solid shape is used for those impacts where the outgoing spin is below 80% of calculated rolling spin (using absolute speed), and an outline shape for those with spin above this value. This arbitrary value was chosen as the rolling spin boundary is not exact, and cannot be calculated with absolute confidence using either horizontal or absolute speed. This graph again shows that for those impacts which slide throughout, the measurement $\Delta V_x / \Delta V_y$ is a good consistent value, and also does not appear to change with speed.

It is also worth noting that although the data shown here seems to be over a fairly small range of horizontal speeds, the important parameter in terms of measuring the friction is the relative velocity between the bottom of the ball and the surface. This will vary from extremely high (for impacts beginning with backspin) to almost zero (for impacts ending at rolling spin) during the contact period. The fact that a consistent value of $\Delta V_x / \Delta V_y$ is produced for all the cases shown where sliding dominates suggests that it is not speed-dependent.

9.10.b The effect of deformation shape on energy loss

Data in this chapter has repeatedly suggested that oblique impacts have a higher vertical COR than normal impacts with the same vertical velocity component. In an attempt to understand this, the deformations during an oblique impact were looked at more closely.

Consider Figure 9.34, showing the COR against spin for surfaces of three different friction. The nominal vertical velocity for 30 ms^{-1} at 24° is 12.2 ms^{-1}. At this speed, a normal impact would have a COR of about 0.7. The incoming spins giving this same vertical COR

for oblique impacts are about 400 rads^{-1} of backspin for the medium and slow surfaces, and 200-300 rads^{-1} of backspin for the fast surface.
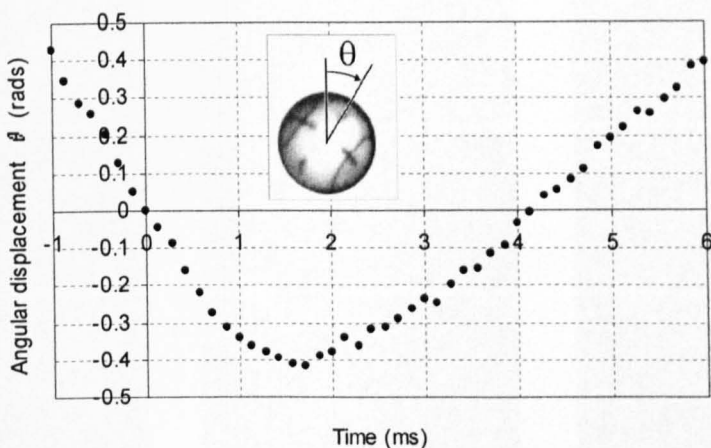
Figure 9.44 Angular displacement against time, for an oblique impact with 400 rads^{-1} of incoming backspin.

An example of angular displacement versus time is shown in Figure 9.44 for an impact on the medium friction surface with 403 rads^{-1} of incoming backspin, which had a vertical COR of 0.70. The rotational data is normalised to give zero displacement at the start of impact. It is immediately apparent that the curve is roughly symmetrical, with low spin rates in the period 1 to 3 ms where the forces are highest. When the video footage is watched, it is clear that the incoming spin rate affects ball deformation. Balls with incoming topspin keep a much more spherical shape than those with backspin, and there is very little deformation of the top half of the ball. In contrast, those with large amounts of incoming backspin experience a buckling of the top portion of the ball, together with vibrational oscillations after impact. Both of these processes will result in energy loss. It is also apparent that the highest buckling of the top portion of the ball occurs when one part of the structure remains at the same angular position, and that the buckling occurs along the same direction as the motion. A comparison of deformation shapes can be seen in Table 9.4 and Table 9.5, which show alternate frames for impacts with 600 rads^{-1} of backspin and 720 rads^{-1} of incoming topspin respectively. Although there is ball deformation in the impact with applied topspin, it is much less than that for the impact with applied backspin, which is reflected in the energy losses seen in the COR data.

Table 9.4 Deformation shapes for a ball impacting at 27 degrees to the horizontal with 600 rads^{-1} of backspin.
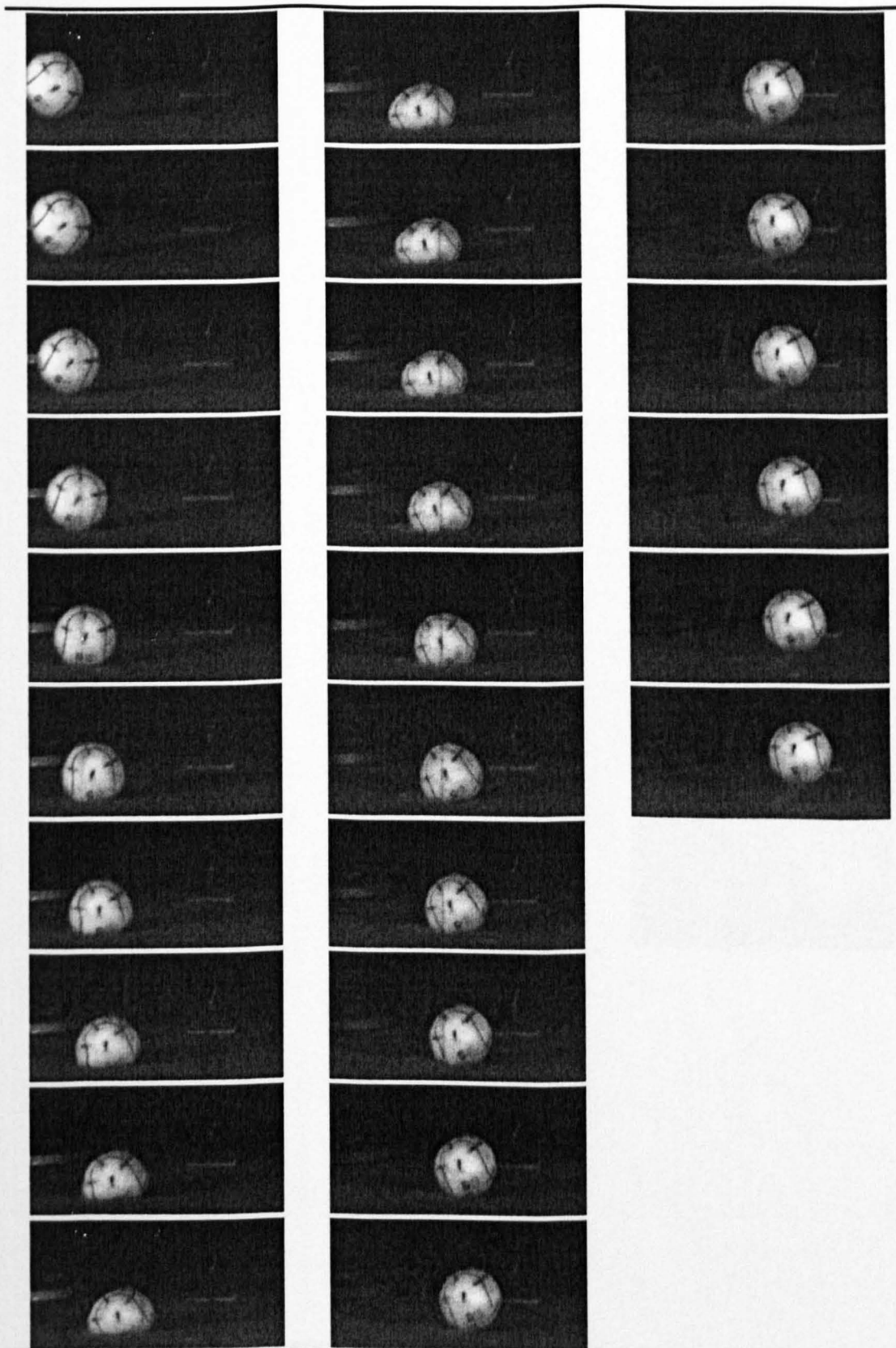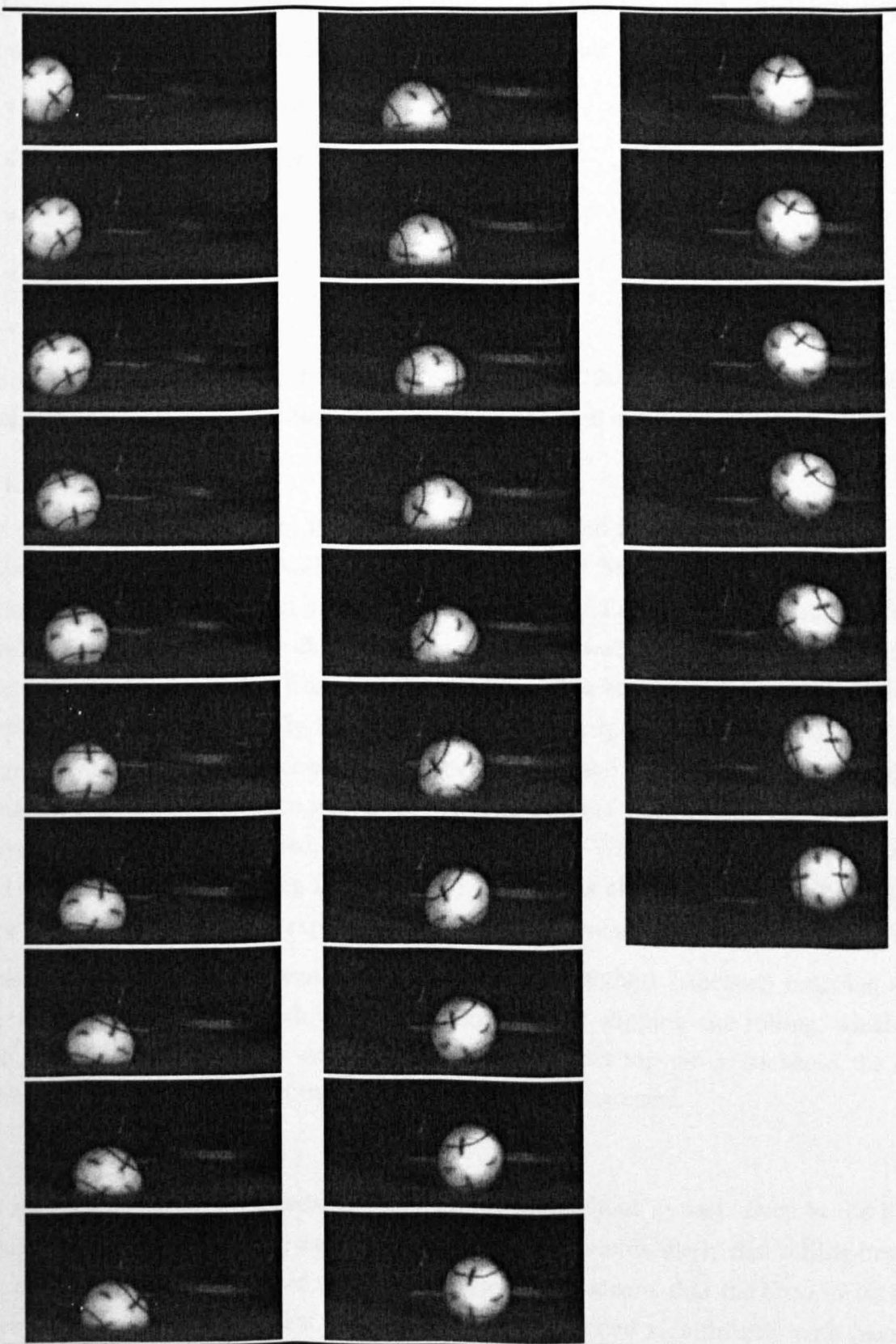
Table 9.5 Deformation shapes for a ball impacting at 23 degrees to the horizontal with 720 rads^{-1} of topspin.

9.11 Summary

In this chapter, a series of experimental oblique impacts was presented which attempted to isolate each in turn of the many factors affecting ball-surface interaction, specifically:

- Ball speed before impact

- Ball angle before impact

- Ball spin before impact

- Ball construction

- Court surface friction

The impacts were filmed at a mixture of 240, 400 and 7000 frames per second, and the footage used to measure velocities and spin rates before and after impact.

9.11.a   The effect of spin

It is clear from Figure 9.12 (b) that for the conditions used in this experiment, there is an incoming spin which caused rolling to occur. This change from slipping throughout to just rolling at the end of the impact happened to occur at around zero incoming spin, but this is merely a function of the angle chosen and the friction between the ball and the surface. On a slower surface with higher friction, balls would need to start with backspin to maintain slipping throughout impact. Figure 9.10 suggests that the speed stays fairly constant for a range of spins if the slipping condition applies. As more and more time is spent rolling the cumulative effect of the frictional force reduces and the ball speeds up. When large amounts of backspin are applied, the vertical COR drops. When there is a small amount of spin or the ball rolls (including large topspin) the COR is almost constant. When the ball slips throughout impact, the expression $\Delta V_x / \Delta V_y$ is almost constant and seems a good measure of the friction between ball and surface. The highest (steepest) outgoing angle occurred for the impacts which were on the boundary of slipping and rolling, which was with almost no incoming spin. As spin was applied as either topspin or backspin, the angle decreased. This was a result of two different physical mechanisms.

9.11.b   The effect of speed

For most of the range of speeds, the ball slipped throughout impact. Even at the lowest speed where it may be rolling as it leaves the surface, it seems likely that rolling has only just occurred before the end of the contact period. This means that the drop in frictional force will have very little effect. The vertical COR dropped significantly with incoming speed, but remains higher than for normal impacts with the same vertical velocity component.

9.11.c The effect of angle

Again there is only one set of impacts which appear to contain rolling, but in this case there is a noticeable effect on the outgoing conditions. The lowest speed and highest spin are achieved for those conditions which are the boundary between sliding throughout and rolling. Moving the angle either way increases the speed and lowers the spin.

9.11.d The effect of ball construction

Ball construction does not have as great an effect on ball speed as might be expected, as speed is dominated by the horizontal component. The COR does vary significantly, and therefore the rebound angle changes. This means that the ball would reach the opposing player at the same time, but at a different height – if it was hit at the same speed. The different balls will of course come off the racket at different speeds however. There was no significant difference in spin generated by the different ball types.

9.11.e The effect of surface friction

As might be expected, the surface friction has a large effect on ball rebound speed. This difference is reduced as incoming topspin is applied, as the different surfaces approach the same trendline of speed versus spin. The slow, medium and fast surfaces seem to achieve rolling with applied spins of zero, 200 and 600 $rads^{-1}$ of topspin respectively. There is no significant COR difference across the surfaces, meaning the balls will bounce to similar heights, but there is a large difference in horizontal component and therefore both time to reach the opponent and angle of trajectory.

9.11.f The effect of ball deformation shapes

The video footage from the main sets of tests suggested that ball deformation was an important factor in energy loss, and that ball deformation depends on the spin rate throughout the impact – and therefore incoming spin and surface friction. A separate experiment found that the vertical deformation stayed constant for balls fired at different angles with the same vertical velocity component (7 ms^{-1}, the same as a normal 100 inch drop test), apart from the steepest angle tested. This angle was the only angle where the ball rolled by the end of the impact (according to simple theory). This experiment also found that the visible part of the ball retains the same shape above the surface and appears to be a truncated sphere. This contrasts with the video footage of impacts with higher vertical velocity components (12 to 15 ms^{-1}), where the ball most definitely changes shape. For these impacts with higher vertical speed, the spin throughout impact seems to be the key to a changing COR due to its effect on ball deformation shapes and therefore energy loss – when the applied spin means that the angular rotation stays low through the impact period where the forces are highest, there is more deflection and thus more energy loss. Momentum causes the part of the ball shell at the rear (if a line is drawn along the velocity

vector) to deform or buckle inwards to varying degrees. When there is topspin applied, this does not happen as this momentum is taken round the shape of the ball by the angular rotation.

10 Oblique impact model

10.1 Introduction

The normal model previously presented proved to simulate ball impacts very well, and gave good predictions of the force data throughout the impact period as well as just outgoing conditions. This suggested that it was a good representation of the physics of the impact and could be extended to a second dimension. In this chapter further properties of horizontal displacement, velocity and force are introduced, as well as the rotation variables needed to predict spin. The model was created as a standalone program as it became too complex to be calculated easily in a spreadsheet. A variety of experimental data was used to validate the model predictions.

10.2 Model Overview

A number of authors have proposed normal models which give reasonable representations of normal impacts, but oblique spinning models are considerably more complicated. One aspect in particular which has never been modelled analytically is the generation of spin, and how the ball deformation affects this.

As in the normal model, the forces on the ball are made up of a combination of structural stiffness, damping and impulsive reaction forces. The first two of these can be directly transferred into an oblique model, but the impulsive force is more complicated. Each of these forces is discussed in more detail below.

One of the first assumptions to be made in the oblique model was that the vertical displacements, velocities and forces (apart from the impulsive force) acted in the same way as for a normal model with the same components. The experimental data in Chapter 9 suggested that this is not strictly the case, but the deformation shapes are far too complex to be easily modelled.

Throughout this chapter, three ball construction types were considered. The oversized ball, although it behaved somewhat differently in terms of force data throughout impact, had rebound characteristics so close to a conventional pressurised ball that it was not considered further, and the decision made not to include it in the oblique model. The only difference between the oversized and normal pressurised ball was the force data, which could not be measured for oblique impacts.

10.2.a   Ball geometry and deformation shapes
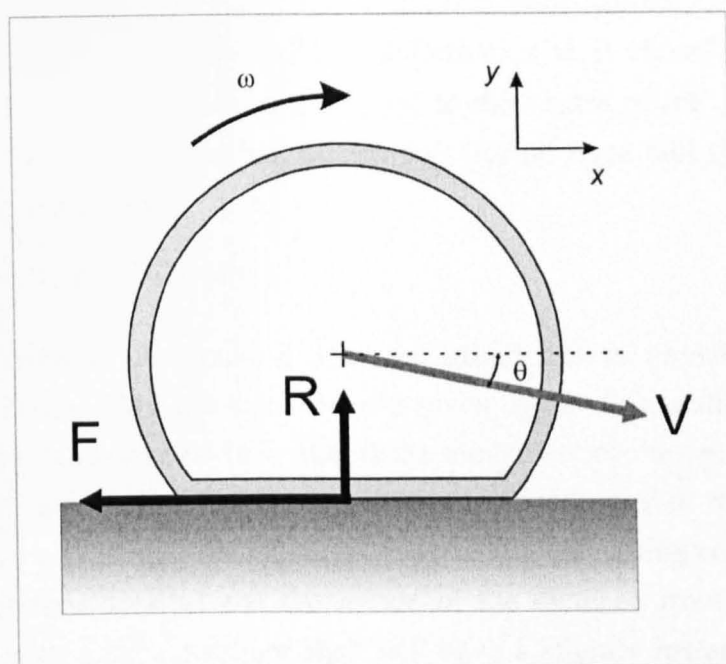
Figure 10.1 Defining the geometry and model space of the ball during oblique impact.

A tennis ball part-way through an oblique impact is show in Figure 10.1. A single variable x was used to define the position in the normal impact model of chapter 8, but the axes are changed when a second degree of freedom is introduced. The variable x is now used to denote horizontal movement, and y the vertical displacement of the centre of mass. The ball has velocity V acting at an angle θ to the horizontal. Forces acting on the ball are a normal reaction force R and a horizontal frictional force F, which will be discussed in more detail.

The geometry of a deformed tennis ball was discussed in detail in Chapter 8. To summarise, the shape that the ball assumes when it is compressed is an important factor in creating an accurate model. The model is defined in terms of a centre of mass displacement, but this must be related to physical ball deformation in order to calculate both the damping and impulsive forces. It is also important when the model is extended to simulate oblique impacts. Spin on the ball is generated by forces which do not act through the centre of mass, and therefore the moment arm (defined as the perpendicular distance between the centre of mass and the line of action of the force causing the moment) is important. After calculating a rotational torque, the moment of inertia of a deformed ball must also be taken into account to find the rotational acceleration.

In summary, the work in Chapter 8 considered two deformation assumptions: buckled (where the ball deformation is inverted inside the original shape) and truncated (where a flat circular contact area is formed). The decision was made to use the truncated shape, as this was felt to be more representative for the relatively minor deformations found in

oblique impacts (where the normal component of impact speed is often less then 10 ms^{-1}). It was found that the ball construction had negligible effect on the relationship between centre of mass position y and physical ball deformation δ. It should be noted that this position y is relative to its original position, not to the centre of the displaced ball. The relationship used for the truncated ball assumption (for all three ball types considered) is given by (for units in metres):

$$\delta = 27.203y^2 + 0.9645y \qquad\qquad [10.1]$$

The reason that the ball construction does not affect this relationship is that a large proportion of the centre of mass displacement is given by the deformation of the bottom of the ball, and the ball construction only affects the movement of the centre of mass relative to the centre of an undeformed ball (or another way of looking at it, relative to the top of the ball). But when considering the moment of inertia, the governing equation is a function of mass (and therefore density) and the square of the distance from centre of mass. A pressureless ball with a thicker rubber shell will have a slightly lower moment of inertia than a conventional pressurised ball due to the mass being shifted towards the centre. The external diameter of the rubber shell remains the same, but the internal diameter moves inwards, lowering both the average radius and the density. The difference between I for pressurised and pressureless balls was found to stay roughly the same as deformation increased, giving pressureless balls on average a value about 2.5% lower. The functions defining the moments of inertia are given in Table 10.1 (again, for SI units).

Table 10.1 Ball moment of inertia as a function of centre of mass movement, for different ball construction types.

Ball deformation type	Moment of inertia I as function of COM movement y
Pressurised / punctured	$I = 3.2428 * 10^{-5} - 0.030558y^2 - 3.4082 * 10^{-5}y$
Pressureless	$I = 3.1541 * 10^{-5} - 0.032638y^2 - 3.9665 * 10^{-6}y$
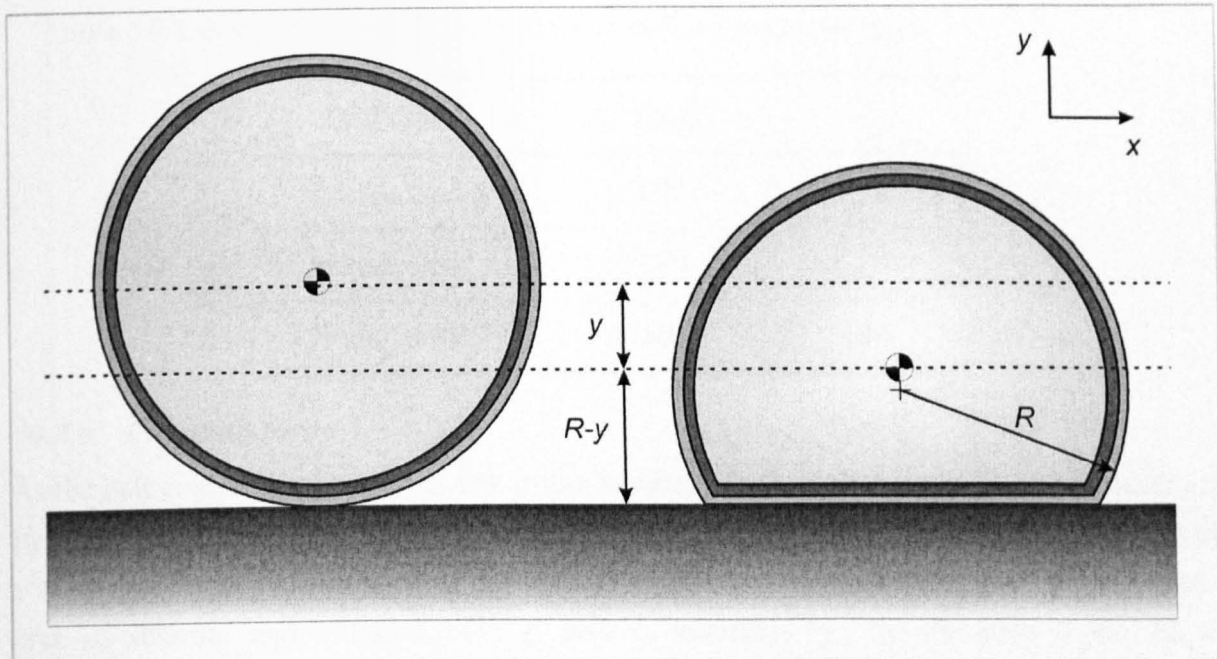
Figure 10.2 Ball geometry showing the moment arm for a frictional force on a deformed ball during oblique impact.

When calculating spin, the moment arm distance is critical. Although a number of previous geometry calculations have been rather complicated, the moment arm is simply the difference between the radius and the centre of mass displacement variable y as used in the model – there is no need to calculate physical ball shapes. This is illustrated in Figure 10.2, which is defined by a centre of mass displacement y. In order to calculate the external ball deformation would need some knowledge of the displacement of the centre of mass relative to the undeformed ball, but the moment arm is just the distance from the centre of mass to the surface – which is R-y on the figure above.

10.2.b Structural force

The structural force is modelled as a spring whose stiffness varies with ball deflection. For a vertical centre of mass displacement y the governing equation giving the stiffness k is given in [10.2] below. The spring stiffness parameters k_0 and A were found in the normal model discussed in Chapter 8, and are given in Table 10.2.

$$k = k_0 e^{Ay}$$ [10.2]

Table 10.2 Spring stiffness model parameters for the various ball types.

Ball type	k_0 (N/m)	A
Pressurised	21000	50
Pressureless	22500	25
Punctured	13600	50

10.2.c Damping force

As the ball compresses, energy is lost in the bending of the rubber wall. This is represented by a damper component. The damping coefficient is a function of ball deformation, and was chosen to be proportional to the contact cross-sectional area. For the rubber contact area of internal and external radii r_i and r_o respectively, the damping force F_D is proportional to the constant C_0 and ball shell velocity V as given by

$$F_D = C_0 \left(r_i + r_o \right)^2 V \qquad\qquad [10.3]$$

The damping coefficient C_0 for each ball type is shown in Table 10.3.

Table 10.3 Model damping parameters for the various ball types.

Ball type	C_0 (Ns/m^3)
Pressurised	4000
Pressureless	3800
Punctured	4500

10.2.d Impulsive force

As in the normal model, an impulsive reaction force is caused by the instantaneous velocity change of material as it comes to rest on the surface. However, the situation is complicated by the spin on the ball – even a ball projected without spin will generate spin during an impact due to the frictional force and the rotational moment this produces. Spin on the ball means that the velocity is not constant across the cross section which is in contact with the ground at any particular instant. For example, topspin will increase the downwards velocity at the front of the ball and decrease it at the back, with a variation in between.
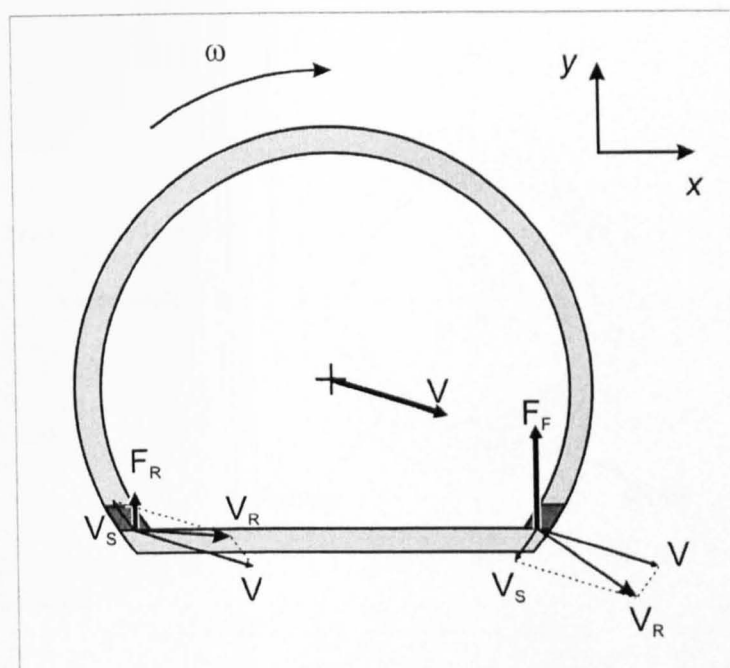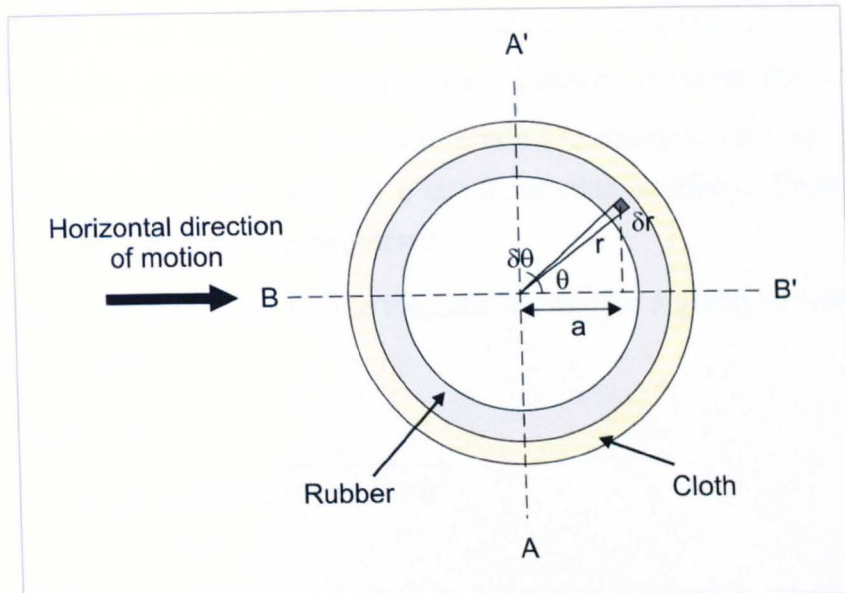
Figure 10.3 Impulsive reaction forces on a spinning ball during an oblique impact, and the resultant velocities (due to spin) causing these forces.

A cross-section through the centre of the ball is shown in Figure 10.3. The ball lands with an oblique velocity V and topspin ω. There is also a velocity component due to the spin, which is shown as V_S relative to the velocity of the ball centre. When V and V_S are combined, the resultant velocity V_R is different at the front and back, leading to differing reaction forces F_R. At a different position around the contact annulus the effective radius about the spin axis will change, affecting the value of V_S. There will therefore be a distribution of velocity and force throughout the contact area. If the topspin is high enough there may be parts of the ball (towards the rear) where the resultant velocity is upwards, and therefore no impulsive force. There can of course be no force in the opposite direction due to this upwards velocity.

(a)

(b)
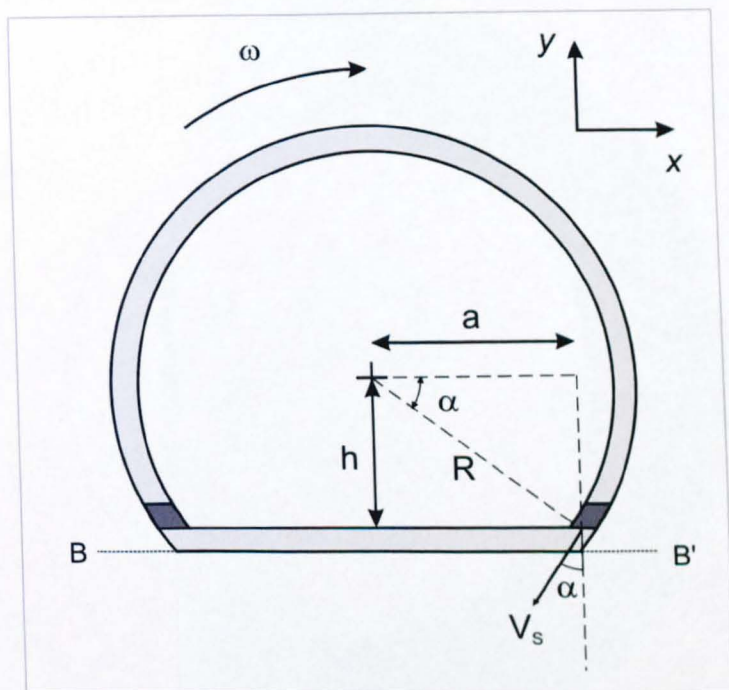
Figure 10.4 Cross-sections of the ball during an oblique impact, showing (a) a horizontal slice of the contact area, and (b) the geometry of the velocity.

For the small element shown in Figure 10.4 (a) - which is at a vertical distance h below the ball centre - the velocity due to spin V_S will be the spin rate ω multiplied by the radius R about the spin axis. This will be given by

$$R = \sqrt{a^2 + h^2}$$
$$= \sqrt{r^2 \sin^2 \theta + h^2}$$

Thus $V_S = \omega R$

$$= \omega \sqrt{r^2 \sin^2 \theta + h^2}$$

where vertical height h is a function of ball deformation. The impulsive force is caused by the vertical component of the spin velocity, i.e. $V_S \cos\alpha$. Because the combination of rotational and translational velocities results in a non-symmetrical velocity profile around the contact area of the ball, there will be a net horizontal impulsive force, but this was found to be extremely small and was neglected.

Thus the resultant vertical velocity for the element shown (for a given vertical speed due to the motion V_y) is given by

$$V_{R_Y} = V_y + V_S$$
$$= V_y + \omega \cos\alpha \sqrt{r^2 \sin^2\theta + h^2}$$
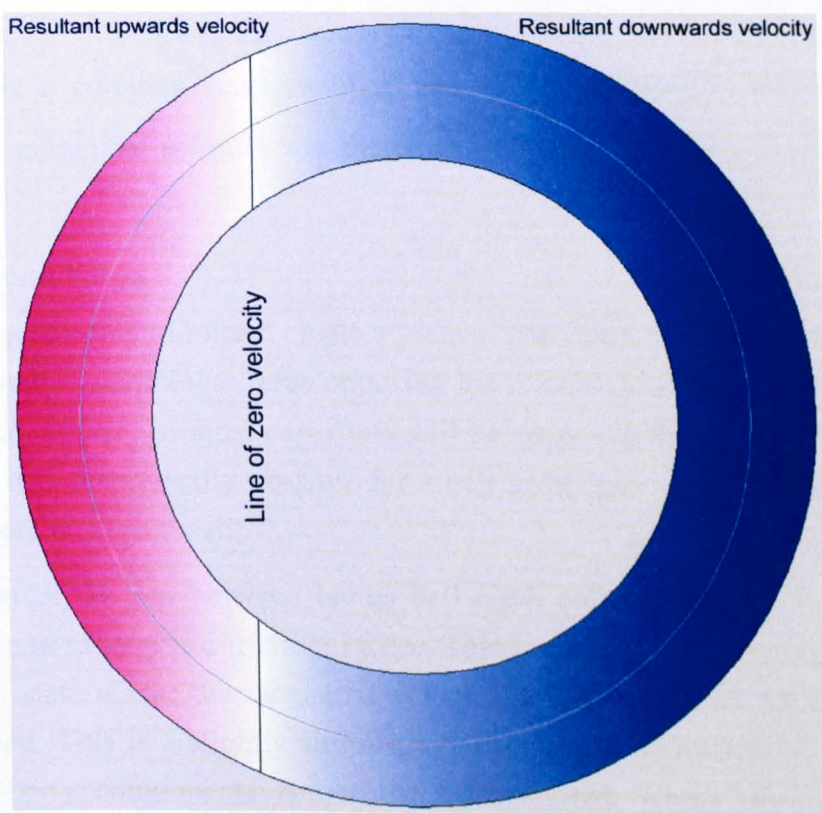
Figure 10.5 Velocity profiles across the ball cross-section.

A program was written to calculate the velocity across the cross-section for visualisation purposes. An example is shown in Figure 10.5, for a slice taken 11.7 mm above the surface. Both the cloth and rubber layers are shown, giving overall values for internal radius and external radius of 16.6 and 25.2 mm respectively. The downwards speed at the time instant chosen was 4 ms^{-1}, and the topspin 400 rads^{-1}. Vertical lines show the boundary of zero velocity; to the right of these lines the velocity is downwards and to the left it is upwards. In either case a darker colour indicates a higher velocity. Because of the axis of spin, the velocity is purely a function of the position towards the front or back of the ball.

As in the normal model, the impulsive force is given by calculating the rate of change of momentum. This momentum change per unit time for the small element shown is equal to the mass of the element hitting the surface per unit time multiplied by the speed. The mass rate is given by the area δA multiplied by the density ρ, multiplied by the speed V_{R_y}. This gives an impulsive force δF for the element,

$$\delta F = \rho \, \delta A \, V_{R_y}^{2}$$

Integrating for the total contact area (which must be done separately for the cloth and the rubber),

$$F = \rho \int_{r_i}^{r_o} \int_{0}^{2\pi} r V_{R_y}^{2} d\theta dr$$

Because V_{R_i} is a complex function of R and θ, this integral is impossible to solve analytically. A numerical solution was therefore written in software, as described later in this chapter.

10.2.e   Frictional force

The various mechanisms of impact create a vertical reaction force. The model assumes that this reaction creates a frictional force opposing the relative motion between the bottom of the ball and the surface. In most cases this will be opposing the horizontal motion of the ball, although it is theoretically possible for a ball to bounce with such a high amount of topspin that there is "topspin slip".

The coefficient of friction between tennis ball cloth and the surface being used in the model was then used to give a frictional force. This is applied until rolling occurs, which is defined as the state where the tangential velocity at the bottom of the ball matches the horizontal speed. This is a slightly simplistic definition, as there will be a distribution of horizontal velocity components across the contact area. Cross (2002) looked at the interaction of ball and surface during impact and concluded that the ball did not simply roll, but "gripped" the surface, causing horizontal vibrations. A physically realistic simulation would allow certain parts of the ball on the contact area to move while others were stationary. This will cause horizontal deformation of the ball shell and is beyond the scope of this model.

10.2.f   Rotational moments and spin generation

The frictional force described above will create a rotational moment about the ball centre of mass, which acts along the interface between the ball cloth and the surface. Using the moment arm discussed earlier, a torque T can be calculated. Taking into account the

relationship between deformation and moment of inertia I, this gives a rotational acceleration and therefore a change of spin rate ω using $T = I \dfrac{d\omega}{dt}$.

Because a non-symmetrical velocity profile is created by the addition of spin, the impulsive force will also create a moment about the centre of mass. Although this is small, it was calculated and included in the total moment.

10.3 Model software

The complexities introduced by applying the impulsive force equations to an oblique impact meant that it was no longer possible to solve it in a simple manner using a spreadsheet. A stand-alone piece of software was therefore written in Visual Basic.

The structural and damping forces were simple calculations, but the impulsive force was worked out numerically for each timestep. The contact area was split into a number of elements (the radius was split into ten, and the angle one hundred, giving a total of a thousand elements). The area of each element was calculated as a proportion of the total contact area.

Apart from the calculations, the model solution method was approached in the same way as for the normal model. Initial boundary conditions of speed, spin and angle are entered, either as absolute values or as horizontal and vertical components. The other parameters are defined on a "per ball" basis, and so the user must simply select the ball type – this then selects the various coefficients as discussed in section 10.2.
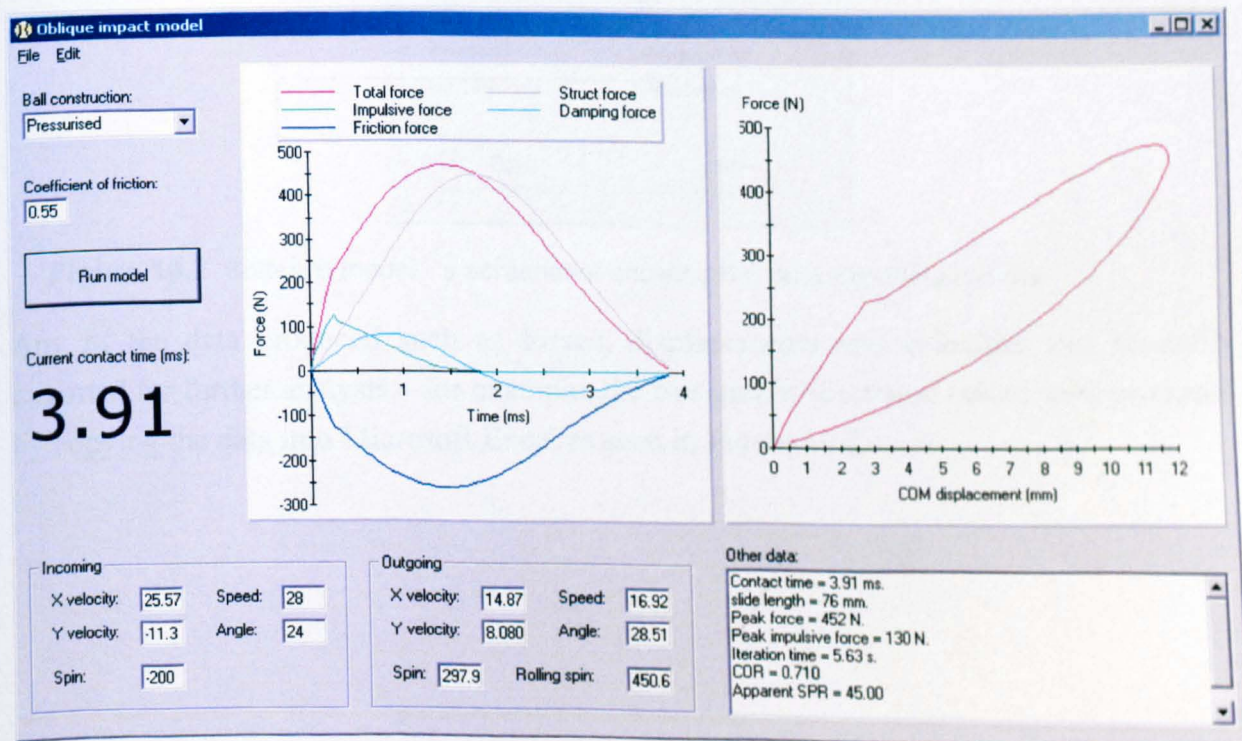
Figure 10.6 Software model - a screenshot of the result of an oblique impact prediction.

A screenshot showing the model results after calculation is shown in Figure 10.6. This gives a quick overview of the results and allows the various forces to be compared. This fairly simple case gives forces as would be expected from a normal model. The structural force is an approximate half sinusoidal, as would be produced by a simple spring. The damping is also a smooth curve which always acts opposing the velocity and so has half the period. The impulsive force rises quickly to give the total force curve its distinctive shape. It also drops fairly quickly, and reaches zero about halfway through the impact. The horizontal frictional force is a simple scaled multiple of the total force, as there is slipping throughout and therefore straightforward frictional interaction.

Various other outgoing parameters can also be seen in the bottom-right hand corner of Figure 10.6, such as the contact time, slide length and COR. Also shown is the "Apparent SPR", which is calculated using the standard SPR equation $\dfrac{\Delta V_x}{\Delta V_y}$. It can be seen that for this case where there is no rolling, this is 45, equal to $100(1-\mu)$.
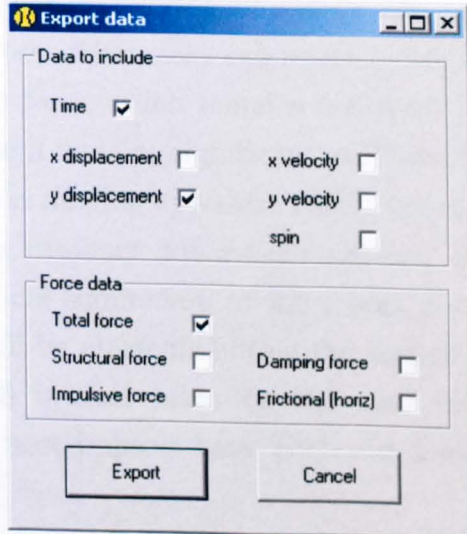
Figure 10.7 Software model - a screenshot showing the data exporting options.

Any of the data produced such as forces, displacements and velocities can be easily exported for further analysis – for example, the two graphs discussed below were produced *by copying the data into Micro*soft Excel as seen in Figure 10.7.
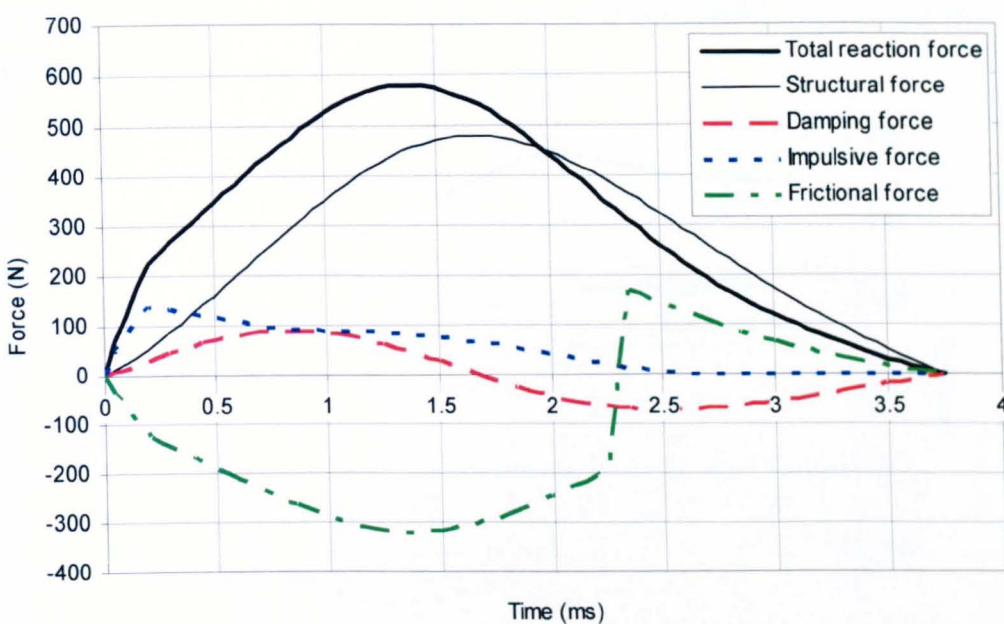
Figure 10.8 Model forces for an oblique impact at 30 ms^{-1} at 24.5° to the horizontal, with 400 rads^{-1} of topspin. All forces except the frictional force are vertical.

A more interesting situation happens during an impact with incoming topspin, as is shown in Figure 10.8. In this case two differences can be seen. The large topspin throughout the impact creates an impulsive force which remains for much longer than for impacts with backspin. In fact, in this case it remains significant well into the second half of the impact, after the ball centre of mass is moving upwards. This is because some portions of the front half of the ball still have a resultant downwards velocity due to the high topspin. The impulsive force is a numerical summation of the forces produced by a large number of elements – so there may still be elements hitting the surface when the ball as a whole is moving upwards (this will in fact often be the case unless the ball impacts with considerable backspin, as most impacts have achieved some amount of topspin by the midway point).

The second difference is a reversal of the frictional force. After about 2.3 ms, the frictional force is positive, which indicates that the ball has enough topspin that the relative motion between ball and surface is in the opposite direction to normal. The intuitive understanding of the situation might suggest that the spin on the ball should reach that needed for rolling, and the friction would "switch on and off", keeping the velocity and spin in step. However, this does not take into account the ball deformations. What happens is that during the middle part of the impact, the ball gains a large amount of spin due to the reduced moment of inertia, while the spin required for rolling increases because of the lowered radius (from the deformed shape). Then as the ball regains its shape, the radius increases back to its original value, and the rolling spin boundary drops "faster" than friction reduces the value

of the overspin. Figure 10.9 shows how the spin increases until overspin occurs and the friction reverses direction.
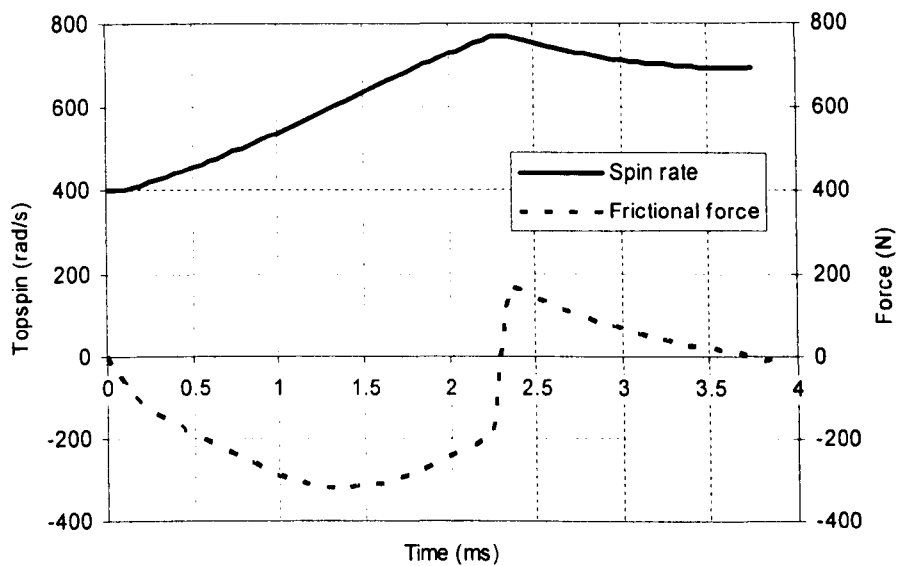
Figure 10.9 Frictional force and spin on the ball during an oblique impact at 30 ms^{-1} at 24.5° to the horizontal, with 400 rads^{-1} of topspin.

10.4 Comparison with experimental data

The various sets of data presented in Chapter 9 were used to validate the model. In each case two of the three incoming variables (speed, spin and angle) were kept nominally constant while the other was varied. In practice the two "constant" variables showed some variability. This variability would be significant enough to affect the rebound characteristics, and so the variation was included in the model boundary conditions, which are described for each set of tests.

Three different surfaces were used. In each case the additional model parameter needed to extend from a normal to an oblique model was coefficient of friction. This was obtained by using a combination of experimental measurements from SPR tests and also the use of a Haines pendulum. The friction values (given later in this chapter) from these two tests matched well.

10.4.a Varying spin tests

These tests measured the rebound conditions for a pressurised ball projected at a nominal speed of 30 ms^{-1} and 24° to the horizontal, with spin ranging from 600 rads^{-1} of backspin to 600 rads^{-1} of topspin. As the spin changed, the impact speed and angle – which was intended to be constant – changed enough to affect the rebound properties. It was therefore important to include this variation in input boundary conditions to the model.
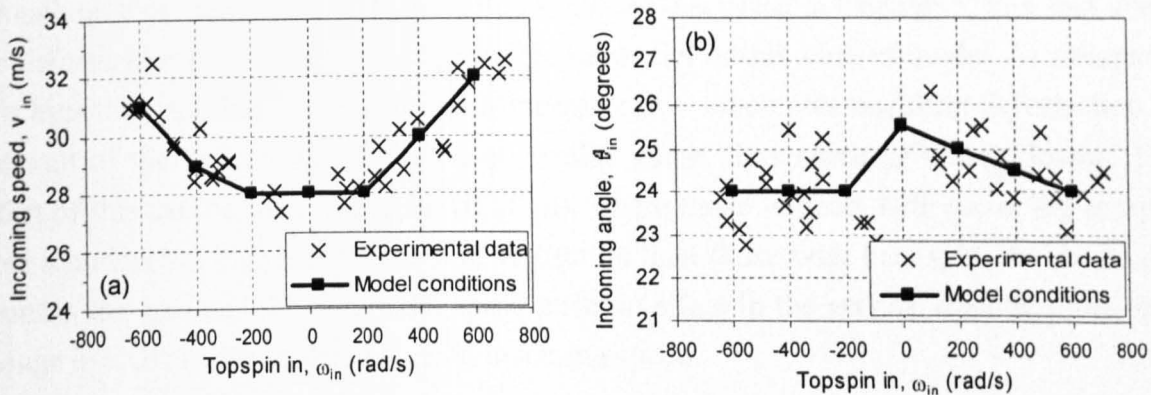
Figure 10.10 (a-b) Model input parameters used at various spins: (a) speed and (b) angle.

Figure 10.10 shows how the impact speed and angle changed with spin, and the nominal value used as a model input parameter at each spin rate.
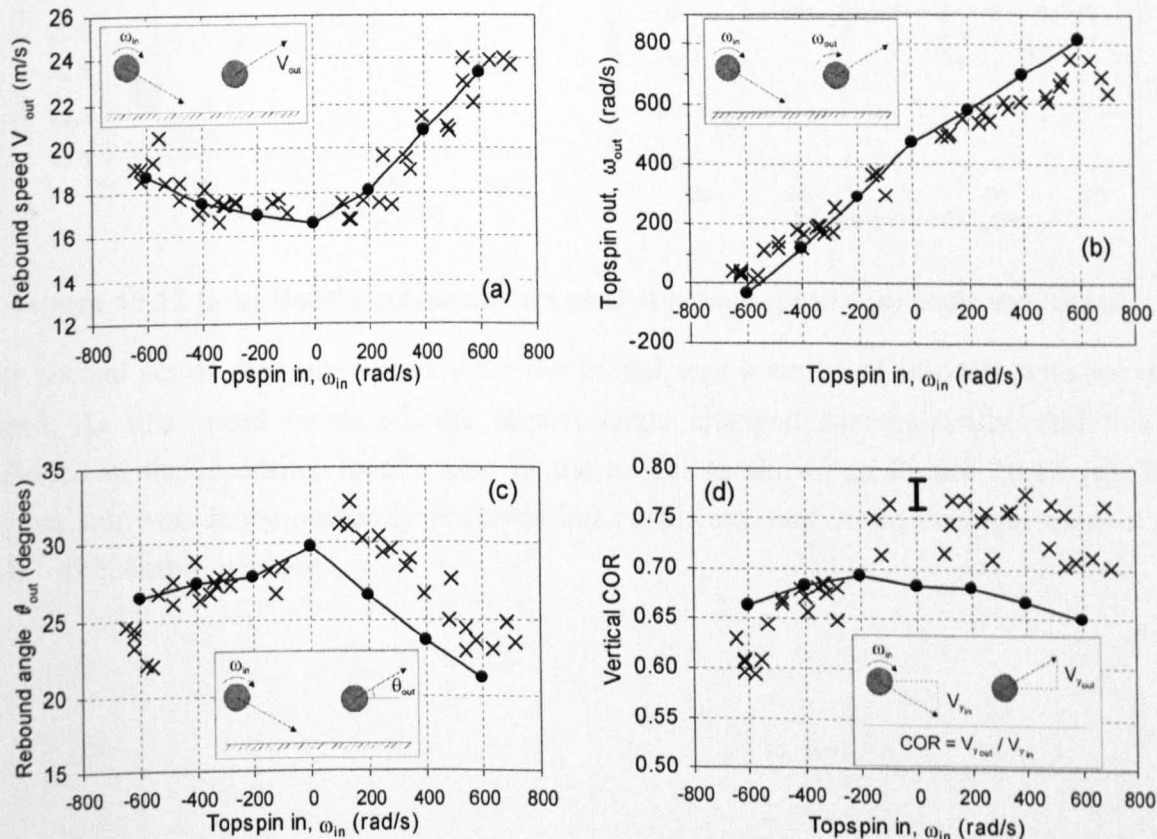
Figure 10.11 (a-d) Comparison of experimental data and model predictions for rebound characteristics of pressurised balls impacting at a nominal speed of 30 ms^{-1} and a nominal angle of 24°, with varying spins.

Figure 10.11 shows the model predictions. The rebound speed predictions are excellent for the full range of input spins. The predicted outgoing spin is a good match for most cases, but becomes too high for large incoming topspin. The rebound angle is accurate for impacts with incoming backspin, but 2 to 3 degrees lower than the experimental values for impacts with incoming topspin. This discrepancy is most likely due to the large topspin

throughout these impacts, and the effect this has. As discussed in Chapter 9, this spin alters the deformation shapes, which is impossible to predict in this kind of model. In summary, it is hypothesised that the impacts with topspin cause much less buckling deformation in the wall of the ball by keeping a more circular shape, thus reducing energy losses. The effect of this can be seen in Figure 10.11 (d), where those impacts with incoming topspin have a noticeably higher coefficient of restitution than those with backspin. As the model assumes the spin and the horizontal speed have no effect in the vertical direction, the only change in COR is due to the change in incoming speed.

10.4.b   Varying speed tests
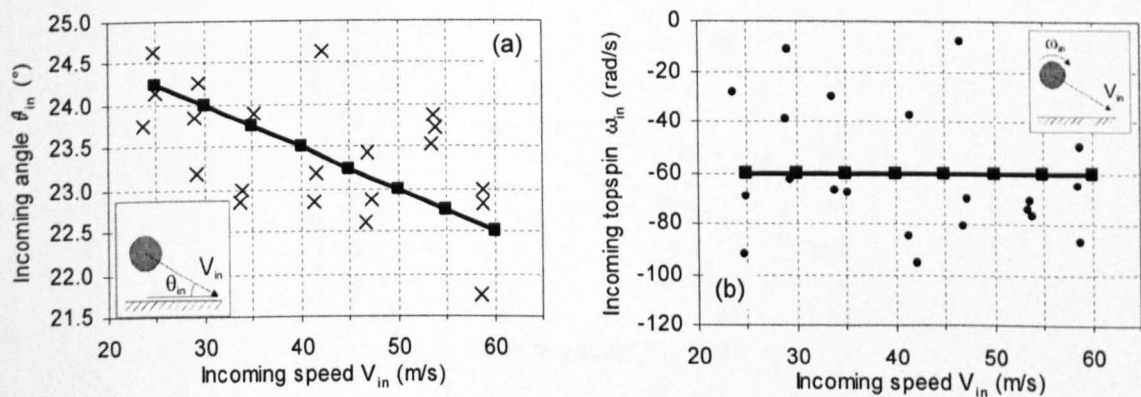
Figure 10.12 (a-b) Model input parameters used at various speeds: (a) angle and (b) spin.

The second set of data used to validate the model was a series of impacts with varying speed. As this speed increased, the impact angle changed systematically, and this is reflected in the incoming speeds used in the model as shown in Figure 10.12 (a). The impact spin was fairly randomly scattered but consistent, and so an average value of 60 rads^{-1} of backspin was used.
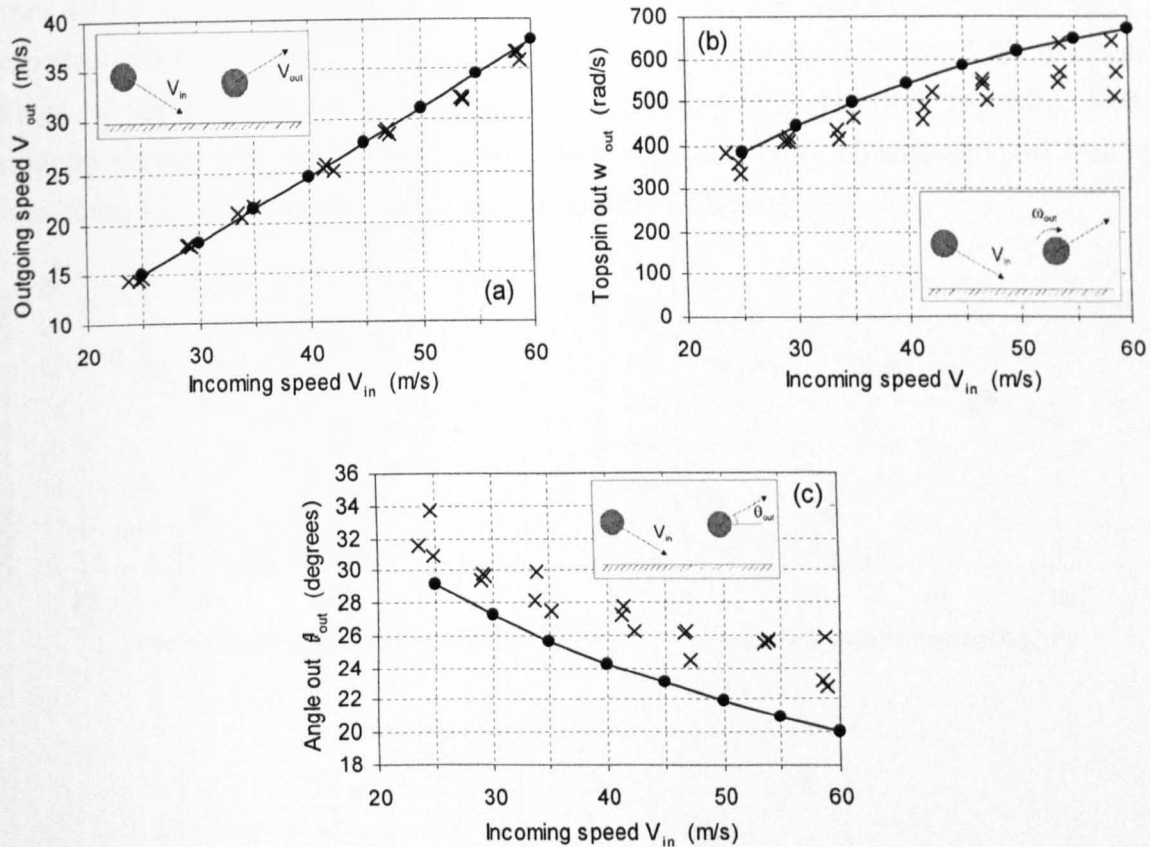
Figure 10.13 (a-c) Comparison of experimental data and model predictions for rebound characteristics of pressurised balls impacting with varying speeds at a nominal angle of 24°, with a nominal value of zero spin.

The rebound speed, spin and angle are shown in Figure 10.13 (a), (b) and (c) respectively. The speed is an excellent match throughout. The model predicts slightly too high spin as the impact speed increases, although the scatter in the experimental data also increases. The angle is consistently 2 to 3 degrees lower than that seen experimentally, suggesting an energy loss that is not reproduced in the model.

10.4.c *Varying angle tests*
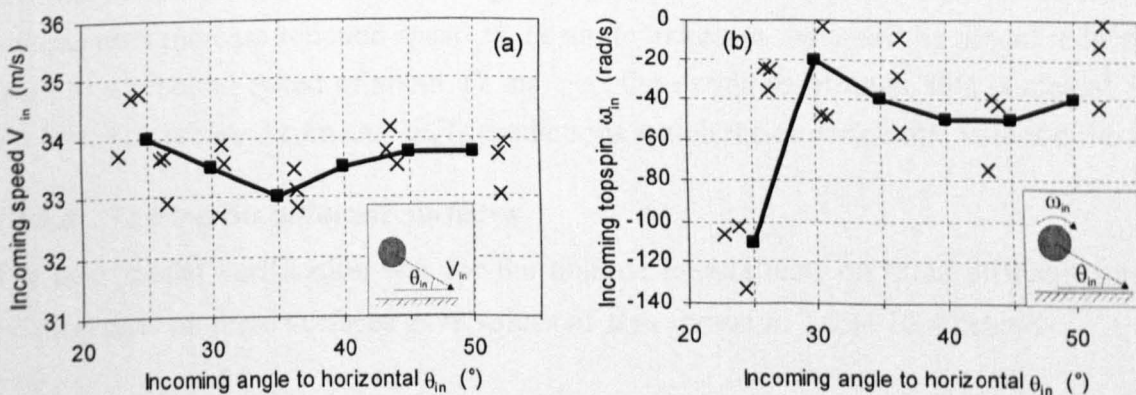
Figure 10.14 (a-b) Model input parameters used at various angles: (a) angle and (b) spin.

Figure 10.14 shows how changes in the angle affected the impact speed and spin. In comparison to the other tests, the speed was fairly consistent (because no change in settings of the Bola projection device were needed, just a physical rotation), with a maximum change of 1 ms^{-1}. The incoming spin was also fairly consistent apart from the values at the shallowest angle, which was noticeably different.
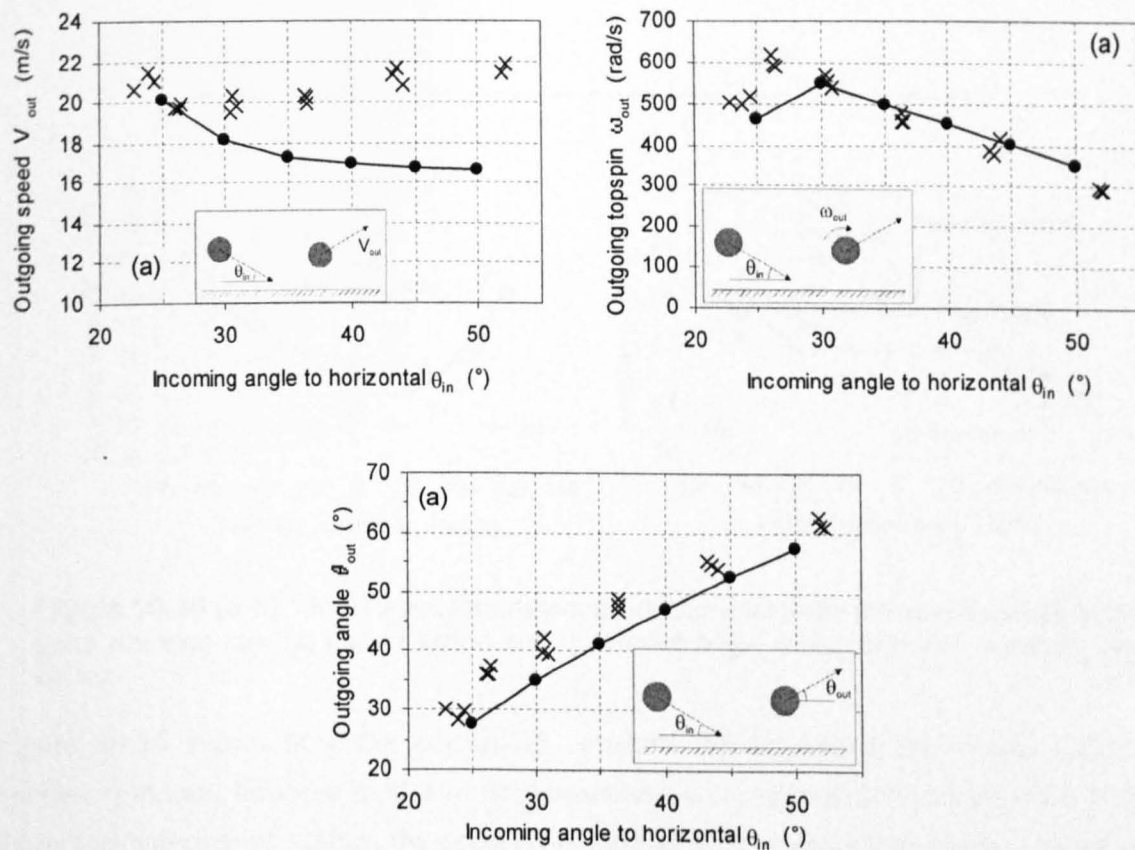
Figure 10.15 (a-c) Comparison of experimental data and model predictions for rebound characteristics of pressurised balls impacting at a nominal speed of 30 ms^{-1} and a nominal value of zero spin, at varying angles.

The model predictions are shown in Figure 10.15. As the angle increases above about 27 degrees, the predictions for rebound speed diverge from the experimental values seen. The oblique tests increase rebound speed as the angle increases, whereas the model reduces and tends to a rebound speed of about 17 ms^{-1}. At the extremes of angle this is almost 5 ms^{-1} too low. The rebound spin and angle predictions match the experimental values quite well.

10.4.d *Testing on different surfaces*

The next model verification was for the oblique impact tests on three different surfaces. Friction tests on these surfaces gave values of μ as shown in Table 10.4 below.

Table 10.4 Coefficients of friction for the three different surfaces used.

Surface	Coefficient of friction μ
Slow	0.61
Medium	0.55
Fast	0.3
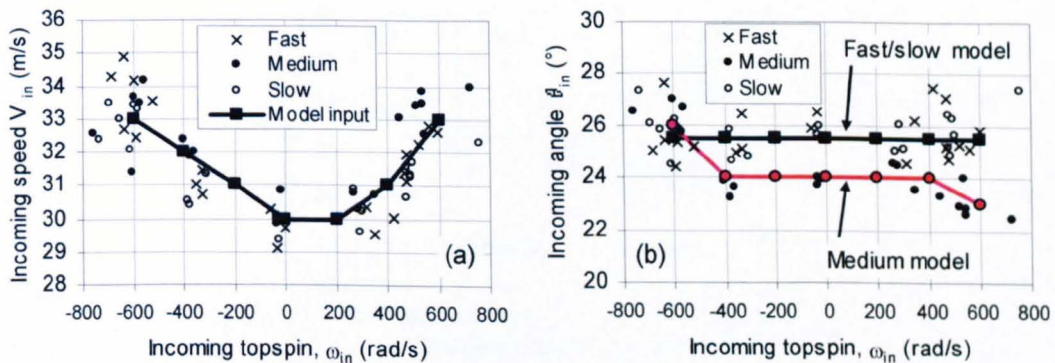
Figure 10.16 (a-b) Model input parameters used to predict three different surfaces at different spins, showing how (a) impact speed and (b) impact angle varied from the nominally constant values.

Figure 10.16 shows how the nominally constant *impact speed and angle varied with* applied spin, and how the model input parameters were adjusted to reflect this. Although there was a degree of scatter, the speed was judged to have the same average value for the tests on each surface. There was a slight difference in the angle data, where the balls projected onto the medium speed surface were consistently lower than the other two surfaces (apart from for the highest amount of applied backspin).
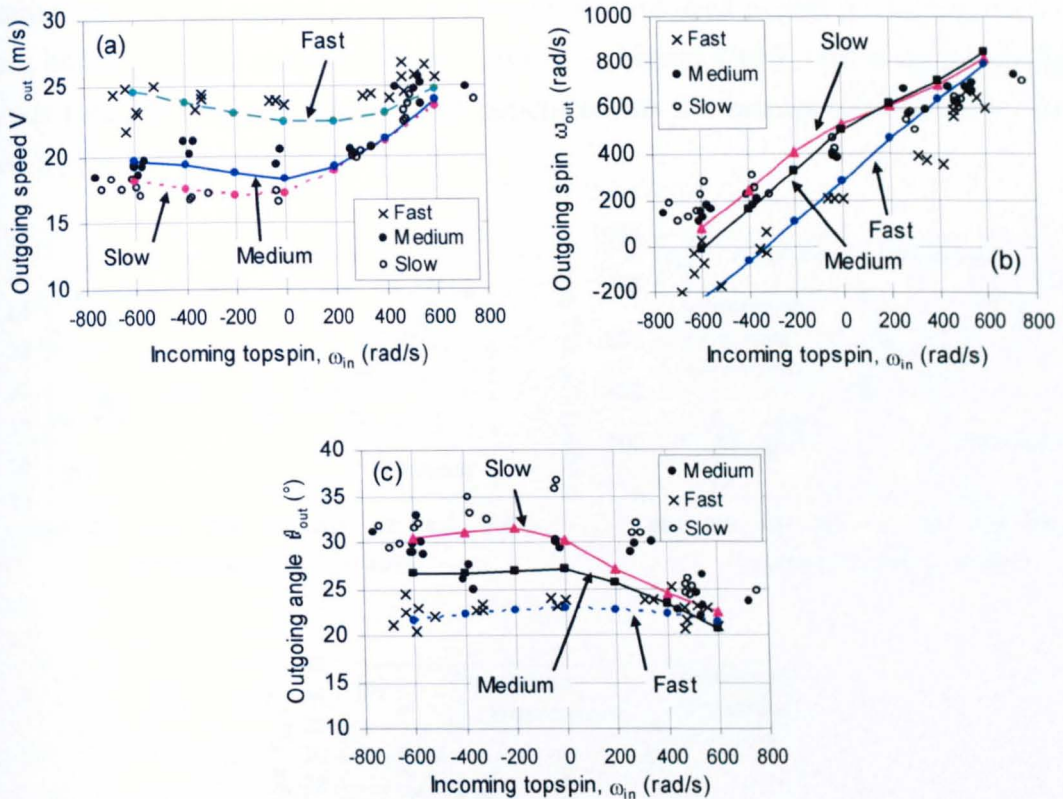
Figure 10.17 (a-c) Experimental values and model predictions for (a) rebound speed, (b) rebound spin and (c) rebound angle for oblique impacts on three different surfaces. In each case the discrete points are experimental data and the lines are model predictions.

Figure 10.17 shows the model predictions. The speed and spin values give extremely good correlations to the experimental data for all three surface types, clearly differentiating between them. The predicted angle is very accurate on the medium and fast surfaces, but gives a value several degrees too low for those impacts on the slow surface with low values of incoming spin (topspin or backspin).

10.4.e   *Testing with different balls*
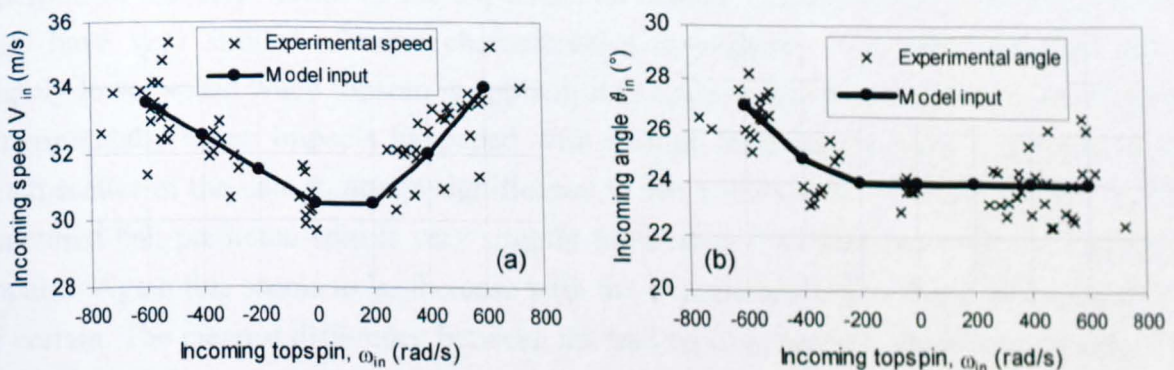
Figure 10.18 Model input parameters used to predict the impact of three different ball constructions at different spins, showing how (a) impact speed and (b) impact angle varied from the nominally constant values.

The parameters for the normal model in Chapter 8 were used to predict the impact of three different ball types. The incoming data is shown in Figure 10.18, and is aggregated for all ball types (pressurised, pressureless and punctured) as the incoming conditions were not affected by the ball construction.
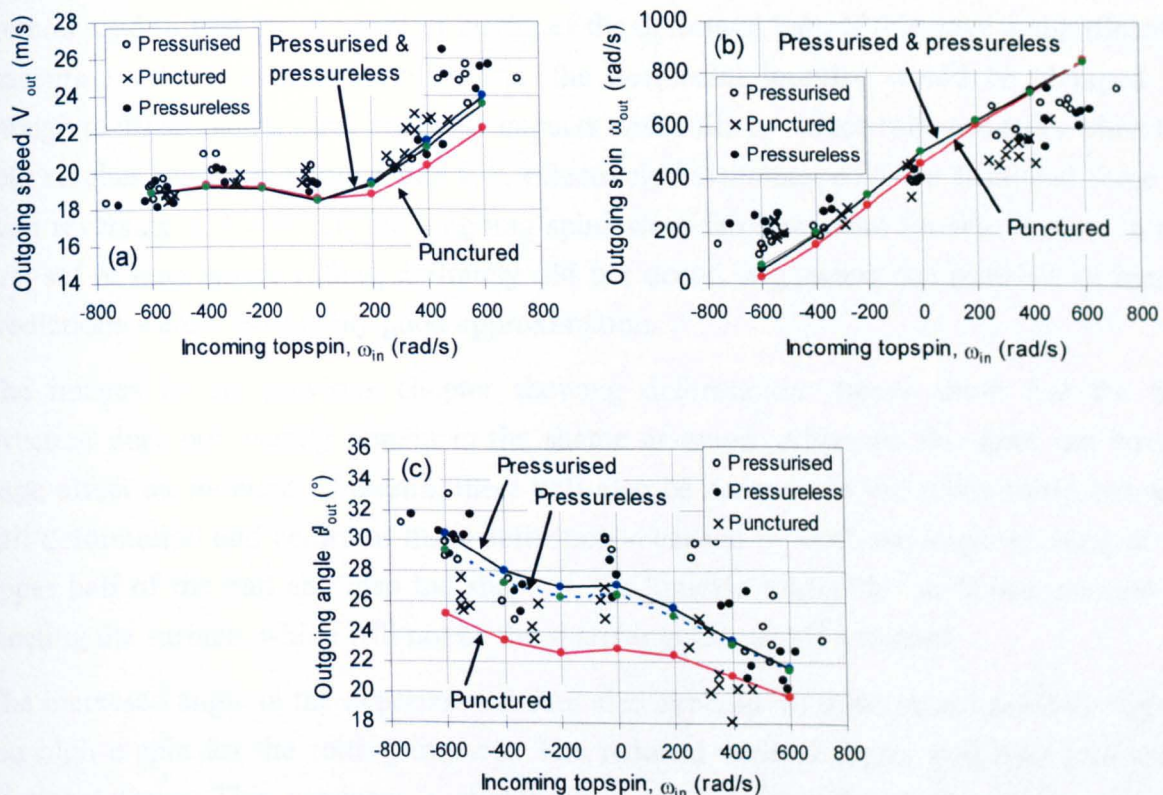
Figure 10.19 (a-c) Model predictions for (a) rebound speed, (b) rebound spin and (c) rebound angle for impacts of three ball types at a nominal speed of 30 ms^{-1} and a nominal angle of 24°. In each case the discrete points are experimental data and the lines are model predictions.

Model rebound predictions are shown in Figure 10.19. There is no significant difference between the predicted behaviour of the different ball types for the speed and spin data, but this follows the same trends as the experimental results. The pressurised and pressureless balls have very similar rebound characteristics throughout. The punctured ball has a slightly lower speed when topspin is applied; it is not possible to see whether this happens experimentally as no impacts happened with enough incoming topspin and there is too much scatter in the data to attach significance to the values at low incoming topspin. The punctured ball predicted spin is very slightly lower than the other two balls for almost all impacts. Again this seems to be the case with the experimental data, but it is impossible to be certain. The clearest difference between the ball types is seen on the rebound angle. The pressurised ball bounces slightly steeper than the pressureless, and both significantly steeper than the punctured ball. This is as would be expected when considering the normal COR values. The experimental data shows the same trend, albeit perhaps 2 to 3 degrees higher in each case.

10.5 Discussion

For most conditions the model gives very good predictions of rebound speed and spin. The rebound angle is less accurate and in a number of cases is several degrees too low, but this is a notoriously hard variable to predict. One source of error investigated was the analytical method used to find the moment of inertia of the deformed ball. If this gave a significantly inaccurate value for moment of inertia, the horizontal impulse would be changed by enough to affect the rebound angle for impacts with rolling – since rolling occurs when the spin reaches the rolling spin value v_x/r, effectively "switching off" the frictional force or even reversing it. However, the outgoing spins were fairy accurate for the impacts in the first set of data where rolling definitely did not occur, suggesting the moment of inertia predictions were a reasonably good approximation.

The images in the previous chapter showing deformation shapes show that the ball structure does not exactly remain in the shame assumed. Although this does not have a huge effect on moment of inertia, there will also be an error in the relationship between ball deformation and centre of mass deflection – caused by both the slight bulging in the upper half of the ball and also the shape in the knuckle where the shell bends round on meeting the surface, which will not be the sharp angular cut-off assumed.

The increased angle in the experimental data also explains why the model predicts slightly too high a spin for the rolling impacts. The reduced vertical forces will lead to a lower frictional force. This produces a slightly increased horizontal velocity component and therefore a higher spin, as spin is "bound" to horizontal speed when rolling occurs.

The deformation shapes discussed in Chapter 9 seem to provide the most likely mechanism for energy loss, which means that impacts generating significant topspin reduce the deformation of the part of the ball away from the surface, decreasing the energy loss. This is seen in the rebound angle data, where the increased vertical velocity component raises the angle. It is interesting that the highest friction surface showed the largest deviation between experiment and model data. It seems likely that the extra spin caused by the higher friction causes the ball deformations to be reduced, and thus the energy losses are lower.

10.6 Adding a spin-related damping term

10.6.a Introduction

It is clear that a major difference between the model and the experimental data lies in the vertical COR seen. If the degrees of freedom of the model are kept separate, there is no way that the COR can change in the way seen repeatedly in experiments. The decision was therefore made to introduce an empirical term which would affect the COR. Figure 10.11 shows that relative to an impact with zero applied spin, there is a definite tendency for the

COR to decrease as the ball impacts with more backspin, and to increase as topspin is applied (the COR only increases slightly, but the impact speed also increases, so the trend is larger than it appears as the COR would be expected to decrease). The point between the two trends seems to be about 100 to 200 rads^{-1} of applied backspin, which happens to be roughly the impact where the average of the incoming and rebound spins is zero. This suggests that the spin does have a direct influence on energy loss, although the exact nature is rather complicated.

An adjustment was made to the damping coefficient so that it would change proportionally to the spin rate – an increased backspin leads to an increased damping coefficient and thus reduced COR, and vice versa. This still gave a damping force proportional to the ball velocity V by the equation $F_D = C_D (r_i + r_o)^2 V$, but the damping coefficient was now changed to the form

$$C_D = C_0 + C_S \omega$$

Values for the spin-compensation damping are shown in Table 10.5. These were found by running the model and considering the COR values for the two impacts with extreme cases for incoming topspin and backspin on the "varying angles" test. It was not possible to predict or measure the values of C_S due to the complicated nature of the physical processes involved – it would require a much more complicated model taking into account the different material properties for each ball. The most likely explanation for the difference between C_S for different balls is that the pressurised ball keeps its shape much more at low spins, and therefore the extra deformation due to spin has more of an effect.

Table 10.5 Model damping parameters for the various ball types.

Ball type	C_S (Ns^2/m^3)
Pressurised	-4
Pressureless	-2
Punctured	-1.5

10.6.b Model results

The same sets of data as used in section 10.4 were used to compare the new model with experiment. Unfortunately it was not possible to show both model predictions on the same graphs for comparison purposes without the data becoming unclear, so in each case only the adjusted model is shown.
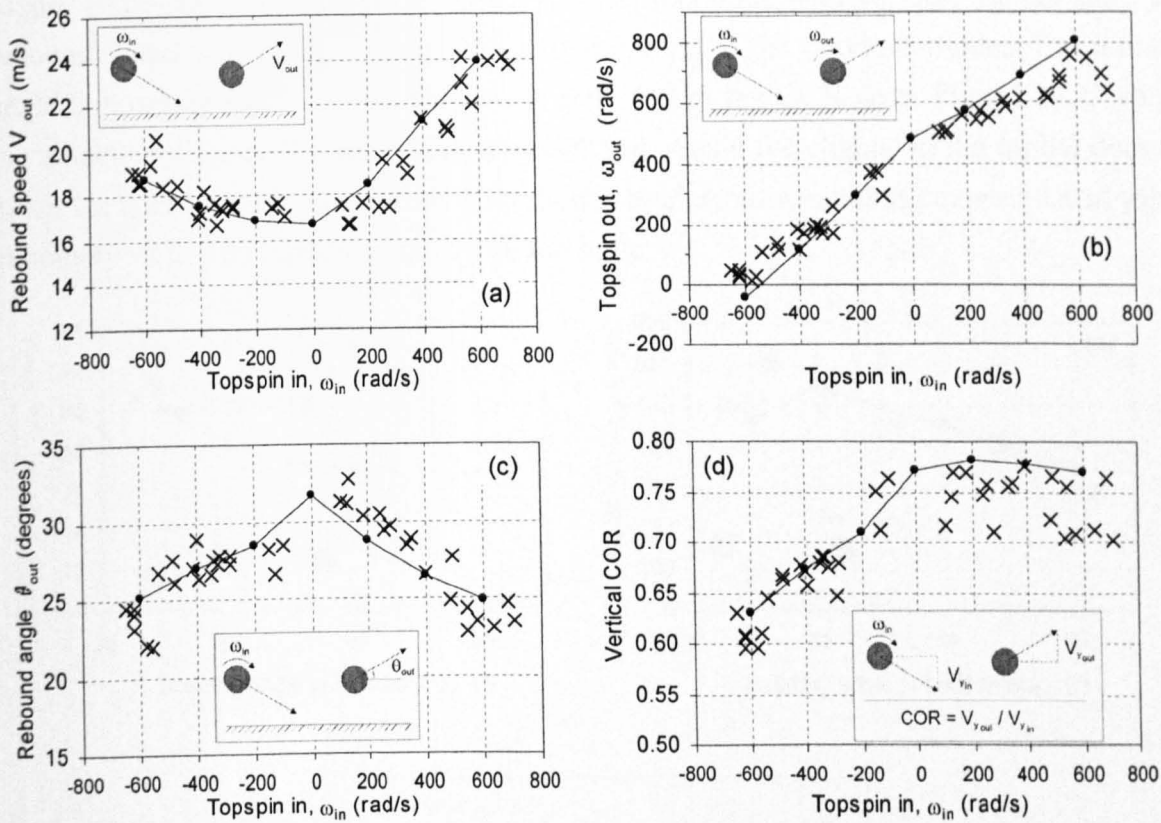
Figure 10.20 (a-d) Model predictions and experimental values for (a) rebound speed, (b) rebound topspin, (c) rebound angle, and (d) vertical COR for impacts with varying spin.
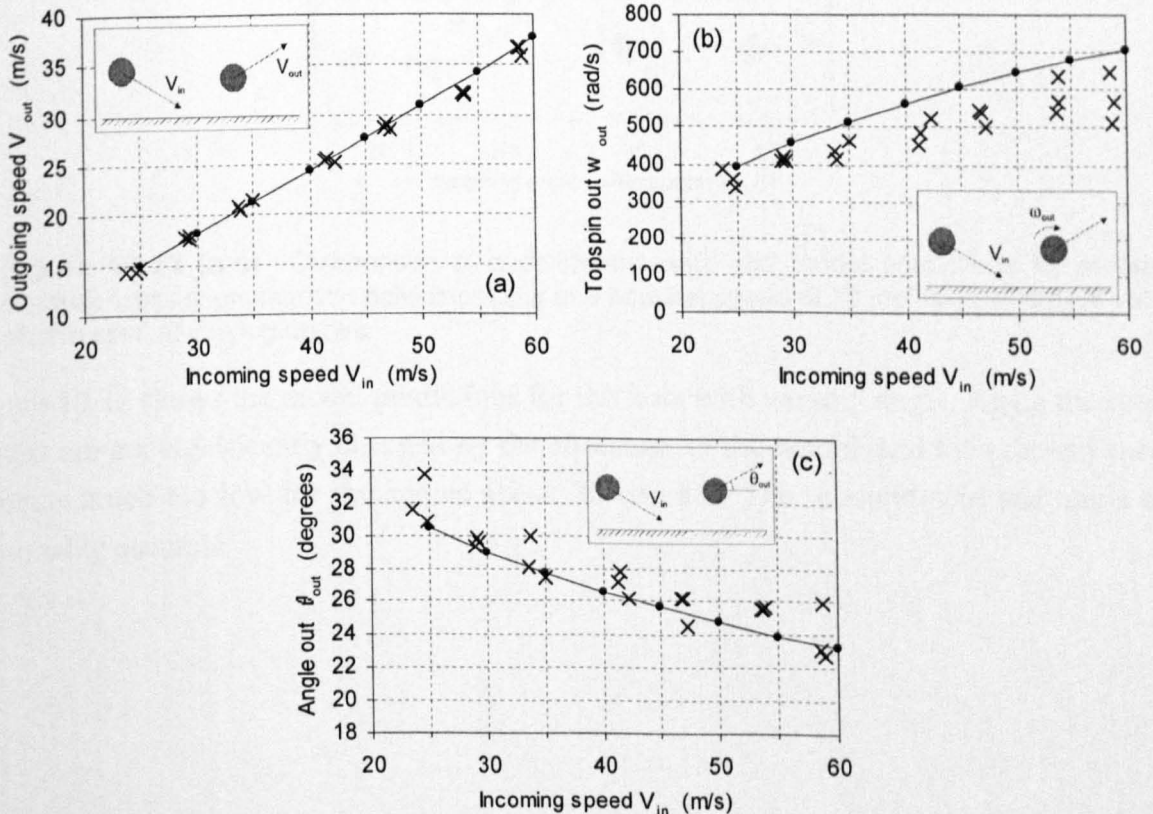
Figure 10.21 (a-c) Comparison of experimental data and model predictions for rebound characteristics of pressurised balls impacting with varying speeds at a nominal angle of 24°, with a nominal value of zero spin.

Figure 10.20 shows how the new model predicts rebounds with varying impact spin. The rebound speed and spin are virtually exactly the same as the previous model. The rebound angle is however much closer, and this is reflected in the COR data. Figure 10.21 shows the model predictions for the "varying speed" test. Again the change to the model does not affect the speed, but it does correct the rebound angles, now matching experimental values extremely well. The rebound spin is still too high.
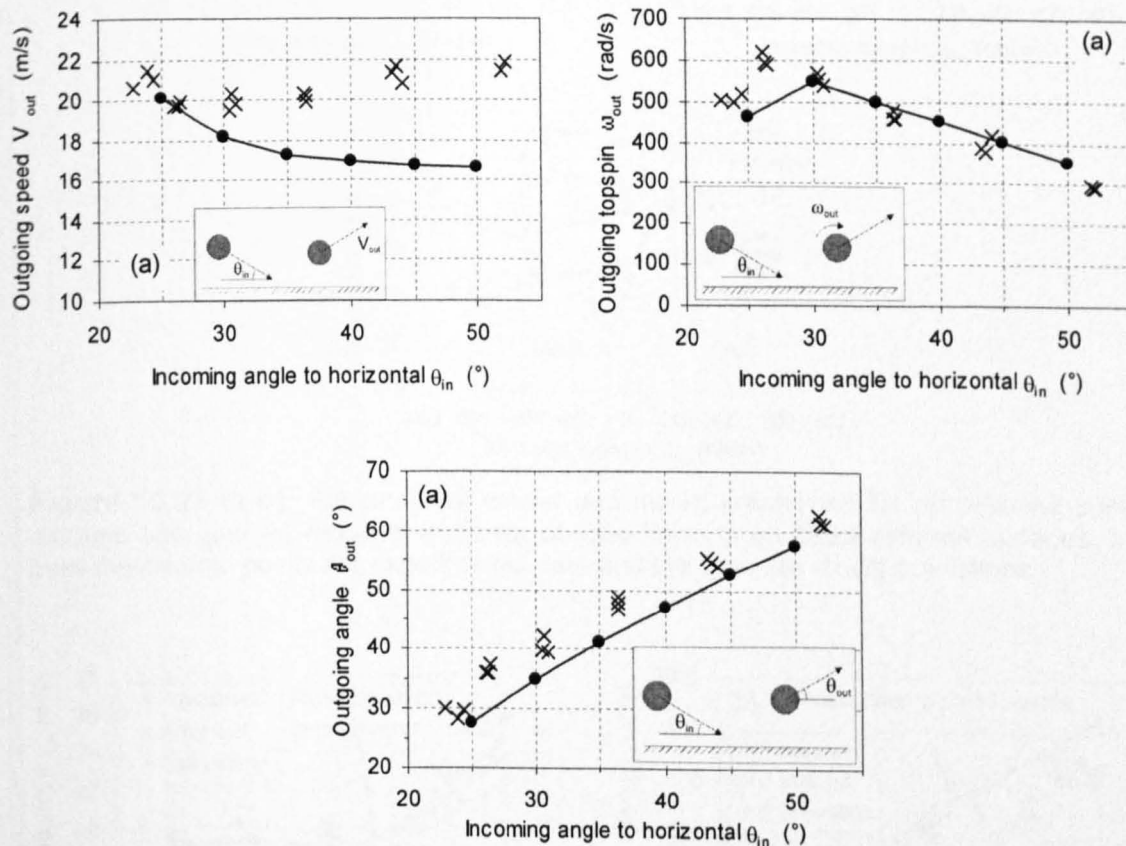
Figure 10.22 (a-c) Comparison of experimental data and model predictions for rebound characteristics of pressurised balls impacting at a nominal speed of 30 ms^{-1} and a nominal value of zero spin, at varying angles.

Figure 10.22 shows the model predictions for the tests with varying angle. Again the speed results are not significantly changed by the alteration to the model, and the rebound speed remains much too low for the angles above 30 degrees. The rebound spin and angle are reasonably accurate.
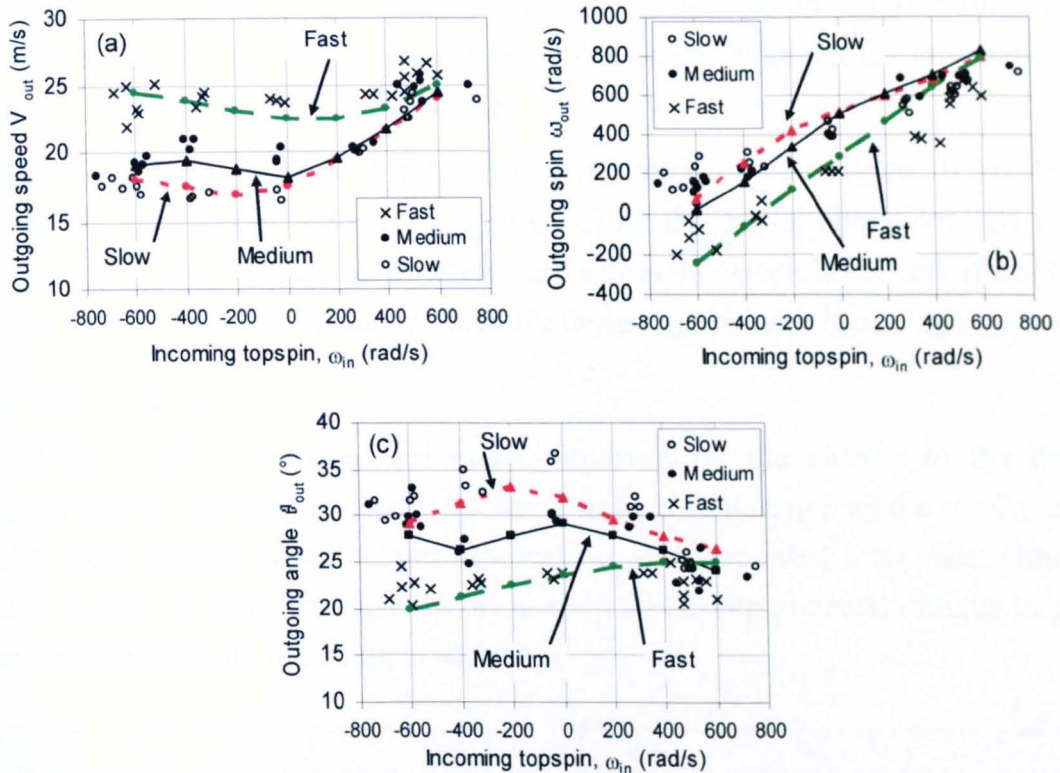
Figure 10.23 (a-c) Experimental values and model predictions for (a) rebound speed, (b) rebound spin and (c) rebound angle for oblique impacts on three different surfaces. In each case the discrete points are experimental data and the lines are model predictions.
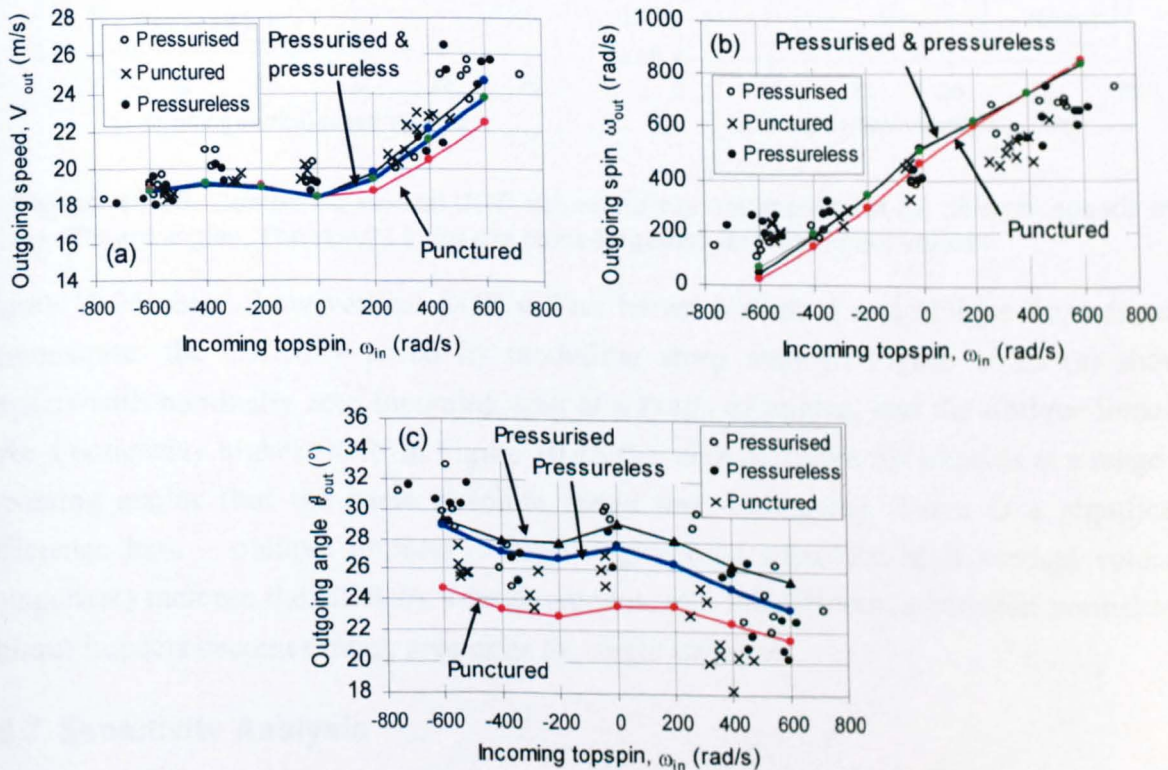
Figure 10.24 (a-c) Model predictions for (a) rebound speed, (b) rebound spin and (c) rebound angle for impacts of three ball types at a nominal speed of 30 ms⁻¹ and a nominal angle of 24°. In each case the discrete points are experimental data and the lines are model predictions.

Figure 10.23 shows the adjusted model predictions for impacts on different surfaces. The model values are much closer to experiment in each case, although the rebound angle is slightly under-predicted on the slow surface.

Model predictions for the three different ball types are shown in Figure 10.24. As in all cases, the rebound speeds are not changed much by the model alteration. The rebound angles are now much closer to experimental values however. Rebound spins for the punctured and pressureless ball are too high for those impacts with incoming topspin.

10.6.c Discussion

Most of the model predictions are much improved by the change to the damping coefficient, and under realistic conditions likely to be seen during play the results are very good. The tests at high impact angles however are still somewhat inaccurate, although it should be noted that even an angle of 24° as used in the experimental oblique impacts is steeper than the majority occurring in a game.
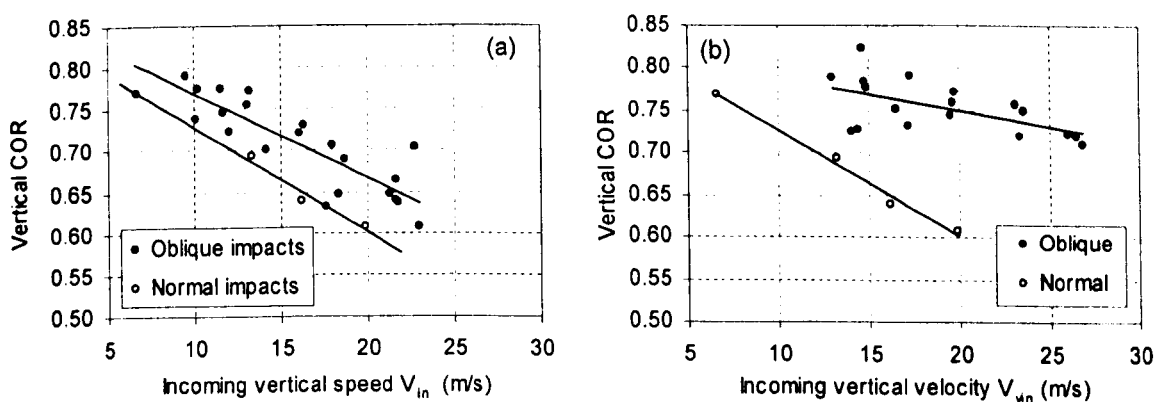
Figure 10.25 Comparing vertical COR values for normal impacts at (a) different speeds and (b) different angles. The results in (b) are plotted against vertical impact velocity.

Figure 10.25 shows how vertical COR differs between normal and oblique impacts, and demonstrates the difficulty posed by modelling steep angles.. Figure 10.25 (a) shows impacts with nominally zero incoming spin at a range of angles, and the oblique impacts have a noticeably higher COR. In Figure 10.25 (b), data is shown for impacts at a range of incoming angles (but the same absolute speed and zero spin). There is a significant difference here – oblique impacts at high angles (and therefore high vertical velocity component) increase the COR by a large amount, and the difference between normal and oblique impacts becomes much greater as the angle increases.

10.7 Sensitivity Analysis

It is instructive to know the sensitivity of the model to each of its defining parameters, which gives an idea of their relative importance and also the necessity for accurate measurement. The static stiffness k_0, the stiffness exponential coefficient A and the

damping coefficient C_0 were all investigated by changing their values by 10 and 20% (for a pressurised ball on the medium speed surface). The "changing spin" set of tests was used as this showed results where there was a clear different between slipping and rolling impacts, and definite trends in the outgoing data.
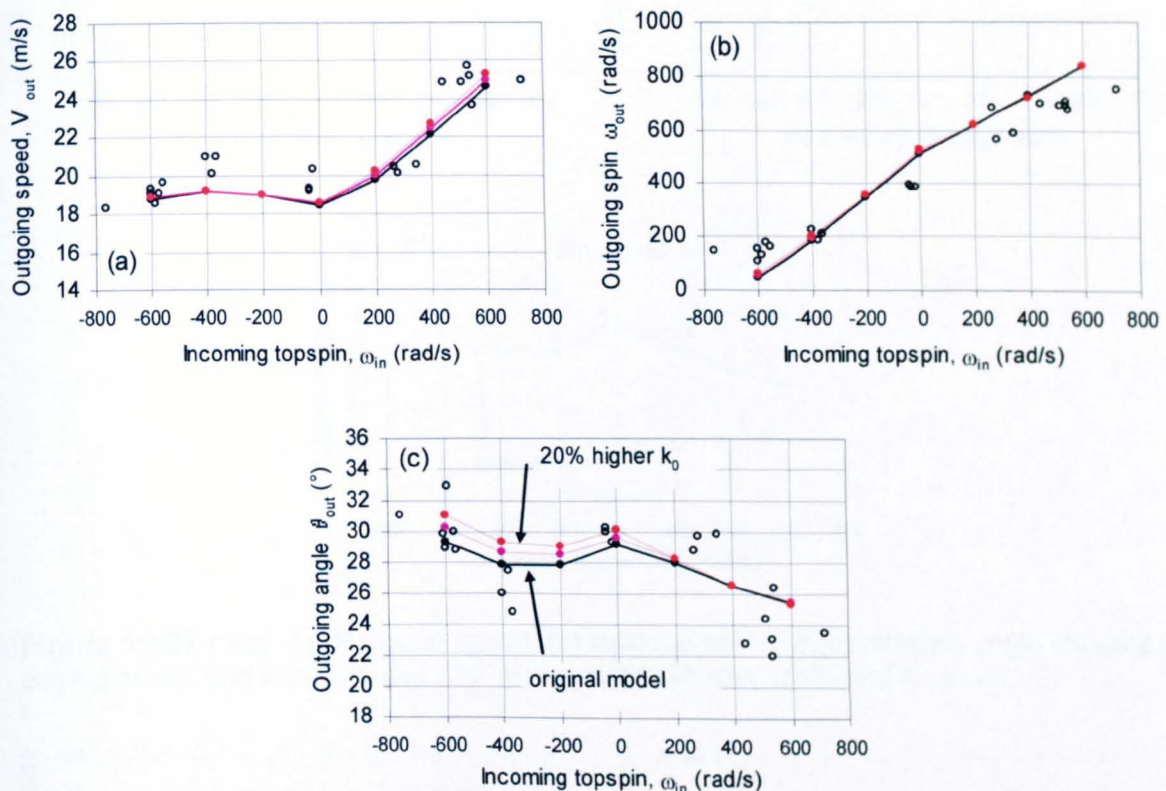
Figure 10.26 (a-c) (a) Rebound speed, (b) rebound spin and (c) rebound angle showing the original model, and with 10% and 20% higher static stiffness k_0 values.

Model predictions are shown in Figure 10.26, Figure 10.27 and Figure 10.28. Changing any of the coefficients by even 20% makes no noticeable difference to the speed and spin – these model outputs cannot be differentiated on the graphs. A small to moderate change in the rebound angle is produced, but this is only evident in the incoming spins which slide throughout impact. It is interesting to note that increasing the damping does not alter the rebound speed of an oblique impact – although the vertical speed is reduced, the horizontal speed is increased as discussed in Chapter 9, leading to a change in angle.

These results suggest that none of the parameters in themselves are particularly sensitive to errors. The different behaviours of various ball constructions seem to be due to combinations of changes of the three variables (or simply much larger changes, as between the stiffnesses of pressurised and punctured balls).
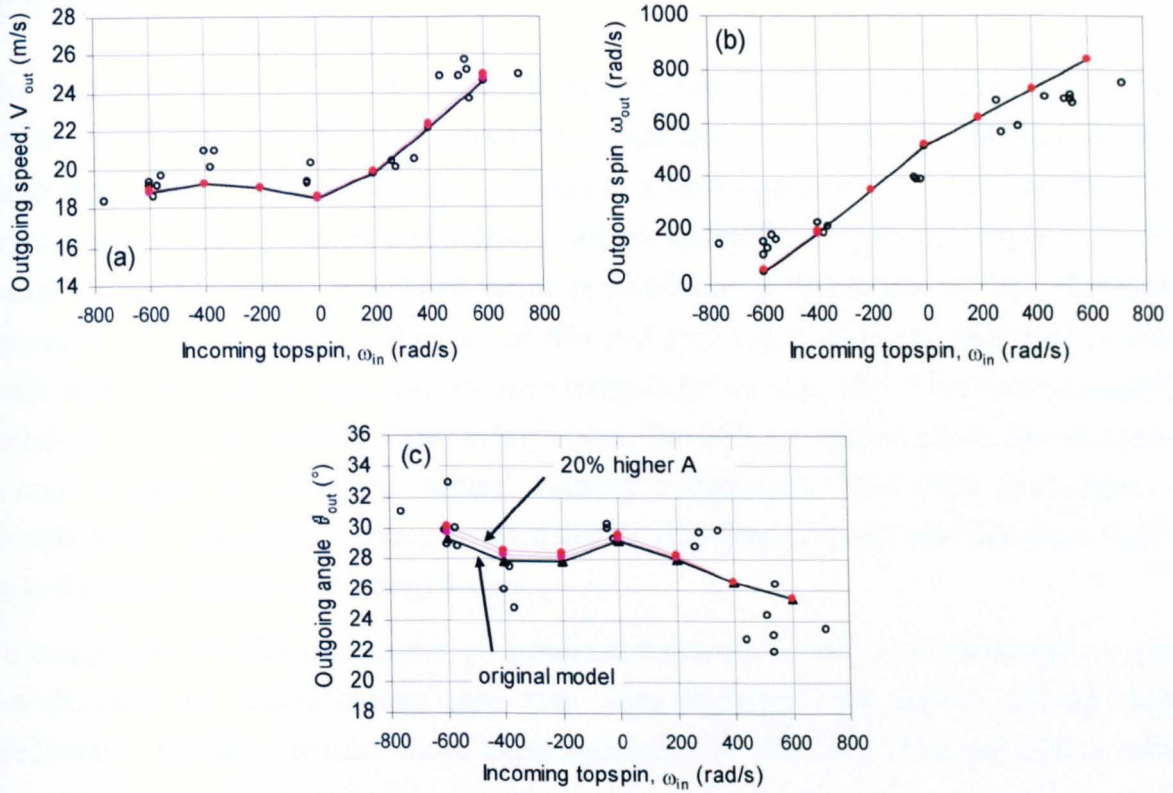
Figure 10.27 (a-c) (a) Rebound speed, (b) rebound spin and (c) rebound angle showing the original model, and with 10% and 20% higher static stiffness coefficient *A* values.
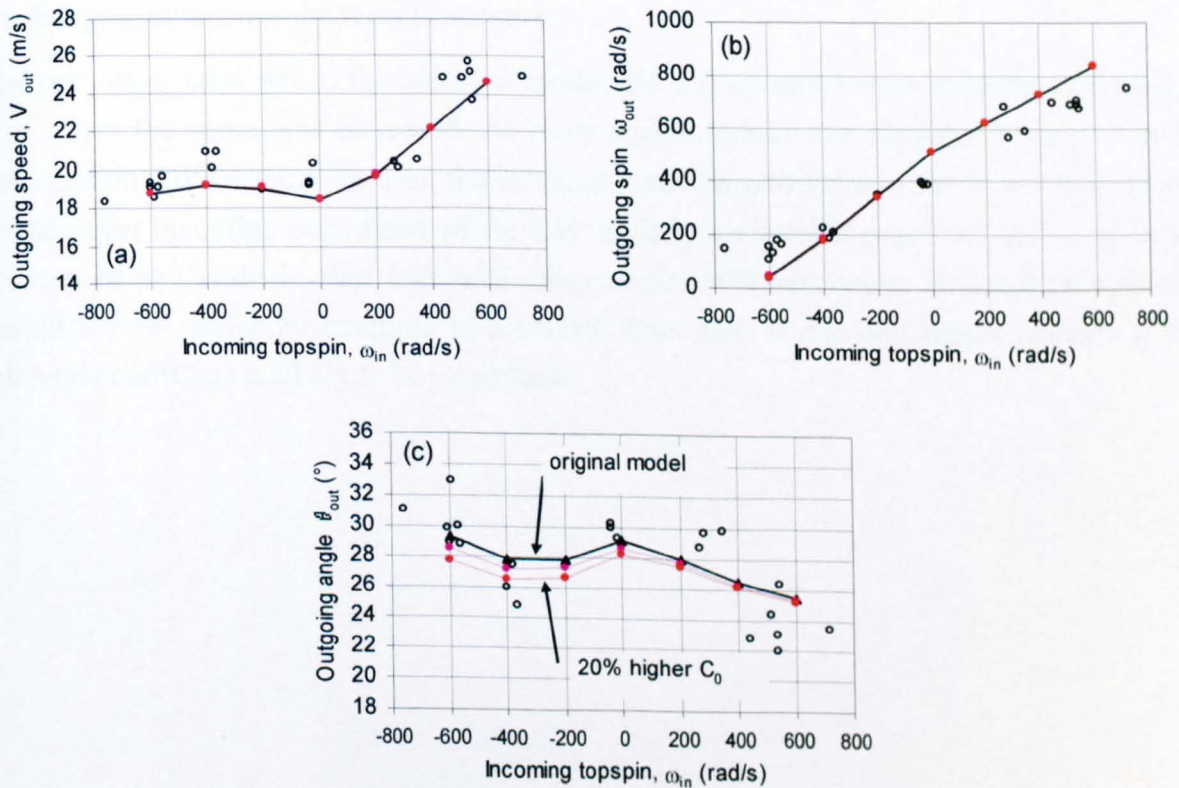
Figure 10.28 (a-c) (a) Rebound speed, (b) rebound spin and (c) rebound angle showing the original model, and with 10% and 20% higher damping coefficient C_0 values.

10.8 Summary

The normal model presented in Chapter 8 was extended to cover the horizontal direction and the spin on the ball. The geometry of the impulsive force makes the oblique situation much more complicated to evaluate, but this is a vital component of the total force and gives the force-time curve its distinctive shape. A spreadsheet could no longer be used to create a quick and simple model and therefore a software solution was written. This model generally gives very good predictions of rebound speed and spin. The predicted rebound angle is in a number of cases two to three degrees lower than that found experimentally, which is due to the vertical COR being higher for oblique impacts than the equivalent normal impacts matching the vertical velocity component. This COR discrepancy is thought to be caused by the spin generated during an oblique impact, and the effect this has on deformation shapes and energy losses.

To compensate for this discrepancy, a simple compensation term was introduced to adjust the damping for instantaneous spin rate. This improved the quality of the model predictions, but does require more experimentation to find the extra parameter, which cannot be measured statically.

The effect of the errors in the model predictions will be discussed in the next chapter, to see how important the errors would be over the course of a ball's trajectory, to see whether the damping compensation term is necessary.

The one set of tests where the adjusted model did not closely match experimental values was where the angle was increased. At steep angles (where the changes in shape due to deformation will be more severe), the rebound speed in particular is much too low. These are however incoming conditions where it is unlikely a model is required, as they will not be seen in any realistic shot and such steep angles will not occur at significant speeds except for the particular example of a smash. This case is not one where predicting the rebound conditions is likely to be important.

11 Tennis GUT

11.1 Introduction

The surface impact model presented in this thesis covers one part of the ball's interaction with its surroundings during a game of tennis. Before it reaches the court surface, the ball has undergone an impact with a racket and a three-dimensional trajectory under the effects of gravity and aerodynamic forces. There is then of course a further trajectory after the ball bounces before it reaches the opposing player.

When working on a single part of the whole tennis "process", it is easy to lose sight of the effect of (often small) changes in a ball's behaviour. This is particularly true in assessing model accuracy – for example, how much effect does a 5% error in predicted speed on rebound have on how the ball behaves through the rest of the shot?

A piece of software was developed to streamline the modelling process by tying together the currently most advanced models in the three main areas: ball-racket impact, aerodynamic trajectory and ball-surface impact. The primary focus was ease of use, so that small changes in one variable (such as racket or ball mass) could be propagated through the models in turn to see their effects.

11.2 Racket impact model

11.2.a   Introduction

Of all the components of the sport of tennis, the two which have changed most dramatically in recent decades are the player and the racket. Improvements in diet, training techniques and a huge change in the marketplace rewards for professional sport have led to modern players being significantly taller, heavier, stronger and faster than ever before.

The most revolutionary change in rackets came when Prince introduced the first oversize racket (Head, 1976). The oversized head means that the "sweet spot" of the racket is much larger, giving a greater margin for error. Modern rackets are incredibly stiff and light, allowing increased swing speeds. A combination of these factors means that shots (in particular the serve) are increasingly being hit with such power and accuracy that it is physically impossible for the receiver to return the ball. (refs about serve speed?).

As governing body for the sport, the ITF has recognised its responsibility to understand the effects of players and equipment on how the game is played at both a professional and recreational level (Coe, 2000; Miller, 2003). Amongst much other research, they built a serve impact simulation machine (Kotze and Mitchell, 2002) capable of producing impact speeds of up to 50 ms^{-1} at specified racket positions.

11.2.b Model description
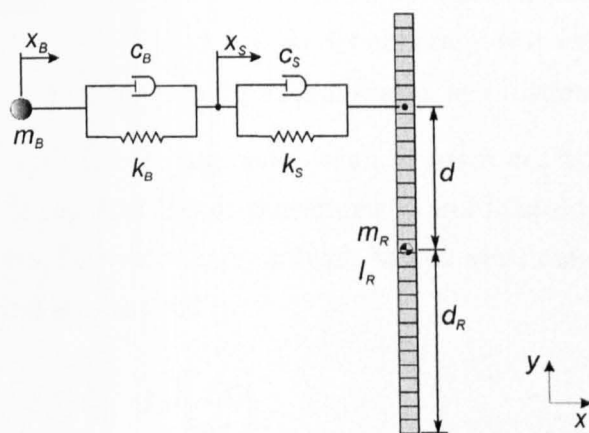
Figure 11.1 The model used to simulate ball impact on a freely suspended racket.

The racket model used here is based on that given by Goodwill and Haake (2003) and is more fully described in that publication. A freely suspended racket was chosen, as this is the most valid way of representing a player's grip (Brody, 1987). The model defines a system consisting of three discrete components: the ball, the stringbed and the racket frame, as shown in Figure 11.1.

The ball is modelled as a point mass connected to the stringbed by a spring (k_B) and dashpot damper (C_B) in parallel. Both of these parameters depend on ball deformation and therefore change during the course of an impact. Their values were empirically found by Goodwill (2002). The stringbed was similarly represented by a parallel spring (k_S) and damper (C_S), whose values were obtained from experimental data. The stiffness ks was found by applying a quasi-static load to a racket stringbed via a rigid 55 mm diameter disc. The damper C_S was given a value of 2 Nsm^{-1} in order to provide a energy loss of 5%, corresponding to the experimental results of Cross (2000).
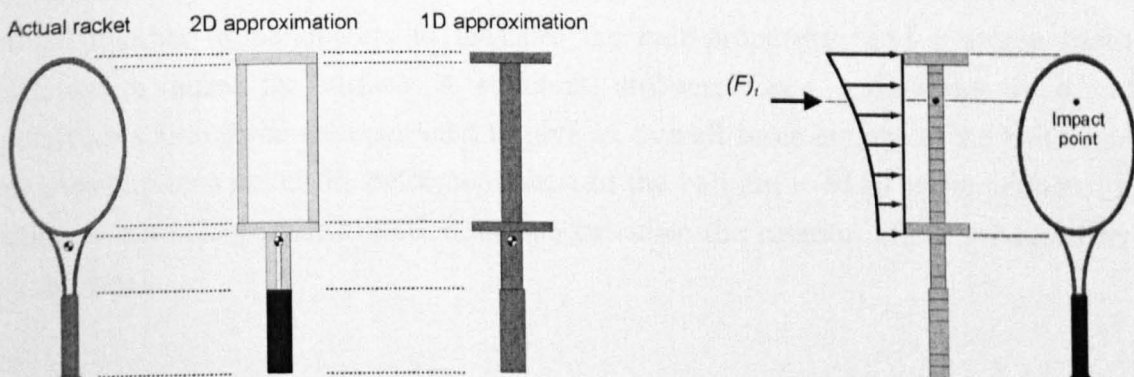
Figure 11.2 (a) One-dimensional representation of the racket, with (b) the assumed loading shape.

The racket model was represented by a simplified one-dimensional shape as shown in Figure 11.2(a). A two-dimensional approximation was first created to represent the varying mass distribution, which provided the same mass and balance point as the racket. This was

then simplified to give a one-dimensional model with the same mass distribution along the longitudinal axis. Cross (1999) formed a similar model and applied the stringbed force as a point load, but Goodwill (2002) found that model accuracy was improved by assuming the stringbed applies a distributed force to the racket frame, as illustrated in Figure 11.2 (b).

The beam can then be split into N segments, each of mass m_n, position along the beam x and length s, where each segment has displacement y_n and is acted on by a force F_n, giving equation [11.1] which can be numerically solved. Model verification and further detail can be found in Goodwill and Haake (2003).

$$m_n \frac{\partial^2 y_n}{\partial t^2} = F_n - \left(EIs \frac{\partial^4 y_n}{\partial x^4} \right)$$

[11.1]

11.3 Aerodynamic model

The aerodynamic model used has been described in Chapter 4. In summary, lift and drag coefficients were taken from the results of Goodwill *et al.* (2004), who mounted both non-spinning and spinning tennis balls in a wind tunnel. C_D and C_L were measured for varying values of spin coefficient S (defined as circumferential velocity V divided by wind speed U). They tested at wind speeds of 25 and 50 ms^{-1}, and found that C_D and C_L changed a small amount for these different Reynolds numbers. For values of S below 0.2 – where lift and drag were measured for both wind speeds – interpolated values were used between the trendlines for the two wind speeds, and for values of S above 0.2 those measured at 25 ms^{-1} were used. It was assumed that the spin rate stayed constant throughout the trajectory.

11.4 Surface impact model

The surface impact model is described in detail in Chapter 10. In summary, it uses a minimal number of parameters to measure the ball properties, and a single frictional coefficient to define the surface. A structural stiffness force, a damping force and an impulsive reaction force are combined to give an overall force acting on the ball centre of mass. Assumptions about the deformed shape of the ball are used to relate centre of mass position to external ball deformation, and to calculate the rotation effect produced by the friction force.

11.5 Putting the models together

11.5.a   User interface and parameter specifications
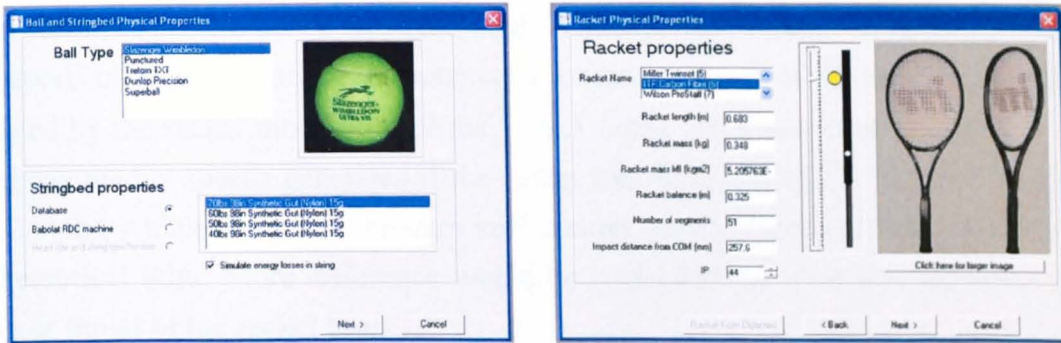
Figure 11.3 The interface to the racket properties.

As already stated, the main aim was ease of use of the software. The interface to the racket model was taken from Goodwill (2002) who constructed a standalone program for this part. Figure 11.3 shows the ball and racket properties screen, where the relevant parameters can be viewed and defined.

The aerodynamic model required much less user input. As it would be difficult to describe lift and drag coefficients numerically at run-time, these were coded into the software for the selection of balls tested. Future work may provide functionality to take data straight from automated wind tunnel tests, but this was not judged practical or necessary.

11.5.b   Output data

Figure 11.4 Trajectory output and numerical data from the model.

The combined trajectory of the shot (including before and after impact) can be shown in several ways. The most visual representation is a three-dimensional view which can be rotated to see the path of the ball from any viewpoint. An example is shown in Figure 11.4. An overhead view can also be used to see the velocity, spin etc at any point on the trajectory.

11.6 Model results

11.6.a   Example data

As an example shot, a serve was recreated. A racket was swung virtually with a racket head speed of 36 ms^{-1}, and an instantaneous rotational speed of 46 rads^{-1}. The ball speed predicted by the racket model is 44.2 ms^{-1} (99.5 mph). An interesting side note is that the model can predict speeds generated if the racket was infinitely stiff – in this case 45.0 ms^{-1} (101.2 mph), which shows that modern stiff rackets are extremely efficient and not far off the theoretical limit. More difference would be noticed if the shot was hit towards either the tip or throat of the racket head.

Elliott *et al.* (1986) found that on average, a player will hit a serve from a vertical position of 1.53 times their height. For a player who is 1.9 m tall, this would give a starting height of approximately 2.9 m. UC Davis (2001) measured the spin on professional serves to average 2000 to 3000 rpm. A spin of 2500 rpm (262 rads^{-1}) was chosen for this example.

A goal seek within the software found that the angle required for the ball to land on the baseline was 2.09 degrees below the horizontal and it impacted at 28.91 ms^{-1} (65 mph) at an angle of 17.47 degrees to the horizontal.
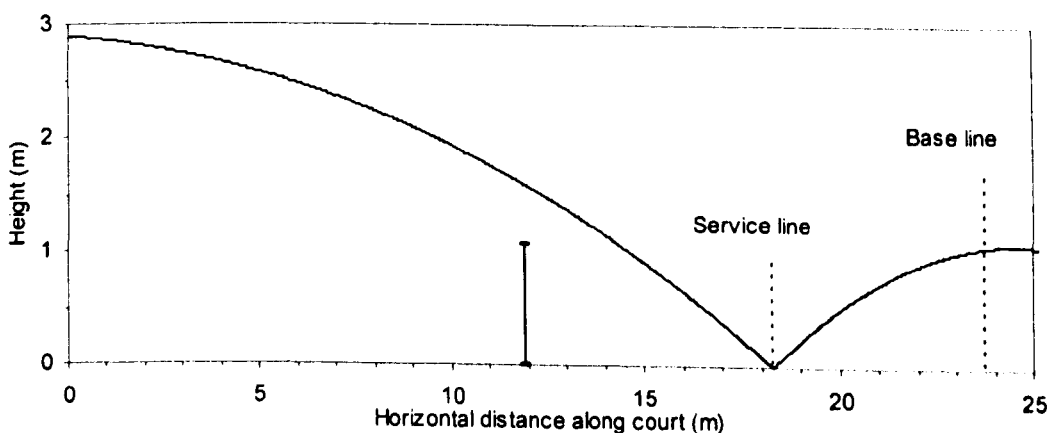
Figure 11.5 Predicted trajectory for a serve hit at 99 mph with spin of 262 rads^{-1}

The surface chosen was a standard uncushioned acrylic, which was measured to have a coefficient of friction of 0.57. The surface impact model predicted a rebound of 20.6 ms^{-1} (46.3 mph) at 18.9 degrees to the horizontal, with a spin of 593 rads^{-1}. After applying the trajectory model again, the speed at the baseline was calculated to be 17.4 ms^{-1} (39.1 mph) and the ball was just still rising – the velocity vector was 2.5 degrees above horizontal. The total time taken was 0.827 seconds, and the complete trajectory is shown in Figure 11.5

11.6.b   Using the GUT model to assess the oblique model

The software was then used to compare the two oblique impact models described in Chapter 10. The main reason for this was to visualise the effect of any differences between

the model predictions and the experimental values measured. An error of 5% would seem reasonable, but how much difference would this make to the way the ball actually behaves?

The data chosen was from the "varying spins" set of experiments. An impact was deliberately chosen that was probably the worst prediction from the initial oblique model, which was the impact with 400 rads^{-1} of incoming topspin. Both oblique models matched the experimental rebound speed of 21 ms^{-1}. Similarly, both had the same rebound spin value, of 700 rads^{-1} of topspin. The experimental value here was somewhat lower, at about 600 rads^{-1}. The main difference was in the rebound angle, where the experimental value was 27 degrees. The first model predicted an angle of 23.6°, and the second model 26.5°. Both of these angles are too low; the addition of too much topspin will emphasise the low trajectory.
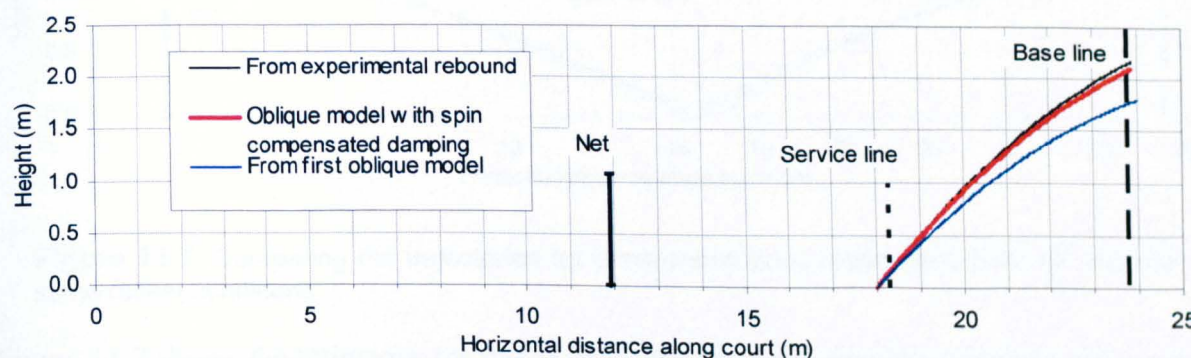
Figure 11.6 Comparing trajectories from two model predictions to that from experimental rebound properties.

The speed, spins and angles were used to predict the trajectory using experimental and model rebound characteristics for the impact which was assumed to be 18 metres along the court (close to the service line). The results are shown in Figure 11.6. All three trajectories are plotted up to the time interval where the experimental trajectory reached the baseline. In each case the horizontal position is almost exactly the same. At this point the experimental rebound characteristics predict a bounce height of 2.16 m. According to the first oblique model the ball has a height of only 1.77 m. This discrepancy of 39 cm is significant. The model with the spin-compensated damping has a height of 2.08 m. This is 8 cm below the experimental position of the ball, meaning the addition of this damping term has reduced the error to about a fifth.

For all other data sets (except those with high impact angles), the difference between model predictions and experimental rebound characteristics was much smaller. A maximum error of 8 cm in the position of the ball after travelling such a large distance was judged to be acceptable. It is also worth noting that the nominal impact conditions chosen throughout were deliberately used as the "worst-case" scenario likely to be seen. Most

impacts produced by real shots would have a considerably lower vertical velocity. This would reduce the effect of deformations on energy loss, making the impact easier to predict. Slower speeds would also produce more accurate trajectories, as even the same proportional errors would leave experimental and prediction ball positions closer together.

11.6.c   Comparing pressurised and pressureless balls

An analysis was performed to see the effect of a pressureless ball on an overall shot. The racket swing speed used in 11.6.a produced a slightly slower ball speed of 43.4 s^{-1} (compared to 44.2 s^{-1} for the pressurised ball).
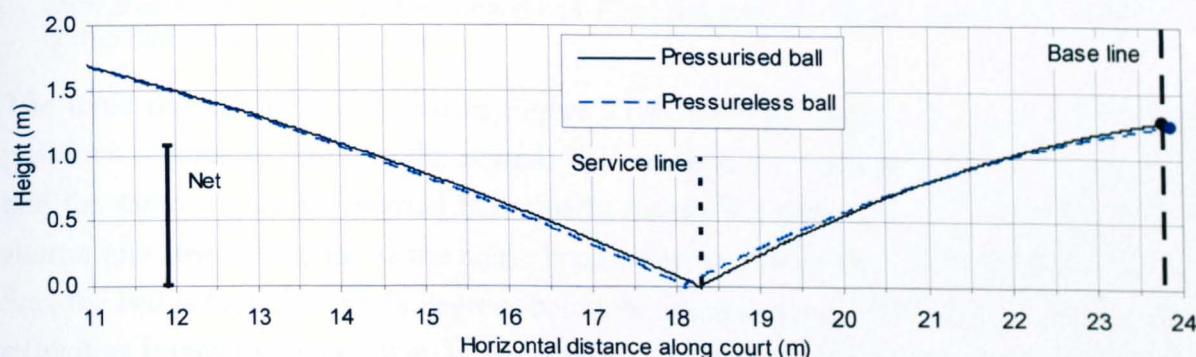
Figure 11.7 Comparing the trajectories for pressurised and pressureless balls hit with the same racket conditions.

Figure 11.7 shows the trajectory for the pressureless ball compared to that for a pressurised ball. The two balls behave in a very similar manner, and the pressureless ball reaches the baseline only 3 cm lower than the pressurised ball. This difference is extremely unlikely to be noticed by a player.

11.6.d   The effect of an oversized ball

The software was also used to analyse the effect of an oversized ball. The serve speed and angle described in 11.6.a was used to calculate the trajectory (before and after impact on the court) of a normal ball. An oversized ball of 6.5% larger diameter (70.3 mm compared to 66 mm) was simulated with the same launch conditions. A goal seek was then used to vary the angle so that the oversized ball landed on the service line. This would be a more realistic simulation of a real serve, as a player would adjust the way he hit the new ball (after some experience) to achieve the same results.
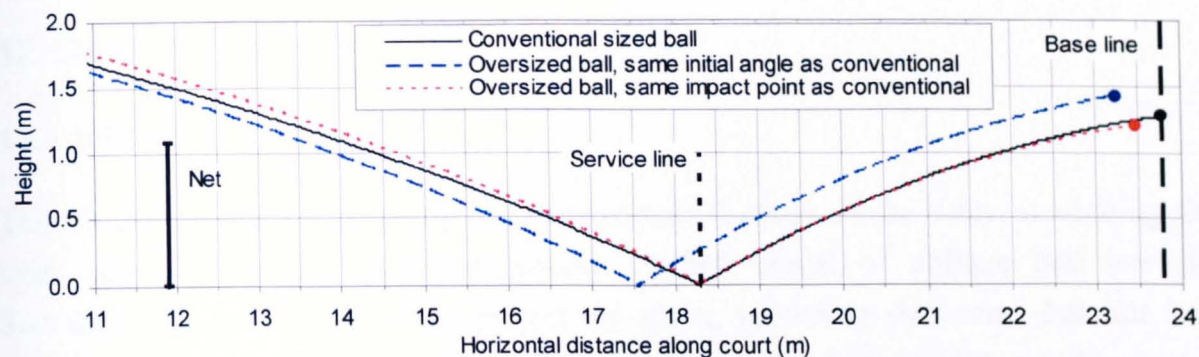
Figure 11.8 Trajectories showing the effect of an oversized ball (at two initial angles) compared to a conventional pressurised ball. Final positions are shown at the time where the normal ball reaches the baseline.

The three trajectories are shown in Figure 11.8; all were plotted to show the finishing positions relative to the time the normal ball reached the baseline. Hitting the oversized ball the same way as the normal ball clearly makes the trajectory dip more, producing a shorter and steeper impact. If the angle is adjusted to ensure the ball lands on the service line, the ball is hit higher (2.38 degrees below horizontal compared to 3.09 degrees) but the extra drag brings its flight down. Interestingly, the normal and oversized balls follow fairly similar trajectories after impact, although the oversized ball is slower and starts to "dip" soon after the time shown, landing well short of the normal ball for its second bounce.

The normal ball reaches the baseline after about 780 ms, and the oversized ball after about 820 ms. This time difference is significant, and would be noticed by the receiving player as a "slower" shot.

11.7 Summary

Although not within the initial remit of the study, a piece of software was developed to aid the use of the oblique impact model, particularly in predicting the effect of a whole shot from one player to the opponent. This software was used to assess the effect of errors in rebound predictions on the ball trajectory after bouncing, and particularly the result when the ball reached the other end of the court.

It is hoped that the software presented here could be of use to the ITF in their role of assessing the effect of technology on the sport of tennis, and perhaps it could prove useful to the tennis industry in general as a predictive tool for comparing potential new products.

12 Conclusions

12.1 Introduction

This chapter provides a summary of the important findings of the study, describing the steps taken to produce an experimentally verified model of oblique ball impacts. Summaries for each stage of the project are given, providing static and dynamic ball properties, model construction and verification. Overall conclusions of the study are also described, together with suggestions for possible related work in the future to progress the research.

12.2 Summary of study

12.2.a Quasi-static ball testing

Balls were compressed at various quasi-static loading rates. It was found that for the loading rates possible in a laboratory, compression strain rate does not have an affect on ball stiffness. Various ball constructions behave in a very similar manner in a static compression test (but of course they have been designed to behave in such a way). If holes are drilled in balls so that the effect of internal pressure is totally removed, the effect of the rubber shell can be seen. Pressureless balls are considerably stiffer, since they rely on the structure to create the stiffness under compression. Pressurised balls rely on a combination of shell stiffness and the rise in internal pressure. Both ball types exhibit a stiffness when drilled which is close to constant.

12.2.b Surface testing

The important properties of a surface in relation to ball impacts were identified as friction, impact absorption and ball bound. A number of established tests exist to quantify each of these properties and these tests were examined. It was found that most of the commonly used friction tests use a rubber surface to simulate the interaction with a player's shoe, and this did not correlate particularly well with the friction found using the cloth on a tennis ball. The Surface Pace Rating is an accepted measure of the "speed" of a court, and theory suggests it is a linear function of the coefficient of friction. One simple test which correlated well with the SPR (which requires expensive equipment to measure) is the Haines Pendulum.

Impact absorption tests rely in general on impacting an instrumented mass on a surface, either directly or via a spring. Again this test is designed to quantify human interaction with the surface, and so the energies involved are orders of magnitude higher than that produced by a tennis ball. A number of tests were considered and it was found that for the vast majority of tennis court surfaces, the surface is so much stiffer than the ball that it may

be considered rigid. This was born out by the ball rebound tests, which showed no significant differences between tennis court surfaces.

12.2.c Normal impacts

Experimental tests

Balls were projected at a force plate at speeds up to 20 ms^{-1}, and the impact and rebound speeds measured with a combination of high speed video and light gates. Four ball types were tested, and for each one the COR dropped with increasing impact velocity. At speeds up to 7 ms^{-1}, the three "off the shelf" balls had very similar rebound speeds. Above this, the pressureless ball rebounded consistently slower than the pressurised and oversized balls, which were very similar. The punctured ball rebounded slower throughout the tests.

The force data showed that the pressurised and oversized balls behave in a similar manner throughout the range of speeds. The punctured ball has almost identical characteristics to the pressurised ball at low speeds, but at higher speeds it behaves more like a punctured ball.

Impact modelling

A one degree-of-freedom model was created to simulate the normal impacts. It consisted of three components: a structural stiffness, a material damping term and an impulsive reaction force term. The relevant parameters for each of these three components were found via a combination of quasi-static compression tests and a minimal number of simple dynamic tests just measuring speeds (one drop test and one higher speed test).

A feature of the model was that it attempted to relate the force components to the physical nature of the impact, and so for example the impulsive force component was described and calculated in an intuitive way rather than an abstract calculation.

The model predicted rebound speeds for the four ball types extremely well and matched the various features of the force data. This gives an insight into a ball's behaviour and the contribution of the various parts of its construction (for example, the relative importance of the rubber shell and the internal pressure at various speeds). The impulsive force was found to be the main contribution to the sharp increase in force seen early in all ball impacts, particularly at higher speeds.

12.2.d Oblique impacts

Experimental tests

A number of tests were performed in an attempt to isolate the various impact variables and to assess the importance of each one. In particular, the speed, spin, angle, ball type and surface type were investigated. It was found that whether or not the ball rolled during

impact had an important affect on the way it rebounded. Sharp changes in the rebound characteristics were observed either side of the limiting rolling conditions, in a very similar way to those predicted by simple Newtonian rigid body models.

One significant observation was that the energy loss was affected by the nature of the impact. A good example of this was the impacts with the same speed and angle, but varying spins. The vertical velocity component on rebound was affected by the incoming spin. On examining the high speed video data, this was found to be caused by the deformation shapes. Although the overall deformation was similar in all cases, incoming topspin reduced the deformations in the part of the ball above the surface, reducing energy loss and increasing COR. The opposite effect was seen with incoming backspin. The impacts which most closely matched the normal COR were those where the *average* spin throughout impact was close to zero, and so the rotation of the ball was minimised during the middle of the impact where the forces were greatest.

Impact modelling

The normal impact model was extended to a three degree-of-freedom situation with the addition of horizontal and rotational components. The initial model assumed that the vertical component was independent of the other two. The impulse force component was found to be a complex function of both translational and rotational velocity, and a stand-alone software solution was programmed to solve the problem.

This initial model was found predict the rebound speeds and spins reasonably well, but the angle was consistently too low. This was because of the effect of ball spin on the vertical COR. A simple damping compensation term was incorporated into the model such that the damping was instantaneously reduced for topspin and increased for backspin. This reduced the prediction errors to an acceptable level.

12.2.e Tennis GUT

When the surface impact model was complete, it was linked to a racket impact model and a trajectory model to give a "Grand Unified Theory" piece of software. This enables the effect of a single property to be tracked throughout a shot (for example, how would a new racket string imparting 50% more spin on the ball affect the way it reached the opposing player on various different speeds of court?). It is hoped that a development of this software could be a useful tool in assessing the impact (or potential impact) of technological changes on the sport.

12.3 Conclusions

- Almost all tennis court surfaces are stiff enough in relation to the ball that they do not contribute to energy losses during ball-surface impact. This means that for modelling purposes in the majority of cases, a tennis court can be considered to be a rigid surface.

- When balls impact normally on a surface, the coefficient of restitution decreases with increasing impact speed. At all speeds, normal and oversized pressurised balls rebound with similar speeds. As speeds increase above those of a drop test (7 ms^{-1}), pressureless balls rebound slower than these two pressurised types. Punctured balls rebound significantly slower than all three other ball types at all speeds.

- All balls create a sharp initial rise in impact force. The magnitude of this initial peak varies with impact speed. At high speed there is a short reduction in force as the shell buckles inwards.

- A viscoelastic model was able to predict the force-time properties of normal impact at all speeds tested (up to 20 ms^{-1}) using parameters which were simple to measure. Features of the impact such as the initial peak in force were created by a combination of structural stiffness, damping and impulsive reaction forces.

- Oblique impact tests showed smaller (but distinguishable) differences between the behaviour of different balls. The trends of the balls' behaviour matched that predicted by Newtonian rigid body models. In particular, the difference between slipping and rolling behaviour was observed and was noteworthy.

- An oblique model with the main addition of a coefficient of friction simulates a variety of impacts well. Only when the impact angle is significantly higher than the vast majority of "real" impacts is the accuracy reduced. An empirical coefficient to compensate for the effects of spin rate on energy loss was included which significantly improved the results.

12.4 Future research

This project has provided a relatively simple normal model which gives good results and whose governing parameters are easy to measure. A series of experimental tests gave a good insight into the oblique rebound characteristics of tennis balls, and a model created which predicted these well in most cases. There are several areas in which it would be interesting to continue the research.

Surface modelling

This study concluded that for the vast majority of tennis courts, treating it as a rigid surface is a good approximation – even including those with shockpads designed to reduce player impact forces. It is recognised however that there are potential uses for simulating the impact on softer surfaces, or particularly the specific case of clay where the surface undergoes permanent deformation which affects the impact. To include such surfaces in the model was not deemed feasible (in part due to the large amount of extra experimental data necessary), but this is an area which could be explored in the future.

Environmental conditions

It has been noted several times that environmental conditions (particularly temperature, humidity and air pressure) will have an effect on the ball impact. Although it was beyond the scope of this study, looking at the influence of each of these properties would be important to gain a fuller knowledge of the behaviour of a ball in all conditions.

Further oblique experimental study

In order to gain more understanding of the nature of an oblique impact, further knowledge of the forces and their interactions is necessary. Although the experimental arrangements are not straightforward, accurate measurements of the horizontal frictional forces would be extremely useful. It seems likely that there is some form of grip-slip interaction between the ball and the surface, although it is not obvious how this would be recreated in a model. Further ultra-high-speed video footage would be useful to try to analyse deformation shapes and their effect on changing COR with different spin. An improved ball projection method which enables independent variables to be kept more consistent would also prove useful.

Increased model complexity

Throughout this study, one of the major underlying aims was to keep the model simple. Not only does this make it easy to understand and use, it makes it much faster to solve. There was also important placed on the value of model parameters which were easy to find. However, the nature of the spring-damper model used means that it is impossible to

predict some forms of behaviour – a tennis ball *simply is not a trivial assembly of two or three component parts.*

To improve the accuracy of the model would require substantial extra work and complexity (such as dealing with horizontal deformations). At some point the question must be asked as to whether this is the correct approach. In striving to create a physically representative model, it may be necessary to turn to other approaches such as finite element analysis. This has the benefit of creating a model which actually looks and behaves like a real tennis ball, but brings with it the downsides of vastly increased model solution times and the potential for "black box syndrome" – where the user tends to accept the forces, shapes and other such predictions as absolute truth.

Software development

The Tennis GUT software described in Chapter 11 was not a particularly important original objective of the project, but as the study progressed it proved to be an intriguing idea – particularly as there was a considerable amount of parallel research being undertaken in the fields of racket modelling and tennis aerodynamics. It is both instructive and practically useful to know how impact conditions propagate through an entire shot. There is potential for the software to be developed into a much more complete and user-friendly package, with a number of potential uses.

12.5 Concluding remarks

It is hoped that the work presented in this study gives a useful insight into understanding the physical processes of impact, as well as one possible approach to modelling and predicting their effects. The experimental results will also be useful for verifying existing and future models. With further development and application (particularly of the software user interface), there is great opportunity for controlling and improving the sport of tennis.

References

Ashcroft, A.D.C. & Stronge W. J. (2003). Dissipation during bounce of tennis balls. In: *Tennis Science and Technology 2* (Ed. by S. Miller), pp. 87-95. Pub. ITF, London.

Bell, M.J., Baker, S.W. & Canaway, P.M. (1985) Playing Quality of Sports Surfaces: A Review. *J. Sports Turf Res. Inst.*, **61**, 26-45.

Bernstein, A.D. (1977) Listening to the Coefficient of Restitution, *American Journal of Physics*, **45**, 41-44.

Bregar, M.J. & Moyer, W.W. (1990) *An automated system for field testing and soil impact analysis*, Natural and artificial playing fields: characteristics and safety features (ASTM STP 1073), pp 115-126.

Brody, H. (1986) The shortened service box. *TennisPro*, September/October, 6.

Brody, H. (1988) Why Slow Courts Give You More Time To Get To The Ball. *TennisPro*, July/August, 8-9.

Brody, H. (1990) The Tennis Ball Bounce Test. *The Physics Teacher*, September, 407-409.

Brody, H. (1992) Measuring the Softness of an Athletic Surface. *The Physics Teacher*, 30, 28-31.

Brody, H. (1994) That's how the ball bounces. *The Physics Teacher*, 494-497.

Brody, H. (1996) A modest proposal to improve tennis. *TennisPro*, January/February, 6-8.

Brody, H. & Cross, R. (2000) Proposals to slow the serve in tennis. In: *Tennis Science and Technology: Proceedings of the 1st International Congress on Tennis Science and Technology* (ed. S.J. Haake & A.O. Coe), pp. 261-268, Blackwell Science, Oxford.

Brown, T.M.C. & Cooke, A.J. (2000) Aeromechanical and aerodynamic behaviour of tennis balls. In: *Tennis Science and Technology: Proceedings of the 1st International Congress on Tennis Science and Technology* (ed. S.J. Haake & A.O. Coe), pp. 145-153, Blackwell Science, Oxford.

Capel-Davies, J. & Miller, S. (2003). Durability of tennis balls worn in a test rig. In: *Tennis Science and Technology 2* (Ed. by S. Miller), pp. 113-121. Pub. International Tennis Federation, London.

Carré, M.J. (2000). *The dynamics of cricket ball impacts and the effect of pitch construction*. PhD thesis, University of Sheffield.

Carré, M.J., Baker, S.W., Newell, A.J & Haake, S.J. (1999) The dynamic behaviour of cricket balls during impact and variations due to grass and soil type. *Sports Engineering*, **2**, 145-160.

Carré, M.J., Johnson, M.J. & Haake, S.J. (2002). Playing performance of tennis court surfaces. In: *The Engineering of Sport 4* (Ed. by S. Ujihashi & S.J. Haake), pp. 200-206. Pub. Blackwell Science Ltd., Oxford.

Chadwick, S.G. & Haake S.J. (2000) Methods to determine the aerodynamic forces acting on tennis balls in flight. In: *Tennis Science and Technology: Proceedings of the 1st International Congress on Tennis Science and Technology* (ed. S.J. Haake & A.O. Coe), pp. 127-134, Blackwell Science, Oxford.

Chadwick, S.G. (2003). *The aerodynamic properties of tennis balls*. PhD thesis, University of Sheffield.

Clegg, B. (1976) An Impact Testing Device for In Situ Base Course Evaluation, *Proceedings of the Australian Road Research Bureau*, **8**, 1-5.

Cislunar Aerospace, Inc. (2001) http://wings.avkids.com/Tennis/

Coe, A.O. (2000). The balance between technology and tradition in tennis. In: *Tennis Science and Technology* (Ed. by S.J. Haake & A.O. Coe), pp. 3-40. Pub. International Tennis Federation, London.

Cooke, A.J. (2000) An overview of tennis ball aerodynamics, *Sports Engineering*, **3**, 123-129.

Cox, A.L. (2003). Surface pace ratings of tennis surfaces. In: *Tennis Science and Technology 2* (Ed. by S. Miller), pp. 367-372. Pub. International Tennis Federation, London.

Cross, R (1999a) The bounce of a ball. *American Journal of Physics*, **67**, 222-227.

Cross, R (1999b) Dynamic properties of tennis balls. *Sports Engineering*, **2**, 23-34.

Cross, R. (2000a) Dynamics of the collision between a tennis ball and a tennis racket. In: *Tennis Science and Technology: Proceedings of the 1st International Congress on Tennis Science and Technology* (ed. S.J. Haake & A.O. Coe), pp. 67-74, Blackwell Science, Oxford.

Cross, R. (2000b) Dynamic testing of tennis balls. In: *Tennis Science and Technology: Proceedings of the 1st International Congress on Tennis Science and Technology* (ed. S.J. Haake & A.O. Coe), pp. 175-182, Blackwell Science, Oxford.

Cross, R (2002) Grip-slip behaviour of a bouncing ball. *American Journal of Physics*, **70** (11), 1093-1102.

Cross, R. (2003). Properties of tennis equipment: balls that bite, rackets that don't vibrate and strings that don't make any difference. In: *Tennis Science and Technology 2* (Ed. by S. Miller), pp. 17-30. Pub. International Tennis Federation, London.

Daish, C.B. (1972) *The Physics of Ball Games*, English Universities Press.

Davies, T.G. & Karim, U.F. (1995) An elastodynamic interpretation of impact test apparatus for soils, *Géotechnique*, **45**, 691-700.

Dignall, R.J. (1999) *The dynamics of tennis ball impacts*. M.Phil transfer report, University of Sheffield.

Dignall, R.J. & Haake, S.J. (2000) Analytical modelling of the impact of tennis balls on court surfaces. In: *Tennis Science and Technology: Proceedings of the 1st International Congress on Tennis Science and Technology* (ed. S.J. Haake & A.O. Coe), pp. 155-162, Blackwell Science, Oxford.

Dixon, S.J., Batt, M.E. & Collop, A.C. (2000) Impact absorbing characteristics of tennis playing surfaces. In: *Tennis Science and Technology: Proceedings of the 1st International Congress on Tennis Science and Technology* (ed. S.J. Haake & A.O. Coe), pp. 227-234, Blackwell Science, Oxford.

Dodd, D. (2003) *Portable Sports Surface Measurement Device: Understanding the requirements for realistic impact simulation*. MEng thesis, University of Sheffield.

Dowell, L.J., Smith, F., Miller, G., Hope, A. & Krebs, G. (1987) The Effect of Angle of Incidence on Rebound Deviation of a Tennis Ball, *J. Hum. Mov. Studies*, **13**, 69-73.

Dunlop Sports Co. Ltd. (1960) New Developments in Ball Testing, internal report.

Dunlop, J.I. (2000) Characterising the service bounce using a speed gun. In: *Tennis Science and Technology: Proceedings of the 1ˢᵗ International Congress on Tennis Science and Technology* (ed. S.J. Haake & A.O. Coe), pp. 183-190, Blackwell Science, Oxford.

Dunlop, J.J., Milner, C.J. & White, K.G. (1992) Sports surface-ball interactions: laboratory measurement techniques. *Journal of the Sports Turf Research Institute*, **68**, 114-123.

Elliott, B.C. (1983) Spin and the Power Serve in Tennis. *J. Hum. Mov. Studies*, **9** (2), 97-104.

Elliott, B., Marsh, A. & Blanksby, B. (1986) A Three-Dimensional Cinematographic Analysis of the Tennis Serve. *International Journal of Sport Biomechanics*, 2, 260-271.

Fischer, W. (1977) Tennis Racket, US Patent 4273331, 8ᵗʰ December 1977.

Fisher, A. (1977) Super racket - is this the shape of things to come in tennis? *Popular Science*, **210**, 44-47.

Groppel, J.L., Dillman, C.J. and Lardner, T.J. (1983) Derivation and validation of equations of motion to predict ball spin upon impact in tennis. *Journal of Sports Sciences*, **1**, 111-120.

Goodwill, S.R. (2002). *The dynamics of tennis ball impacts on tennis rackets*. PhD thesis, University of Sheffield.

Goodwill, S.R. & Haake, S.J., (2002) Why were spaghetti string rackets banned in the game of tennis? In: *The Engineering of Sport 4* (Ed. by S. Ujihashi & S.J. Haake), pp. 231-237. Pub. Blackwell Science Ltd., Oxford.

Goodwill, S.R., Chin, S.B. & Haake, S.J. (2004). Wind tunnel testing of spinning and non-spinning tennis balls. *Journal of Wind Engineering & Industrial Aerodynamics*, in review.

Haake, S.J. (1994) Golf ball impacts, greens and the golfer. In: *Science and Golf II: Proceedings of the World Scientific Congress of Golf* (Ed. by A.J. Cochran & M.R. Farrally), pp65-70. Pub. E & FN Spon, London.

Haake, S.J., Carré, M.J. & Goodwill, S.R. (2003). Modelling of oblique tennis ball impacts on tennis surfaces. In: *Tennis Science and Technology 2* (Ed. by S. Miller), pp. 133-137. Pub. International Tennis Federation, London.

Haake, S.J., Chadwick, S.G., Dignall, R.J., Goodwill, S.R. & Rose, P. (2000) Engineering tennis – slowing the game down. *Sports Engineering*, **3**, 131-143.

Haake, S.J., Rose, P. & Kotze, J. (2000) Reaction time testing and grand slam tie-break data. In: *Tennis Science and Technology: Proceedings of the 1ˢᵗ International Congress on Tennis Science and Technology* (ed. S.J. Haake & A.O. Coe), pp. 269-275, Blackwell Science, Oxford.

Haines, R. (2002) Haines Pendulum Instruction Booklet.

Hamilton, G.F. (2000). *The Development of Test Methods to Characterise Sports Surfaces*. MSc thesis, University of Sheffield.

Head, H. (1976) Tennis Racket, *US Patent 3,999,756.*

Hendee, S.P., Greenwald, R.M. & Crisco, J.J. (1998) Static and dynamic properties of various baseballs, *Journal of Applied Biomechanics*, 14, 390-400.

Henderson, R.L., Waddington, D.V. & Morehouse, C.A. (1990) Laboratory Measurements of Impact Absorption on Turfgrass and Soil Surfaces, Natural and artificial playing fields: characteristics and safety features (ASTM STP 1073), pp 127-135.

Holmes, G. & Bell, M.J, (1986) Technical Note - Playing Surface Hardness and Tennis Ball Rebound Resilience, *J. Sports Turf Res. Inst.*, 62, 207-210.

Hope, A., Dowell, L.J., Smith, F., Miller, G. & Krebs, G. (1988) A comparison of the effects of angle of incidence of slow, medium and fast incidence velocities on velocity deviation of a tennis ball, *Journal of Human Movement Studies*, 15, 299-305.

Hubbard, M. & Strong, W.J. (2001), "Bounce of hollow balls on flat surfaces", *Sports Engineering* 4(2), 49-61.

ITF (1997) *An Initial ITF Study on Performance Standards for Tennis Court Surfaces,* June 1997, Pub. International Tennis Federation, London.

ITF (2000a) *Rules of Tennis.* Pub. Wilton, Wright & Son Ltd, London.

ITF (2000b) *Court Surface Classification Scheme,* Pub. International Tennis Federation, London.

ITF (2004) http://www.itftennis.com

Johnson, K.L. (1983) The bounce of "superball", *International Journal of Mechanical Engineering Education*, 11, 57-63.

Johnson, S.H. & Lieberman, B.B. (1994) An analytical model for ball-barrier impact Part 2: A model for oblique impact. In: *Science and Golf II: Proceedings of the World Scientific Congress of Golf* (Ed. by A.J. Cochran & M.R. Farrally), pp315-320. Pub. E & FN Spon, London.

Johnson, W., Reid, S.W. & Trembaczowski-Ryder, R.E. (1972), "Impact, rebound and flight of a well-inflated pellicle as exemplified in association football", The Manchester Association of Engineers, Session 1972-73, 5, 1-25.

Kirk, R.F. (2003). *Oblique Impacts of Tennis Balls on Oblique Surfaces.* MEng thesis, University of Sheffield.

Kotze, J. & Mitchell, S.R. (2002). A tennis serve impact simulation machine. In: *The Engineering of Sport 4* (Ed. by S. Ujihashi & S.J. Haake), pp. 477-484. Blackwell Science Ltd., Oxford.

Leigh, D.C. & Lu, W.Y. (1992) Dynamics of the Interactions Between Balls, Strings, and Racket in Tennis, *International Journal of Sport Biomechanics*, 8, 181-206.

Lieberman, B.B. & Johnson, S.H. (1994) An analytical model for ball-barrier impact Part1: Models for normal impact. In: *Science and Golf II: Proceedings of the World Scientific Congress of Golf* (Ed. by A.J. Cochran & M.R. Farrally), pp309-314. Pub. E & FN Spon, London.

Lindemuth, J. (1971) The Effect of Air Resistance on Falling Balls, *American Journal of Physics*, 39, 757-759

Magnus, J.R. & Klaassen, F.J.G.M. (1999) The Effect of New Balls in Tennis: Four Years at Wimbledon, *Statistician (Journal of the Royal Statistical Society, Series D)*, **48**, 239-246,

Martin, R.B. (1990) *Problems associated with testing the impact absorption properties of artificial playing surfaces*, Natural and artificial playing fields: characteristics and safety features (ASTM STP 1073), pp 77-84.

Mastrad Ltd. (2004) http://www.mastrad.com/tortus.htm

McMahon, T.A. & Greene, P.R. (1979) The influence of track compliance on running, *Journal of Biomechanics*, **12**, 893-904.

Mehta, R. & Pallis, J. (2001). The aerodynamics of a tennis ball, *Sports Engineering*, **4**, 1-13.

Miller, S. (2003). Speed is of the Essence. In: *Tennis Science and Technology 2* (Ed. by S. Miller), pp. 3-13. Pub. International Tennis Federation, London.

Miller, S. & Capel-Davies, J. (2003). Using standard surfaces to validate surface pace measurement devices. In: *Tennis Science and Technology 2* (Ed. by S. Miller), pp. 139-145. Pub. International Tennis Federation, London.

Miller, S. & Messner, S. (2003). On the dynamic coefficient of restitution of tennis balls. In: *Tennis Science and Technology 2* (Ed. by S. Miller), pp. 97-104. Pub. International Tennis Federation, London.

Nigg, B.M. (1990) The validity and relevance of tests used for the assessment of sports surfaces, *Medicine and Science in Sports and Exercise*, **22**, 131-139.

Pallis, J.M. & Mehta, R.D. (2000) Tennis science collaboration between NASA and Cislunar Aerospace. In: *Tennis Science and Technology: Proceedings of the 1st International Congress on Tennis Science and Technology* (ed. S.J. Haake & A.O. Coe), pp. 135-144, Blackwell Science, Oxford.

Percival, A.L. (1976), "The impact and rebound of a football", The Manchester Association of Engineers, Session 1976-77, 5, 17-28.

Rogers III, J.N. & Waddington, D.V. (1990) *Portable apparatus for assessing impact characteristics of athletic field surfaces*, Natural and artificial playing fields: characteristics and safety features (ASTM STP 1073), pp 96-110.

Rose, P., Coe, A. & Haake S.J. (2000) The variation of static and dynamic tennis ball properties with temperature. In: *Tennis Science and Technology: Proceedings of the 1st International Congress on Tennis Science and Technology* (ed. S.J. Haake & A.O. Coe), pp. 169-174, Blackwell Science, Oxford.

Robinson, R.G. (1977) *Stevens Machine for Testing Deformation of Lawn Tennis Balls*, Wimbledon Lawn Tennis Museum.

Smith, P.A., Spencer, C.D. & Jones, D.E. (1981) Microcomputer listens to the coefficient of restitution, *American Journal of Physics*, **49**, 136-140.

South, N. (1996) *Aeromechanical Behaviour of the Tennis Ball*. MEng project report, Cambridge University.

Stepanek, A. (1988) The aerodynamics of tennis balls – The topspin lob, *Am. J. Phys.*, 56 (2), 138-142.

Stevens, P.H. (1925) Improvements in and Means for Testing Balls, Particularly those Used in Games, such as Lawn Tennis, *UK Patent 230,250*.

Teasdale, C. (2003). *Friction of artificial sports surfaces*. MEng thesis, University of Sheffield.

Ujihashi, S. (1994) Measurement of dynamic characteristics of golf balls and identification of their mechanical models. In: *Science and Golf II: Proceedings of the World Scientific Congress of Golf* (Ed. by A.J. Cochran & M.R. Farrally), pp302-308. Pub. E & FN Spon, London.

Van Gheluwe, B. & Deporte, E. (1992) Friction Measurement in Tennis on the Field and in the Laboratory, *International Journal of Sport Biomechanics*, **8**, 48-61.

Walker, C.A. (1996) Experimental mechanics and artificial turf, In: *The Engineering of Sport* (ed. S.J. Haake), pp239-242. Pub. Balkema, Rotterdam.

Wassing (2004) http://www.wassing.com/_uk/sport/tennis_e.htm

A Ball specifications from The Rules of Tennis

Extracts from the Rules of Tennis are listed below (ITF, 2000a).

The ball shall be more than 1.975 ounces (56.0 grams) and less than 2.095 ounces (59.4 grams) in weight.

The ball shall be more than 2.575 inches (6.541 cm) and less than 2.700 inches (6.858 cm) in diameter.

The ball shall have a bound of more than 53 inches (134.62 cm) and less than 58 inches (147.32 cm) when dropped 100 inches (254.00 cm) upon a flat, rigid surface e.g. concrete. The ball shall have a forward deformation of more than .220 of an inch (.559 cm) and less than .290 of an inch (.737 cm) and return deformation of more than .315 of an inch (.800 cm) and less than .425 of an inch (1.080 cm) at 18 lb. (8.165 kg) load. The two deformation figures shall be the averages of three individual readings along three axes of the ball and no two individual readings shall differ by more than .030 of an inch (.076 cm) in each case.

An additional section was added to the rules in 2000 describing two new types of balls.

From 1ˢᵗ January 2000 until 31ˢᵗ December 2001 two further types of tennis ball may be used on an experimental basis.

The first type is identical to those described in paragraphs a. to c. above except that the ball shall have a forward deformation of more than .195 inches (.495 cm) and less than .235 inches (.597 cm) and return deformation of more than .295 inches (.749 cm) and less than .380 inches (.965 cm). This type of ball shall be described as Type 1 and may be used in either a pressurised or non-pressurised form.

Another type is identical to those described in paragraphs a. to c. above except that the size shall be more than 2.750 inches (6.985 cm) and less than 2.875 inches (7.302 cm) in diameter as determined by ring gauges and detailed in Appendix I section (iv). This type of ball shall be described as Type 3 and may be used in either a pressurised or non-pressurised form.

All other type of ball defined by Rule 3 shall be described as ball Type 2.

For the purpose of tournaments played under this experiment:

1. Ball Type 1 (fast) should only be used for play on court surface types which have been classified as Category 1 (slow pace) (see Appendix I).

2. Ball Type 2 (medium) should only be used for play on court surface types which have been classified as Category 2 (medium/medium-fast pace) (see Appendix I).

3. Ball Type 3 (slow) should only be used for play on court surface types which have been classified as Category 3 (fast pace) (see Appendix I).

For non-professional play any ball type may be used on any surface type.

The Rules of Tennis give a list of regulations describing how each of the approval tests should be performed. Extracts from these are listed below.

Tests should be made at a temperature of approximately 20° Centigrade and relative humidity of 60%.

The limits given are for tests conducted in an atmospheric pressure resulting in a barometric reading of approximately 30 inches (76 cm). Other standards may be fixed for localities with differing average temperature, humidity and pressure.

Metal ring-gauges are used to test the ball diameter. Two circular openings have the minimum and maximum diameters specified for the particular ball type. The inner surface of the gauge has a convex profile with a radius of one-sixteenth of an inch (.159 cm). The ball should not drop through the smaller opening by its own weight and should drop through the larger opening by its own weight.

Before carrying out any of the tests, a ball should be pre-compressed by approximately one inch (2.54 cm) on each of three mutually perpendicular axes. This should be carried out three times on each axis, and the tests completed within two hours of pre-compression.

B Normal impact model – force-deflection results

B.1 Introduction

Supplemental data is presented to complement that given in Chapter 8. Force-deflection graphs comparing model predictions to experimental data are shown for normal impacts between approximately 6 and 20 ms^{-1}, for the four ball types considered in that chapter.

B.2 Model results

B.2.a Pressurised ball
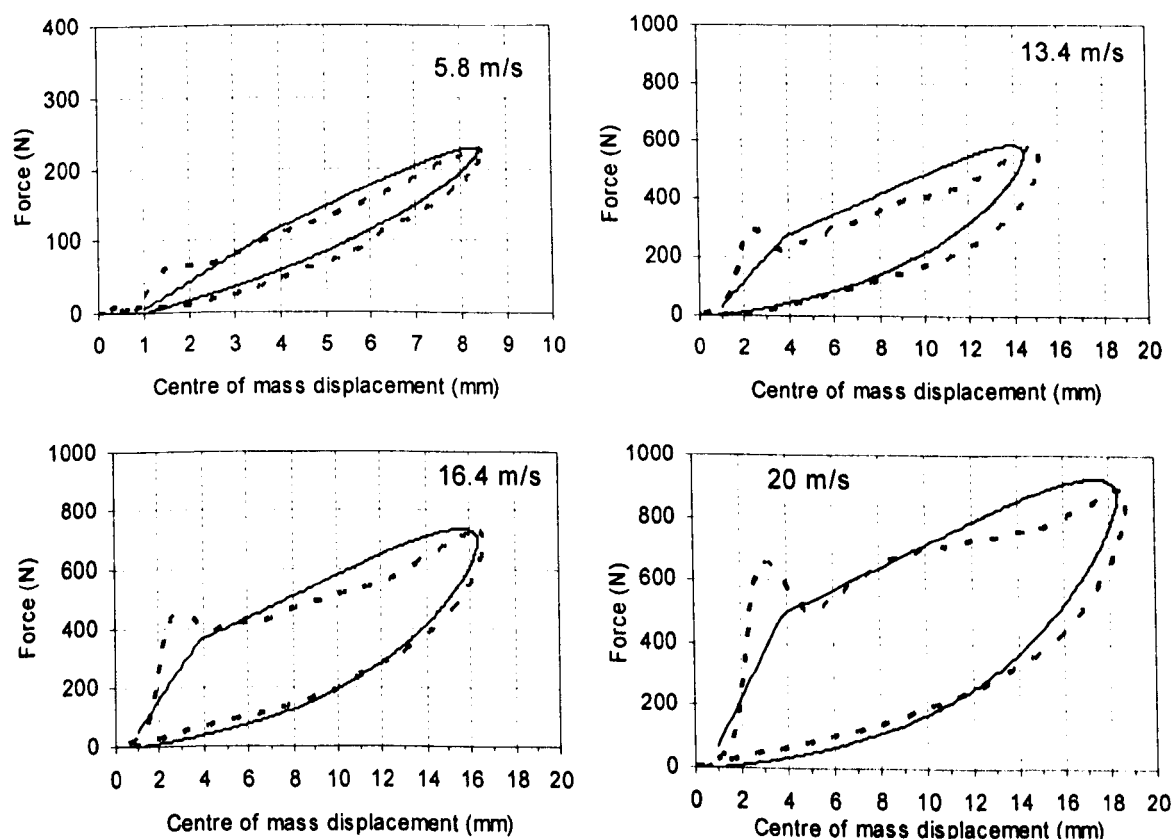
Figure B.1 Comparison of experimental data (dashed lines) and model data (solid lines) for force against centre of mass displacement, for a pressurised ball impacting normally between 5.8 and 20 ms^{-1}.
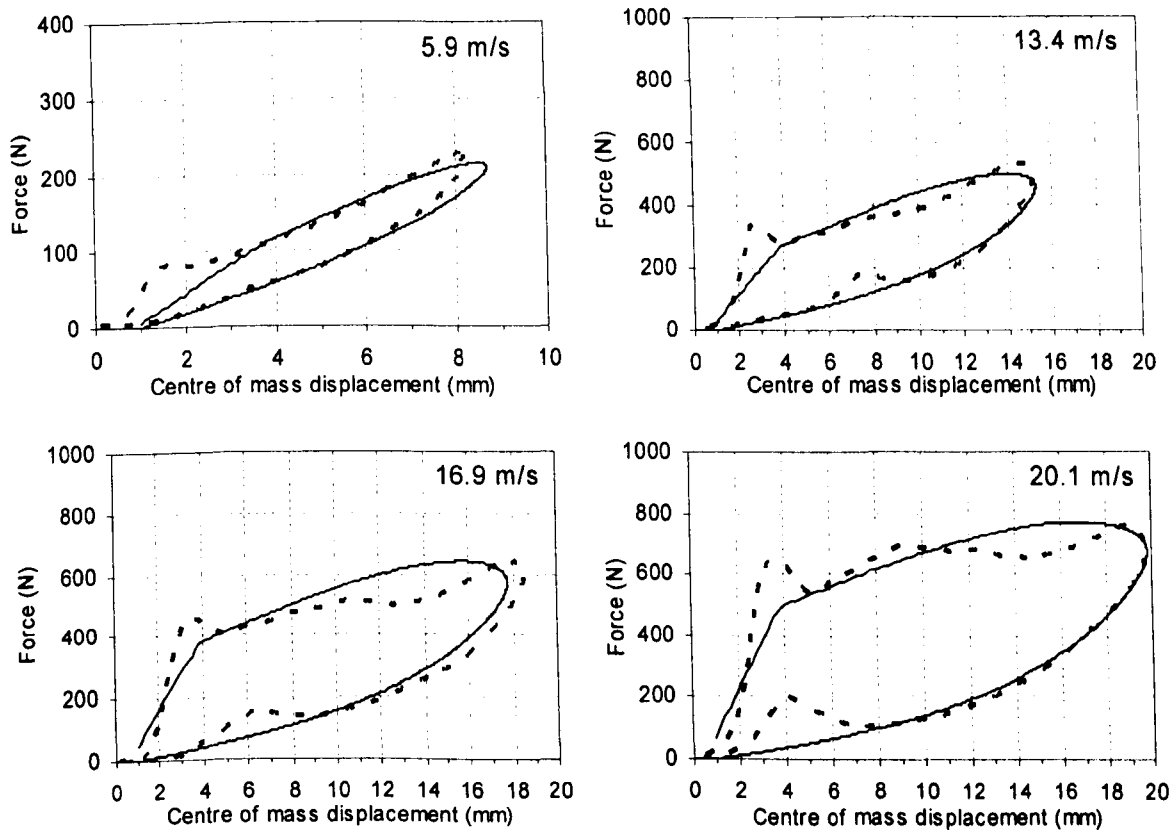
B.2.b   Pressureless ball

Figure B.2 Comparison of experimental data (dashed lines) and model data (solid lines) for force against centre of mass displacement, for a pressureless ball impacting normally between 5.9 and 20.1 ms^{-1}.
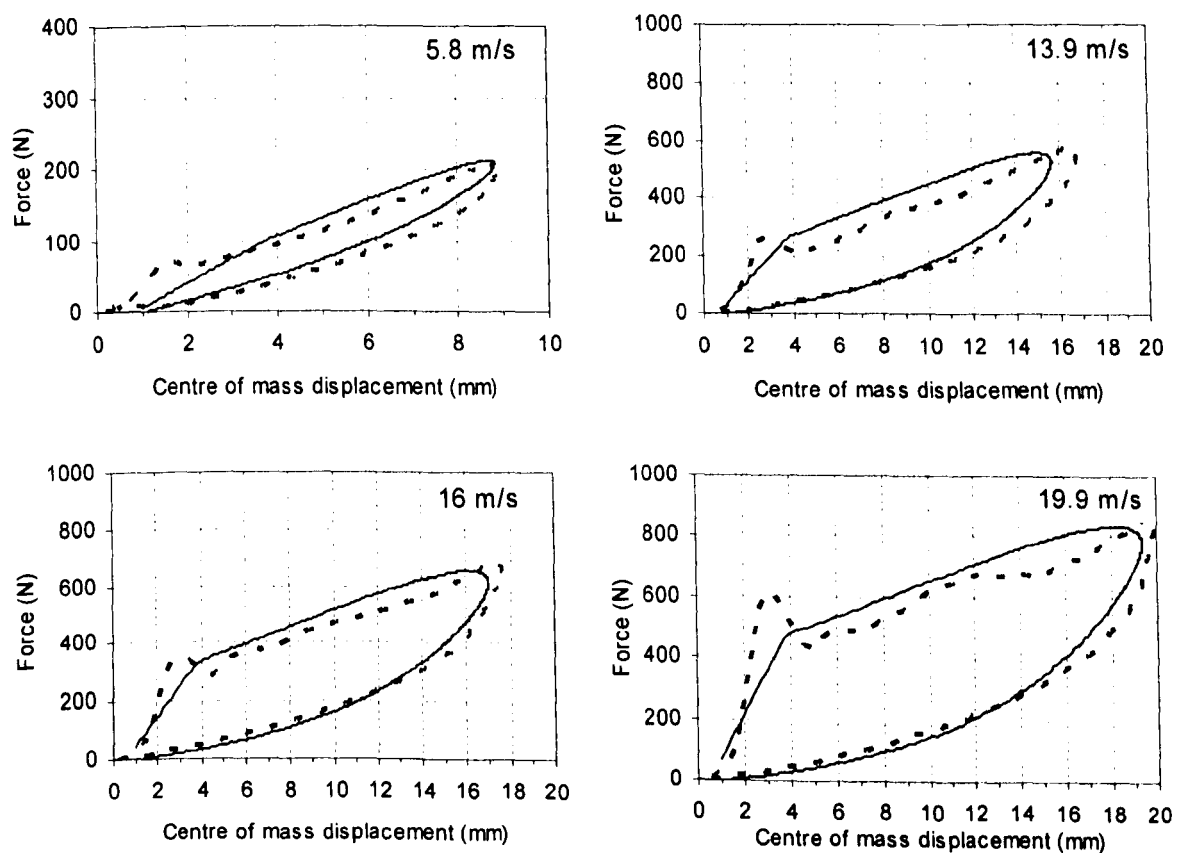
B.2.c　Oversized ball

Figure B.3 Comparison of experimental data (dashed lines) and model data (solid lines) for force against centre of mass displacement, for an oversized ball impacting normally between 5.8 and 19.9 ms^{-1}.
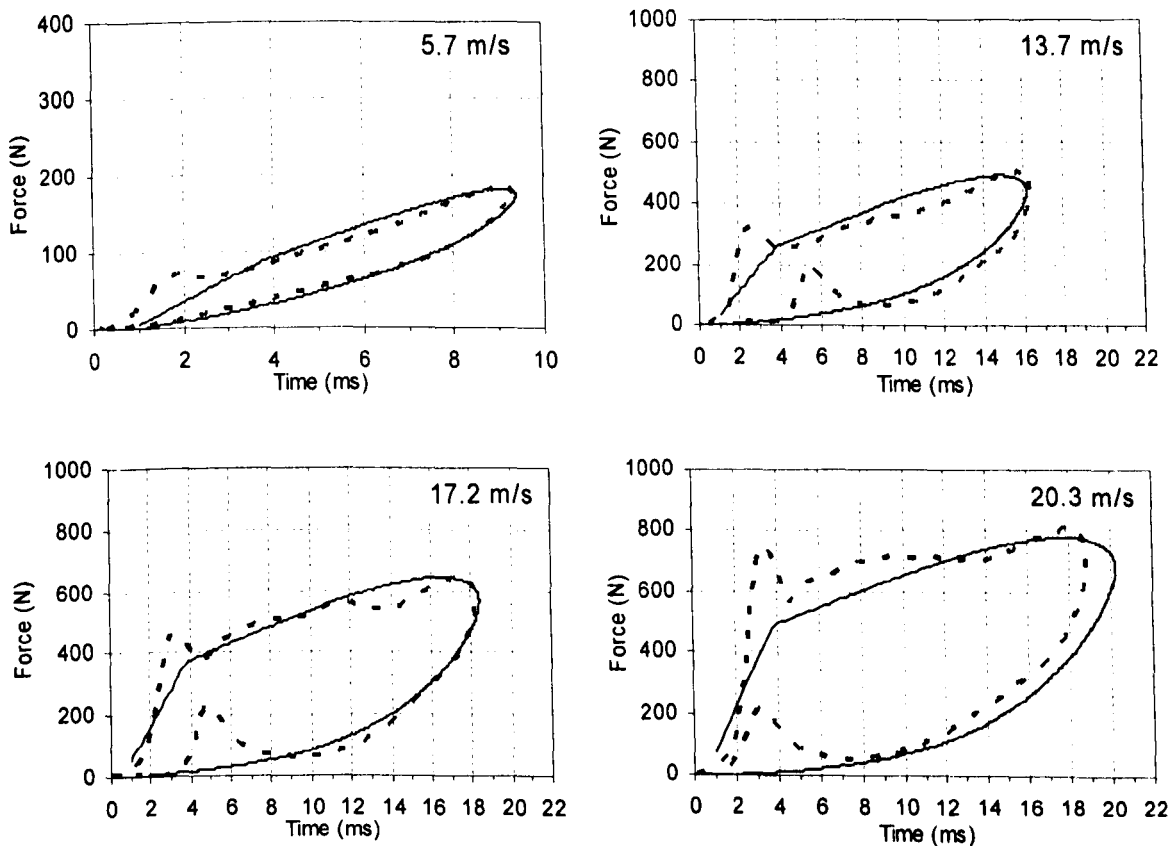
B.2.d   Punctured ball

Figure B.4 Comparison of experimental data (dashed lines) and model data (solid lines) for force against centre of mass displacement, for a punctured ball impacting normally between 5.9 and 20.1 ms^{-1}.

C Oblique impact data

C.1 Introduction

This section presents some of the raw data from the various oblique tests, which may prove useful in the future. Table C.1 shows a summary of the nominal impact conditions describing each test. For conciseness, relevant SI units are used throughout, where no units are quoted.

Table C.1 Summary of the various parameters for oblique impact tests. The parameter of interest in each test is shaded.

	Surface	Ball type	V_{in} (m/s)	θ_{in} (degrees to horiz)	ω_{in} (rads^{-1})
Varying spin, speed & angle	Medium	Pressurised	30	24	-600 to 600
			25 to 60	24	0
			30	24 to 52	0
Changing surface	Fast ($\mu = 0.3$)	Pressurised	30	24	-600 to 600
	Medium ($\mu = 0.55$)				
	Slow ($\mu = 0.61$)				
Changing ball type	Medium	Pressurised	30	24	-600 to 600
		Pressureless			
		Punctured			

Appendix C

C.2 Varying spin tests

Spin ref	Ball #	In Vx	Vy	Vr	angle	Topspin	Out Vx	Vy	Vr	angle	Topspin	ΔSpin	<– rolling spin –> from Vx	from Vr	% of Vx roll spin	% of Vr roll spin	Δ Vx	Δ Vy	ΔVx/ΔVy	horiz COR	vert COR	abs COR	θout/θin
B3	1	28.19	-12.64	30.89	24.15	-618.80	16.90	7.67	18.55	24.40	45.40	664.2	517.5	568.3	8.8	8.0	-11.3	20.3	0.56	0.5995	0.607	0.601	1.011
	2	28.50	-12.78	31.23	24.15	-621.70	17.44	7.77	19.09	24.03	25.20	646.9	531.2	581.6	4.7	4.3	-11.1	20.6	0.54	0.6120	0.608	0.611	0.995
	3	28.34	-12.23	30.87	23.35	-620.50	17.05	7.29	18.55	23.16	37.00	657.5	520.5	566.1	7.1	6.5	-11.3	19.5	0.58	0.6017	0.596	0.601	0.992
B2.5	1	28.34	-12.54	30.99	23.88	-646.60	17.35	7.90	19.06	24.48	45.40	692	531.2	583.7	8.5	7.8	-11.0	20.4	0.54	0.6120	0.630	0.615	1.025
	2	28.59	-12.23	31.10	23.17	-577.30	17.96	7.28	19.38	22.06	13.10	590.4	547.2	590.4	2.4	2.2	-10.6	19.5	0.54	0.6284	0.595	0.623	0.952
	3	29.95	-12.58	32.48	22.78	-558.30	19.05	7.67	20.53	21.92	25.90	584.2	581.4	626.8	4.5	4.1	-10.9	20.2	0.54	0.6360	0.610	0.632	0.963
B2	1	27.10	-12.31	29.77	24.43	-484.50	15.72	8.18	17.72	27.48	139.90	624.4	481.4	542.7	29.1	25.8	-11.4	20.5	0.56	0.5800	0.664	0.595	1.125
	2	27.02	-12.16	29.63	24.22	-480.10	16.59	8.12	18.46	26.07	116.90	597	505.2	562.4	23.1	20.8	-10.4	20.3	0.51	0.6138	0.668	0.623	1.076
	3	27.88	-12.85	30.70	24.76	-535.70	16.46	8.29	18.43	26.72	108.70	644.4	502.5	562.6	21.6	19.3	-11.4	21.1	0.54	0.5906	0.645	0.600	1.079
B1.5	1	26.76	-11.66	29.19	23.55	-329.00	15.52	7.99	17.45	27.25	191.80	520.8	475.3	534.6	40.4	35.9	-11.2	19.7	0.57	0.5799	0.685	0.598	1.157
	2	27.69	-12.28	30.29	23.92	-390.60	16.29	8.06	18.18	26.33	169.00	559.6	496.3	553.7	34.1	30.5	-11.4	20.3	0.56	0.5884	0.657	0.600	1.101
	3	26.33	-12.39	29.10	25.20	-284.10	15.62	8.03	17.56	27.20	173.90	458	476.6	535.9	36.5	32.4	-10.7	20.4	0.52	0.5931	0.648	0.603	1.079
B1	1	26.56	-12.00	29.14	24.32	-282.70	15.44	8.16	17.46	27.86	259.80	542.5	472.9	534.9	54.9	48.6	-11.1	20.2	0.55	0.5813	0.680	0.599	1.146
	2	26.20	-11.24	28.51	23.22	-340.50	14.82	7.71	16.71	27.49	197.40	537.9	451.4	508.9	43.7	38.8	-11.4	19.0	0.60	0.5656	0.686	0.586	1.184
	3	26.13	-11.62	28.59	23.97	-350.60	15.75	7.90	17.62	26.63	184.30	534.9	480.8	537.8	38.3	34.3	-10.4	19.5	0.53	0.6028	0.680	0.616	1.111
B0.5	1	26.03	-11.41	28.42	23.67	-411.50	15.16	7.74	17.02	27.05	183.90	595.4	464.3	521.4	39.6	35.3	-10.9	19.2	0.57	0.5824	0.678	0.599	1.143
	2	26.17	-12.00	28.79	24.64	-320.00	15.39	8.10	17.39	27.75	169.70	489.7	468.9	529.8	36.2	32.0	-10.8	20.1	0.54	0.5881	0.675	0.604	1.126
	3	26.10	-12.39	28.89	25.40	-400.40	15.12	8.32	17.25	28.82	114.90	515.3	461.4	526.6	24.9	21.8	-11.0	20.7	0.53	0.5792	0.671	0.597	1.135
0	1	25.79	-11.10	28.07	23.30	-124.80	15.78	7.91	17.65	26.63	374.90	499.7	483.3	540.7	77.6	69.3	-10.0	19.0	0.53	0.6120	0.713	0.629	1.143
	2	25.20	-10.64	27.35	22.89	-98.40	15.02	8.13	17.08	28.42	297.90	396.3	457.6	520.3	65.1	57.3	-10.2	18.8	0.54	0.5962	0.764	0.625	1.242
	3	25.61	-11.03	27.89	23.29	-145.70	15.42	8.27	17.50	28.20	368.20	513.9	470.8	534.2	78.2	68.9	-10.2	19.3	0.53	0.6022	0.750	0.628	1.211
T0.5	1	25.63	-11.77	28.20	24.67	133.40	14.06	9.04	16.72	32.74	506.70	373.3	430.8	512.1	117.6	98.9	-11.6	20.8	0.56	0.5487	0.768	0.593	1.327
	2	25.71	-12.70	28.67	26.29	104.00	14.99	9.09	17.53	31.23	502.00	398	456.6	534.0	109.9	94.0	-10.7	21.8	0.49	0.5831	0.716	0.611	1.188
	3	25.09	-11.62	27.65	24.84	126.50	14.34	8.64	16.74	31.07	498.50	372	437.7	511.1	113.9	97.5	-10.7	20.3	0.53	0.5716	0.744	0.606	1.251
T1	1	25.72	-11.58	28.21	24.24	180.30	15.22	8.92	17.64	30.37	555.20	374.9	466.2	540.4	119.1	102.7	-10.5	20.5	0.51	0.5918	0.770	0.625	1.253
	2	26.02	-11.85	28.59	24.48	239.30	15.05	8.86	17.47	30.47	541.80	302.5	458.5	532.0	118.2	101.8	-11.0	20.7	0.53	0.5786	0.748	0.611	1.245
	3	25.48	-12.16	28.23	25.51	278.60	15.18	8.63	17.46	29.61	548.30	269.7	463.3	532.9	118.4	102.9	-10.3	20.8	0.50	0.5958	0.710	0.618	1.161
T1.5	1	26.17	-12.08	28.82	24.77	345.40	16.60	9.17	18.96	28.91	585.30	239.9	508.5	580.8	115.1	100.8	-9.6	21.2	0.45	0.6343	0.759	0.658	1.167
	2	27.57	-12.31	30.19	24.07	330.90	17.17	9.31	19.53	28.45	606.50	275.6	523.1	595.0	115.9	101.9	-10.4	21.6	0.48	0.6230	0.756	0.647	1.182
	3	26.71	-12.70	29.58	25.42	255.30	17.10	9.62	19.62	29.36	572.10	316.8	521.9	598.8	109.6	95.5	-9.6	22.3	0.43	0.6400	0.757	0.663	1.155
T2	1	27.94	-12.37	30.55	23.89	396.20	19.13	9.60	21.40	26.66	612.80	216.6	585.8	655.5	104.6	93.5	-8.8	22.0	0.40	0.6846	0.776	0.700	1.116
	2	26.95	-12.23	29.59	24.42	481.30	19.03	8.84	20.99	24.92	628.30	147	579.7	639.3	108.4	98.3	-7.9	21.1	0.38	0.7063	0.723	0.709	1.021
	3	26.64	-12.62	29.48	25.35	492.00	18.40	9.65	20.77	27.67	610.30	118.3	561.6	634.1	108.7	96.2	-8.2	22.3	0.37	0.6907	0.764	0.705	1.092
T2.5	1	29.19	-13.16	32.02	24.27	685.80	21.81	10.05	24.01	24.75	694.20	8.4	667.8	735.4	103.9	94.4	-7.4	23.2	0.32	0.7470	0.764	0.750	1.020
	2	29.19	-12.47	31.74	23.13	577.00	20.21	8.83	22.05	23.59	753.30	176.3	615.6	671.8	122.4	112.1	-9.0	21.3	0.42	0.6923	0.708	0.695	1.020
	3	28.34	-12.54	30.99	23.88	540.10	20.92	9.48	22.97	24.37	684.00	143.9	638.6	701.1	107.1	97.6	-7.4	22.0	0.34	0.7382	0.756	0.741	1.021
T3	1	29.66	-13.16	32.45	23.93	637.80	21.99	9.37	23.90	23.08	746.60	108.8	673.5	732.1	110.8	102.0	-7.7	22.5	0.34	0.7415	0.712	0.737	0.964
	2	29.66	-13.48	32.57	24.44	710.20	21.76	9.45	23.72	23.47	638.10	-72.1	662.7	722.5	96.3	88.3	-7.9	22.9	0.34	0.7337	0.701	0.728	0.960
	3	29.42	-13.32	32.30	24.35	539.00	22.15	9.37	24.05	22.93	664.40	125.4	676.0	734.0	98.3	90.5	-7.3	22.7	0.32	0.7527	0.703	0.745	0.942

C.3 Varying speed tests

Speed ref (mph)	Ball #	In Vx	Vy	Vr	angle	Topspin	Out Vx	Vy	Vr	angle	Topspin	<- rolling spin -> ΔSpin	from Vx	from Vr	% of Vx roll spin	% of Vr roll spin	(abs) delta Vx	delta Vy	horiz COR	vert COR	abs COR	θ_{out}/θ_{in}	ΔVx/ΔVy
60	1	22.40	-10.28	24.65	24.64	-92.10	11.94	7.96	14.35	33.67	359.50	451.6	365.8	439.5	98.3	81.8	10.5	18.2	0.5331	0.774	0.582	1.367	0.574
	2	22.70	-10.18	24.88	24.14	-69.30	12.55	7.51	14.63	30.90	335.10	404.4	382.4	445.6	87.6	75.2	10.1	17.7	0.5530	0.738	0.588	1.280	0.574
	3	21.67	-9.53	23.67	23.75	-28.80	12.25	7.53	14.38	31.58	385.20	414	373.8	438.8	103.0	87.8	9.4	17.1	0.5653	0.790	0.607	1.330	0.552
70	1	26.49	-11.71	28.96	23.85	-39.50	15.52	8.73	17.81	29.35	406.90	446.4	475.4	545.4	85.6	74.6	11.0	20.4	0.5861	0.745	0.615	1.230	0.536
	2	26.87	-11.51	29.23	23.20	-11.20	15.57	8.93	17.95	29.83	418.70	429.9	474.2	546.6	88.3	76.6	11.3	20.4	0.5795	0.775	0.614	1.286	0.553
	3	26.74	-12.05	29.33	24.26	-63.20	15.36	8.73	17.66	29.60	409.80	473	468.8	539.2	87.4	76.0	11.4	20.8	0.5743	0.724	0.602	1.220	0.548
80	1	32.06	-14.21	35.07	23.90	-67.50	19.12	9.95	21.56	27.48	462.40	529.9	585.7	660.2	78.9	70.0	12.9	24.2	0.5965	0.700	0.615	1.150	0.536
	2	31.17	-13.23	33.86	23.00	-66.90	17.78	10.24	20.52	29.93	413.60	480.5	541.7	625.0	76.4	66.2	13.4	23.5	0.5706	0.774	0.606	1.301	0.570
	3	31.01	-13.07	33.65	22.85	-29.80	18.48	9.87	20.95	28.12	434.50	464.3	564.1	639.6	77.0	67.9	12.5	22.9	0.5960	0.756	0.623	1.231	0.546
90	1	38.14	-16.33	41.49	23.18	-37.20	22.68	11.95	25.64	27.79	485.00	522.2	694.6	785.2	69.8	61.8	15.5	28.3	0.5947	0.732	0.618	1.199	0.547
	2	38.43	-17.63	42.28	24.64	-95.30	22.60	11.11	25.18	26.19	521.80	617.1	688.3	767.0	75.8	68.0	15.8	28.7	0.5880	0.630	0.596	1.063	0.551
	3	38.04	-16.03	41.28	22.85	-84.80	22.52	11.57	25.32	27.20	454.60	539.4	687.4	772.8	66.1	58.8	15.5	27.6	0.5920	0.722	0.613	1.190	0.562
100	1	43.52	-18.35	47.23	22.86	-70.40	25.99	11.86	28.57	24.52	499.50	569.9	796.0	875.0	62.7	57.1	17.5	30.2	0.5973	0.646	0.605	1.073	0.580
	2	43.02	-18.65	46.88	23.44	-81.10	26.04	12.83	29.03	26.24	539.50	620.6	793.0	884.1	68.0	61.0	17.0	31.5	0.6053	0.688	0.619	1.120	0.539
	3	43.12	-17.95	46.70	22.60	-8.40	25.80	12.66	28.73	26.13	548.70	557.1	787.4	877.1	69.7	62.6	17.3	30.6	0.5982	0.705	0.615	1.156	0.566
110	1	49.09	-21.37	53.54	23.52	-74.40	28.99	13.84	32.13	25.52	543.20	617.6	888.0	983.9	61.2	55.2	20.1	35.2	0.5906	0.648	0.600	1.085	0.571
	2	49.19	-21.77	53.79	23.87	-71.00	29.01	13.88	32.16	25.56	569.50	640.5	883.7	979.6	64.4	58.1	20.2	35.6	0.5899	0.638	0.598	1.071	0.566
	3	49.29	-21.67	53.84	23.73	-76.80	28.79	13.84	31.95	25.67	635.50	712.3	878.9	975.2	72.3	65.2	20.5	35.5	0.5842	0.639	0.593	1.082	0.577
120	1	54.17	-22.79	58.77	22.81	-87.30	32.99	16.02	36.67	25.89	511.50	598.8	1010.5	1123.3	50.6	45.5	21.2	38.8	0.6091	0.703	0.624	1.135	0.546
	2	54.17	-22.99	58.84	22.99	-49.60	33.08	13.92	35.89	22.82	567.80	617.4	1007.7	1093.3	56.3	51.9	21.1	36.9	0.6107	0.606	0.610	0.992	0.571
	3	54.38	-21.69	58.54	21.75	-64.90	33.68	14.42	36.64	23.17	643.20	708.1	1028.2	1118.4	62.6	57.5	20.7	36.1	0.6195	0.665	0.626	1.066	0.573

C.4 Varying angle tests

Ang ref	Ball #	In Vx	Vy	Vr	angle	Topspin	Out Vx	Vy	Vr	angle	Topspin	ΔSpin	rolling spin from Vx	from Vr	% of Vx roll spin	% of Vr roll spin	(abs) delta Vx	delta Vy	horiz COR	+ve Vyin	vert COR	abs COR	θout/θin	ΔVx/ΔVy
angle1	1	20.37	-26.04	33.06	51.96	-43.70	10.22	18.81	21.41	61.49	292.60	336.3	313.0	655.7	93.5	44.6	10.2	44.8	0.5015	26.04	0.723	0.648	1.184	0.226
	2	20.81	-26.51	33.70	51.86	-13.30	9.83	19.10	21.48	62.77	296.00	309.3	299.3	654.2	98.9	45.2	11.0	45.6	0.4722	26.51	0.721	0.637	1.210	0.241
	3	20.75	-26.82	33.92	52.27	-1.80	10.59	19.06	21.80	60.93	289.90	291.7	323.4	665.6	89.7	43.6	10.2	45.9	0.5104	26.82	0.711	0.643	1.166	0.221
angle2	1	24.59	-23.14	33.76	43.27	-74.60	12.08	17.55	21.30	55.44	386.60	461.2	370.1	652.5	104.5	59.3	12.5	40.7	0.4915	23.14	0.758	0.631	1.281	0.307
	2	24.72	-23.60	34.17	43.67	-39.90	12.48	17.69	21.65	54.80	378.00	417.9	380.2	659.6	99.4	57.3	12.2	41.3	0.5050	23.60	0.750	0.634	1.255	0.296
	3	24.06	-23.35	33.53	44.15	-43.10	12.20	16.83	20.78	54.05	416.50	459.6	372.5	634.5	111.8	65.6	11.9	40.2	0.5072	23.35	0.720	0.620	1.224	0.295
angle3	1	26.63	-19.67	33.11	36.44	-56.30	13.54	14.96	20.17	47.86	458.90	515.2	414.5	617.8	110.7	74.3	13.1	34.6	0.5082	19.67	0.761	0.609	1.313	0.378
	2	26.96	-19.81	33.45	36.30	-29.10	13.41	15.28	20.33	48.73	476.30	505.4	408.5	619.4	116.6	76.9	13.6	35.1	0.4974	19.81	0.772	0.608	1.342	0.386
	3	26.43	-19.49	32.84	36.40	-8.90	13.68	14.52	19.95	46.70	459.80	468.7	417.6	608.9	110.1	75.5	12.8	34.0	0.5176	19.49	0.745	0.607	1.283	0.375
angle4	1	29.16	-17.27	33.89	30.65	-3.10	15.09	13.65	20.35	42.13	552.90	556	462.2	623.2	119.6	88.7	14.1	30.9	0.5176	17.27	0.790	0.600	1.375	0.455
	2	28.79	-17.23	33.55	30.89	-48.90	15.31	12.60	19.83	39.47	540.00	588.9	466.2	603.9	115.8	89.4	13.5	29.8	0.5315	17.23	0.732	0.591	1.278	0.452
	3	28.18	-16.57	32.69	30.45	-48.00	15.03	12.46	19.53	39.66	569.40	617.4	458.9	596.1	124.1	95.5	13.2	29.0	0.5334	16.57	0.752	0.597	1.302	0.453
angle5	1	29.47	-14.68	32.92	26.48	-25.10	15.82	12.08	19.90	37.35	587.90	613	484.7	609.6	121.3	96.4	13.6	26.8	0.5370	14.68	0.823	0.605	1.411	0.510
	2	30.23	-14.78	33.65	26.06	-24.40	15.98	11.61	19.75	35.98	617.50	641.9	486.8	601.6	126.8	102.6	14.2	26.4	0.5287	14.78	0.785	0.587	1.381	0.540
	3	30.18	-14.91	33.66	26.28	-35.40	15.95	11.58	19.71	35.97	596.10	631.5	487.0	601.7	122.4	99.1	14.2	26.5	0.5286	14.91	0.777	0.586	1.369	0.537
angle6	1	31.65	-14.37	34.76	24.41	-133.10	18.20	10.45	20.99	29.85	518.20	651.3	557.5	642.8	92.9	80.6	13.4	24.8	0.5752	14.37	0.727	0.604	1.223	0.542
	2	31.74	-14.02	34.69	23.83	-102.40	18.88	10.18	21.44	28.33	499.50	601.9	574.9	653.2	86.9	76.5	12.9	24.2	0.5948	14.02	0.726	0.618	1.189	0.532
	3	31.08	-13.08	33.72	22.82	-106.70	17.85	10.31	20.61	30.02	502.70	609.4	544.8	629.2	92.3	79.9	13.2	23.4	0.5742	13.08	0.788	0.611	1.315	0.566

Appendix C

C.5 Changing balls – medium surface, pressurised and punctured balls

Note: P denotes pressurised, N denotes punctured.

surf	ball type	spin	V_{xin}	V_{yin}	Vin	ω_{in}	θ_{in}	V_{xout}	V_{yout}	Vout	ω_{out}	θ_{out}	COR	COR_{abs}	μ	SPR	% roll	θ_{out}/θ_{in}
medium	P	-3	27.94	-14.25	31.36	-603.7	27.02	16.61	9.53	19.15	106.8	29.85	0.67	0.61	0.48	52.4	21.2	1.10
medium	P	-3	29.15	-14.54	32.58	-759.6	26.51	15.71	9.48	18.35	149.0	31.10	0.65	0.56	0.56	44.1	31.3	1.17
medium	P	-3	29.67	-14.41	32.99	-588.5	25.89	15.58	10.11	18.57	131.4	32.96	0.70	0.56	0.57	42.5	27.8	1.27
medium	P	-2	30.50	-15.33	34.14	-557.3	26.69	17.24	9.45	19.66	160.7	28.74	0.62	0.58	0.53	46.5	30.8	1.08
medium	P	-2	30.18	-14.55	33.51	-568.3	25.74	16.53	9.55	19.09	177.4	30.01	0.66	0.57	0.57	43.4	35.4	1.17
medium	P	-2	30.26	-14.79	33.68	-599.4	26.05	16.86	9.34	19.28	152.6	28.99	0.63	0.57	0.56	44.5	29.9	1.11
medium	P	-1	29.58	-13.09	32.35	-402.9	23.86	18.85	9.21	20.98	224.2	26.05	0.70	0.65	0.48	51.9	39.2	1.09
medium	P	-1	29.34	-12.82	32.02	-361.6	23.60	19.02	8.79	20.95	210.9	24.80	0.69	0.65	0.48	52.2	36.6	1.05
medium	P	-1	29.32	-12.57	31.90	-378.6	23.20	17.84	9.29	20.12	183.3	27.50	0.74	0.63	0.53	47.5	33.9	1.19
medium	P	0	28.16	-12.51	30.81	-18.1	23.96	17.71	9.98	20.33	386.3	29.39	0.80	0.66	0.46	53.5	72.0	1.23
medium	P	0	27.58	-12.11	30.12	-36.7	23.71	16.67	9.63	19.25	396.1	30.00	0.79	0.64	0.50	49.8	78.4	1.27
medium	P	0	27.25	-12.15	29.84	-34.4	24.03	16.73	9.74	19.35	387.3	30.21	0.80	0.65	0.48	51.9	76.4	1.26
medium	P	1	28.15	-12.28	30.71	349.7	23.56	17.83	10.26	20.57	590.4	29.91	0.84	0.67	0.46	54.2	109.3	1.27
medium	P	1	28.00	-12.78	30.78	266.6	24.54	17.83	9.82	20.36	680.3	28.85	0.77	0.66	0.45	55.0	125.9	1.18
medium	P	1	27.55	-12.57	30.28	281.9	24.52	17.39	9.96	20.04	568.8	29.78	0.79	0.66	0.45	54.9	107.9	1.21
medium	P	2	30.36	-13.09	33.06	444.9	23.32	22.96	9.62	24.89	694.3	22.74	0.74	0.75	0.33	67.4	99.8	0.98
medium	P	2	30.03	-12.52	32.54	548.3	22.63	21.15	10.53	23.63	671.1	26.46	0.84	0.73	0.39	61.5	104.7	1.17
medium	P	2	30.75	-13.01	33.39	515.7	22.93	22.58	10.25	24.80	690.6	24.42	0.79	0.74	0.35	64.9	100.9	1.06
medium	P	3	30.55	-13.62	33.45	537.9	24.03	23.84	9.64	25.71	686.6	22.01	0.71	0.77	0.29	71.1	95.1	0.92
medium	P	3	31.41	-12.99	33.99	722.7	22.46	22.87	9.92	24.93	749.3	23.45	0.76	0.73	0.37	62.7	108.1	1.04
medium	P	3	31.19	-13.11	33.83	541.0	22.80	23.14	9.87	25.15	706.8	23.10	0.75	0.74	0.35	65.0	100.8	1.01
medium	N	-3	28.80	-14.83	32.39	-547.2	27.25	16.90	8.15	18.76	189.8	25.73	0.55	0.58	0.52	48.2	37.1	0.94
medium	N	-3	29.27	-14.64	32.73	-518.5	26.57	16.87	8.14	18.73	193.7	25.76	0.56	0.57	0.54	45.6	37.9	0.97
medium	N	-3	29.85	-14.82	33.33	-541.6	26.40	16.63	7.92	18.42	172.7	25.47	0.53	0.57	0.55	41.9	34.3	0.96
medium	N	-2	28.81	-14.84	32.41	-523.6	27.25	16.69	8.06	18.53	200.0	25.78	0.54	0.57	0.53	47.0	39.5	0.95
medium	N	-2	29.72	-15.09	33.33	-549.4	26.91	16.74	8.74	18.88	245.5	27.56	0.58	0.57	0.55	45.5	48.4	1.02
medium	N	-2	29.61	-14.76	33.08	-550.2	26.49	16.78	8.30	18.72	237.7	26.32	0.56	0.57	0.56	44.4	46.7	0.99
medium	N	-1	27.63	-13.29	30.66	-304.5	25.69	17.66	8.00	19.39	264.0	24.36	0.60	0.63	0.47	53.2	49.3	0.95
medium	N	-1	28.96	-13.42	31.92	-289.9	24.87	17.77	7.73	19.38	226.4	23.51	0.58	0.61	0.53	47.1	42.0	0.95
medium	N	-1	28.57	-13.40	31.56	-276.0	25.13	17.81	8.65	19.80	291.1	25.89	0.65	0.63	0.49	51.2	53.9	1.03
medium	N	0	28.85	-12.93	31.62	-41.9	24.15	18.30	8.51	20.18	457.8	24.94	0.66	0.64	0.49	50.8	82.6	1.03
medium	N	0	28.26	-11.97	30.69	-58.0	22.95	17.47	8.56	19.45	447.5	26.10	0.72	0.63	0.53	47.4	84.5	1.14
medium	N	0	28.61	-12.91	31.39	-40.7	24.29	17.70	9.01	19.86	327.7	26.97	0.70	0.63	0.50	50.2	61.1	1.11
medium	N	1	29.49	-12.68	32.11	250.0	23.27	19.14	8.15	20.81	470.3	23.07	0.64	0.65	0.50	50.3	81.1	0.99
medium	N	1	29.49	-12.41	32.00	313.1	22.82	19.18	8.55	21.00	497.8	24.03	0.69	0.66	0.49	50.8	85.7	1.05
medium	N	1	29.47	-12.65	32.07	289.3	23.23	18.42	8.53	20.30	456.3	24.84	0.67	0.63	0.52	47.8	81.8	1.07
medium	N	2	29.46	-12.73	32.10	321.3	23.36	20.93	7.61	22.27	533.8	19.98	0.60	0.69	0.42	58.1	84.1	0.86
medium	N	2	30.10	-12.71	32.67	397.7	22.89	21.59	7.10	22.72	559.3	18.20	0.56	0.70	0.43	57.0	85.5	0.80
medium	N	2	28.97	-13.20	31.83	354.3	24.50	20.60	8.02	22.11	545.7	21.28	0.61	0.69	0.39	60.6	87.4	0.87
medium	N	3	30.68	-12.66	33.19	473.3	22.43	21.25	7.87	22.66	626.6	20.33	0.62	0.68	0.46	54.1	97.3	0.91
medium	N	3	30.37	-13.75	33.34	416.5	24.36	21.40	7.94	22.83	465.0	20.36	0.58	0.68	0.41	58.6	71.7	0.84
medium	N	3	29.27	-13.16	32.09	354.9	24.21	21.54	8.09	23.01	486.6	20.59	0.62	0.72	0.36	63.7	74.5	0.85

Appendix C

C.6 Changing balls – medium surface, pressurised and punctured balls

Note: L denotes pressureless

surf	ball type	spin	V_{xin}	V_{yin}	V_{in}	ω_{in}	θ_{in}	V_{xout}	V_{yout}	V_{out}	ω_{out}	θ_{out}	COR	COR$_{abs}$	μ	SPR	% roll	θ_{out}/θ_{in}
medium	L	-3	30.39	-14.83	33.81	-716.4	26.02	15.44	9.51	18.14	228.3	31.61	0.64	0.54	0.61	38.6	48.8	1.22
medium	L	-3	31.39	-16.33	35.38	-516.1	27.48	15.56	9.61	18.29	186.9	31.71	0.59	0.52	0.61	39.0	39.7	1.15
medium	L	-3	30.88	-14.52	34.13	-575.5	25.17	15.59	9.11	18.05	198.6	30.32	0.63	0.53	0.65	35.3	42.0	1.20
medium	L	-2	29.36	-15.78	33.33	-584.1	28.25	17.09	9.52	19.56	239.2	29.13	0.60	0.59	0.49	51.5	46.2	1.03
medium	L	-2	31.15	-15.59	34.84	-537.6	26.59	16.53	9.67	19.15	264.0	30.33	0.62	0.55	0.58	42.1	52.7	1.14
medium	L	-2	30.04	-15.70	33.89	-624.0	27.59	15.83	9.36	18.40	262.8	30.60	0.60	0.54	0.57	43.3	54.8	1.11
medium	L	-1	30.22	-13.21	32.98	-341.1	23.62	18.12	8.55	20.04	323.0	25.26	0.65	0.61	0.56	44.4	58.8	1.07
medium	L	-1	29.64	-13.05	32.39	-333.1	23.77	17.27	8.80	19.38	281.3	27.00	0.67	0.60	0.57	43.4	53.8	1.14
medium	L	-1	29.98	-12.87	32.62	-362.1	23.23	18.06	9.08	20.21	274.3	26.69	0.71	0.62	0.54	45.7	50.1	1.15
medium	L	0	27.68	-12.17	30.23	-24.8	23.73	16.50	9.02	18.80	434.6	28.66	0.74	0.62	0.53	47.2	86.9	1.21
medium	L	0	27.74	-12.18	30.30	-12.3	23.71	17.40	8.58	19.40	395.5	26.24	0.70	0.64	0.50	50.2	75.0	1.11
medium	L	0	27.17	-11.99	29.70	1.5	23.81	17.03	8.95	19.24	405.1	27.71	0.75	0.65	0.48	51.6	78.5	1.16
medium	L	1	28.80	-13.72	31.90	395.1	25.48	18.79	9.11	20.89	551.1	25.86	0.66	0.65	0.44	56.2	96.8	1.02
medium	L	1	30.10	-13.29	32.91	365.9	23.82	19.51	9.38	21.65	556.1	25.69	0.71	0.66	0.47	53.3	94.1	1.08
medium	L	1	28.24	-12.65	30.94	454.6	24.13	19.08	9.55	21.33	524.5	26.60	0.76	0.69	0.41	58.7	90.7	1.10
medium	L	2	27.96	-14.01	31.27	575.2	26.62	22.50	9.44	24.40	657.5	22.77	0.67	0.78	0.23	76.7	96.4	0.86
medium	L	2	30.49	-13.88	33.50	580.3	24.47	22.81	8.66	24.40	603.5	20.78	0.62	0.73	0.34	65.9	87.3	0.85
medium	L	2	32.11	-14.62	35.28	625.0	24.48	23.70	9.94	25.70	672.1	22.75	0.68	0.73	0.34	65.8	93.6	0.93
medium	L	3	30.85	-12.73	33.37	468.4	22.43	23.37	9.36	25.17	749.7	21.82	0.73	0.75	0.34	66.1	105.9	0.97
medium	L	3	30.21	-14.83	33.66	592.8	26.15	24.02	8.86	25.61	660.0	20.26	0.60	0.76	0.26	73.9	90.7	0.77
medium	L	3	29.66	-14.54	33.03	455.7	26.11	24.74	9.46	26.49	629.9	20.93	0.65	0.80	0.20	79.5	84.0	0.80

C.7 Changing surface – fast and slow surfaces with pressurised balls

surf	ball type	spin	V_{xin}	V_{yin}	V_{in}	ω_{in}	θ_{in}	V_{xout}	V_{yout}	V_{out}	ω_{out}	θ_{out}	COR	COR_{abs}	μ	SPR	% roll	θ_{out}/θ_{in}
fast	P	-3	28.97	-15.17	32.70	-634.9	27.63	19.87	9.04	21.83	-28.1	24.46	0.60	0.67	0.38	62.4	-4.7	0.89
fast	P	-3	31.51	-14.96	34.88	-633.8	25.40	23.05	9.51	24.94	-118.5	22.43	0.64	0.71	0.35	65.4	-17.0	0.88
fast	P	-3	31.05	-14.50	34.27	-687.4	25.04	22.78	8.79	24.41	-195.8	21.11	0.61	0.71	0.36	64.5	-28.4	0.84
fast	P	-2	30.34	-14.27	33.53	-521.6	25.18	23.27	9.43	25.11	-177.2	22.06	0.66	0.75	0.30	70.1	-25.1	0.88
fast	P	-2	31.12	-14.14	34.18	-595.9	24.44	21.74	8.10	23.20	27.0	20.42	0.57	0.68	0.42	57.8	4.1	0.84
fast	P	-2	29.28	-13.87	32.40	-588.5	25.35	21.17	8.92	22.97	-69.6	22.86	0.64	0.71	0.36	64.4	-10.8	0.90
fast	P	-1	28.12	-13.08	31.01	-355.0	24.95	21.57	9.01	23.38	-6.7	22.66	0.69	0.75	0.30	70.3	-1.0	0.91
fast	P	-1	28.18	-14.00	31.46	-328.0	26.42	22.56	9.44	24.46	63.4	22.71	0.67	0.78	0.24	76.0	9.3	0.86
fast	P	-1	27.78	-13.02	30.68	-328.4	25.10	22.15	9.55	24.12	-31.2	23.32	0.73	0.79	0.25	75.0	-4.6	0.93
fast	P	0	26.05	-13.03	29.13	-33.9	26.57	21.98	9.40	23.91	212.3	23.15	0.72	0.82	0.18	81.9	31.9	0.87
fast	P	0	27.22	-13.20	30.26	-59.2	25.87	21.92	9.74	23.99	210.7	23.97	0.74	0.79	0.23	76.9	31.7	0.93
fast	P	0	26.84	-12.80	29.73	-0.3	25.50	21.64	9.55	23.66	207.8	23.81	0.75	0.80	0.23	76.8	31.7	0.93
fast	P	1	27.58	-12.61	30.33	317.4	24.56	22.16	9.81	24.23	390.6	23.88	0.78	0.80	0.24	75.8	58.2	0.97
fast	P	1	26.51	-13.04	29.54	348.3	26.19	22.28	9.83	24.35	374.6	23.80	0.75	0.82	0.18	81.5	55.5	0.91
fast	P	1	26.62	-13.86	30.01	424.2	27.51	21.87	10.21	24.14	354.2	25.03	0.74	0.80	0.20	80.3	53.4	0.91
fast	P	2	27.97	-14.29	31.41	468.6	27.06	23.56	9.99	25.59	561.8	22.98	0.70	0.81	0.18	81.8	78.7	0.85
fast	P	2	28.28	-13.04	31.14	475.6	24.75	22.80	8.99	24.51	626.6	21.51	0.69	0.79	0.25	75.1	90.7	0.87
fast	P	2	28.88	-13.60	31.92	470.1	25.22	25.00	9.45	26.72	589.5	20.70	0.69	0.84	0.17	83.2	77.8	0.82
fast	P	3	29.36	-14.22	32.62	599.4	25.84	23.99	9.17	25.68	599.3	20.93	0.65	0.79	0.23	77.0	82.4	0.81
fast	P	3	29.70	-13.92	32.80	561.2	25.11	24.48	10.35	26.58	645.4	22.91	0.74	0.81	0.21	78.5	87.0	0.91
fast	P	3	29.18	-13.80	32.28	518.8	25.31	23.78	10.20	25.87	671.0	23.21	0.74	0.80	0.23	77.5	93.1	0.92
slow	P	-3	29.69	-14.36	32.97	-652.6	25.81	15.14	8.68	17.45	125.0	29.84	0.60	0.53	0.63	36.9	27.2	1.16
slow	P	-3	30.05	-14.72	33.46	-690.8	26.09	15.85	8.94	18.20	110.9	29.42	0.61	0.54	0.60	40.0	23.1	1.13
slow	P	-3	28.77	-14.87	32.38	-731.2	27.33	14.87	9.19	17.48	195.1	31.73	0.62	0.54	0.58	42.2	43.3	1.16
slow	P	-2	29.17	-13.31	32.06	-611.3	24.53	15.94	8.79	18.20	156.2	28.87	0.66	0.57	0.60	40.1	32.3	1.18
slow	P	-2	29.95	-14.76	33.39	-597.0	26.24	14.94	9.19	17.54	226.4	31.60	0.62	0.53	0.63	37.3	50.0	1.20
slow	P	-2	29.98	-14.52	33.31	-577.9	25.84	14.41	9.00	16.99	280.4	31.98	0.62	0.51	0.66	33.8	64.2	1.24
slow	P	-1	27.61	-12.68	30.39	-372.5	24.67	14.05	9.20	16.80	251.7	33.22	0.73	0.55	0.62	38.0	59.1	1.35
slow	P	-1	28.43	-13.15	31.33	-306.9	24.82	14.45	9.20	17.13	230.6	32.50	0.70	0.55	0.63	37.5	52.7	1.31
slow	P	-1	27.45	-13.27	30.49	-381.1	25.80	13.65	9.50	16.63	305.3	34.84	0.72	0.55	0.61	39.4	73.8	1.35
slow	P	0	27.01	-12.97	29.97	-36.4	25.64	14.03	10.11	17.29	464.1	35.76	0.78	0.58	0.56	43.7	109.1	1.39
slow	P	0	26.37	-12.85	29.33	-22.5	25.99	13.25	9.89	16.54	421.5	36.74	0.77	0.56	0.58	42.3	105.0	1.41
slow	P	1	27.35	-12.80	30.19	304.4	25.09	17.34	10.37	20.21	503.8	30.87	0.81	0.67	0.43	56.8	95.9	1.23
slow	P	1	26.56	-12.99	29.57	290.5	26.06	16.83	10.50	19.83	579.4	31.96	0.81	0.67	0.41	58.5	113.6	1.23
slow	P	1	27.99	-13.09	30.90	272.6	25.06	17.14	10.30	20.00	543.9	31.00	0.79	0.65	0.46	53.6	104.7	1.24
slow	P	2	28.24	-14.06	31.54	474.5	26.46	20.92	9.88	23.13	644.2	25.29	0.70	0.73	0.31	69.4	101.6	0.96
slow	P	2	28.34	-13.13	31.23	487.6	24.86	20.22	9.91	22.52	625.7	26.09	0.75	0.72	0.35	64.8	102.1	1.05
slow	P	2	27.71	-13.06	30.64	477.2	25.22	20.45	9.26	22.45	626.2	24.36	0.71	0.73	0.33	67.5	101.0	0.97
slow	P	3	28.55	-13.73	31.68	501.0	25.69	22.03	10.29	24.31	638.6	25.03	0.75	0.77	0.27	72.9	95.7	0.97
slow	P	3	28.09	-13.87	31.33	493.6	26.28	21.60	9.75	23.70	598.9	24.30	0.70	0.76	0.27	72.5	91.5	0.92
slow	P	3	28.68	-14.86	32.30	756.2	27.39	21.74	9.95	23.91	716.0	24.60	0.67	0.74	0.28	72.0	108.7	0.90